University of Thessaly
School of Engineering
Department of Mechanical Engineering

Doctoral Thesis

The effect of pulmonary surfactant on alveolar dynamics

Konstantinos Bouchoris

Supervisor: Prof. Vasilis Bontozoglou

Submitted in partial fulfillment of the requirements for the degree of Doctor of Philosophy in Mechanical Engineering at the University of Thessaly

Volos, Greece
2023

The effect of pulmonary surfactant on alveolar dynamics

by

Konstantinos Bouchoris

Abstract

Understanding of the properties of pulmonary surfactant (PS) and of its effect on alveolar dynamics during the breathing cycle is of paramount importance for lung physiology and pathophysiology. As a first step, a minimum model is proposed that describes the temporal dynamics of an interface uniformly laden with PS and undergoing consecutive compression/relaxation cycles. The model is based on Frumkin/Langmuir equilibrium and on an equation of state that includes the intrinsic compressibility of the densely packed monolayer. Adsorption/desorption dynamics is taken to be kinetically-limited, and film collapse during extreme compression is accounted for by a sublayer reservoir and a simple kinetic expression for monolayer replenishment during re-expansion. The model is validated and found to agree quantitatively with independent data in the literature, taken at physiologically relevant conditions. The best-fit values of the key model parameters are found to be physically meaningful and the characteristics of dilatational elasticity are discussed.

The above model is subsequently introduced in the description of the spatio-temporal dynamics of an oscillating alveolus. The latter is taken as a spherical cap, lined internally with a surfactant-laden liquid film, and the dynamics of this liquid film are investigated by a lubrication approximation. A novel boundary condition, supported by experimental data and scaling arguments, is applied at the rim. The condition enforces mass conservation of water and surfactant by matching the 'large-scale' dynamics of the alveolus to 'small-scale' equilibrium over mid-alveolar septa of small but finite thickness. Linear and weakly nonlinear analysis around the conditions in a non-oscillating cap indicates that the intensity of shearing motion in the liquid, induced by Marangoni stresses, is related to the film thickness over the rim, and shearing velocity at the interface is predicted an order-of-magnitude lower than the velocity of radial oscillation. Though Marangoni stresses dominate the interfacial dynamics, capillary stresses affect significantly the interior flow field. In particular, they produce spatial modulations in flow rate, surface concentration of surfactant and wall shear stress, whose length scale varies with $Ca^{-1/3}$, i.e. is determined by a balance between capillary and viscous forces. Non-zero adsorption kinetics modifies at first order only the amplitude and phase of surface concentration, but affects all other variables at second order. In particular, it sets a steady drift of surfactant away from the alveolus and towards the rim. In view of the above, an attempt is made to relate the present predictions to physiological findings about air flow and particle deposition inside alveoli, and about shear stress-inflicted damage in diseased lungs. Finally, a parametric analysis pertaining to the geometrical parameters of the alveolus model and the surfactant is presented in order to deriving possible physiological and pathophysiological implications.

Η επίδραση του πνευμονικού επιφανειοδραστικού στη δυναμική των κυψελίδων

Κωνσταντίνος Μπουχώρης

Περίληψη

Η κατανόηση των ιδιοτήτων του πνευμονικού επιφανειοδραστικού (pulmonary surfactant) και της επίδρασής του στην δυναμική των κυψελίδων κατά την διάρκεια της αναπνοής είναι καθοριστικής σημασίας στην πνευμονική φυσιολογία και παθοφυσιολογία. Αρχικά, έχει προταθεί ένα μαθηματικό μοντέλο που περιγράφει την δυναμική απόκριση με τον χρόνο μιας υγρής διεπιφάνειας που είναι χωρικά ομοιόμορφα επικαλυμμένη με PS και υπόκειται σε διαδοχικούς κύκλους συμπίεσης/διαστολής. Το μοντέλο βασίζεται στην ισόθερμο ισορροπίας Frumkin/Langmuir και σε μια καταστατική εξίσωση που συμπεριλαμβάνει την εγγενή συμπιεστότητα της επιφανειοδραστικής μονοστιβάδας σε υψηλές συγκεντρώσεις. Η δυναμική της προσρόφησης/εκρόφησης θεωρείται ως κινητικά ελεγχόμενη και η κατάρευση της μονοστιβάδας κατά τη διάρκεια της μέγιστής συμπίεσης λαμβάνεται υπόψη μέσω μίας υποεπιφανειακής δεξαμενής επιφανειοδραστικού και μιας απλής κινητικής έκφραση για την αναπλήρωση της διεπιφάνειας σε επιφανειοδραστικό κατά την επανα-διαστολή της. Το μοντέλο επικυρώνεται με τα αποτελέσματα να συμφωνούν ποσοτικά με ανεξάρτητα αποτελέσματα της βιβλιογραφίας που αφορούν φυσιολογικές συνθήκες. Οι βέλτιστες τιμές των κύριων παραμέτρων του μοντέλου είναι αποδεκτές απο φυσικής άποψης. Επιπλέον, αναλύονται τιμές που αφορούν την διασταλτική ελαστικότητα.

Εν συνεχεία, το εν λόγω μοντέλο χρησιμοποιείται για την περιγραφή της χωρικής και χρονικής δυναμικής/απόκρισης μιας ταλαντευόμενης κυψελίδας. Η τελευταία θεωρείται ως ενα σφαιρικό κέλυφος, επικαλυμμένο εσωτερικά με εναν υγρό υμένα η διεπιφάνεια του οποίου είναι επικαλυμμένη με επιφανειοδραστικό. Η δυναμική του υγρού υμένα μελετάται μέσω της θεωρίας λίπανσης. Μια νέα συνοριακή συνθήκη, η οποία υποστηρίζεται από πειραματικές ενδείξεις και ενισχύεται από τη σύγκριση χαρακτηριστικών κλιμάκων, εφαρμόζεται στην είσοδο της κυψελίδας. Η συνθήκη επιβάλλει την τοπική διατήρηση της μάζας του υγρού και του επιφανειοδραστικού, συνδυάζοντας την δυναμική στην κλίματα της κυψελίδας με την τοπική ισορροπία στην μικρο-κλίμακα του ανοίγματος που χαρακτηρίζεται από το μη-μηδενικό πάχος του χείλους.

Γραμμική και ασθενώς μη-γραμμική ανάλυση του προβλήματος γύρω από την θέση ισορροπίας (ακίνητη κυψελίδα) δείχνει ότι η ένταση της διατμητικής ροής στον υμένα, η οποία προκαλείται από τάσεις Marangoni, σχετίζεται με το πάχος του υμένα πάνω στο άνοιγμα της κυψελίδας, και η διατμητική ταχύτητα ακριβώς πάνω στη διεπιφάνεια είναι κατά μία τάξη μεγέθους μικρότερη από την ακτινική ταχύτητα του ταλαντευόμενου τοιχώματος. Προκύπτει ότι ενω οι τάσεις Marangoni κυριαρχούν στην δυναμική της διεπιφάνειας, οι τριχοειδείς τάσεις επιδρούν σημαντικά το πεδίο ροής στο εσωτερικό του υμένα. Συγκεκριμένα, παράγουν χωρικές διακυμάνσεις στην ογκομετρική παροχή του υγρού, της επιφανειακής συγκέντρωσης επιφανειοδραστικού και της διατμητικής δύναμης στο τοίχωμα το χαρακτηριστικό μήκος των οποίων μεταβάλλεται ως $Ca^{-1/3}$, προκύπτει δηλαδή από την ισορροπία τριχοειδών και ιξωδών δυνάμεων. Η κινητική του επιφανειοδραστικού λόγω μη-μηδενικής προσρόφησης επηρεάζει στην προσέγγιση 1ης τάξης μόνο το εύρος και τη φάση ταλάντωσης της επιφανειακής συγκέντρωσης και επηρεάζει όλες τις υπόλοιπες μεταβλητές κατά 2η τάξη. Συγκεκριμένα, θέτει μια σταθερή με το χρόνο εκροή επιφανειοδραστικού μακριά από την κυψελίδα, προς την κατεύθυνση του χείλους. Βασει των παραπάνω, επιτελείται μια προσπαθεια συσχέτισης των προβλέψεων του μοντέλου με δεδομένα φυσιολογίας σχετικά με την ροή αέρα και

την εναπόθεση σωματιδίων στο εσωτερικό των κυψελίδων, καθώς και την πρόκληση τραύματος λόγω τάσεων σε ασθενικούς πνεύμονες. Τέλος, παρουσιάζεται μια παραμετρική ανάλυση σχετικά με τις γεωμετρικές και τις επιφανειοδραστικές παραμέτρους του μοντέλου με σκοπό την εξαγωγή πιθανών φυσιολογικών και παθοφυσιολογικών συμπερασμάτων.

Examination Committee

Certified by the members of the Dissertation Committee

Prof. Vasilis Bontozoglou, Supervisor
Department of Mechanical Engineering
University of Thessaly

Prof. Nikolaos Pelekasis,
Department of Mechanical Engineering
University of Thessaly

Prof. Nikolaos Andritsos,
Department of Mechanical Engineering
University of Thessaly

Prof. Athanasios Papathanasiou,
Department of Mechanical Engineering
University of Thessaly

Prof. John Tsamopoulos,
Department of Chemical Engineering
University of Patras

Assoc. Prof. George Karapetsas,
Department of Chemical Engineering
Aristotle University of Thessaloniki

Prof. Demetrios T. Papageorgiou,
Department of Mathematics
Imperial College London

Acknowledgements

With the completion of the present dissertation, it is a great opportunity to thank all of those who encouraged me during this 3.5-year-long ”Odyssey”. First and foremost, I express from the bottom of my heart my gratitude to my supervisor, Professor Vasilis Bontozoglou for all that he has done by entrusting me with this research opportunity. It would have been impossible to complete it without his guidance and constant support, thus I admire him so much not only as an academic teacher and scientist but as a person and a mentor. I will forever be morally indebted to him; I cannot imagine having a better supervisor. I would also like to thank Prof. Nikolaos Andritsos for the great cooperation and his trust as a teaching assistant during my Ph.D. studies. Further, I express my gratitude to Professors Nikolaos Pelekasis, Nikolaos Andritos, Athanasios Papathanasiou, John Tsamopoulos, Demetrios T. Papageorgiou and Associate Professor George Karapetsas for accepting to be members of the dissertation committee. I feel deeply honored to have a committee of such a high scientific caliber and impact. I would like to personally thank Prof. Demetrios T. Papageorgiou for his special interest in my work and his constructive corrections and comments. Many thanks to Nikoletta Sachinidou and Faye Chronopoulou for their great help concerning bureaucratic matters during my studies. This dissertation was financially supported by ELPEN Pharmaceutical, Athens, Greece and from scholarships of the postgraduate studies program of the Department of Mechanical Engineering.

Nevertheless, I cannot thank enough my friends and people close to me for their support and mutual understanding. My dear friends Nikos, Rafail, and Vasilis thank you so much for the happy moments and your support during difficult times from the very beginning, you are my fellowship. One cannot wish for better friends. Of course, I cannot thank enough my friend Vaggelis Dougas and his family; his ”leap of faith” months prior to the completion of my dissertation shall be an example to me. I hope I’ve been a good friend. Special thanks to dear colleagues Kiriaki-Evangelia Aslani, Despoina Karamichailidou, and Anna Katsiavria for the interesting conversations about fluid mechanics and life in general. I greatly acknowledge the support of my university friends

Apostolis, Marina, Stavros and Stefania for the joyful moments all of these years. Besides, the moral assistance of Faye Papakosta is greatly appreciated. Lastly, I want to express my gratitude to mrs Katerina for her endless love and for standing as a second mother to me after my mothers passing. I dedicate this dissertation to her.

Contents

List of Figures

List of Tables

List of useful symbols in S.I. units

σ	Surface tension	$\mathrm{N\,m^{-1}}$
Γ	Surface concentration	$\mathrm{mol\,m^{-2}}$
Γ_∞	Saturation interfacial concentration	$\mathrm{mol\,m^{-2}}$
C	Bulk concentration	$\mathrm{mol\,m^{-3}}$
B	Reservoir content	mol
Π	Surface pressure	$\mathrm{N\,m^{-1}}$
u	Velocity	$\mathrm{m\,s^{-1}}$
p	Pressure	Pa
R	Radius	m
μ	Dynamic viscosity	$\mathrm{kg\,m^{-1}\,s^{-1}}$
ρ	Mass density	$\mathrm{kg\,m^{-3}}$
α	2D intrinsic compressibility	$\mathrm{m\,N^{-1}}$
E_A	Surface dilatational elasticity	$\mathrm{N\,m^{-1}}$
A	Surface Area	$\mathrm{m^2}$
A_μ	Area occupied per molecule	$\mathrm{m^2}$
E_G	Gibbs elasticity	$\mathrm{N\,m^{-1}}$
a	Frumkin parameter	dimensionless
$k_{\mathrm{ads}}C_{10}$	Adsorption rate	$\mathrm{s^{-1}}$
k_{des}	Desorption rate	$\mathrm{s^{-1}}$
k_r	Reservoir exchange rate	$\mathrm{s^{-1}}$
$\mathcal{R}$	Universal gas constant	$8.314\ \mathrm{J\,mol^{-1}\,K^{-1}}$
N_{Avog}	Avogadro number	$6.022\times10^{23}\ \mathrm{mol^{-1}}$
g	Gravitational accelaration	$9.81\ \mathrm{m\,s^{-2}}$
Ω	Mean molar area	$\mathrm{m^2\,mol^{-1}}$
T	Absolute temperature	K
h	Alveolar liquid film thickness	m
Q	Volumetric flowrate	$\mathrm{m^3\,s^{-1}}$
Q_Γ	Surfactant flowrate	$\mathrm{mol\,s^{-1}}$
D_s	Interfacial diffusion coefficient	$\mathrm{m^2\,s^{-1}}$

Chapter 1

Scope and outline of the thesis

1.1 Motivation of the study

The lung is a vital part of human physiology as it is responsible for the intake of oxygen during inhalation and the release of carbon dioxide during exhalation. This exchange of gases, called respiration or simply breathing, necessitates a large surface area that is always in contact with the environment. This area is provided by the terminal part of the respiratory system, the acinus, which consists of the respiratory airways and a very large number of small cavities called alveoli.

As alveoli are constantly exposed to ambient air, they may be reached by particulate matter floating in the air, for example nanoparticles emanating from natural or human activities [176]. Deposition of airborne particles or pathogenic micro-organisms (e.g. viruses) may pose serious health risks. On the other hand, such deposition processes may be desirable, as in the case of inhaled drugs aiming at local or systemic delivery [166]. Fortunately, evolution [185] has provided the lung of mammals with a biological substance called *pulmonary surfactant* (PS), a mixture of lipids and proteins that resides on the surface of a thin, watery layer that lines internally the alveoli [162]. This layer forms a protective barrier for the intrusion of undesirable substances. However, the main role of pulmonary surfactant is to reduce drastically the surface tension at the interface of the alveolar fluid, thus facilitating the expansion of alveoli during inhalation and their stability during exhalation. The variation of surface tension during breathing, i.e. during expansion and contraction of the alveolar interface, is a complex function of the composition, concentration and solubility of the pulmonary surfactant, even for the simplest case of a spatially uniform surface distribution. This motivated a modeling effort undertaken in the present dissertation, which predicts the elasticity attributed on the interface by a dense surfactant monolayer by incorporating both a compositional and an intrinsic contribution and also taking into consideration solubility effects.

However, the surfactant monolayer is not necessarily uniform during alveolar expansion and contraction. Any spatial variation in surface concentration gives rise to Marangoni stresses, which attempt to move the surface fluid layer from regions of lower towards regions of higher surface tension. An interesting application based on this phenomenon is the Surfactant Replacement Therapy (SRT), a treatment of prematurely born infants by instilling pulmonary surfactant in their trachea, which subsequently moves towards the distal parts of their lungs as a result of Marangoni stresses [80, 162]. The above complication introduced by spatial nonuniformities, motivated a detailed, spatiotemporal modeling of the alveolar dynamics, undertaken in the present dissertation. A key starting point is the formulation of a physically realistic boundary condition at the alveolar rim, which is responsible for the onset of Marangoni stresses.

1.2 Dissertation structure and contents

The present dissertation is comprised of two main computational studies. The first concerns the development and validation of a novel analytical model which describes the dynamic behavior of pulmonary surfactant. The model accounts for the intrinsic surface compressibility of the densely packed surfactant monolayer. The second study focuses on the hydrodynamic analysis of the alveolar fluid of terminal alveoli by considering a model of a single alveolus - envisioned as an oscillating cap which is internally lined with a thin surfactant-covered liquid layer.

Chapter 2 is an overview of the respiratory system. Emphasis is given on the characteristics of PS concerning composition, function and mechanical behavior.

Chapter 3 underlines the main features of a surfactant from basic thermodynamic principles. Equilibrium behavior is analyzed first, followed by the dynamic behavior of surface tension and the surfactant mass balance when surfactants adsorb at non-stationary surfaces. Then, the main theory of transport of surfactants coupled with hydrodynamics is presented, along with Marangoni phenomena and dilatational surface elasticity.

Chapter 4 is a literature review of previous studies concerned with efforts to mathematically model the change of surface tension in alveoli and the investigation of the fluid mechanics of the PS-coated layer in alveoli.

Chapter 5 covers the development of a new analytical model describing lung surfactant adsorption/desorption under physiological conditions and surface periodic motion.

Chapter 6 concerns the hydrodynamic investigation of the alveolar liquid at physiological conditions and in the limit of small oscillations by applying novel boundary conditions and implementing the model developed in Chapter 5.

Chapter 7 presents a parametric analysis of the hydrodynamic model presented in Chapter 6 concerning the geometrical parameters of the alveolus, the alveolar fluid, and the surfactant properties, providing possible physiological implications.

Appendix A includes the analytic expressions of Chapter 6 about linear and weakly nonlinear analysis and Appendix B how Marangoni forces are balanced by capillarity at the surface, concerning the analysis in Chapter 6. Finally, the dissertation ends with Bibliography.

1.3 Novelty and scientific contributions

The novel contributions of the present dissertation refer to the modeling of (i) the temporal dynamics of pulmonary surfactant and (ii) the detailed flow and transport phenomena occurring during alveolar expansion and contraction. With respect to the former, the following are noted:

1. An analytical model of lung surfactant dynamics has been developed, based on fundamental thermodynamics and assuming kinetically controlled adsorption. A novelty of the model lies in the inclusion of the 2D intrinsic surface compressibility, α[1], a parameter that describes the behavior of dense/near-saturated monolayers and expresses the decrease in the molar area of adsorbed surfactant with surface pressure.

2. Model predictions are in quantitative agreement with independent data, by best-fit of a small number of parameters. More important, the best-fit outcomes of equilibrium surface tension and interfacial compressibility reproduce the physiologically correct values.

With respect to the hydrodynamics of the surfactant-laden layer lining internally each alveolus, the following have been accomplished:

1. The alveolus has been modeled as an oscillating spherical cap, and a novel boundary condition has been proposed to hold at its rim. The validity of the new boundary conditions is strongly supported by recent independent experimental findings and by scaling arguments.

---

[1] Note that though the intrinsic compressibility is denoted by ϵ in [20], it is herein symbolized as α in order to avoid confusion with ϵ used in Chapter 6.

2. Non-zero film thickness over the rim (which is experimentally confirmed) has been shown to lead to shearing flow in the alveolar lining, triggered by Marangoni stresses. However, though Marangoni stresses dominate the interfacial dynamics, capillary and viscous stresses have been found to affect significantly the interior flow field and the wall shear stress.

3. The results of linear analysis have provided predictions of physiological interest, such as estimates of the wall shear stress in healthy and diseased lungs. They also offer inferences for the effect of the fluid layer on the ”wall” boundary conditions for airflow computations and on the motion of deposited particles. Weakly nonlinear analysis has revealed that surfactant solubility gives rise at second order to steady streaming of surfactant away from the alveolus.

Chapter 2

The Respiratory system

2.1 Structure of the Respiratory System

The human respiratory system is composed of three major regions [76]. The first is the Extrathoracic Region, where air from the external environment is inhaled via the nasal (nose) or the oral part (mouth) and mainly acts as a filter, which determines the percentage of inhaled particles actually reaching the lung. Then follows the Tracheobronchial Region (TB). It consists of two main lungs, right and left, which are connected to the trachea via their primary bronchi and, eventually, to the main upper airway of the nasal and oral parts [57]. The airways generated from the main bronchi consist of a bifurcating tube network of conducting airways. Each level of branching is called a generation. Specifically, the branching tube network of the lung is presented by a serial sequence of Y-shaped bifurcations, as can be seen in Fig. 2.1. The available morphometric lung models consider a parent airway that splits into two daughter airways at each bifurcation [76]. The daughter tubes may be symmetric [180] or asymmetric [78]. The total number of generations in an adult lung is about 23, with the airway diameter decreasing with the generation number. The TB region extends approximately until the 16th generation where the terminal bronchioles are met; it marks the entrance to the acinus, a cave-shaped group of sacs, such as those depicted in Fig. 2.1 and in Fig. 2.2. From the 17th and (or even from the 19th generation), there start to appear small air cavities attached to the lateral side of the walls, called the alveoli [57] and the region under concern is known Alveolar-Pulmonary region [76], also called the Respiratory zone [57].

The airways of the tracheobronchial region pump ambient air from the trachea carrying oxygen during inhalation and exhale CO2 following the same path but in the opposite direction. The gas exchange between O2 and CO2 is carried out in alveoli. On average, there are about 3.0×10^8 alveoli in the human body, covering an effective area of about 90-100 m^2 [123, 51], with Ochs

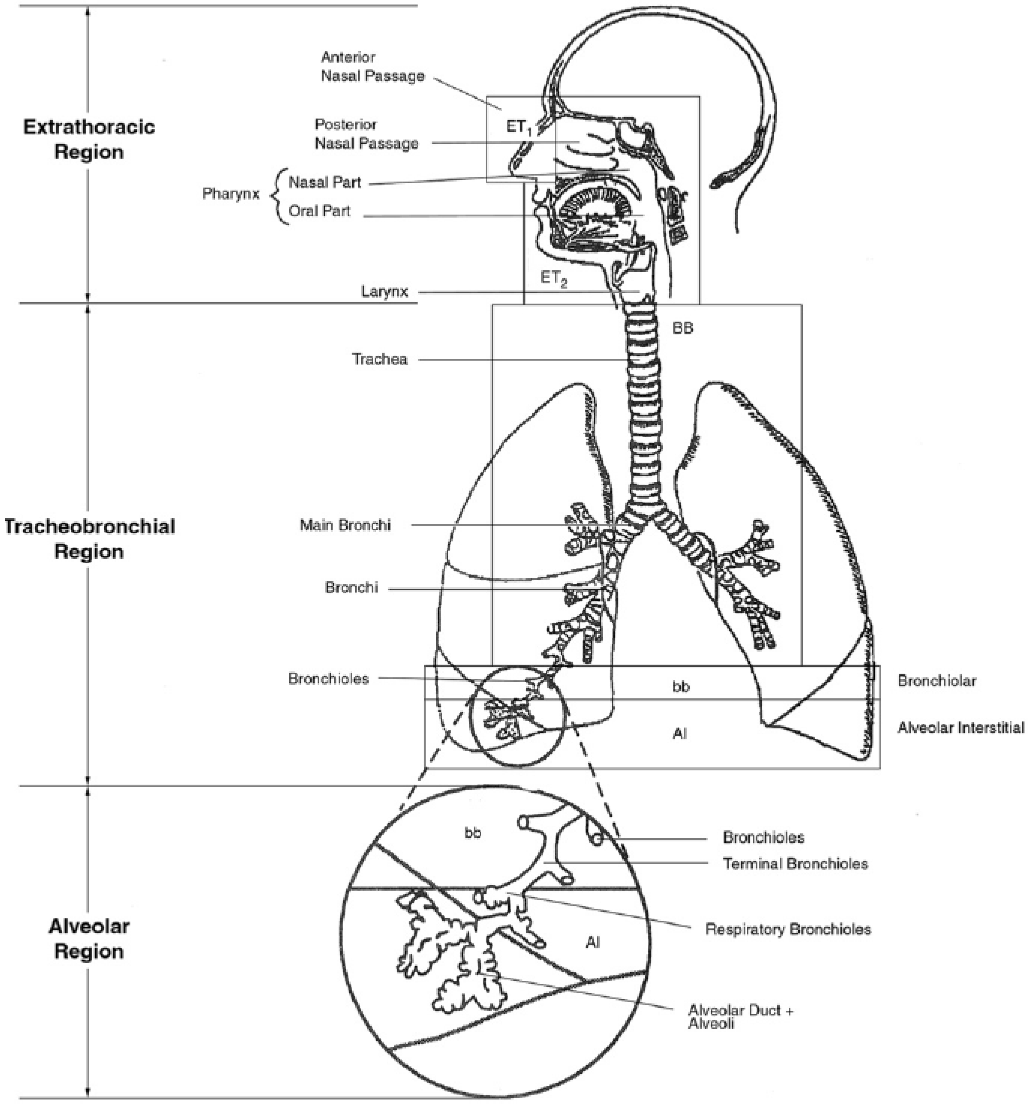

Figure 2.1: A depiction of the respiratory system with a clear depiction of the bifurcating system of airway ducts, adapted from [76].

et al. [123] showing 4.8×10^8 as the most probable number of alveoli. The actual shape of alveoli is not unique, Tsuda et al. [169] in their review state that alveoli are classified into 6 shapes with 3/4 of the alveolus being spheroid with a mean depth of 174 microns. Alveoli can first be counted at 29 weeks gestation with their diameter and wall thickness gradually increasing with age till birth [75]. Of course, their size and number increase after birth as well, with the number of alveoli at birth being 1/3 or half the adult number.

The exchange between the alveolar gas and blood occurs through a membrane that separates the capillary containing the bloodstream from the alveolar gas, as seen in Fig.2.2.

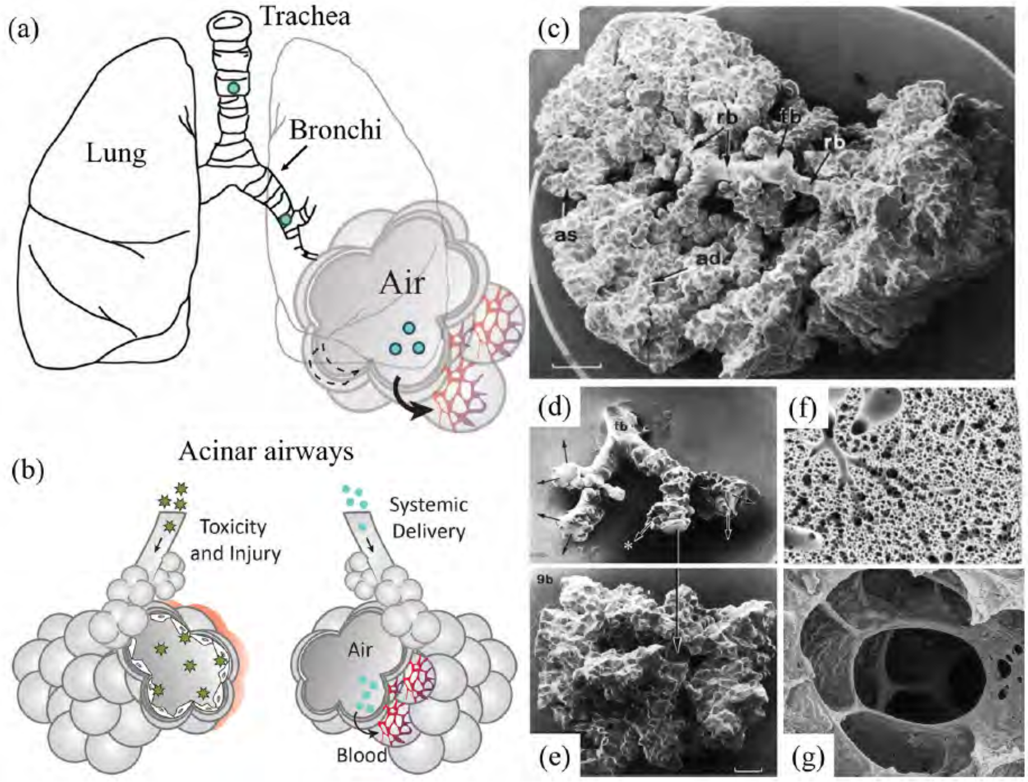

Figure 2.2: A more detailed schematic arrangement of the deep lungs, adapted from [166]. a) Airborne particles (blue dots) are transported from the trachea down the acinus region. Such particles can either be micro/nanoparticles of pathogenic nature or aerosolized drugs. b) Terminal alveoli are externally coated by the blood capillaries depicted by a red network. c)-g) Different Scanning Electron Micrographs (SEM) of the acinus. Gas exchange takes place between alveolar sacs and blood capillaries hugging the shell of alveoli in a). Inhaled particles first need to traverse the alveolar liquid in the interior of the sacs before entering the bloodstream.

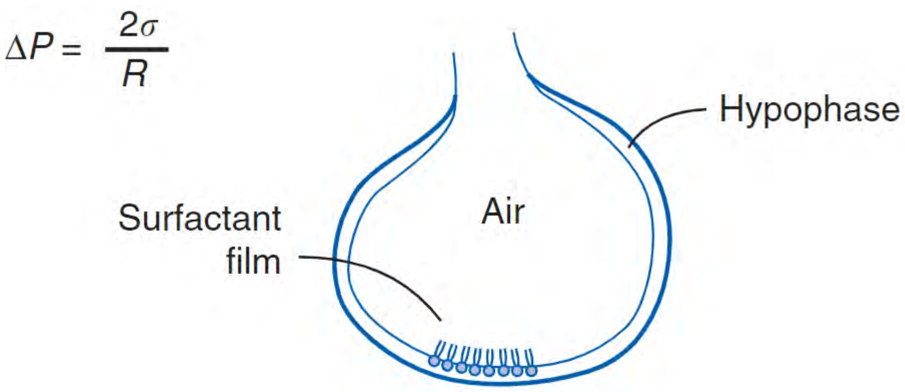

Figure 2.3: Schematic arrangement of the pulmonary liquid within an alveolus, taken from ref. [122]. Exactly at the air-water interface, the formation of a thin surfactant film can be seen. The required pressure to inflate alveoli is determined by the Young-Laplace law. Notice the arrangement of the adsorbed molecules; their heads point toward the bulk since they are hydrophilic while their tails are away from the surface due to their hydrophobicity.

2.2 The pulmonary surfactant system

2.2.1 Basic elements

The interior of the lung airways is laden with a thin liquid layer [57]. For the first 15 generations, this lining consists of two layers. The topside layer, in direct contact with the inhaled air, is the mucus layer which exhibits several non-Newtonian rheological properties such as viscoelasticity, yield stress and shear thinning [162, 59]. It is mainly composed of water and a very small amount of glycoproteins, salts and lipids [162]. The glycoproteins are called mucin, which induce non-Newtonian rheology to the top layer. Below the mucus and adjacent to the airways is the serous layer, a watery fluid with cilia. Cilia set the whole layer in flow, washing away bacteria, pathogen and particulate matter eventually. Beyond the 14-15th generation until the alveolar region, cells producing mucins begin to decrease in population [162] and the layer is essentially Newtonian [57]. The liquid lining the interior of alveoli is perhaps their most important property. At the surface of this layer, a monolayer consisting of surface active agents-surfactants is formed, as can be seen in Fig. (2.4) and in Fig. (2.5a) where a schematic depiction of a typical alveolus is presented along with the bodies participating in the production process, such as type II cells, tubular myelin and lamellar bodies [136]. This monolayer consists of surfactant molecules and is called the *pulmonary surfactant* or *lung surfactant* (PS/LS for brevity). Two main categories of PS are identified for in-vitro experiments and for PS-replacement therapies. Natural, which are endogenous surfactant extracts from the lungs of animals - e.g. cows, pigs - and synthetic

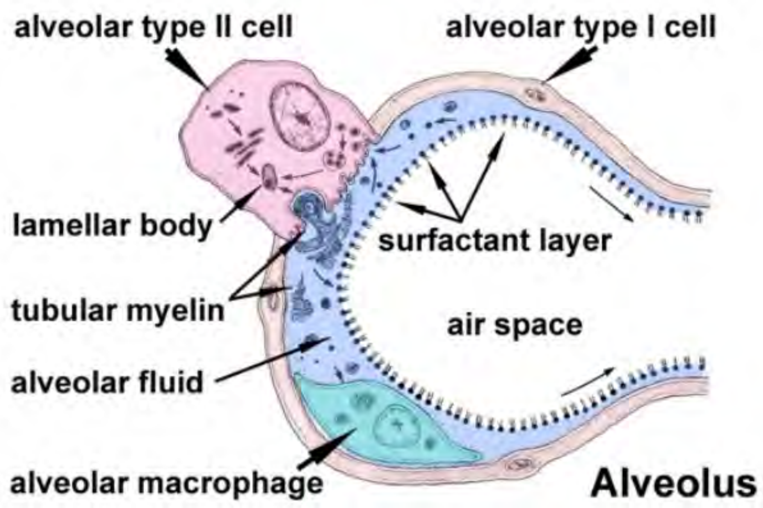

Figure 2.4: Aqueous/vapor interface in the alveoli of lungs taken from [81]. Surfactant is produced by type II cells which are adjacent to the alveolar epithelium.

which are synthesized without containing any natural extracts [147]. Generally, the former are considered more efficient for clinical purposes.

Native lung surfactant is locally produced in alveoli by Alveolar Type II cells; surfactant is secreted into the alveolar fluid by these cells and after being suspended into the liquid, it reduces the surface tension of the aqueous layer via adsorbing at its gas/liquid surface. By decreasing surface tension during breathing, the energy required to inflate alveoli is reduced due to increased lung compliance [193]. The characteristics of surface active molecules and thermodynamic principles according to which they reduce surface tension of liquid interfaces are analyzed in Chapter 3.

2.2.2 Functions and composition

The pulmonary surfactant is not a single component; it is a highly complex mixture of lipids - phospholipids in particular- and a relatively small amount of proteins [136, 193, 128]. These lipids and proteins are synthesized within alveoli by alveolar Type II epithelial cells [128] covering the alveolar wall in contact with alveolar fluid. When functioning in the desired way, lung surfactant should be able to **a)** rapidly adsorb at the air/water interface with the corresponding characteristic time being a few seconds, **b)** decrease surface tension to very low value during exhalation and **c)** mitigate surface tension increase on expansion during inhalation [9]. Besides, it must show good re-spreadability after surfactant monolayer collapse and prevents the collapse of alveoli [72]. The adsorbed surfactant monolayer is known to sustain large compressions during contraction, resulting in extremely low values of surface tension, specifically less than

5 mN m^{-1} [33, 121, 128] and probably falls below 1 mN m^{-1} [146]. Lipids are the most abundant of the lung surfactant components, approximately 90-92 % by weight, with phospholipids being the dominant category [9, 128]. The most abundant component of mammalian lung surfactant phospholipids and that with the highest surface activity[1] is dipalmitoylphosphatidylcholine, commonly known as DPPC [132]. DPPC is 40-80 % by weight of the phospholipid content [193] and it is mainly responsible for the reduction of surface tension to the ultra low values mentioned above. Nevertheless, DPPC has long been excluded as a candidate for artificial lung surfactants, as it exhibits poor re-spreadability onto the air/water surface and its adsorption rate is low [193, 48, 121]. Surfactant Proteins (henceforth SP) constitute approximately 7-10 % by weight of lung surfactant. The most important of SPs are four, named SP-A, B, C and D [136, 128, 193, 51]. Each of these proteins contributes uniquely to the normal function of the lung surfactant system. SP-A ameliorates surface activity of the surfactant at the film interface and, along with SP-D, enhances the defense of the immune system by binding to the hydrocarbonates of external pathogens

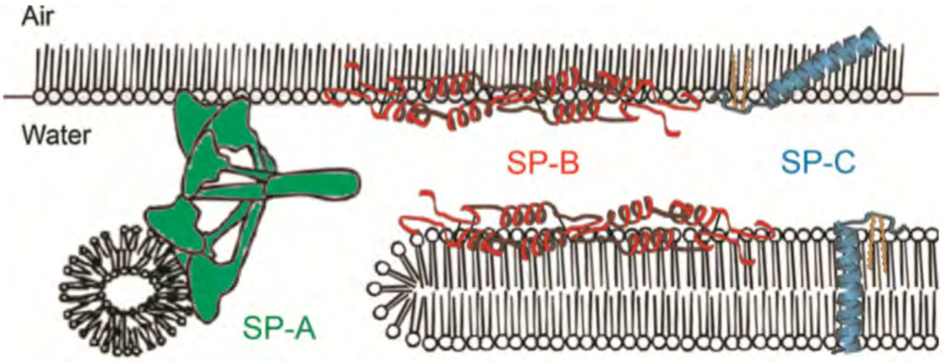

(a) Pulmonary surfactant monolayer along with its proteins, adapted from [128].

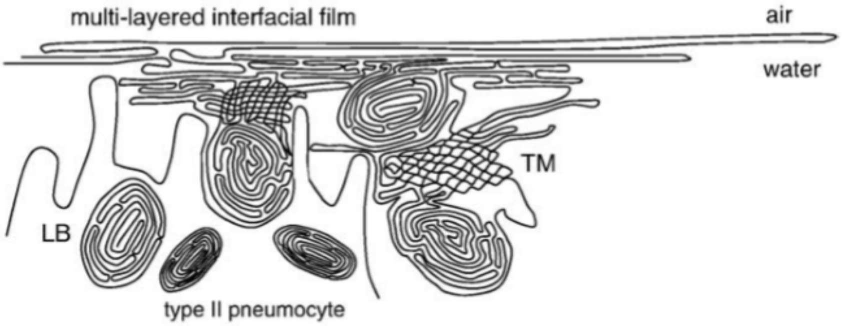

(b) Membrane-like structures (vesicles, aggregates) of the pulmonary surfactant [132].

Figure 2.5: A schematic configuration of the exact molecular nature of the pulmonary surfactant system inside the alveolar fluid. Notice the ordered geometrical configuration of the monolayer residing at the surface, while bilayers and complex vesicles occupy the hypophase.

---

[1] Between surface active species, the most surface active is that which decreases surface tension with the lowest bulk concentration [185]

such as bacteria, fungi and viruses. Both SP-B, SP-C contribute to maintaining stable adsorbed films of surfactant at the air-liquid surface of the alveolar fluid [51]. Nevertheless, lack or deficiency of these proteins is associated with problems; lack of SP-B leads to respiratory pathologies while SP-C deficiency is lethal [9].

Well within the acinar region, the site where alveoli are located, lung surfactant adsorbs from the subphase to the surface and besides lowering surface tension, it forms a stable and continuous monomolecular layer with the surfactant headgroup pointing towards the bulk of the liquid phase as seen in Fig. 2.5. This is a general aspect of biological surfactants, which, unlike chemical surfactants, have hydrophilic heads much larger than their hydrophobic part (the tail). Since their headgoups interact with water molecules, a strong support for the compositionally dominant phospholipids to assemble and form a stable monolayer is provided [135]. As a result, the effective form of the surfactant system at the surface of the alveolar liquid when addressed from a macroscopic point of view, either experimental or theoretical, is that shown in Fig. 2.3. In other words, it can be envisioned as a continuous molecular layer. Nevertheless, it should be stated that if we take a closer look at the surface with the surfactant and its subphase, its form is rather complex; a simple depiction of the pulmonary surfactant system, as described in the previous sentence, is presented in Fig. 2.5, where it is depicted that the alveolar surfactant is composed of multiple interconnected membrane-like 3-D structures [132, 128]. Once synthesized by alveolar Type II cells, surfactant is secrated in the form of peculiar concentric lamelar bodies [9] and vesicles [136] and then they are transformed into tubular myelin. Then, tubular myelin releases the bulk amount of phospholipids to create the actual interfacial film ([136]) seen in Fig. 2.5. This process is schematically depicted in Fig. 2.4. Despite the complex structures composing lung surfactant, the whole system, subphase and surface, can be safely envisaged as a unique structure [132]. Accordingly, throughout the present dissertation, the lung surfactant is considered to be continuously distributed within the alveolar liquid. Hence, the mathematical description of the adsorption process follows the standard equations of change ([126, 141, 111]) employed for surfactant-associated flows. The kinetics owing to adsorption-desorption along with equations of change are thoroughly discussed in Chapter 3. Note, however, that a considerable amount of research papers have employed computational models of Molecular Dynamics for the investigation. Via this approach, the discrete nature of molecules is accounted for since the characteristic length scales used in Molecular Dynamics belong to the nanoscale. Study of lung surfactants through molecular dynamics is well outside the scope of interest herein, therefore the interested reader is referred to the review of Baoukina and Tieleman 2016 [9].

2.2.3 Phase Transitions

As stated, the pulmonary surfactant forms a stable monolayer at the alveolar liquid surface, which, during respiration, is periodically subjected to expansion/contraction imposed by the geometrically self similar motion of alveoli [169]. As a result of this motion, it undergoes multiple phase transitions. Typically, these phases are seen in experiments where a surfactant mixture is spread on a surface and is then subjected to a direct and slow compression. Effectively, we talk about two-dimensional (2D) assemblies of surfactant molecules on aqueous surfaces, exactly as depicted in Fig.2.5a. These are called Langmuir monolayers. Examples of studies in which Langmuir monolayers of lung surfactants or lipid/proteins mixtures relevant to lung surfactant were studied accordingly are abundant in the literature [195, 185, 60, 32].

Langmuir monolayers are extensively employed when investigating various problems in Physics, Chemistry and, especially, Biology; they provide a simple way to experimentally study significant aspects of surfactant mixtures such as their molecular structure, phase transitions, fluid dynamics and even microrheological properties [135]. In the case of biological surfactants, with phospholipids being a characteristic example, Langmuir monolayers provide information on lipid-protein interactions [132, 135].

In such experiments, an insoluble monolayer is formed at a surface (usually an aqueous surface) and then gradually compressed, while the temperature is held constant. The outcome of these experiments is reported as a continuous curve (*isotherm*) of the surface pressure, Π, versus the molecular or molar surface area i.e. the area per adsorbed molecule or per mole, A_μ. Surface pressure is the difference between the surface tension of a clean surface (no surfactant), σ_o and the surface tension at a non-zero surface concentration, $\Pi = \sigma_o - \sigma$. At room temperature, water possesses the well-known value of $\sigma_o = 72\ \mathrm{mN\,m^{-1}}$, at physiological conditions however, the temperature is 37 °C and σ_o is a bit lower, taking the value of $70\ \mathrm{mN\,m^{-1}}$ [128, 58].

Since the monolayer is insoluble, the total amount of surfactant at the surface is always constant, and thus the surface concentration, Γ, and the molar area of surfactant are related by the expression $A_\mu = 1/\Gamma$[2]. Experimental apparatuses employed in such experiments include, among others, the Langmuir balance; an extensive insight of these methods is provided in the reviews of

---

[2] The area per molecule is given by $A_\mu = 1/(N_{\mathrm{Avog}}\Gamma)$

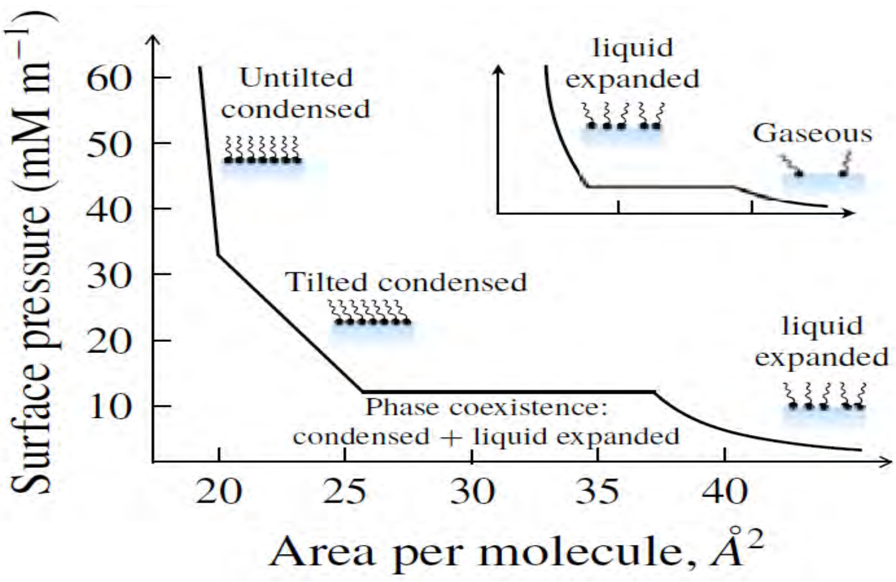

Figure 2.6: Typical $\Pi - A$ curve at specific temperature - isotherm [111]. Every segment of the curve represents a different phase state.

[185, 128, 199].

A typical $\Pi - A_\mu$ isotherm is given in Fig. 2.6. The direction of compression is from the right part of the curve to the left. At the beginning, the molar area of the surfactants is the largest and $\Pi \sim 0$. This implies that the monolayer is in a Gaseous phase (G) and the distance between surfactant molecules is very large and the surface density is low. Monolayer compression leads to a more dense monolayer, where molecules are in a disordered and fluid state called *liquid expanded* (LE) phase. Note that in this state, molecules begin to interact with each other via their hydrophobic tails. The latter are now in contact and the surface pressure is above zero [104]. Note that when in a gaseous state, hydrophobic tails have little contact with each other [104]. The distinction between LE and G phases is realised from the lift-off in Fig. 2.6. As compression continues, the monolayer undergoes a first-order transition to the *liquid condensed* (LC) phase [104]. Interestingly, the latter transition is simply observed via a plateau in the $\Pi - A$ isotherm implying a coexistence of LE, LC phases. In reality, the characteristic plateau of a compression isotherm denoting LE-LC coexistence is not strictly parallel to area axis, as seen in experimental data in Fig. 2.7. Compression isotherm for BLES preparation at room temperature shows a LE-LC coexistence plateau as an inclined line and not parallel to A_μ axis. Also, experimentally derived compression isotherms for DPPC clearly demonstrate a strong effect of temperature at the coexistence plateau as seen in Fig. 2.8a. In addition, the composition of the monolayer affects the slope of the plateau and the surface pressure above which coexistence begins, e.g. addition of SP-B, SP-C in DPPC solutions as seen in Fig. 2.8b. Nonetheless,

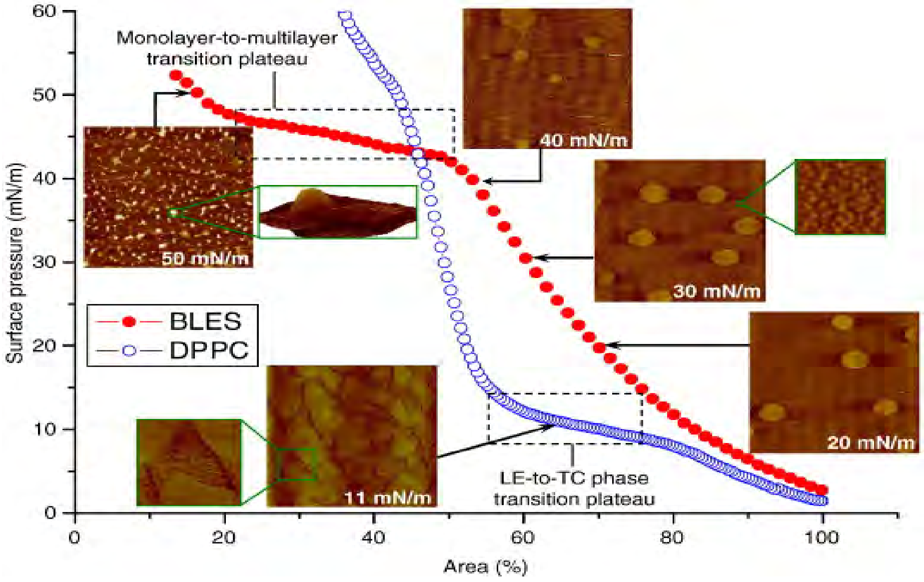

Figure 2.7: Experimental $\Pi - A$ compression isotherms for monolayers consisiting of DPPC and BLES (bovine lipid extract surfactant), the latter being an animal-derived surfactant used for clinical purposes [198]. The superimposed images represent an insight into the microdomain film structures obtained via AFM. Compression experiments were carried out via the Langmuir-Wilhelmy balance method.

the qualitative behavior remains the same; as compression continues beyond the coexistence plateau, the monolayer enters the condensed phase marked by an abrupt increase in surface pressure.

2.2.4 The mechanical behavior of PS monolayer

The structure and mechanical properties of the adsorbed monolayer of pulmonary surfactant have been investigated for more than half a century [185, 146, 128] as they show remarkable features, the understanding of which could contribute to the design of more efficient replacement surfactants. Experimental works on the tensiometry of PS solutions have revealed a behavior unique to a surfactant due to the large variations of surface tension of the film during a typical respiratory cycle [193, 185, 104]. A characteristic property is the minimum surface tension achieved at adsorption equilibrium. At physiological conditions and dynamic cycling it is around $20 - 25\ \mathrm{mN\,m^{-1}}$, however, during dynamic cycling which mimics the actual breathing (i.e. physiological) patterns, surface tension oscillates around σ_{eq} in a wide range of values; during the expiratory phase it decreases well below the aforementioned equilibrium value [197, 146, 154] reaching virtually zero values [193].

Dynamic response of PS solutions is studied by spreading a model of PS - commonly DPPC with SPs and other lipids [104, 187, 186, 184] - on a bubble or a droplet ([150, 1, 199, 198, 189]). The millimeter-sized bubble/droplet

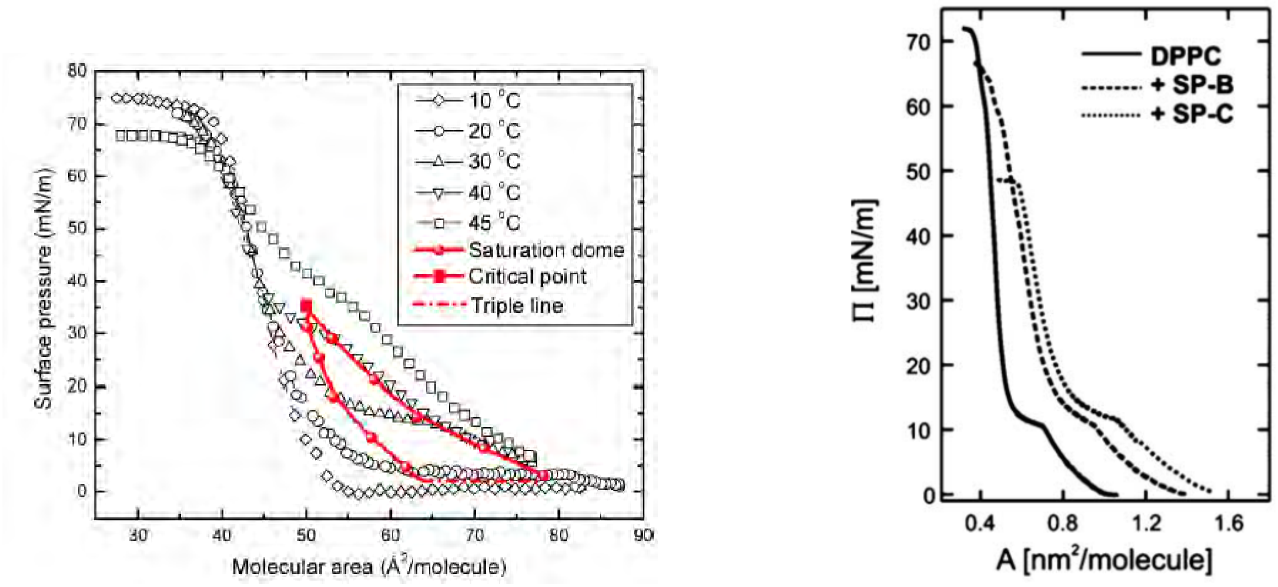

(a) (b)

Figure 2.8: a) Compression isotherms of DPPC in a wide range of temperatures (taken from [198]). b) Compression isotherms of DPPC showing the effect of addition of SP-B/SP-C [185].

oscillates periodically mimicking the motion alveoli execute during expiration. If we examine the behavior of surface tension during steady state - that is the diagram does vary but negligibly between successive cycles - surface tension increases during expansion (inhalation), and depending on the concentration, it can even reach a plateau at maximum expansion [149, 127] and decreases as soon as contraction of the surface (exhalation) succeeds expansion, as can be seen in Fig. 2.9. What is evident in Fig. 2.9a is that $\sigma - A$ loops exhibit a hysteresis.

As the surface area nears its maximum reduction, surface tension tends to reach σ_{min} and remains constant before the next cycle begins, in other words it reaches a plateau parallel to the relative area axis. This happens because the monolayer reaches a saturation concentration. At this stage, an ejection of surfactant material from the surface is observed which can be envisioned as ”squeeze out”. Understandably, having nowhere else to go, squeezed-out material enter the subphase, but extensive evidence shows it remains attached to the surface [128, 185]. Nonetheless, ejected material may re-enter the surface during initiation of the next cycle as expansion of the surface provides more available area for expelled material to re-occupy; though peculiar as the authors state in [104], the whole process is reversible. This phenomenon is known as pulmonary surfactant collapse [193].

Microscopy has shown that the mechanical behavior of a monolayer under gradually increasing compression involves transitions from a LE phase to a

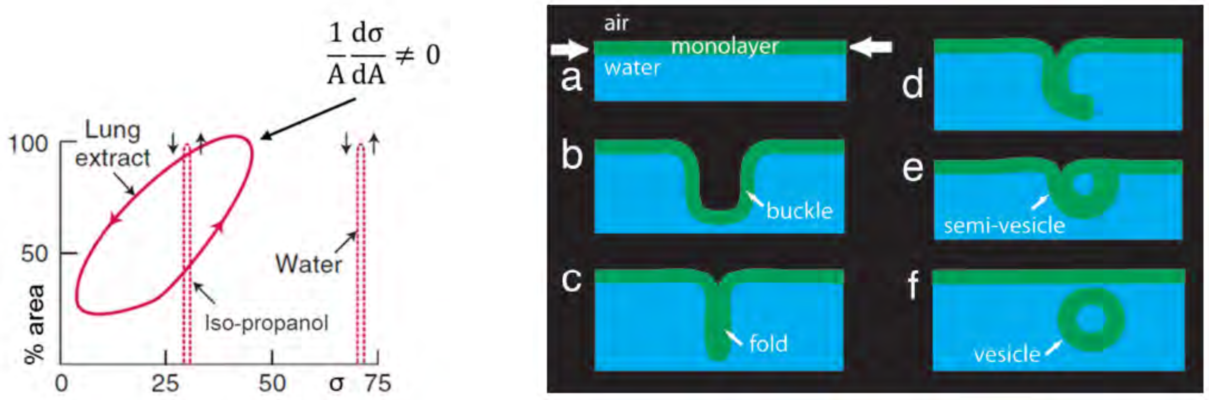

a)

b)

Figure 2.9: a) Typical surface tension versus relative area curve for lung surfactant, water and iso-propanol under constant temperature. Notice the hysteresis in the loop for lung surfactant, which is absent in the case of water and iso-propanol, the latter being also a surfactant. This hysteresis indicates the unique surface behavior of lung surfactant, surface compression and expansion behave differently from each other [58]. b) Schematic representation of the pulmonary surfactant collapse, adapted from [7]. White arrows represent compression of the monolayer.

structurally more stable TC phase and eventually to a collapsed film [37, 195, 190, 199]. The extraordinary stability of pulmonary surfactant is classically explained by the above referenced “squeeze-out” mechanism, which claims that the less stable fluid components (the SPs) are gradually removed from the interfacial monolayer during film compression, resulting in a monolayer enriched in DPPC and consisting of nearly homogeneous TC phase [155, 153, 192, 140]. Alternatively, it may also be explained in terms of metastable behavior of super-compressed fluid films [190, 146].

At any rate, the transition of the lung surfactant under collapse is different from the classical squeeze-out of lipid films that leads to the permanent departure into the subphase of lipid vesicles. In particular, the collapse of the monolayer appears to occur through buckling and folding events [104] that form protrusions extending in various directions, while remaining continuous with the interfacial monolayer [107, 152, 135, 7, 9], as seen in the schematic in Fig. 2.9b. The thickness of the protrusions, presented in Fig.3 c)-d) in [104], being in the order of 10 nm further supports the idea that the surfactant reservoir is different from the bulk in the subphase. These structures may act as reservoirs for rapid replenishment of the film during expansion. The presence of SP-B contributes to the transport of lipids from the subphase to the interface [8].

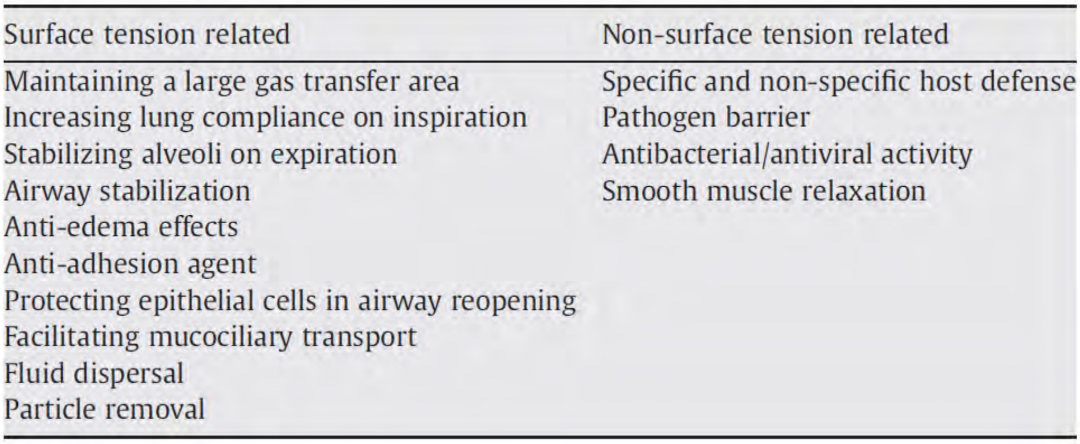

Surface tension related	Non-surface tension related
Maintaining a large gas transfer area	Specific and non-specific host defense
Increasing lung compliance on inspiration	Pathogen barrier
Stabilizing alveoli on expiration	Antibacterial/antiviral activity
Airway stabilization	Smooth muscle relaxation
Anti-edema effects	
Anti-adhesion agent	
Protecting epithelial cells in airway reopening	
Facilitating mucociliary transport	
Fluid dispersal	
Particle removal	

Figure 2.10: Physiological functions of pulmonary surfactant [199].

2.2.5 Physiology and Purposes

The dynamic response of the pulmonary surfactant to periodic area expansion and contraction during a breathing cycle is a critical input for understanding a variety of issues of lung physiology and physiopathology [132]. The typical $\sigma - A$ loop should reach values close to $0\,\mathrm{mN\,m^{-1}}$ during maximum compression, seen at the bottom of Fig. 2.9a. Such values for surface tension, though very low for a watery film, are vital for breathing; if the minimum, equilibrium values are around these values the lung is compliant enough for normal respiration [58].

The proper manufacture of surfactant by Type II cells occurs late at gestation [58] and, as a result, prematurely born infants suffer from what is known as neonatal Respiratory Distress Syndrome (RDS or nRDS), a disease emanating from stiff lungs due to the lack of sufficient surfactant. Fortunately, a therapy for nRDS has been developed in which replacements of the pulmonary surfactant are instilled into the trachea, and through subsequent breaths, the liquid bolus - drug carrier - takes the form of a plug that traverses the downstream bifurcations of the respiratory system. This therapy uses surfactant extracted from animals (native surfactant) or synthetic surfactant [34, 168], and is called Surfactant Replacement Therapy (SRT) [58].

Finally, the main properties of lung surfactant along with its defensive abilities, are listed in Fig.2.10

Chapter 3

Thermodynamics and Transport Phenomena at Surfaces

3.1 Introduction

Surface tension behavior of aqueous surfactants is central in diverse areas of science and engineering with applications in both biological and biochemical processes [142]. Surface tension reducing agents are used in anti–icing sprays used on commercial aircraft to enable take-off [115], in the study of active colloids [42]; surfactants also influence foamability and foam stability, film drainage [160], wettability and spreading [161], coating flows [38], and the formation of soap-lather. In fast processes, apart from the equilibrium value, the dynamic surface tension (DST) behavior is also important. The simplest example of such systems is an aqueous layer in contact with air. In many technological applications where interfaces are present, the value of surface tension is constant along the surface [38]. However, this is not always the case, since the presence of surface active molecules called surfactants, or temperature variations along the interface, produce changes in surface tension. While the mathematical modeling of free surface layers from the scope of fluid physics incorporating the effect of surface tension is well established and presented in many textbooks, e.g. [4], the origins of surface tension and the factors that may alter its value are not trivially understood. The reason for this is that surface tension is a **thermodynamic variable** acting in a similar fashion as pressure does in 3-D fluids, a realization that highlights the necessity to obtain fundamental knowledge on the thermodynamics of surfactant systems.

In the present Chapter, a rigorous mathematical analysis of equilibrium of liquid/gas surfaces is presented based on the second law of Thermodynamics for a closed system, following the famous Gibbs convention for the treatment of the interface. Accordingly, a thermodynamic definition of surface tension and surface excess concentration of surfactants is derived, followed by a description of equilibrium adsorption isotherms. Then, dynamic - out of thermodynamic equilibrium - adsorption along with Marangoni phenomena and the elasticity modulus are discussed.

3.2 Surface tension and its physical meaning

Surface tension is a basic parameter of fluid mechanics appearing in problems and applications where two macroscopic phases are in contact separated by an interface, for instance, when liquid is in contact with a gas.

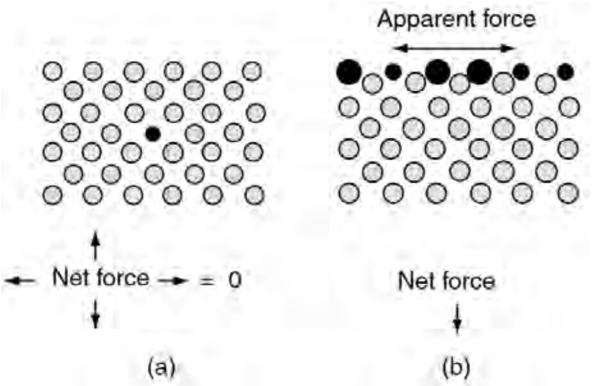

Figure 3.1: A schematic representation of the forces acting on a bulk molecule/atom (a) and on a surface molecule/atom (b). The Net force exerted on a surface unit will be non-zero pointing toward the bulk phase [120].

When modeling fluid problems with free surfaces, surface tension participates in the boundary conditions written at the liquid-gas interface, hence, it is a macroscopic property of surfaces. Though its definition can be based on standard thermodynamic arguments, its physical "roots" originate from the way matter is distributed across surfaces, consequently, in order to achieve a better understanding of interfacial tension, one should carefully inspect the molecular arrangement near an arbitrary formed interface, Fig. 3.1.

Consider a liquid phase with its surface being in contact with air and pay attention to the arrangement of molecules/atoms in the bulk and at the surface. At every molecule/atom, a finite amount of force is exerted on it by neighboring units. In the bulk phase, molecules or atoms are being pulled and pushed from all sides by intermolecular forces of equal strength, as seen in Fig. 3.1 a). Thus, the net force acting on an arbitrary bulk molecule is zero [120]. On the surface, however, the situation is quite different. Intermolecular attractions from the liquid phase will be greater than the ones of the gaseous phase and, thus, the net force acting on a surface unit, e.g. atom or molecule, will be pointing toward the bulk. Consequently, interfacial forces are unbalanced. Surface forces pulling along the surface, then, represent the surface tension or surface energy [120]. Practically, the action of surface tension at interfaces between liquids and gases (in combination with the three-phase contact angle of the system) results in the formation of menisci, as can be seen in Fig. 3.2, where surface tension ”curves” the interface near a solid wall, an example we can meet in everyday life.

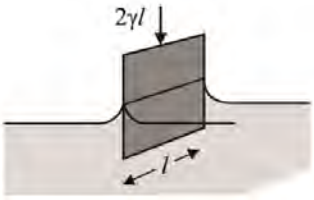

Figure 3.2: Formation of a meniscus near a vertical thin solid sheet representing a Wilhelmy plate [120]. Note that surface tension is a line force, so the exerted force is twice the force exerted on one side of length l.

For the liquid film lining internally the alveoli, the force by surface tension opposes their expansion and thus must be overcome during breathing. In order to facilitate breathing effort, surface tension must be as low as possible.

3.3 Equilibrium surface behaviour

Consider two different phases A and B in contact, divided by an interface as it is depicted in Fig. 3.3. For simplicity, we consider a liquid, A, in equilibrium with a gaseous phase, B. The two macroscopic phases are separated from each other and the system as a whole is in **thermodynamic equilibrium**. Accordingly, the chemical potential across the system must be constant. Usually, existence of thermodynamic equilibrium implies the simultaneous existence of **mechanical equilibrium**, the converse is not true, though. Consequently, there is no macroscopic fluid motion in the system. In order to study the aforementioned system from the thermodynamic perspective, the well-known **Gibbs Convention** is used. According to Gibbs, the surface separating the

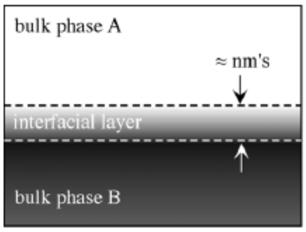

Figure 3.3: An envision of a typical interface between a liquid and a gaseous phase, adapted from [12].

two phases can be treated as an infinitesimal boundary layer of zero volume, characterized by surface area A and surface tension σ. For the sake of simplicity and hereafter the surface is referred to by the symbol "s". The actual thickness of the surface layer is estimated in the order of a few nm [12], therefore it can safely be omitted. Nevertheless, there exist other models as well, such as Guggenheim's model, which accounts for a finite surface volume, however, it will not be of concern in this dissertation. Gibbs model is employed as a theoretical tool in most applications due to its practicality [22, 2], and has been shown to yield results in very good agreement with direct surface tension measurements as a function of surfactant concentration [112]. Let V^A, V^B be the volume occupied by phases A and B, respectively. The total volume of the system is $V = V^A + V^B = constant$. Totally, N different species are considered. Besides, extensive thermodynamic properties, such as the number of molecules of the i^{th} species, n_i, the internal energy U and entropy, S, are additive, allowing one to determine the thermodynamic properties of the whole system. In order to derive the thermodynamic relations concerning the interface, we consider the **Helmholtz** Free energy. The latter is defined as $F = U - TS$, where T is the absolute temperature, and for the whole system the Helmholtz free energy is:

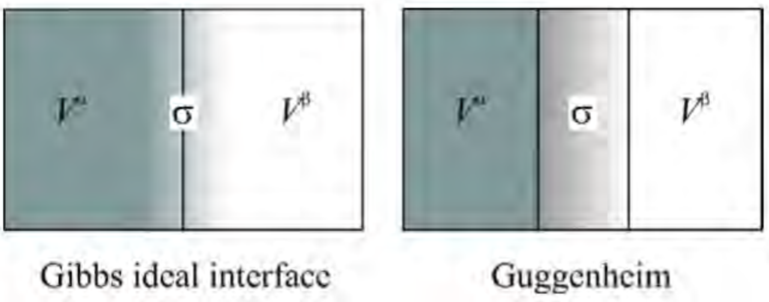

Figure 3.4: Schematic arrangement of two phases along with their mutual interface, taken from [22] according to Gibbs (left) and Guggenheim (right). Both approaches treat the surface as a third phase.

$$F = F^A + F^B + F^s \tag{3.1}$$

An infinitesimal and reversible change in the system's Helmholtz energy is:

$$dF = dF^A + dF^\beta + dF^s \rightarrow$$

$$dF = dQ^A - p^A dV^A - TdS^A - S^A dT + \sum_{i=1}^{N}(\mu_i^A dn_i^A) + dQ^B - p^B dV^B - TdS^B - S^B dT + \sum_{i=1}^{N}(\mu_i^B dn_i^B) + dQ^s + \sigma dA - TdS^s - S^s dT + \sum_{i=1}^{N}(\mu_i^s dn_i^s) \rightarrow$$

$$dF = -p^A dV^A - S^A dT + \sum_{i=1}^{N}(\mu_i^A dn_i^A) - p^B dV^B - S^B dT + \sum_{i=1}^{N}(\mu_i^B dn_i^B) + \sigma dA - S^s dT + \sum_{i=1}^{N}(\mu_i^s dn_i^s) \quad (3.2)$$

The fact that thermodynamic equilibrium was assumed, requires the chemical potential of every substance be equal in every phase. Therefore, it follows that [22]

$$\mu_i^A = \mu_i^B = \mu_i^s = \mu_i \quad (3.3)$$

which simplifies the expression for dF as follows:

$$dF = -p^A dV^A - S^A dT + \sum_{i=1}^{N} \mu_i dn_i^A - p^B dV^B - S^B dT + \sum_{i=1}^{N} \mu_i dn_i^B + \sigma dA - S^s dT + \sum_{i=1}^{N} \mu_i dn_i^s \quad (3.4)$$

Since the whole system is closed, there is no net change in the amount of moles for each one of the N species, so $dn_i = dn_i^A + dn_i^B + dn_i^s = 0$ or $dn = \sum_{i=1}^{N}(dn_i^A + dn_i{}^B + dn_i{}^s) = 0$. Thus eq. (3.4) reduces to

$$dF = -p^A dV^A - S^A dT - p^B dV^B - S^B dT + \sigma dA - S^s dT \quad (3.5)$$

Eq. (3.5) expresses a reversible and infinitesimal change in the system's Helmholtz free energy under equilibrium. At equilibrium, keeping the volume of each phase, temperature, and the amounts of material constant, the free energy is minimal:

$$\boxed{dF|_{\text{eq}} = 0} \quad (3.6)$$

The system described in Fig. 3.4 is closed which implies that every change in volume of phase A should be opposite to that of B, so that $dV^A = -dV^B$. Therefore, from eq.(3.5) and $dT = 0$ we have $-(p^B - p^A)dV^B + \sigma dA = 0$ or

$$(p^A - p^B) = \sigma \frac{dA}{dV^B} = \sigma \left(\frac{1}{R_{\mathrm{I}}} + \frac{1}{R_{\mathrm{II}}} \right) \tag{3.7}$$

The last expression is the famous Young-Laplace Law derived for a smooth surface of arbitrary shape. Consequently, the postulation that the surface behaves as a third phase in equilibrium with A and B provides an alternative approach in deriving a fundamental equation of capillary phenomena and interfacial fluid mechanics in general. The Young-Laplace law is of fundamental significance in Physical Chemistry [2]; if a spherical surface is considered (a droplet in a gas, for instance) then eq.(3.7) reduces to the widely known

$$\boxed{\Delta p = \frac{2\sigma}{R}} \tag{3.8}$$

where R is the radius of the droplet or the bubble and Δp is the pressure jump across the interface. Eq.(3.8) is used for calculating the pressure difference required for expanding alveoli by assuming the alveolus as a spherical bubble [10], where R is the alveolar radius and is around 100 μm.

Returning to the Helmholtz energy, it has already been shown that a reversible and under equilibrium change of a bulk phase's F is:

$$dF^j = dW_r^j - S^j dT + \sum_{i=1}^{N} \mu_i dn_i^j$$

where $dW_r^j = -p^j dV^j$ $(j = A, B)$ is the reversible volumetric work due to change in the area of the separating surface. The latter implies that a similar infinitesimal change in Helmholtz energy of s is:

$$dF^s = \sigma dA - S^s dT + \sum_{i=1}^{N} \mu_i dn_i^s \tag{3.9}$$

where $\sigma dA = dW_r^s$. The equation above indicates that the Helmholtz free energy is a homogeneous function of the extensive properties S^s, A and n_i^s, when the intensive properties T, σ and μ_i are kept constant. Thus, it may be written in the form

$$F^s = \sigma A - S^s T + \sum_{i=1}^{N} \mu_i n_i^s \tag{3.10}$$

The result above is of great importance since it allows one to derive a thermodynamic definition of surface tension. To be specific, it is the energy per unit area needed to increase the surface in a system, for example, a liquid in contact with air

$$\sigma = \left(\frac{dF^s}{dA}\right)_{T,n_i} \tag{3.11}$$

Eq. (3.10) is generally valid [2] and its differential should be equal to the one provided by eq.(3.9). Differentiating eq.(3.10) yields

$$dF^s = -S^s dT - T dS^s + \sigma dA + A d\sigma + \sum_{i=1}^{N} \mu_i dn_i^s + \sum_{i=1}^{N} d\mu_i n_i^s \tag{3.12}$$

Equating the last expression with eq.(3.9) leads to

$$S^s dT + A d\sigma + \sum_{i=1}^{N} n_i d\mu_i = 0 \tag{3.13}$$

Dividing the last expression with the interfacial area, A, leads to the well-known Gibbs-Duhem equation [112].

$$\boxed{s^s dT + \sum_{i=1}^{N} \Gamma_i^s d\mu_i + d\sigma = 0} \tag{3.14}$$

where s^s is the entropy per unit of surface area and $\Gamma_i = n_i^s / A$ is the so-called surface excess. The surface entropy can be deduced from eq.(3.14),

$$s^s = \frac{S^s}{A} = -\left(\frac{d\sigma}{dT}\right)_{A,p} \tag{3.15}$$

Since the surface entropy is non-negative, the above result shows that under equilibrium, surface tension between two different phases decreases with temperature. At the same time, surface entropy is increased and molecules at the surface are less ordered than in the bulk liquid phase [22].

Surface tension between two macroscopic phases A and B is one of the few required parameters to characterize a free surface. It constitutes a macroscopic and calculable property of a surface whose definition stems from the expression of the Helmholtz free energy, as was demonstrated above. Specifically, it was shown that the physical interpretation of surface tension is the way surface energy varies due to small changes in interfacial area, always under equilibrium. The use of Helmholtz free energy is more convenient for a free surface since a surface has zero volume and, hence, no volumetric work. Recalling the expression for the work needed for a differential change in area dA, $dW = \sigma dA$

and incorporating it in U^s, so that $U^s = TS^s + \sigma A$, it follows that the surface Helmholtz free energy is equivalent with Gibbs free energy:

$$\sigma = \frac{\partial F^s}{\partial A} = \frac{\partial G^s}{\partial A} \tag{3.16}$$

3.4 Gibb's Adsorption Isotherm

In the above subsection, the Gibb's-Duhem equation for a free surface of N species was derived

$$s^s dT + \sum_{i=1}^{N} \Gamma_i^s d\mu_i^s + d\sigma = 0$$

where T is the absolute temperature, s^s the surface entropy per unit area, μ_i^s denotes the chemical potential of the i^{th} species and Γ_i^s the surface excess of the i^{th} substance. At this particular point it is noted that no coordinate system was defined, thus all the above results are general and independent of geometry. However, the exact location of the surface has not yet been specified and Γ_i^s are defined relative to an arbitrarily chosen diving surface. To address this issue, let us consider a system of two components, 1 (solvent) and 2 (solute) with surface excesses Γ_1^s and Γ_2^s, respectively. Since the Gibbs Convention was employed to describe the equilibrium behaviour of surface tension, it directly follows from it that the solvent has zero surface excess concentration [2, 120, 22]. Accordingly, it is possible to choose the location of the surface so that $\Gamma_1^s = 0$, thus eq.(3.14) can be simplified. In the present dissertation we are concerned about lung surfactant monolayers at physiological conditions only, i.e at constant temperature around $T = 37\,^{\circ}\mathrm{C}$. Therefore, the differential dT is henceforth zero. Writing eq.(3.14) under isothermal conditions yields

$$d\sigma = -\Gamma_2^s d\mu_2 \tag{3.17}$$

Dropping the subscript "2" and the superscript "s" for simplicity (Γ_i^s values are defined only at the surface) results in the well-known Gibbs adsorption isotherm for a two-component system:

$$d\sigma = -\Gamma d\mu \tag{3.18}$$

where Γ denotes the surface excess, also called surface concentration of the solute [102]. Solving for Γ leads to the mathematical definition of the surface excess according to Gibbs convention

$$\Gamma = -\left(\frac{\partial \sigma}{\partial \mu}\right)_T \tag{3.19}$$

The last expression is valid for systems comprised of the solvent and a single species N = 1. For N > 1 species, the latter simply becomes,

$$\Gamma_i = -\left(\frac{\partial\sigma}{\partial\mu_i}\right)_T \tag{3.20}$$

The Gibbs adsorption isotherm relates the variation of surface tension to changes in surfactant concentration within the bulk of a solvent and constitutes one of the fundamental equations of surface Physical-Chemistry [2]. It holds only at equilibrium conditions. In the case of an ideal or nearly ideal solution, the chemical potential for the i^{th} substance can easily be calculated by the well-established Guggenheim equation [2]:

$$G_i = G_i^o + n_i\mathcal{R}T\ln C_i \tag{3.21}$$

where C_i is the bulk concentration of the i^{th} substance. According to the thermodynamic definition of the chemical potential of a certain species, i, $\mu_i = \partial G_i/\partial n_i$, which leads to the final expression for the chemical potential[1]

$$\mu_i = \mu_i^o + \mathcal{R}T\ln C_i \tag{3.22}$$

thus, $d\mu_i = \mathcal{R}T d\ln C_i$. In the last two expressions, G_i^o, μ_i^o are constants characterizing the standard state of the component. If surfactants of a single species are assumed then substitution of eq.(3.22) in eq.(3.20) leads to the well-known Gibbs adsorption isotherm for an ideal solution[2]

$$\boxed{\Gamma = -\frac{1}{\mathcal{R}T}\frac{d\sigma}{d\ln C}} \tag{3.23}$$

All of the above relations are generally valid since no coordinate system was initially defined. Though the thermodynamic treatment of the surface is now established, its exact position remains to be defined. In fact, it is difficult to exactly calculate the position of the dividing plane with respect to a specific coordinate system, thus, we choose a schematic way to do this. Consider an axis across the horizontal direction of Fig. 3.4 so that the axis is perpendicular to the surface. The vertical axis represents the concentration profile of every substance. We further assume a two-component system composed of one surfactant with concentration profile C_2, and the solvent, e.g. water, with profile

---

[1] Nevertheless, there is an approach discussed elsewhere ([173]) where the solvent adsorption is no-zero since it does not assume a fixed dividing surface position. Since herein only aqueous surfactant solutions are within the scope of interest, this approach induces negligible discrepancies with Gibbs's method.

[2] For non-ideal systems, instead of C, the Gibbs adsorption equation uses the chemical activity $X = \gamma C$ in principle. However, for many surfactant systems using C directly is a reasonable since γ is approximately independent on the concentration [112].

C_1. If the two above profiles are to be measured, the obtained results will be similar to those of Fig. 3.5.

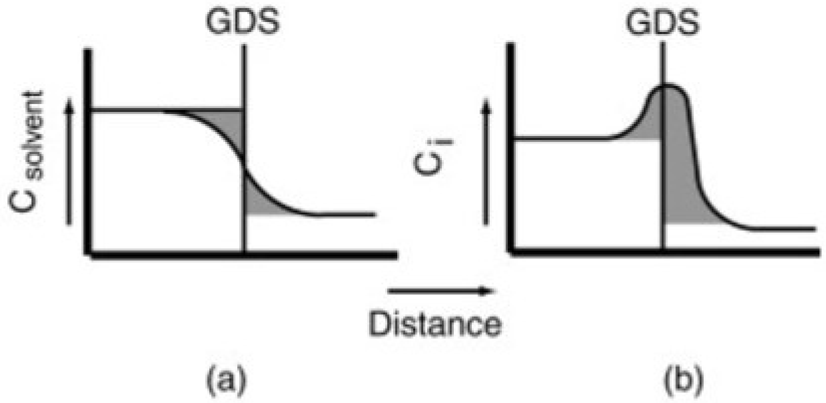

Figure 3.5: Concentration profiles for two substances with respect to the dividing plane, taken from [120]. The form of the concentration distribution of the surfactant is not unique as long as the solvent has zero surface excess.

As intuitively expected, C_2 is uniform in the bulk regions α, β, however, near the dividing surface it decreases continuously as it steps from α to β. C_1 exhibits a qualitatively similar behaviour. The fundamental difference between the two profiles of Fig. 3.5 is the gray area confined between the profile and the concentrations in the bulk. Gibbs convention theorizes that the position of the dividing plane is such that the gray area in Fig. 3.5 before and after it are **equal** for the solvent, so there is no net solvent excess concentration at s. In return, the surface excess of the second component (the solute-surfactant) is **non zero**. Based on Fig. 3.5, it is deduced that the surface excess concentration of the j_{th} substance is the following:

$$\Gamma_j^s = \int_{-\infty}^{GDS} (C_i(x) - C_j^A)dx + \int_{GDS}^{\infty} (C_j(x) - C_j^B)dx \tag{3.24}$$

where $j = 1, 2$. For the solvent ($j = 1$), the two integrals are algebraiclly opposite and $\Gamma_{j=1}^s = 0$, while $\Gamma_{j=2}^s = \Gamma$ is non-zero. This particular definition of Γ has two advantages over any other definition. First, Gibbs adsorption isotherm eq.(3.23) implies that Γ can be calculated solely by measurable quantities, specifically surface tension, temperature and surfactant bulk concentration. Second, the choice of the interface is intuitively evident given that $C_1 \gg C_2$. Different profiles of $C_2(x)$ lead to the same amount of surface excess as shown in Fig. 3.6, as long as $\Gamma_{j=1}^s = 0$ [22]. In the left case, the distribution of molecules 2 stretches out beyond the interface, but the concentration is nowhere increased. In the second case, the concentration of the molecules 2 is actually increased.

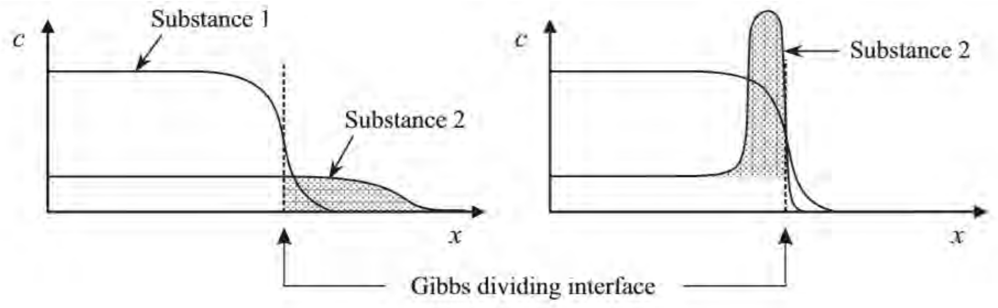

Figure 3.6: Concentration profiles for two substances with respect to the dividing plane, adapted from [120].

More importantly, the grey area reveals that the 2nd substance, namely the surfactant, tend to concentrate closely to the dividing surface or simply the surface. Indeed, if we dissolve a surfactant into a liquid, say water, we will observe that these molecules ”migrate” from the bulk to the surface. This migration process is called adsorption.

Returning to the final form of Gibbs adsorption equation eq.(3.23), it is deduced that since Γ is positive, any increase of the bulk concentration, C decreases the surface tension of the interface, or simply put, surfactants adsorb at liquid surfaces and they decrease surface tension. This result constitutes the main reason these agents are called “*surface active*”.

3.5 Equilibrium adsorption isotherms and surface equations of state

In order to exploit the Gibb’s adsorption equation it is necessary to have knowledge on how surface concentration, Γ is connected to its bulk counterpart, C. In general, bulk concentration is a function of surface adsorption, $C = C(\Gamma)$. More complex isotherms arise for more complex monolayers or solutions, however, in this dissertation we restrict our attention to simple monolayers of conventional surfactants, a trend also followed by previous researchers who studied pulmonary surfactant dynamics with analytical models [127, 149, 99]. Knowledge of the exact relationship between Γ and C allows one to determine the way surface tension varies due to change of equilibrium surfactant adsorption, under constant temperature, expressing, eventually, surface tension as a function of surfactant concentration only from eq.(3.23).

The simplest adsorption isotherm is the **Henry** adsorption isotherm, in which Γ is linearly dependent on the concentration of surfactant in the bulk, C.

$$C(\Gamma) = K_H \Gamma \tag{3.25}$$

Here, K_H is defined as the ratio $k_{\mathrm{des}}/k_{\mathrm{ads}}$ the equilibrium adsorption constant and has dimensions of length [28]. k_{ads}, k_{des} are sorption rates, both of which are assumed constant and independent of the concentration of adsorbed surfactants. The validity of Henry's isotherm is restricted to dilute concentrations and its range of application is rather limited [116]. Nonetheless, it has already been employed for studying the fluid dynamics of the lung surfactant covering the liquid within alveoli [178, 179] or the liquid lining pulmonary airways [196]. Substituting Henry's isotherm in eq.(3.23) allows one to separate variables and integrate from a state with no added surfactant to a finite interfacial concentration Γ where surface tension is simply $\sigma(\Gamma)$. It follows that

$$-\int_{\sigma_o}^{\sigma} \frac{d\sigma}{\mathcal{R}T} = \int_0^{\Gamma} \Gamma d \ln C = \int_0^{\Gamma} \Gamma \frac{dC}{C} \tag{3.26}$$

or

$$\sigma = \sigma_o - \mathcal{R}T\Gamma \tag{3.27}$$

with σ_o denoting the surface tension of a clean surface. The last expression is the so-called surface equation of state or EOS for abbreviation. Henceforth, the same strategy is employed for every isotherm in order to deduce the respective EOS. Continuing further with ideal isotherms, the most widely used ideal but non-linear adsorption isotherm is the famous **Langmuir** isotherm.

$$K_L C = \frac{\Gamma}{\Gamma_\infty - \Gamma} \tag{3.28}$$

where $K_L = k_{\mathrm{ads}}/k_{\mathrm{des}}$. The Langmuir EOS is derived as above, yielding

$$\sigma = \sigma_o + \mathcal{R}T\Gamma_\infty \ln\left(1 - \frac{\Gamma}{\Gamma_\infty}\right) \tag{3.29}$$

Though simple in a mathematical sense, Langmuir's model is successful in capturing the key physics of equilibrium monolayers [142]. Unlike Henry's adsorption isotherm, Langmuir's model is based on specific assumptions about the nature of the monolayer, which, following the authors in [43], are the following:

1. The surfactant-formed monolayer is assumed to behave like a 2-D lattice where a finite amount of adsorption sites can fit [142]. Each site on the lattice is equivalent, meaning that they are of equal area.

2. The adsorption probability at an empty site is independent of the occupancy of neighbouring sites.

3. There are no molecular interactions between the adsorbed molecules.

According to Langmuir's model, only one surfactant molecule can be "inserted" on a specific adsorption site and since there is a maximum number of such sites, it expresses the maximum number of molecules that can geometrically fit on the surface, indirectly providing information about the surface packing arrangement [142]. The aforementioned number is expressed by Γ_∞ which is called the surface closed-packing concentration or saturation concentration. It is the maximum concentration the surface can attain, beyond which any further addition of surfactants does not alter surface tension. Typical values of Γ_∞ are about 10^{-6} mol m^{-2} [27]. Both Henry's and Langmuir's model belong to the class of **ideal models**.

The term ideal corresponds to the pressumption that molecules adsorbed at the surface form a monolayer so dilute they behave as point-like particles and they do not interact with each other [111]. In reality, nonetheless, this is not the case. In order to account for the existence of molecular interactions between adsorbed surfactant molecules, **Frumkin's** isotherm is used, which accounts for **non-ideality**. Such interactions are pair-wise and occur only between adsorbed neighbouring molecules [142]. Frumkin's model is an extension of the Langmuir model [15]. In order to derive it, Langmuir's isotherm is written in the following form

$$k_{\text{ads}} C(\Gamma_\infty - \Gamma) - k_{\text{des}}\Gamma = 0 \tag{3.30}$$

where in this case the adsorption-desorption rates depend on the surface concentration obeying Arrhenius-type kinetics [101, 102, 106]

$$k_j = k_j^o e^{-\frac{E_j}{\mathcal{R}T}} \tag{3.31}$$

where $j = a, d$ stand for adsorption and desorption, respectively. This approach is more realistic than the assumptions of Langmuir's model; generally speaking, adsorption and desorption are activated processes and depend on surface concentration, Γ [101, 142]. In particular, Frumkin suggested that the activation energies E_j depend linearly on Γ [101]

$$E_j = E_j^o + \mathcal{R}T v_j \theta \tag{3.32}$$

where $\theta = \Gamma/\Gamma_\infty$ is called surface coverage, E_j^o is a reference activation energy and v_j energy barriers. Γ_∞ is the maximum packing concentration and is the maximum possible concentration the interface can theoretically attain. Combining eq.(3.30)-(3.32) provides the Frumkin's adsorption isotherm.

$$K_F C = e^{-2a\theta}(\frac{\theta}{1-\theta}) \tag{3.33}$$

where

$$a = (v_a - v_d)/2 \tag{3.34}$$

is the dimensional Frumkin interaction parameter and $K_F = \frac{k_{0,a}}{k_{0,d}} e^{-\frac{E_a - E_d}{\mathcal{R}T}}$. Eq. (3.33) is the Frumkin isotherm. Then, applying Gibbs adsorption equation leads to Frumkin's equation of state for surface tension

$$\sigma = \sigma_o + \mathcal{R}T\Gamma_\infty \left[\ln\left(1 - \frac{\Gamma}{\Gamma_\infty}\right) + a\left(\frac{\Gamma}{\Gamma_\infty}\right)^2 \right] \tag{3.35}$$

The Frumkin parameter, a, expresses Van der Waals forces between surfactant molecules at the surface. Further, it is a measure of mixing at the surface [26]. According to its definition, it can either be positive (net repulsion) or negative (attractive forces). Note that the opposite sign convention for a is also used [142]. Essentially, it expresses non-ideality since molecules can interact with each other. In the zero interaction limit, $a = 0$, eq. (3.35) coincides with Langmuir's equation of state [15].

Up to this point, the above three state equations emanating from their respective isotherms are the most frequently used in surfactant studies and in fluid dynamics of surfactant-laden flows. Nonetheless, there exist more isotherms that may account for re-orientation, aggregation or ionization phenomena as well, and the interested reader is referred to [129, 58].

3.6 Dynamic surface tension and adsorption-desorption

A fluid surface in equilibrium with the underlying liquid, where a specified surfactant has dissolved, has the equilibrium concentration, Γ_{eq}. The latter is calculated using the state equation as $\sigma_{\text{eq}} = f(\Gamma_{\text{eq}})$. This is the case for motionless surfaces. In reality, however, static surfaces are less frequently met than surfaces in motion due to flow in the bulk. In such cases, the process of surfactant adsorption-desorption cannot be described via the Gibbs Adsorption Isotherm [101]. At the same time, this realization implies that the surface tension cannot be deduced from the aforementioned equilibrium tools, since, as it is connected to the surface concentration and the latter varies with time, surface tension is now a time-dependent surface thermodynamic variable. In such cases we talk about the so-called dynamic surface tension, DST for brevity.

Instead of a strict definition of DST, its meaning can be understood if one considers a simple experiment. Imagine a water surface in contact with air. No surfactant is present and surface tension has a known value, σ_o. As soon as a small drop of surfactant is deposited at the surface, the reader-experimenter observes surface tension to decrease with time due to gradients of the chemical potential (bulk-surface) and the combined effect of adsorption-desorption takes place. After some time, surface tension reaches a stationary value. At that point, equilibrium is reached and the chemical potential at the surface balances that of the bulk. Time required for equilibrium is not always pre-known; it depends on the system solute-solvent and can range from miliseconds to minutes or even days [26]. The time dependent behaviour of surface tension until equilibration described in the above thought experiment is called DST. Of course, Γ and C will then be connected to each other via the equilibrium adsorption isotherm. During the transient period, surface tension is considered dynamic. Calculating the dynamic behaviour of surface tension from a purely theoretical perspective is not the only way available; There are many experimental methods for this purpose, which are well described in the review of Chang & Franses [28].

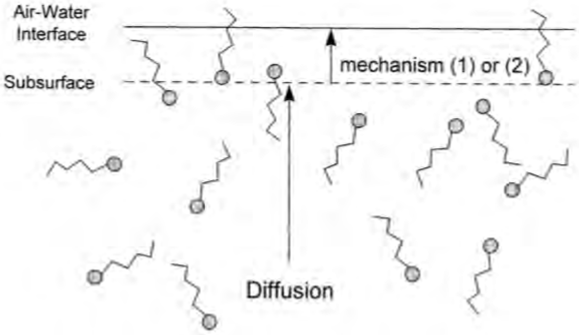

Figure 3.7: Schematic depiction of the path followed by a surfactant monomer from the bulk of the solution to the surface, taken from [43]. Note the distinction between the bulk of the liquid and the subsurface. A random monomer firstly needs to diffuse via the solvent to reach the subsurface. Then, in the absence of adsorption barriers, it immediately diffuses to the surface, otherwise it reaches the surface through adsorption by overcoming the related energy barriers.

The transport of surfactants from the bulk of a solution to the surface depends on whether diffusion or adsorption is the dominant process. As stated above, surfactants adsorb from the bulk to the interface, forming structures known as monolayers and at the same time they decrease surface tension. During this process, the path of a typical surfactant monomer from the bulk to the interface is generally regarded to consist of two routes: A) Transport from the bulk of the solution to the subsurface via diffusion. B) Once the monomer reaches the subsurface, it, then, reaches the surface following one of two possible mechanisms [43]. 1) It diffuses from the subsurface to the surface. 2) There might be an adsorption barrier preventing it from adsorbing. Schematically the path followed by a typical surfactant molecule far from the surface, i.e in the bulk region, to the surface is shown in Fig. 3.7.

What follows next is the mathematical description of the two mechanisms followed by surfactant monomers to adsorb at the surface, along with the assumptions under which they hold.

3.6.1 Kinetically-controlled transfer

Dynamic surfactant adsorption phenomena where adsorption/desorption energy barriers are present, are modeled by using a kinetic expression. In order to describe adsorption out of equilibrium, emphasis is given in deriving a differential equation describing the time dependence of the concentration of surfactant monolayer. According to the authors in [159], when a surfactant monolayer is formed and sustained away from equilibrium, its concentration can be expressed as a function of time and the surface area it occupies:

$$\Gamma = \Gamma(t, A) \tag{3.36}$$

thus the net rate of change of the interfacial concentration, Γ, is

$$\frac{d\Gamma}{dt} = \left(\frac{\partial \Gamma}{\partial t}\right)_A + \left(\frac{\partial \Gamma}{\partial A}\right)_t \frac{dA}{dt} \tag{3.37}$$

According to the general expression of the surfactant mass balance, which holds only at the surface, two factors contribute to change of surfactant amount; one is due to changes of the interfacial area with respect to time (last term on the right side) and the other emanates from kinetic transport of surfactant material from the surface/subphase to the subphase/surface. To be specific, in the last expression, the term $\partial\Gamma/\partial t|_A$ is independent of the temporal variation of the interfacial area; thus it is only the net kinetic flux of surfactants at the surface. Following the authors in [177], we can denote the latter as $\partial\Gamma/\partial t|_A = j_n$. Mathematically, such an expression is the algebraic summation of the fluxes due to adsorption, desorption, surfactant evaporation and exclusion of surfactant material from collapse of the surfactant monolayer [159]. In the most simple case, the surface is kept undisturbed ($A =$ constant) and evaporation, collapse phenomena are absent. The temporal variation of the concentration is balanced by the surfactant kinetic flux at the surface [111, 101]:

$$\frac{d\Gamma}{dt} = j_{\text{ads}} - j_{\text{des}} \tag{3.38}$$

where j_{ads}, j_{des} are the fluxes of adsorption and desorption, respectively. Eq.(3.38) is generally valid for constant surface areas. However, there are cases where large surface disturbances are present, contributing to interfacial concentration. This is the case for lung surfactants since, during respiration, the surface area of the alveolar fluid is imposed to large deformations from inflation/deflation of alveoli. The surface concentration is $\Gamma = \frac{N}{A}$ with N denoting the number of moles of the adsorbed surfactant and if we combine it with eq.(3.37), we obtain the following surfactant mass balance [177]

$$\boxed{\frac{dN}{dt} = \frac{d}{dt}(\Gamma A) = A(j_{\text{ads}} - j_{\text{des}})} \tag{3.39}$$

or

$$\boxed{\frac{d\Gamma}{dt} + \Gamma\frac{d\ln A}{dt} = j_{\text{ads}} - j_{\text{des}}} \tag{3.40}$$

where A is the area of the surface at which adsorption/desorption phenomena occur. The last expression is a generalization of eq.(3.38), valid for oscillatory surfaces [177]. At equilibrium, $d/dt = 0$ and the two kinetic fluxes are equal. Generally speaking, both fluxes depend on the amount of surfactant already adsorbed at the surface and the adsorptive flux depends also on the subsurface concentration. “Subsurface” refers to the layer immediately adjacent to the surface, only a few $\mathring{A}$ beneath the surface [27]. As stated, the difference between the adsorptive and desorption flux is usually denoted by the symbol j_n, it physically expresses the net exchange of surfactant molecules between the interface and the subsurface and depends on the surfactant already adsorbed at the surface and the surfactant concentration in the bulk of the solution [111]

$$\boxed{j_n = j_{\text{ads}}(\Gamma, C) - j_{\text{des}}(\Gamma)} \tag{3.41}$$

For insoluble surfactants, there is no exchange of molecules with the bulk phase and $j_n = 0$. Each flux is characterized by a process rate, k_{ads} for adsorption and k_{des} for desorption, which can either be constant or surface coverage dependent [28]. Mathematically, they are expressed as [111]

$$j_{\text{ads}} = k_{\text{ads}} F(\Gamma, C_s) \tag{3.42}$$

$$j_{\text{des}} = k_{\text{des}} G(\Gamma, C_s) \tag{3.43}$$

where F, G are functions of the surface excess and bulk concentration calculated at the interface Γ, C_s, respectively. The exact form of F, G depend on the adsorption equilibrium isotherm obtained after a sufficient amount of time passes and equilibration is established. An extensive list of the expressions of the two fluxes available in the literature can be found in [111].

At equilibrium, concentration in the bulk was taken to be constant as macroscopic motion and area variations were absent. Since here there are no equilibrium conditions, the surfactant concentration in the bulk, C, is expected to vary spatially as we move from the bulk to the interface. In this case, only the subsurface component of bulk concentration participates in the kinetic equation predicting the evolution of its surface counterpart. Therefore, if ones assumes one-dimensional bulk transport and a coordinate system positioned at the surface and Ox axis pointing towards the liquid phase, C_s is $C(x=0,t)$ in eq.(3.42),(3.43), where 0 denotes the subsurface. The simplest kinetic equation for eq.(3.38), which will be thoroughly used in this dissertation in order to model the kinetics of Lung Surfactant, is the Langmuir-Hinshelwood equation [26]

$$\boxed{\frac{d\Gamma}{dt} = k_{\text{ads}} C_s (\Gamma_\infty - \Gamma) - k_{\text{des}} \Gamma} \tag{3.44}$$

Since at equilibrium $d/dt = 0$, then the Langmuir isotherm eq.(3.28) is recovered. Note that other more complex models than the Langmuir-Hinshelwood equation have been developed [116, 26, 17, 18], some of which concerning ionic surfactant solutions [19]. Physically, a detailed balance between adsorbed and dissolved surfactants must hold for equilibrium. As the authors note in [111], "as many surfactants must adsorb to a surface as desorb in any given time" during equilibrium, which is attained after a long time ($\lim_{t\to\infty} d\Gamma/dt = 0$). Furthermore, it is notable that if both of the above fluxes are multiplied by the same factor, then the equilibrium isotherm obtained by equating eq.(3.38) to zero remains unchanged. An excellent review dedicated to dynamic adsorption-desorption at air/water interfaces can be found in [28]. Thus, the expression for the dynamical exchange of surfactants between the surface and the subsurface is now a differential equation[3] where the unknown is the concentration of adsorbed molecules. Of course, eq.(3.44) implies a spatially uniform surfactant concentration and Γ is a function of time only. By intuition, one would expect Γ to vary across the surface as well, however, this more realistic case is discussed later in this chapter.

---

[3] If the assumption of local thermodynamic equilibrium is valid for a system sorption rates are much faster than diffusion rates [27], then an alternative approach exists which does not demand of dealing with a differential equation, at least at the surface. $\Gamma(t)$ is then equal to its equilibrium value calculated for the instantaneous subsurface concentration. From eq.(3.44) $\Gamma(t) = \Gamma_\infty \frac{k_a C(0,t)}{k_a C(0,t)+k_d}$ and C obeys the standard convective-diffusion equation in the bulk.

3.6.2 Diffusion-controlled transfer

The main assumption of this model is that the dependence of surface tension on time, which is connected to the surface concentration, is caused by transport of molecules to the surface. If no disturbances are present, this transport is controlled by diffusion [116]. Besides, in diffusion-controlled kinetics, the subsurface is assumed to be in local equilibrium with the surface [163], fact that implies that monomers instantaneously adsorb at the interface as soon as they reach the subsurface. By neglecting any flow in the subphase, transport of surfactant agents takes the standard-diffusion form:

$$\frac{\partial C}{\partial t} = \mathcal{D}\nabla^2 C \tag{3.45}$$

where C is the bulk surfactant concentration and $\mathcal{D}$ is the diffusion coefficient of the surfactant in the bulk. The surfactant flux from the bulk to the surface during adsorption, j_n, is connected to the interfacial component of the concentration [116], serving as a boundary condition to the problem.

$$\frac{d\mathit{\Gamma}}{dt} = j_n = \mathcal{D}\frac{\partial C}{\partial x}\bigg|_{x=s} \tag{3.46}$$

In the more general case where the surface area varies with time, e.g when surfactant adsorbs at the surface of an oscillating drop, the mass balance is [143]

$$\frac{d\Gamma}{dt} + \Gamma\frac{d\ln A}{dt} = \mathcal{D}\frac{\partial C}{\partial x}\bigg|_{x=s} \tag{3.47}$$

3.7 Flow and transport phenomena in surfactant-laden liquids

Up to this point, we have been restricted to equilibrium arguments, such as Gibbs's Adsorption Isotherm, or to purely temporal variation of spatially uniform surfactant concentration. When the underlying liquid is flowing, the above theory describing dynamic surface tension is generalized in the context of Transport Phenomena and the transport of surfactant within the bulk and at the surface is coupled with the fluid mechanics of the liquid (the solvent). For this reason, we need to address surfactant mass transfer in combination with the dynamics of the flowing liquid.

Interfacial flows with insoluble or soluble surfactants are intensely studied in the recent literature [111], and the presence of the surface-active agent proves to have a decisive role on the stability characteristics and transitions, as well as

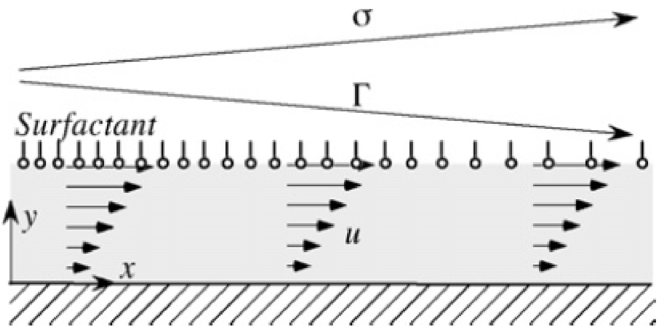

Figure 3.8: A schematic configuration of a flowing film covered with surfactant, adapted from [65]. The decreasing Γ from the left to the right induces flow within the liquid layer.

on accompanying transport phenomena [50, 14, 131, 38, 88, 93, 79, 39, 36, 151]. Of fundamental interest in such flows is the intricate coupling of the dynamics of the surfactant—i.e. surface elasticity and viscosity, adsorption-desorption kinetics—with the dynamics of the flow field. Quite frequently in micro-flows, the Reynolds number is very small and flow dynamics is dictated by the dynamics of the boundaries. Among the wide variety of applications, prominent is the study of various aspects of lung physiology, where thin, surfactant-laden films coat the airways and the alveoli [52, 66, 115, 57, 94, 49, 119]. In the case of alveoli, which is the focus of the present dissertation, it is the periodic inflation and deflation of alveolar walls during the breathing cycle that drives the flow.

3.7.1 Fluid Mechanics

Consider a flowing incompressible liquid layer with a free surface in contact with gas. A surfactant of single species is dissolved in the bulk and forms a monolayer at the interface as schematically shown in Fig. 3.8. The flow is described by the velocity field $\boldsymbol{u}(\boldsymbol{x}, t)$, and the location of the free surface is given by the zero-level function $S(\boldsymbol{x}_s, t) = 0$ and is denoted by a subscript s. The liquid is assumed to possess constant thermophysical properties at isothermal conditions. Also, we consider the layer to be rheologically Newtonian. Then the dynamics of the flow obey the continuity and Navier-Stokes equations

$$\boxed{\boldsymbol{\nabla} \cdot \boldsymbol{u} = 0} \tag{3.48}$$

and

$$\boxed{\rho\left(\frac{\partial \boldsymbol{u}}{\partial t} + \boldsymbol{u} \cdot \boldsymbol{\nabla} \boldsymbol{u}\right) = -\boldsymbol{\nabla} p + \mu \nabla^2 \boldsymbol{u} + \rho \boldsymbol{g}} \tag{3.49}$$

where μ is the dynamic viscosity, ρ is the mass density of the liquid, p is the pressure field and $\boldsymbol{g}$ is the gravitational acceleration. At the interface, we impose

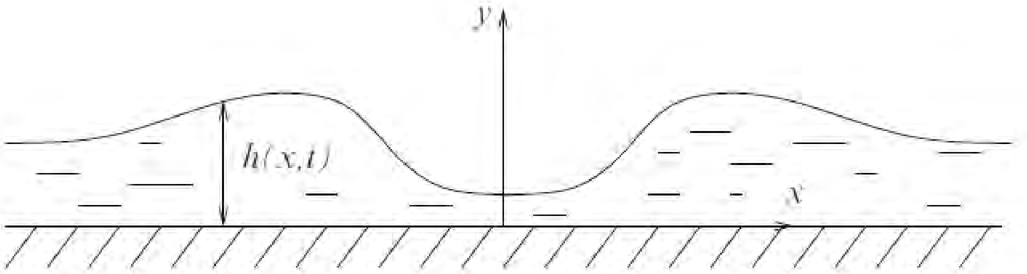

Figure 3.9: A simple schematic of a thin liquid film on a plane substrate, adapted from [4].

the kinematic boundary condition

$$\boxed{\frac{DS}{Dt} = \frac{\partial S}{\partial t} + \boldsymbol{u} \cdot \boldsymbol{\nabla} S = 0} \tag{3.50}$$

where D/Dt is the material derivative and $\boldsymbol{u} = \boldsymbol{u}(\boldsymbol{x}_s, t)$. In order to derive the kinematic condition, we need the spatiotemporal position of the interface. For instance, in Fig. 3.9 if we denote the film height by $h(x,t)$, the interface's position is $y = h(x,t)$ and $S = y - h = 0$ while the unit normal to the interface is $\boldsymbol{n} = -\boldsymbol{\nabla} S / |\boldsymbol{\nabla} S|$. The kinematic condition ensures the continuity of the liquid's mass exactly at the interface. Similarly, the following force balance holds at the interface as well [126, 4]

$$\boxed{(\boldsymbol{T}_2 - \boldsymbol{T}_1) \cdot \boldsymbol{n} = \sigma(\boldsymbol{\nabla}_s \cdot \boldsymbol{n})\boldsymbol{n} - \boldsymbol{\nabla}_s \sigma} \tag{3.51}$$

where $\boldsymbol{T}_i$ is the total stress tensor of the i^{th} phase $(i = 1 : liquid, i = 2 : gas)$ and is generally composed of viscous and Maxwell stresses [38], $\boldsymbol{\nabla}_s = (\mathbf{I} - \boldsymbol{nn}) \cdot \boldsymbol{\nabla}$ is the surface gradient operator, $\boldsymbol{n}$ the unit vector at the surface and σ is the surface tension. The above stress balance accounts for two possible mechanisms through which surface tension can affect the fluid dynamics of the flow considered. The first term on the RHS, $\sigma(\boldsymbol{\nabla}_s \cdot \boldsymbol{n})\boldsymbol{n}$ represents the capillary pressure and is normal to the interface, while $\boldsymbol{\nabla}_s \sigma$ emanates from variations of σ along the interface and is tangential.

The dimensions of alveoli, discussed in Chapter 2, in combination with the properties of the alveolar lining allow us to simplify the Navier-Stokes equations by exploiting two dimensionless numbers, the Reynolds and the Bond number, defined as

$$Re = \frac{\rho U l}{\mu}, \quad Bo = \frac{\rho g l^2}{\sigma} \tag{3.52}$$

Here U is a characteristic velocity, ρ, μ and σ are physical properties of the aqueous layer and $g = 9.81\ \mathrm{m\,s^{-2}}$. The characteristic length scale, l, can be represented by either the mean thickness of the alveolar fluid or the alveolar radius. Acinar air flow and –even more so– flow within the alveolar liquid lining are examples of low Reynolds number flows where viscous effects are dominant and so $Re \ll 1$ [65]. Gravitational effects are negligible as well since $Bo \ll 1$ [3]. Accordingly, for such flows the Navier-Stokes equation is substituted by the following, quasi-steady Stokes equation [63, 179, 89, 62]

$$\boxed{\boldsymbol{\nabla} p = \mu \nabla^2 \boldsymbol{u}} \tag{3.53}$$

3.7.2 Surfactant transport

When a surfactant is soluble, the variation of bulk concentration, C, is described by the standard convection-diffusion equation

$$\boxed{\frac{\partial C}{\partial t} + \boldsymbol{u} \cdot \boldsymbol{\nabla} C = \mathcal{D} \nabla^2 C} \tag{3.54}$$

where $\mathcal{D}$ is the molecular diffusivity in the bulk. The appropriate boundary condition for surfactant at the free surface is the following local mass balance [141, 58], which is a generalization of eq.(3.39)

$$\boxed{\frac{\partial \Gamma}{\partial t} + \boldsymbol{\nabla}_s \cdot (\Gamma \boldsymbol{u}_s) + (\boldsymbol{u} \cdot \boldsymbol{n}) \Gamma (\boldsymbol{\nabla}_s \cdot \boldsymbol{n}) = \boldsymbol{\nabla}_s \cdot (\mathcal{D}_s \boldsymbol{\nabla}_s \Gamma) + j_n} \tag{3.55}$$

In the above equation, $\mathcal{D}_s$ is the surfactant surface diffusivity along the interface and j_n the net sorptive flux of surfactants (eq.3.41). The latter is the rate of exchange of surfactant molecules between the surface and the bulk, acting as a source term in eq.(3.55). If the surfactant is insoluble, then $j_n = 0$ [111].

On the left side of eq.(3.55), $\boldsymbol{\nabla}_s \cdot (\Gamma \boldsymbol{u}_s)$ expresses surfactant transport via convection and $(\boldsymbol{u} \cdot \boldsymbol{n}) \Gamma (\boldsymbol{\nabla}_s \cdot \boldsymbol{n})$ accounts for the effect of stretching of the surface on surfactant surface concentration. Interestingly, one may easily prove that the stretching term equals $\Gamma \frac{d \ln A}{dt}$ for uniform surface variations.

In order to decide whether j_n will be represented by eq.(3.41) or eq.(3.46), the characteristic times of adsorption and diffusion need to be compared. They are respectively defined as $t_{\text{ads}} = (k_{ads} C_s)^{-1}$, $t_{\text{diff}} = l^2/\mathcal{D}$ with $\mathcal{D}$ denoting the diffusion coefficient of the dissolved surfactant [141, 102] and l the characteristic diffusion length. When one characteristic time is much larger, j_n can be represented by the respective mechanism alone [111]. Under the existence of adsorption barriers, j_n is substituted by eq.(3.41) while in the diffusion-controlled adsorption scenario $j_n = \mathcal{D} \boldsymbol{\nabla} C \cdot \boldsymbol{n}$. If both times are comparable to each other and, subsequently, both transfer mechanisms are active, then $\mathcal{D} \boldsymbol{\nabla} C \cdot \boldsymbol{n} = j_{ads}(\Gamma, C_s) - j_{des}(\Gamma, C_s)$, $C_s = C(x_s, t)$ as utilized in [91, 179, 119]. In overall, the mechanisms of interfacial surfactant transport are schematically

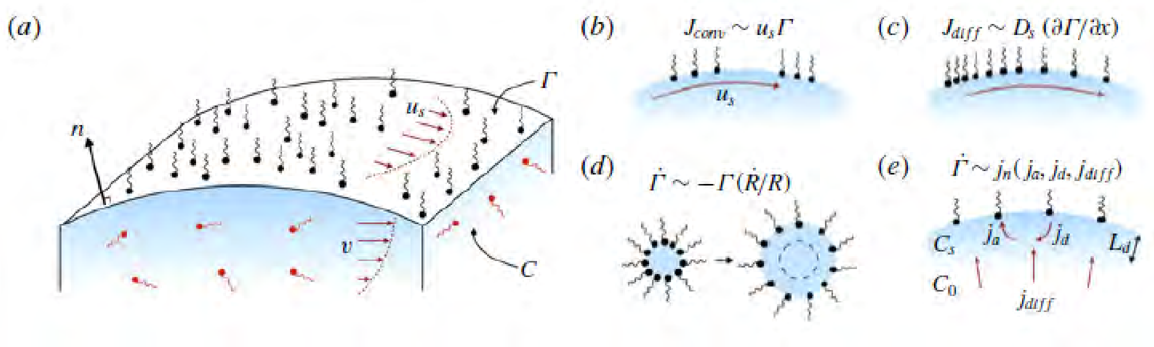

Figure 3.10: A visual summary of the physical mechanisms of surfactant transport. b) interfacial convection c) molecular diffusion, d) stretching of the interface and e) adsorption/desorption. The schematic is taken from [111].

summarised in Fig. 3.10. It is important to note that the above equations can describe surfactant dynamics for bulk concentrations below the CMC; if concentrations higher than CMC are concerned, there are two coupled equations describing the bulk dynamics, one for bulk monomers for C, eq.(3.54) and an additional for the micelles, with concentration M [87].

$$\frac{\partial M}{\partial t} + \boldsymbol{u} \cdot \boldsymbol{\nabla} M = \mathcal{D}_m \nabla^2 M + j_m \tag{3.56}$$

where $\mathcal{D}_m$ is the micelle diffusion coefficient and $j_m = k_m C^m - k_n M$ is the flux of micelles and k_m is the rate at which a micelle is created in the bulk from n monomers while k_n the rate of micelle breakup. Then eq.(3.54) is augmented by $-nj_m$ on its rhs. Though pulmonary surfactant in the alveolar fluid exhibits a complex form consisting of aggregates and micelles, adsorption at the surface of the alveolar lining is kinetically limited rather than diffusion limited [127] and the bulk concentration can be assumed constant with a well-mixed subphase, thus eq.(3.54),(3.56) will not be used for modeling in this dissertation.

The set of equations (3.53),(3.48), (3.55), (3.54) and (3.56) along with the boundary conditions eq.(3.51),(3.50) constitute a set of coupled partial differential equations suitable for describing the spatiotemporal dynamics of the alveolar fluid. The coupling of momentum and surfactant mass transfer is essentially ensured by the surface tension gradient in eq.(3.51) which is called Marangoni stress. Since $\sigma = \sigma(\Gamma)$, the Marangoni stress may be written as

$$\boxed{\boldsymbol{\nabla}_s \sigma = \frac{\partial \sigma}{\partial \Gamma} \boldsymbol{\nabla}_s \Gamma} \tag{3.57}$$

Investigating adsorption-desorption kinetics with spatial non-uniformities not only involves higher mathematical complexity[4] but new phenomena as

---

[4] Surfactant kinetics are now described via a system of PDEs. Seeking the solution of the coupled system is

well. According to Johnson and Stebe (1994) [84], there are two physicochemical mechanisms that can explain the way surfactant adsorption impacts interfacial motion, Marangoni stresses or Gibbs-Marangoni Elasticity, known as Marangoni Effects and, secondly, the treatment of the surface as a 2-D fluid with independent properties. The latter mechanism will not be analyzed in this dissertation as it is relevant for monolayers where surface viscosity is important, which is not the case for pulmonary surfactant monolayers in the range of breathing frequencies. The interested reader is referred to [156, 111] for more information.

3.7.3 Marangoni stresses and surface rheology

Consider a surfactant monolayer of arbitrary surface excess concentration, Γ, where the latter is nonuniform along the surface. As a result, a surface gradient $\boldsymbol{\nabla}_s\Gamma$ is established, implying at the same time from eq.(3.14) that the surface gradient in the surfactant chemical potential μ_s is non zero. A molecule with position at the surface, $\boldsymbol{x}_s$, experiences a force [111]

$$\boldsymbol{f}(\boldsymbol{x}_s) = -\boldsymbol{\nabla}_s\mu_s = -\left(\frac{\partial\mu_s}{\partial\Gamma}\right)\boldsymbol{\nabla}_s\Gamma(\boldsymbol{x}_s) \tag{3.58}$$

which drives the molecule along the surface. Particle inertia and mobility are essential in calculating the particle velocity field at the surface. Besides, neighboring particles also affect the motion of a particular particle. Accurate modeling of the particle's motion at the surface demands the employment of suspension dynamics theory and will not be discussed here since it is beyond the scope of this dissertation. The interested reader is referred to [111] and references therein for more information.

The force calculated by eq.(3.58) strongly implies a departure from thermodynamic equilibrium, as seen by the subscript in the gradient operator. In other words, even if the surfactant chemical potential in the bulk is constant, any deposition or spreading of extra surfactant at the separating surface will produce interfacial stresses. Indeed, it can be shown that eq.(3.58), is connected to a surface traction, generated by the gradient of Γ.

$$\boldsymbol{t}_s = (\boldsymbol{T}\cdot\boldsymbol{n})|_{interface} = -\Gamma\boldsymbol{\nabla}_s\mu \tag{3.59}$$

where $\boldsymbol{T}$ is the stress tensor of the fluid beneath the surface [111]. Recalling the generalised form of the Gibbs Adsorption Isotherm with the neglect of

---

usually difficult to deal with, even in the case of 1-D motion, and numerical methods are used for the solution of the whole physicochemical-hydrodynamic problem.

temperature variations, $d\sigma + \Gamma d\mu = 0$, the above surface traction is simply written as

$$\boxed{\boldsymbol{t}_s = \boldsymbol{\nabla}_s \sigma} \tag{3.60}$$

Thus, a spatially non-uniform surfactant concentration induces shear stresses at any fluid interface, equal to the surface gradient of the surface tension. This stress is the well-known **Marangoni stress**.

Surface tension gradients induced by surfactant concentration gradients can drive or balance viscous shear stress following eq.(3.60) [111]. An initially clean and static surface will be set in motion if a small surfactant-laden drop is deposited on it, as shown below in Fig. 3.11 a). Another example of surfactant-induced Marangoni stresses is the "Reynolds ridge", where a surfactant-coated interface is compressed or dilated against a floating barrier. Such a configuration creates Marangoni stresses that act against the compression/dilation of the surface, as can be seen from the direction of the velocity profiles in Fig. 3.11 b).

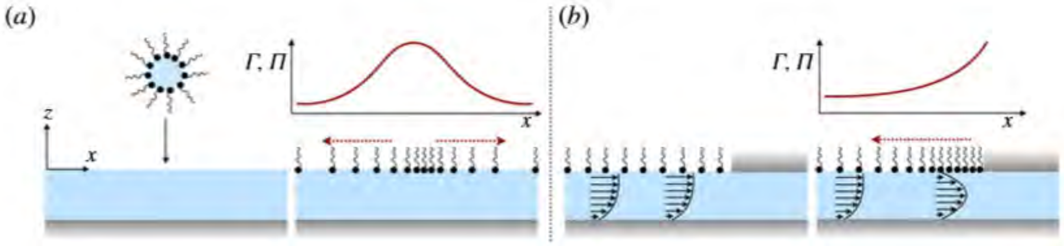

Figure 3.11: Two different examples of Marangoni flows induced by interfacial gradients of Γ, adapted from [111]. a) Surfactant spreading induced by the deposition of a surfactant-laden droplet and b) Surface compression due to flow, specifically, towards an interfacial barrier. Surfactant accumulation near the barrier induces a reverse Marangoni flow. Note that the induced velocities follow the decrease of the concentration profile (red arrows).

The variation of surface tension with surface surfactant concentration, which is responsible for the onset of Marangoni stresses, may be expressed in terms of the Marangoni modulus [111] or Gibbs elasticity [109], E_G

$$\boxed{E_G = -\frac{d\sigma}{d\ln\Gamma}} \tag{3.61}$$

However, the reaction of an interface to dilational stresses actually refers to the change in surface tension as a function of the change in interfacial area. As a measure of this reaction, the surface elasticity is defined as [109, 143, 177]

$$\boxed{E_A = \frac{d\sigma}{d\ln A}} \tag{3.62}$$

The two elasticities may become identical only when dealing with insoluble (and simple) surfactants. If the amount of insoluble surfactant residing on the surface is denoted by N and there are no relaxation effects, then, $dN = d(A\Gamma) = 0$ and $d\ln A = -d\ln\Gamma$.

In the general case, the change in surface tension depends not only on the change of surface area but also on the rate of change of the area, i.e. the surface exhibits visco-elastic behavior. When deformations are small (as, for example, in an oscillating-bubble experiment), the parameters may be linearized around the equilibrium values. Then, the surface elasticity becomes a complex number, with the dilational elasticity as the real part, and the effect of time manifesting as the imaginary part (dilational viscosity) [10, 177]. Combining eqs.(3.61) and (3.62), we may write [111, 177]

$$\boxed{E_A = E_G\left(-\frac{d\ln\Gamma}{d\ln A}\right)} \tag{3.63}$$

Thus, transient phenomena are related to the first term on the rhs. These include the adsorption-desorption processes of a soluble surfactant, as well as molecular re-orientation and phase changes in the adsorbed monolayer. However, for the pulmonary surfactant and normal breathing frequencies, only adsorption-desorption processes are of practical significance.

Determination of surface rheology of PS solutions is critical for understanding the behavior of PS solutions under physiologically relevant conditions and is carried out by a variety of experimental techniques. The main idea behind every method is that an amount of the surfactant under investigation is spread on a surface and a surfactant film is interfacially formed. Then, the surface is compressed or cycled in predetermined frequencies, altering its area and the surface tension of the film. Through various techniques, e.g ADSA [150], the values of surface tension and elasticity modulus, $d\sigma/d\ln A$, are measured. The usefulness of the elasticity modulus is explicit in studies devoted to characterizing PS candidates; according to [32] ”the dilatational and shear properties of the interface between the epithelial lining fluid and gas in the lung alveoli may determine whether the lung can expand easily and uniformly during breathing”. These methods are known as *in-vitro* methods. The most commonly used are the Langmuir-Wilhelmy balance, the captive bubble surfactometer, the pulsating bubble surfactometer, the constrained sessile droplet, and the pendant drop [199, 149]. These apparatuses are schematically depicted in Figs 3.12-3.14. The pattern of cycling is not unique as it can be dynamic expansion-compression or quasi-static.

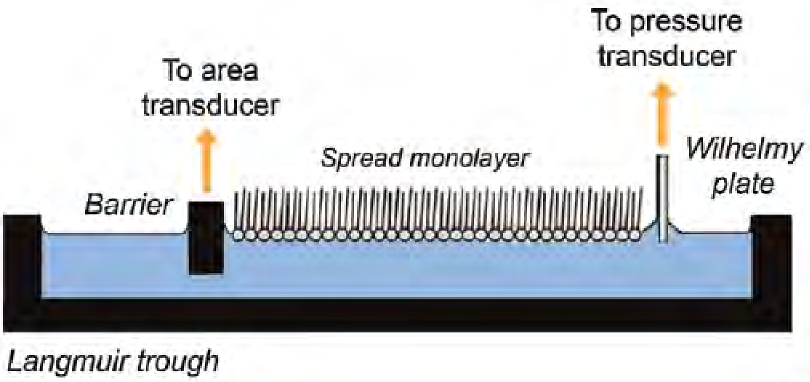

Figure 3.12: The Langmuir trough apparatus, adapted from [128].

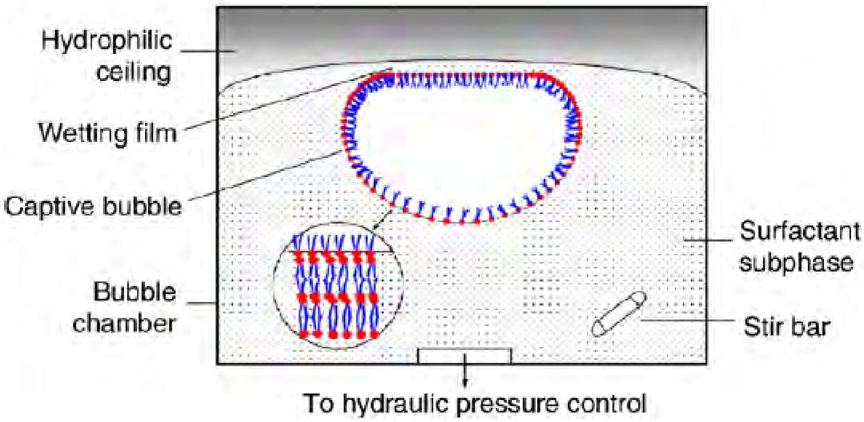

Figure 3.13: The Captive Bubble Surfactometer apparatus, adapted from [199].

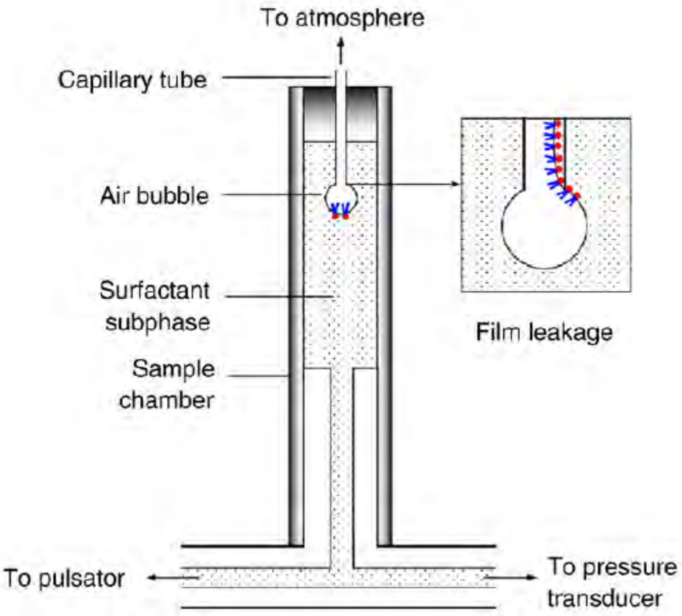

Figure 3.14: The Pulsating Bubble Surfactometer apparatus, adapted from [199].

Chapter 4

Literature Review

Horn and Davis [77] conducted an analytic study to examine the causes of hysteresis in $\sigma - A$ loops in oscillating bubbles, by applying their model on the pulmonary surfactant of mammalian lungs. They concluded that this observation is mainly due to viscoelasticity of the interface, however, they did not account for interfacial processes to depend on interfacial concentration. Besides, monolayer collapse phenomena were not accounted for, a phenomenon pronounced in the dynamic behavior of PS solutions at high concentrations. Motivated by the need to provide an analytic model to explain the changes of lung surfactant, Kamm and colleagues from MIT [127], were the first to propose a mathematical model which described every state an adsorbed PS film passes through during successive cycles at physiological conditions, the latter referring to temperature and frequency. Their model accounted for the PS monolayer collapse described above. Mathematically, after the monolayer reached a maximum value (Γ_{max}, the saturation concentration where the molecules are tightly packed next to each other, this parameter is explained in the next chapter) its concentration remained as such, behaving as insoluble. The obtained computer simulations were compared to experimental surface tension-area results obtained from bubble surfactometer. Further, their results were an early indication at that time of the fact that every particular constituent of lung surfactant (and mainly those presented in 2.2.2) has a specific effect on the rheology of the monolayer and consequently some of them are needed when designing artificial lung surfactants. This is the reason why many clinical pulmonary surfactants are mainly composed of DPPC and SP-C, B [133].

Later on, [54] in a similar fashion developed a more sophisticated model which accounted for the existence of secondary surfactant layers just beneath the surface, simulating the dynamics of a spherical surface (a bubble in particular) in which surfactant this time was varied within the liquid bulk via convection-diffusion. Simulations were in good agreement compared with PBS experiments at a physiological rate (20 cycles/min), underlining the importance of multilayers in simulating the behavior of PS at low surface tensions.

Motivated by the partial lack of quantitative agreement, a phenomenological model was proposed by Saad et al. [149, 150] known as the compression relaxation model (CRM). Their model directly utilized surface tension as a dependent parameter - previous authors used surfactant concentration instead - which was considered to alter due to the combined action of sorption kinetics and elasticity using, in total, 4 model parameters. Monolayer collapse was utilized by not allowing σ to further increase by compression as soon as σ_{min} was reached. Their model was successfully implemented to fit data of $\sigma - A$ loops obtained by dynamic compression/expansion of BLES exogenous surfactant in a constrained sessile droplet (CSD) device. They also used the adsorption-limited model of [127] and the diffusion-controlled model for comparison. It was shown that the data fitting with the CRM was better than the other models for 5 experimental cases in total. BLES preparations in the CSD apparatus were examined for both humid and dry conditions motivated by the results of [1] and a special case where humid BLES mixed with albumin, a serum protein. Generally, albumin inhibits the adsorption of phospholipids and deteriorates the activity of surfactant; this phenomenon is investigated elsewhere [48] as it is outside the scope of the dissertation. Though humidity in the lungs is 100% RH, the authors in [1] found that solutions of BLES surfactant at dry conditions (20% RH) were more stable than those at 100% RH, exhibiting higher dilatational elasticity at the same time. This effect was confirmed by the best-fit values of CRM, while being able to confirm the effect of albumin on PS films, where the film possesses lower expansion/compression elasticities and collapse occurs at physiologically prohibiting σ_{min}.

More recently, Xu et al 2020 [189] proposed a novel experimental technique named constrained droplet surfactometry to study adsorbed films of BLES and provide AFM observations of the PS monolayer structure. The PS solutions at given concentration were allowed to adsorb at the droplet surface and reach equilibrium. Then, subphase replacement took place and the equilibrium film was subjected to oscillations at physiological conditions. Their data suggested that the adsorption-induced squeeze out at the PS film can be explained via a nucleation-growth mechanism and, as a result, the films at low surface tension are enriched in DPPC with the attached surfactant reservoir.

Up to this point, the referenced research concerned mainly experimental studies, where bulk flow phenomena were dismissed. Nonetheless, the action of PS has been associated with affecting the flow field of the liquid layer lining the alveolar epithelium. The effort to elucidate the physicochemical hydrodynamics of the alveolar fluid began in the early 90s mainly by Grotberg and colleagues [82, 59, 83], investigating the spreading of surfactants on thin liquid films overlying horizontal substrates. The authors were motivated by the need to investigate the delivery of exogenous surfactant into the lungs as is the case in SRT. At the same time period, Gradon and Podgorski considered the intrinsic geometrical nature of alveoli in order to address the question of what mechanism supports the self-cleansing properties of the lung surfactant system. In a series of sequential research papers [137, 139, 138], these authors postulated that since the alveolar duct airways exhibit almost cylindrical geometry and alveoli an almost spherical configuration, then the surfaces coated with liquid are proportional to the instantaneous values of d_{duct} and d_{alv}^2, respectively, with them being periodic functions of time. As a result, differences in surfactant concentration between the alveolus and the duct emerge, inducing Marangoni flows, which result in fluid flowing out of the alveoli cleansing them from impurities, such as deposited particles. They also made the hypothesis that outflow of surfactant and impurities is the result of the combined existence of surface tension gradients and expansion-contraction of the alveolar wall. In other words, they suggested that cleansing of particles deposited on the alveolar wall and other impurities, e.g. phagocytes, is a mechanism of purely hydrodynamic origin.

In order to validate their hypothesis, they assumed the alveolar liquid to be a continuous thin layer covered with insoluble surfactants at its surface. The geometry concerned a single alveolus of spherical [139] or cylindrical [137] shape, while air outside the film was ignored. The resultant system of equations was derived via Lubrication Theory, assuming the film thickness being much smaller than the alveolar periphery. Although their mathematical model was considerably simple - as explicitly stated by the authors themselves - it was capable of validating their hypothesis as it showed a net film displacement at the alveolar openings. They further showed that in a single breathing cycle there was a net liquid outflow at the alveolar edge. The associated results underlined the influence of bulk viscosity, surfactant concentration on the alveolus edge and breathing patterns on cleansing time, with the influence of the latter demonstrating longer expiration to be favorable. Thus, the first evidence of a purely hydrodynamic mechanism behind the transport of impurities and surfactants deep in the lungs was established.

Espinosa and Kamm [45] studied the flow of a viscous and surfactant laden layer over a flat, distensible membrane via the thin layer approximation. The membrane was rigid at one end and distensible at the other, corresponding to the direction towards the mouth and the alveoli. Their motivation was to study the effects of various time scales, representing different phenomena, on the clearance flows toward the mouth in the thin liquid lining the airways in a single breathing cycle. Their model assumed only marangoni stresses due to surfactant concentration gradients with the surfactant kinetics being sorption-controlled and disregarded capillarity. Bulk concentration was assumed constant.

Zelig and Haber [63] developed a numerical model simulating hydrodynamic flow within an alveolus adapting a spherical shape corresponding to more realistic geometry, similar to [139]. Uniform production of surfactant at the alveolar wall was assumed. At the course of every breathing cycle, the tangential cleansing velocity at the alveolar rim was found to increase with decreasing the half-cone angle at the entrance, and, simultaneously, the latter had direction towards the outer region of the alveolus. Their research showed no remarkable effect of interfacial diffusion coefficient on the flow.

Wei et al (2003) [178] performed a numerical study on a geometry similar to [45], accounting this time for surfactant transport in the bulk (soluble surfactant). Their results were in qualitative agreement with [45] as flow toward the rigid boundary was increased for lower values of surface tension. Solubility increased flow toward the extensible edge of the membrane, which corresponds to the interior of the alveoli in a real system, for increased liquid volume residing with the alveolus. Calculated flow patterns were favorable in expiration.

Wei et al (2005) [179] considered a two-dimensional configuration for a spherical alveolus coated with a thick fluid layer and deployed the stream function formulation of Haber et al [61]. Note that alveolar wall motion in all the above studies, except [45, 178], considered self-similar motion. Their simulations predicted streamlines reversible in time, as was found in Wei et al 2003, [178], exhibiting vortices exactly at the end of inspiration and expiration. Results, thus, imply a tendency of fluid and particle transport toward the opening, out of the alveolus. More recently, Kang et al [89] deployed Lubrication Theory, similar to the studies of Podgorski and Gradon, in spherical coordinates assuming both Marangoni and Capillary forcing to be important.

Chapter 5

Temporal dynamics of pulmonary surfactant - Proposing a new model

5.1 Introduction

The first problem[1] addressed in this dissertation is concerned with the development, validation and investigation of an analytical minimum model describing the dynamics of lung surfactant at physiological conditions. With the ”minimum” term we emphasize the need for developing a model with the minimum required number of parameters in order to describe the specific kinetics of this surfactant.

A model of interfacial dynamics may schematically be considered to consist of the following two components: (i) a description of the mechanisms and rates of exchange of surfactant molecules between the interface and the bulk, and (ii) a description of the mechanical properties of the monolayer, expressed by the variation of surface tension as a function of interfacial area and surface concentration of adsorbed surfactant.

In the general case, coupling of the mode of deformation to the subphase flow field may result in the spatial variation of surface concentration along the interface. That situation leads to the generation of Marangoni stresses and may be delineated only by the simultaneous solution of the adjoint fluid mechanics problem, subject to appropriate boundary conditions [73, 111, 93]. However, in the present study, only the temporal side of the problem is considered, i.e. it is assumed that the interface deformation is symmetric and does not generate spatial gradients in the surface concentration of adsorbed surfactant.

Molecular exchange between the interface and the bulk is generally considered to be governed by resistances in series, for example, diffusion of surfactant aggregates from the bulk to the subsurface and jump to the interface by overcoming an activation energy [175, 197, 69]. The limiting resistance is usually

---

[1] The work presented in this chapter is published in [20].

inferred by indirect evidence, e.g. by assuming that transport is governed by diffusion and comparing the diffusivity derived from best-fit of the data to the expected range of values.

In this respect, there is mounting evidence [116, 127, 80, 118, 149] that the behavior of pulmonary surfactants is best described by kinetically controlled models, though agreement with data is in some aspects only qualitative [127, 80]. In a similar fashion with the literature, we propose a new model describing the DST of pulmonary surfactant solutions in which Adsorption is kinetically controlled, so adsorption energy barriers are present, implying that the bulk concentration at the surface C_s can be assumed constant and time independent [111]. Kinetics of the subphase material as a result of monolayer collapse is accounted for and modeled as Langmuir-like. The novelty of the model is the inclusion of an intrinsic two-dimensional compressibility of the adsorbed monolayer as presented in [97, 98], allowing for a non-constant molecular area at saturation, $\Omega = 1/\Gamma_\infty = \Omega(\Gamma)$.

5.2 Modeling and mathematical formulation

5.2.1 Assumptions

A small volume, V, of pulmonary surfactant preparation is considered, with surface area, A, exposed to air. The preparation is modeled as a single active species, which resides in the form of vesicles in the bulk with constant concentration, C, and is adsorbed at the interface with surface concentration, Γ. The adsorbed surface concentration is spatially uniform but varies in time as a result of expansion/contraction of the interfacial area, A, and of deviation from adsorption equilibrium. Thus all dependent variables, along with surface pressure $(\sigma_o - \sigma)$ are time dependent-only; $\Gamma = \Gamma(t)$, $A = A(t)$, $\sigma = \sigma(t)$. A schematic representation of the problem is depicted in Fig.(5.1). Bulk flow phenomena due to pressure, viscosity and gravity are neglected. Marangoni flows are neglected as well, implying that surface tension is also uniform along the surface. Though the model to be developed is general, the realization in mind is that of a constrained sessile drop undergoing periodic area variation, as in the experiments of Saad et al (2010) [149] and Xu et al (2020) [189], with which the model predictions will be validated.

It is noted that the description of the pulmonary surfactant dynamics by a single hypothetical active species is not dictated only by the desire to keep the model simple, but appears also to be justified by experiments. In particular, it has been argued that "... Attempts to quantify this behavior [i.e. the behavior

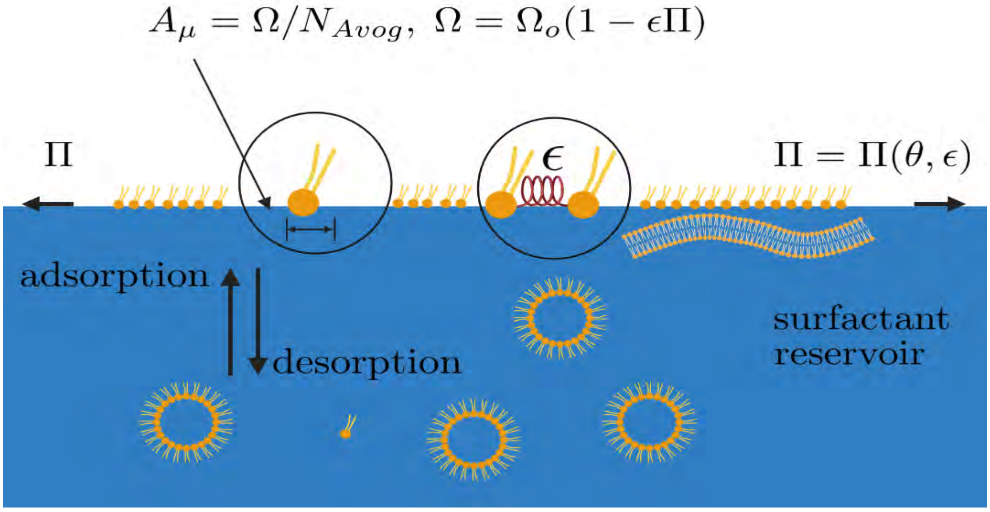

Figure 5.1: Schematic arrangement of the system described by eq.(5.7). The so-called surfactant reservoir is essentially attached to the interface and is distinct from the bulk. Though the depicted micelles (ring-like structures) are far away from the interface, they are shown magnified for clarity.

of the surfactant mixture] show that the assumption of additive contribution of the individual components to the behavior of the layers fails in general for DPPC/surfactant protein mixtures... Therefore, it becomes more plausible to describe the behavior by treating the whole mixture like an individual component and to discuss changes of the parameters based on the influence of the proteins on the behavior of DPPC.” [185].

5.2.2 Equilibrium properties

Adsorption equilibrium is described by the Frumkin isotherm eq.(3.33). In this frame, interface and monomer bulk concentrations, respectively Γ_{eq} and C_1, are related by

$$KC_1 = e^{-2a\theta_{\mathrm{eq}}} \frac{\Gamma_{\mathrm{eq}}}{\Gamma_\infty - \Gamma_{\mathrm{eq}}} = e^{-2a\theta_{\mathrm{eq}}} \frac{\theta_{\mathrm{eq}}}{1 - \theta_{\mathrm{eq}}} \tag{5.1}$$

Here, K is the equilibrium constant or the ratio of adsorption rate over desorption, a is the interaction constant between adsorbed molecules, Γ_∞ is the surface concentration at interfacial saturation and $\theta = \Gamma/\Gamma_\infty$ is the monolayer coverage and $\theta = \Gamma_{\mathrm{eq}}/\Gamma_\infty$

As discussed, native or artificial lung surfactant is mainly composed of phospholipids. As far as the latter are concerned, their critical micelle concentration is very small, $C_{10} \approx 10^{-9} - 10^{-10}$ M [113], and is exceeded many times by the total concentration C of the preparation. Thus, the monomer concentration,

C_1, that appears in eq.(5.1), and also later in the rate expressions, is taken equal to the small constant, C_{10}, and may be absorbed in K.

The above description is complemented by the equation of state, which relates equilibrium surface tension, σ_{eq}, or equivalently, surface pressure $\Pi_{\mathrm{eq}} = \sigma_{\mathrm{o}} - \sigma_{\mathrm{eq}}$ to surface concentration of adsorbed surfactant. Term σ_{o} represents the surface tension of the air/water interface at zero surfactant content; at 37 °C, which is the physiological temperature, σ_{o} is about 70 $\mathrm{mN\,m^{-1}}$ [199, 128]. The equation of state is formally derived by combining Frumkin isotherm, eq.(5.1), with Gibbs equation eq.(3.23)

$$d\sigma_{\mathrm{eq}} = -d\Pi_{\mathrm{eq}} = -\mathcal{R}T\Gamma_{\mathrm{eq}}\frac{dC_1}{C_1} \tag{5.2}$$

which is valid for a Gibbs dividing surface and an ideal bulk phase [69].

5.2.3 Intrinsic compressibility

As presented before in the literature review, research on lung surfactant frequently includes tensiometry and surface rheology in order to assess its behavior under physiologically relevant conditions. Therefore, any analytical model describing pulmonary surfactant kinetics should be coupled in some fashion with surface rheological parameters, such as those provided by the surface compression modulus.

The mean molar area, Ω, is defined as the inverse of the saturation concentration, Γ_∞, which is usually assumed constant. However, looking at experimental curves of surface pressure versus molecular area (A_μ, nm^2/molecule) (for instance figs 2-3 in [198] and fig.1 in [195]), not only reveals the great extent of compression a pulmonary surfactant can attain (nearly zero surface tension) but also the strong variance of A_μ per phase. Moreover, in the region of interest, i.e. TC region beyond the plateau, in Fig. 2.6 the $\Pi - A_\mu$ curve follows a linear trend. Based on this observation, we choose to write the molar area as a linear function of surface pressure.

$$\Omega = \Omega_{\mathrm{o}}(1 - \alpha\Pi) \tag{5.3}$$

where Ω_{o} is molar area at zero surface pressure, i.e. without surfactant, and α is 2D intrinsic surface compressibility introduced in [97, 98]. By definition, saturation concentration is the inverse of Ω, finally yielding

$$\Gamma_\infty = \frac{1}{\Omega} = \frac{1}{\Omega_{\mathrm{o}}(1 - \alpha\Pi)} \tag{5.4}$$

Though Γ_∞ is usually accepted as constant when Langmuir/Frumkin model is utilized, this is not strictly true; It is rather an idealization based on the hard-core model [47]. The latter result is more important than it might seem. Γ_∞ is not constant, as it depends on the instantaneous value of surface concentration, rendering eq.(5.7) nonlinear even for ideal state equation ($a = 0$). At the same time, it depends on a new parameter, which is a property of the molecule. According to the authors who firstly introduced α, it might express the variation of the angle of the molecules upon surface compression, accompanied by an increase in the thickness of the surface layer [98]. Alternatively, it may be seen as the difficulty to compress an initially clean surface ($\Pi = 0$, $\Omega = \Omega_\text{o}$) to form a monolayer ($\Pi > 0$, $\Omega < \Omega_\text{o}$).

To our knowledge, eq.(5.3) allows for a more realistic representation of the molar area occupied by the monolayer, especially in the case of pulmonary surfactant. At physiological conditions surface pressure exceeds 35 $\text{mN}\,\text{m}^{-1}$ [185], and the pulmonary surfactant monolayer lies in the TC phase, which holds for pure DPPC monolayers -the simplest lung surfactant model [9]- as well [104].

In order to understand mechanistically this assumption, we follow the original reasoning of Fainerman et al. [47]. We also take into account that, under high surface pressures, the monolayer of pulmonary surfactant (or its simplistic model, a pure DPPC monolayer) is in a condensed tilted state, as has been shown by grazing incidence X-ray diffraction [193, 185, 104]. In this view, intrinsic compressibility accounts for the change in tilt angle of adsorbed molecules with surface pressure. With decreasing tilt angle, the molecules occupy less area, thus the decrease in molar surface area with pressure, as described by eq.(5.3).

In terms of Ω, the monolayer coverage is $\theta = \Gamma\Omega$, and thus the surface concentration at interfacial saturation, Γ_∞, varies with surface pressure, Π, and is given by [98]

$$\frac{\Pi\Omega_\text{o}}{\mathcal{R}T}\left(1-\alpha\frac{\Pi}{2}\right) = -\ln(1-\theta) - a\theta^2 \tag{5.5}$$

on the understanding that saturation adsorption Γ_∞ is not constant, but depends on the instantaneous value of surface pressure. In the above equation, $\Pi = \sigma_\text{o} - \sigma$, $\mathcal{R}$ is the gas constant and T the absolute temperature. According to a standard assumption, eq.(5.5) is taken to be valid also at conditions away from equilibrium, i.e. the dynamic surface tension is the same function of the instantaneous interfacial concentration as at equilibrium. Thus, the subscript "eq" has been dropped from eqs (5.3)-(5.5) and from now on.

The elasticity of the interface is a key property for the description of deformations accompanied by change in surface area [149]. In the above model, Gibbs elasticity may be directly derived from the equation of state, and is given by the following expression:

$$\frac{1}{E_{\mathrm{G}}} = \left(-\frac{d\sigma}{d\ln\Gamma}\right)^{-1} = \frac{\Omega_{\mathrm{o}}}{\mathcal{R}T}\frac{(1-\alpha\Pi)}{\left(\frac{\theta}{1-\theta}-2a\theta^{2}\right)} + \frac{\alpha}{1-\alpha\Pi} \tag{5.6}$$

Eq.(5.6) represents two elasticity mechanisms in series, the first of which is compositional, i.e. related to variations in surface concentration, and the second is intrinsic, i.e. related to the surface compressibility of the monolayer. Upon saturation ($\theta \longrightarrow 1$), the interface retains finite elasticity due to the intrinsic contribution. It is noted that the application of simple isotherms (such as Frumkin or Langmuir) without the compressibility correction of eq.(5.3), gives at close packings unrealistically high values of Gibbs elasticity, which tend to infinity at saturation [177].

5.2.4 Kinetics

During deformations that result in changes of interfacial area, the total amount of adsorbed surfactant, ΓA, is assumed to vary by three mechanisms: (i) adsorption from the bulk, (ii) desorption to the bulk and (iii) exchange with a surfactant reservoir of total content B. Thus,

$$\frac{d(A\Gamma)}{dt} = A(j_{\mathrm{ads}} - j_{\mathrm{des}} + j_{\mathrm{ex}}), \tag{5.7a}$$

$$\frac{dB}{dt} = -Aj_{\mathrm{ex}}, \tag{5.7b}$$

where j_{ads}, j_{des} and j_{ex} are the fluxes corresponding to surfactant transport by mechanisms (i), (ii) and (iii). With respect to the latter, extensive evidence [107, 152, 104, 48, 135, 189] shows that the 3-dimensional structures, which form during the collapse of the pulmonary surfactant monolayer at $\Pi > \Pi_{\mathrm{max}}$, remain continuous with the interfacial monolayer, and are thus available for rapid replenishment of the film during expansion. The reservoir content, B, of the model represents the cumulative amount of surfactant residing in all these three-dimensional structures.

Interestingly, the rate of change of the total amount of surface active material, $M = A\mathit{\Gamma} + B$, equals the right scale of eq.(3.39). It is to be underlined that the ejected surfactant, as a result of monolayer collapse, remains closely attached to the interface [128]. Though j_{ex} is kinetically similar to the desorptive flux, it is distinct from desorption. Macroscopically, the surfactant reservoir should be envisioned lying on the same plane as the interface, an argument supported by the fact that the protrusions of surface material into the liquid subphase are only a few nanometers in length [7, 9].

Previous theoretical models accounted for reversible collapse of the monolayer in different ways. The adsorption-limited model of Otis et al [127] assumed that the squeezed-out surfactant molecules return immediately to the bulk. Later, Gaver and Krueger [99] developed a detailed model which assumed the existence of a second layer between the interface and the bulk, and represented collapse and re-spreading by distinct fluxes.

In the present model, collapse is assumed to take place when $\Pi \geq \Pi_{\max}$, with $\Pi_{\max}$ an input to the model. The surface concentration, $\Gamma_{\max}$, reached at the onset of collapse, is determined from $\Pi_{\max}$ by application of the equation of state, eq. (5.5). During subsequent compression, the adsorbed surface concentration remains constant at $\Gamma = \Gamma_{\max}$, while excess surfactant is removed from the monolayer and added to the reservoir content, B.

The re-spreading of surfactant from the reservoir to the monolayer during expansion of the interface is described by a simple flux term (see eqs(5.7b) and (5.9) below) with a phenomenological constant that accounts in an average sense for the multitude of three-dimensional structures and the complexity of their interaction with the monolayer. Thus, re-spreading represents a process distinct from adsorption by surfactant vesicles, as it requires no fusion for re-insertion into the surface [146]. In this regard, incorporating j_{ex} in the surfactant mass balance accounts for this mechanism.

The terms appearing in eq.(5.7a) are calculated as follows: Adsorption and desorption rates are described by the kinetics implied by the Frumkin isotherm [111],

$$j_{\mathrm{ads}} - j_{\mathrm{des}} = k_{\mathrm{ads}} C_{10} (\Gamma_\infty - \Gamma) - k_{\mathrm{des}} \Gamma e^{-2a\theta} = k_{\mathrm{ads}} C_{10} \left[(\Gamma_\infty - \Gamma) - \frac{\Gamma}{K C_{10}} e^{-2a\theta} \right] \tag{5.8}$$

As indicated by eqs (5.7a,5.7b), re-insertion of surfactant molecules to the interface from the reservoir content, B, is expressed by an independent rate, j_{ex}. This choice is supported by extensive evidence [152, 135, 48, 107, 6] that collapsed bilayers remain continuous with the interfacial monolayer. The rate, j_{ex}, is modeled as proportional to the deviation of surface concentration from saturation. Thus,

$$j_{\mathrm{ex}} = k_{\mathrm{r}} (\Gamma_\infty - \Gamma) \tag{5.9}$$

Parameters k_{ads} and k_{r} are determined by best-fit to the experimental results of Saad et al [149] and Xu et al [189].

5.2.5 Model formulation

The temporal evolution of surface concentration, Γ, is calculated by numerical integration of the system expressed by eq.(5.7-5.8). Each simulation starts at equilibrium with empty reservoir, therefore $\Gamma(t=0)=\Gamma_{\text{eq}}$ and $B(t=0)=0$ are the initial conditions of this initial value problem. However, different forms emerge for $\Gamma < \Gamma_{\max}$ and $\Gamma = \Gamma_{\max}$, and also for $B=0$ and $B>0$. At the beginning of the simulation, $\Gamma < \Gamma_{\max}$ when also $B=0$, the system to be integrated is

$$\frac{d\Gamma}{dt} = k_{\text{ads}} C_{10}\left[(\Gamma_\infty - \Gamma) - \frac{\Gamma}{KC_{10}} e^{-2a\theta}\right] - \frac{\Gamma}{A}\frac{dA}{dt} \tag{5.10a}$$

$$\frac{dB}{dt} = 0 \tag{5.10b}$$

The situation described by eq.(5.10) may correspond to either expansion or compression of the interface with the reservoir devoid of surfactant due to the initial condition $B(0)=0$. This set of equations actually holds for the entire deformation cycle in case the compression stage does not reach $\Pi_{\max}$. Also, the surfactant reservoir remains unchanged; since collapse is initiated only at $\Gamma_{\max}$, when also $\Pi = \Pi_{\max}$, the associated flux, j_{ex}, is zero resulting in eq.(5.10b).

If $\Gamma < \Gamma_{\max}$ but $B>0$ then Γ is augmented also by transfer from the reservoir, thus

$$\frac{d\Gamma}{dt} = k_{\text{ads}} C_{10}\left[(\Gamma_\infty - \Gamma) - \frac{\Gamma}{KC_{10}} e^{-2a\theta}\right] - \frac{\Gamma}{A}\frac{dA}{dt} + k_{\text{r}}(\Gamma_\infty - \Gamma) \tag{5.11a}$$

$$\frac{dB}{dt} = -Ak_{\text{r}}(\Gamma_\infty - \Gamma) \tag{5.11b}$$

Considering next the second case, modelling collapse, $\Gamma = \Gamma_{\max}$, two different scenarios are followed, according to whether there is a tendency for addition of surfactant to the interface or removal from it. To this end, let us examine the term

$$J = k_{\text{ads}} C_{10}\left[(\Gamma_\infty - \Gamma) - \frac{\Gamma}{KC_{10}} e^{-2a\theta}\right] - \frac{\Gamma}{A}\frac{dA}{dt} \tag{5.12}$$

If $J \geq 0$, this implies that more surfactant accumulates in the multilayer reservoir, and the system to be integrated becomes

$$\frac{d\Gamma}{dt} = 0, \tag{5.13a}$$

$$\frac{dB}{dt} = AJ, \tag{5.13b}$$

The situation described by eq.(5.13) corresponds to an interface compressed beyond monolayer collapse, with surface concentration remaining constant, $d\Gamma/dt = 0$, and the surfactant being removed from the interface and stored in the reservoir. During this stage, surface tension will remain constant as well, since surface tension is determined from eq.(5.5). Finally, the combination $\Gamma = \Gamma_{\max}$ and $J < 0$ corresponds to the end of compression (which has led to collapse and subsequent growth of the reservoir content) and the start of relaxation of the interface. At that instant, the system to be integrated becomes

$$\frac{d\Gamma}{dt} = J, \tag{5.14a}$$

$$\frac{dB}{dt} = 0, \tag{5.14b}$$

At this stage, Γ decreases over time, resulting in relaxation. Further relaxation results in $\Gamma = \Gamma_{\max}$ and we return once again to eq.(5.11).

5.3 Solution procedure

The dynamic behavior of the system (e.g. a sessile drop) is driven by the temporal variation of the interfacial area, $A(t)$. Thus, the surface area and – from it – dA/dt, are input parameters of the developed model. The remaining predetermined parameters are Ω_{o}, Π_{eq} (σ_{eq}), $k_{\mathrm{ads}}C_{10}$, α, a, $\Pi_{\max}$ and k_{r}, the last two of which enter the problem only when compression is strong enough to result in collapse of the adsorbed monolayer. Also, the strength of the preparation is determined by the concentration, C, of added surfactant vesicles.

Inclusion of σ_{eq} in the best-fit parameters is considered an advantage of the present model since the equilibrium surface tension is a key thermodynamic property of pulmonary surfactant solutions [149]. It is also noted that the equilibrium constant, KC_{10}, is not an independent parameter, but is calculated - given the above values - from the combination of eqs (5.1) and (5.5).

Simulations start at equilibrium conditions with the selected σ_{eq}, from which $\Gamma_{\infty,\mathrm{eq}}$ and Γ_{eq} are computed, the former from eq.(5.4) and the latter by numerical solution of the equation of state, eq.(5.5). Γ_{eq} is the equilibrium interfacial concentration of the surfactant and satisfies the isotherm in eq.(5.1) and is a thermodynamic variable as it is directly related to σ_{eq}, while $\Gamma_{\infty,\mathrm{eq}}$ is a consequence of the model in order to more accurately model the behavior of liquid-condensed surface layers [98]. The value of surface concentration, Γ, at each of the next time steps is found by numerical integration of eqs.(5.7a) and

Table 5.1: Best fit values of model parameters. H and D are abbreviations for humid and dry conditions, respectively.

C ($\frac{\mathrm{mg}}{\mathrm{ml}}$)	σ_{eq} ($\frac{\mathrm{mN}}{\mathrm{m}}$)	σ_{min} ($\frac{\mathrm{mN}}{\mathrm{m}}$)	$k_{\mathrm{ads}}C_{10}$ (s^{-1})	KC_{10}	k_{r} (s^{-1})	α ($\frac{\mathrm{m}}{\mathrm{mN}}$)	CR (%)
0.5 (H)	24.0± 0.5	5.0	13.0± 1.2	111.3	12.0± 2.0	0.0051± 0.0002	20.0
0.5 (D)	22.0± 0.6	2.0	0	129.5	12.0± 2.0	0.0053± 0.0002	21.3
2.0 (H)	24.5± 0.5	12.0	35.0± 3.0	106.4	12.0	0.0051± 0.0002	23.1
2.0 (D)	23.0± 0.6	2.0	0	118.6	12.0	0.0053± 0.0002	15.0
1.0 (H)	24.0± 0.5	3.0	22.0± 2.0	108.6	14.0± 2.0	0.0053± 0.0002	31.0

(5.7b), and the corresponding surface pressure by solution of eq.(5.5), now with known Γ and Π as the unknown.

Numerical solution was achieved by the development of a source code in Matlab environment. Integration is straightforward and may be performed by any of the standard (constant or variable timestep) methods, as long as compression does not lead to collapse and the reservoir content, B, remains zero. In the opposite case, i.e. when Π_{max} is reached during the compression stage, the system to be integrated at each time step revolves between eqs.(5.10)-(5.14) depending on the condition of the interface as described in section 2.3. These abrupt changes in the system dynamics introduce numerical difficulties, and it was found that the most suitable integration algorithm is the simple Euler scheme, with sufficiently small timestep to assure accuracy. In particular, 100 timesteps per deformation cycle were typically used, and accuracy was confirmed by comparison of representative runs with 1000 timesteps per cycle.

5.4 Results

The above developed model was used to reproduce the data of Saad et al (2010) [149], which were taken with two different BLES formulations ($C = 0.5\ \mathrm{mg\,ml}^{-1}$ and $C = 2.0\ \mathrm{mg\,ml}^{-1}$) and for two different values of relative humidity (wet air, RH= 100%, and dry air, RH< 20%) at temperature 37 °C. The data were reported as Figs. 4 a-d and 5 a-d in Saad et al (2010) [149], and were plotted by them as surface tension, σ, versus interfacial area, A, and versus time, t, respectively. As far as the surface area is concerned, we use the relative area instead, defined as the ratio of its dimensional instantaneous value over its maximum. Also, we define the compression ratio (CR) as the ratio of the maximum area reduction over the initial area prior to dynamic cycling [1], and the latter is taken as the maximum area. Thus A lies between $1 - \mathrm{CR}$ and 1. The temporal forcing (variation of interfacial area) in the experiments involved two

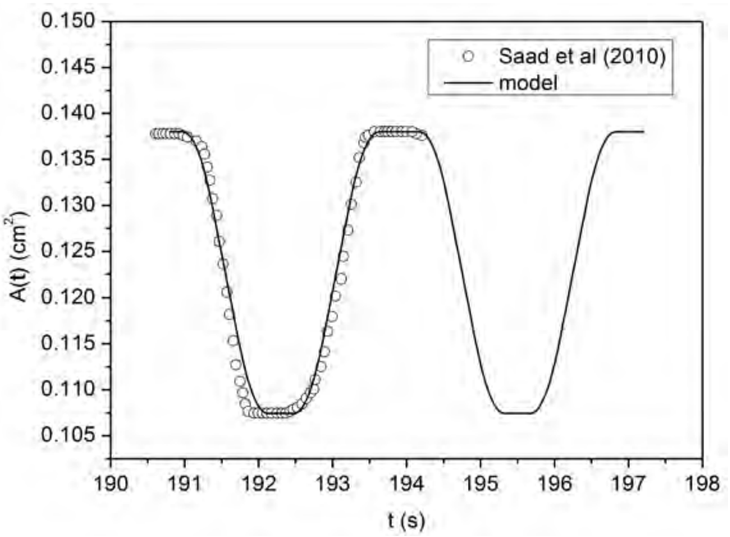

Figure 5.2: Temporal variation of interfacial area, $A(t)$, used by the present model compared with $A(t)$ in the experiments of [149].

constant-slope ramps separated by two constant-area segments. In the model, the function $A(t)$ was composed of the above linear segments, with the regions of slope discontinuity smoothed by small circular arcs. The model shape for one period is shown in Fig. 5.2, compared to the reported experimental cycle. Different curvatures could be introduced at the onset of the ramps, in order to improve further the agreement with the data of Fig. 5.2. However, given that detailed $A(t)$ data are not available for each of the runs, this elaboration was deemed unnecessary. The nominal values of oscillation periodicity and compression ratio in the experiments were 3 s/cycle and 20% respectively. However, digitization of the figures showed that a more accurate estimate of periodicity was $t_{\text{per}} = 3.2$ s. Also, the compression ratio (in particular the minimum value of A) was revealed to vary slightly per case, and these small differences were included in the simulations, as can be determined from Table 1, where the values of all the included parameters are summarised.

Figures 5.3 and 5.4 show results of the simulations superimposed on the original data in Saad et al (2010) [149]. Fig. 5.3 plots the variation of surface tension versus interfacial area, and Fig. 5.4 the variation of surface tension versus time. Each of the subfigures refers to a combination of high/low BLES concentration and wet/dry air. The agreement between measurements and simulations appears to be quantitatively satisfactory. The model results plotted actually refer to the fifth cycle of periodic compression-expansion. Simulations exhibit transient behavior during the first cycle and become fully periodic after the end of the second cycle. Only in the case 2b (low C, dry air) there is a very small but persistent drift of the compression leg.

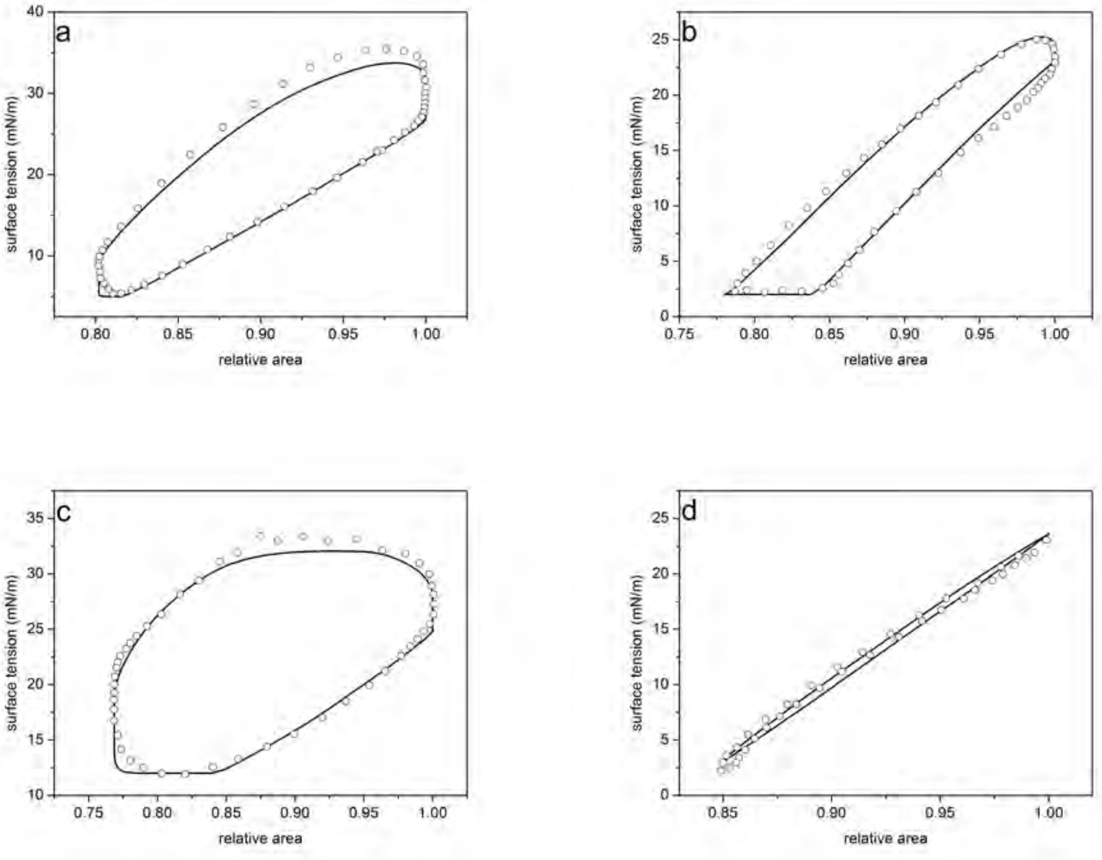

Figure 5.3: Predictions of surface tension variation with relative area (solid lines) compared to the experimental data (circles) from ref. [149] : a) C =0.5 mg ml^{-1} (humid air), b) C =0.5 mg ml^{-1} (dry air), c) C =2 mg ml^{-1} (humid air), d) C =2 mg ml^{-1} (dry air).

Application of the model necessitated pre-determination of a number of parameters. The maximum surface pressure, Π_{max}, was read directly from the data. The molar surface area was set equal to $\Omega_{\text{o}} = 3.0 \times 10^5$ m^2 mol^{-1}, based on a molecular cross-section $A_\mu = 0.5$ nm^2. This estimate is derived from experimental Π versus A_μ isotherms for DPPC monolayers [55, 185]. In particular, the linear part of the isotherms at high surface pressures (i.e. in the condensed phase) is extrapolated to $\Pi = 0$.

This approach, and the selected value of Ω_{o}, are further supported by the data of Zuo et al (2016) [198]. Using constrained drop surfactometry, these authors showed that, at temperatures below the critical point, $T_{\text{cr}} = 41.1$ °C (also called the melting temperature of DPPC [132]), the Π versus A_μ compression isotherms of DPPC all collapse to a single line at high surface pressures. This line describes accurately the data for the physiologically relevant range of surface pressures [195] and, when extrapolated to $\Pi = 0$, gives $A_\mu = 0.5$ nm^2/molecule.

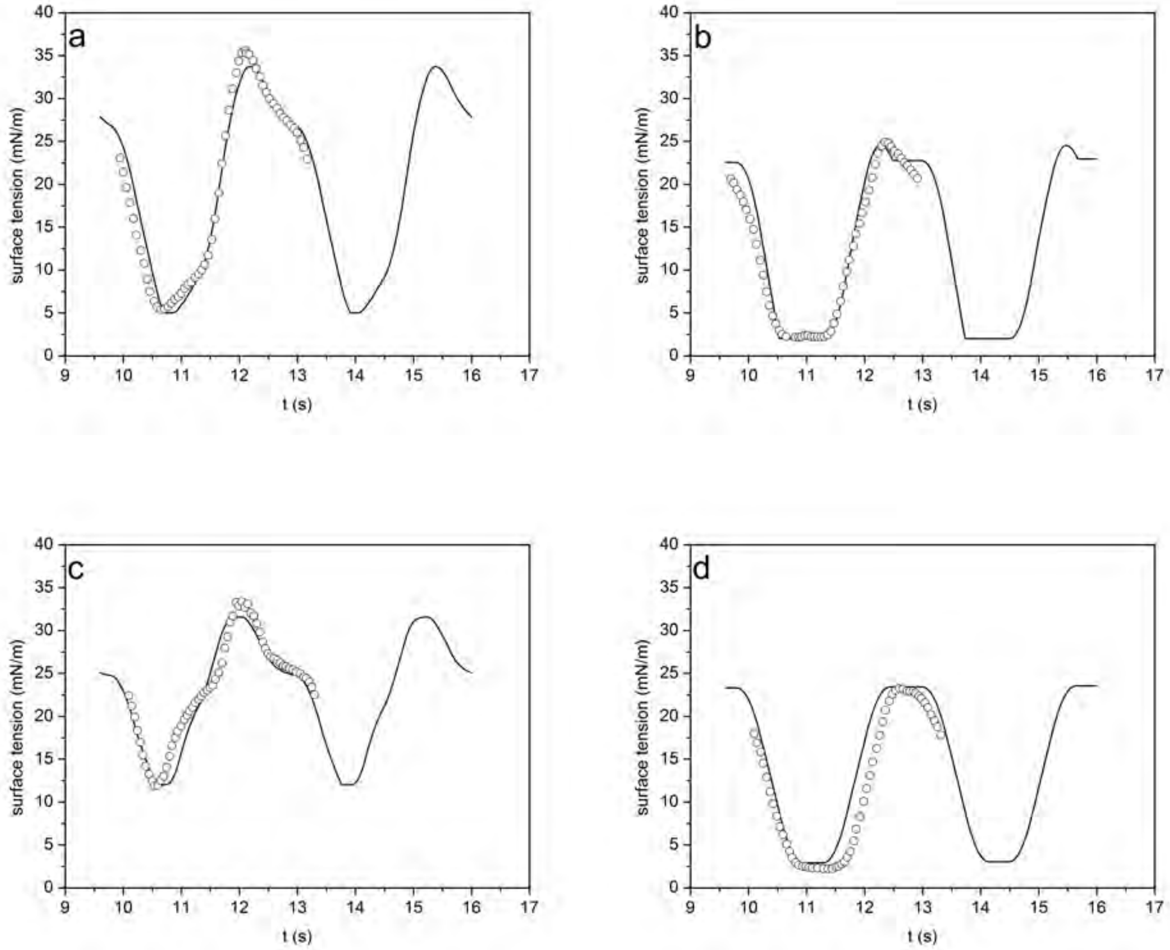

Figure 5.4: Predictions of surface tension variation with time during two consecutive cycles (solid lines), compared to the experimental data (circles) from ref. [149] : a) C =0.5 mg ml^{-1} (humid air), b) C =0.5 mg ml^{-1} (dry air), c) C =2 mg ml^{-1} (humid air), d) C =2 mg ml^{-1} (dry air).

The remaining parameters, $k_{\mathrm{ads}}C_{10}$, Π_{eq}, α and k_{r}, were varied in order to optimize visually the agreement with measurements. Their best-fit values are reported in Table 5.1, and are discussed in the next section. It is noted that the Frumkin interaction parameter, a, was always set equal to zero, i.e. the Langmuir version of the isotherm was implemented.

The applicability of the model was further tested by comparison with the more recent data of Xu et al [189], taken by dynamic cycling of a C = 1.0 mg ml^{-1} solution of Infasurf at 37 °C. The solution was subjected to sinusoidal area oscillations with periodicity 3 s/cycle and compression ratio 30%, following one or multiple replacements of the subphase. Of the near-identical cycles of the data of Xu et al, those taken after one replacement of the subphase (characterized as 1X) are reproduced in Fig. 5.5. The previously selected value

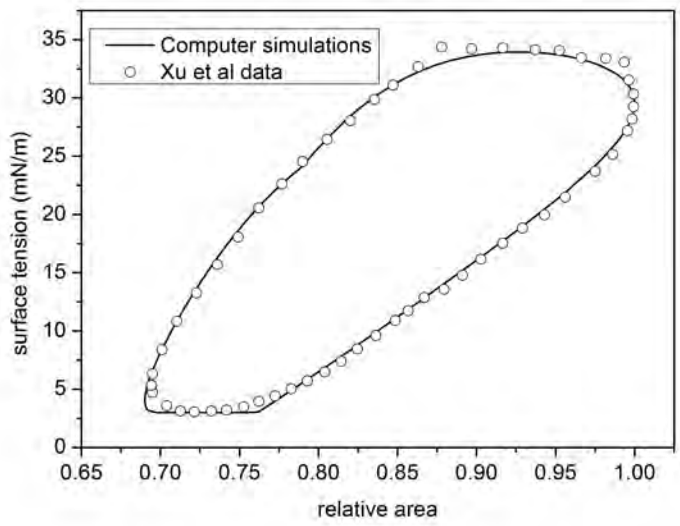

Figure 5.5: Prediction of surface tension variation with relative area, compared with experimental data from [189]

of Ω_o was used again for the molar surface area, and the best-fit values of the model parameters are reported in the last row of Table 5.1. The outcome of the comparison is depicted in Fig. 5.5, and quantitative agreement is observed.

5.5 Discussion

5.5.1 Optimum parameter values

The satisfactory, quantitative agreement between predictions and data, demonstrated in Figs 5.3, 5.4 and 5.5 argues in favor of the potential usefulness of a minimum dynamical model like the one presently advocated. It is further encouraging that the best fit values, which are summarized in Table 5.1 and will be discussed next, are consistent and physically meaningful.

First, it is noted that the values of equilibrium surface tension selected by the best-fit process, are around $\sigma_{\mathrm{eq}} = 22 - 25$ mN m^{-1}. This range agrees with the outcome of all measurements in the literature, which indicate that the equilibrium surface tension is independent from the total surfactant concentration [185, 146, 128, 199], and also from the water content in the air [197].

Focusing next on the case of wet air (100% RH), it is observed that the best-fit values of the adsorption rate constant, $k_{\mathrm{ads}}C_{10}$, depend on the total concentration of the preparation (0.5, 1.0 and 2.0 mg ml^{-1} respectively) and more specifically increase with it. It is argued in the literature [146, 48] that factors such as the total concentration and the exact composition of the preparation affect the kinetics of adsorption and desorption (though not the equilibrium). Thus, the adsorption rate constant of the present model emerges as a key parameter, because it accounts for these effects.

Though the data shown in Fig. 5.5 correspond to Infasurf lung surfactant, while researchers in [149] studied BLES solutions, it is reasonable to expect that both data sets will be successfully predicted by the same model, since the two surfactants are natural extracts devoid of proteins SP-A, SP-D, possess the same amount of SP-B, SP-C and have similar lipid composition [147]. Bearing this in mind, it is encouraging that the data in Fig. 5.5, which are taken with Infasurf concentration of 1 $\mathrm{mg\,ml^{-1}}$, are simulated by an adsorption rate constant that lies between the values of $k_{\mathrm{ads}}C_{10}$ for 0.5 and 2 $\mathrm{mg\,ml^{-1}}$ concentrations of BLES.

In view of the above, it is pertinent to compare the values of $k_{\mathrm{ads}}C_{10}$ with those predicted by other computational studies in the literature related to pulmonary surfactant. Muradoglu et al use $k_{\mathrm{ads}} = 1.7 \times 10^3\ \mathrm{cm^3\,g^{-1}\,s^{-1}}$ in an attempt to simulate the propagation of a liquid plug in the lower lung airways [119] and for the propagation of liquid plug covered with surfactant aimed for SRT in neonatal airways [125]. A similar value is used by Espinosa and Kamm [45], where $k_{\mathrm{ads}} = 1.0 \times 10^5\ \mathrm{cm^3\,g^{-1}\,min^{-1}}$. According to [45], the typical bulk concentrations along the airway tree range from $C \sim 0.01 - 10\ \mathrm{mg\,ml^{-1}}$ while in in-vitro studies, surfactant preparations are restricted up to 3 $\mathrm{mg\,ml^{-1}}$ in bulk concentrations [150]. Simulations concerning SRT using native surfactant preparations of $0.01 - 1\ \mathrm{mg\,ml^{-1}}$ give $k_{\mathrm{ads}} = 6.0 \times 10^5\ \mathrm{cm^3\,g^{-1}\,min^{-1}}$ per [80]. Typically, C can be higher, reaching 25 $\mathrm{mg\,ml^{-1}}$ as utilized in SRT using the commercially available surfactant called Survanta [125]. These reported values give an estimate of $k_{\mathrm{ads}}C$ in the range $\sim 10^{-2}$–$10\ \mathrm{s^{-1}}$ in order of magnitude. Our simulations considered $C = 0.5 - 2\ \mathrm{mg\,ml^{-1}}$ corresponding to $k_{\mathrm{ads}}C_{10} = O(10)$ $\mathrm{s^{-1}}$, as depicted in Table 5.1 and, thus, the values of the present model are in agreement with those of literature.

The variation of the adsorption rate, k_{ads}, with bulk concentration, C, shown in Table 5.1, is explicable by the currently accepted mechanism for surfactant adsorption. According to extensive experimental and computational evidence [175, 64, 8, 128], lipids adsorb through direct interaction of entire surfactant aggregates with the interface. Thus, it is expected that the adsorption rate will be an increasing function of the number-density of aggregates in the bulk, and therefore of the total bulk concentration.

The predicted increase in the adsorption rate constant with bulk concentration is weaker than linear and appears to gradually decline. Based on this outcome, some conjectures may be made about the behavior in the limits of very low and of very high surfactant loadings. For low number-density of aggregates, it is reasonable to expect a linear dependence of k_{ads} on C, in parallel with the classical Langmuir kinetics for dilute solutions (though presently not for monomers but for aggregates). At the other end, with increasing preparation strength, the dependence on aggregate concentration is expected to become weaker and eventually level off.

The above line of thought has implications also for the rate of desorption. If the proposed model is correct, and given that the equilibrium constant, K, is independent from bulk concentration, desorption rate must also increase with aggregate density. Such behavior may be explained if it is conjectured that desorption also occurs through direct interaction of aggregates with the interface (aggregate-assisted desorption). In support of such speculation, it is recalled [128] that the collapse of natural or model pulmonary surfactants does not lead to ejection of material into the bulk (as happens with simple insoluble monolayers [191, 148]), but is actually a reversible process with formation of assemblies that remain attached to the surface [152, 105, 146]. Thus, it appears as a plausible possibility that the transport of molecules from the compressed interface to the bulk is accomplished only through direct interaction of the interface with aggregates.

Returning to Table 5.1 and considering now the two cases with dry air, it is observed that agreement with the data necessitates setting $k_{\mathrm{ads}} \approx k_{\mathrm{des}} \approx 0$. Thus, the model confirms that the monolayer in contact with dry air behaves as totally insoluble, i.e. it is highly stable. On the contrary, a monolayer in contact with wet air is less stable, as has been observed long ago experimentally [35, 182, 197].

With respect to the dry-air cases, the present approach is closely related to the adsorption-limited model, developed for dynamic compression/expansion cycling by Otis et al (1994), Ingenito et al (1999) and Morris et al (2001) [127, 80, 118]. These authors treated the monolayer as insoluble only when surface tension dropped below the minimum equilibrium value, which was taken as 22.2 $\mathrm{mN\,m^{-1}}$ [80]. This is very close to the best-fit values, $\sigma_{\mathrm{eq}} = 22 - 23$ $\mathrm{mN\,m^{-1}}$, of the present simulations. Also, careful inspection of Figs 5.3b, 5.3d reveals that the largest portion of the $\sigma - A$ curve lies below σ_{eq}, thus justifying the assumption of zero surfactant solubility.

An important outcome of the model is the best-fit value of the monolayer compressibility, α. The prediction is found to vary slightly from case to case, with all values lying in the expected range for the tilted condensed (TC) regime [185, 188]. More important, the predictions are close to the compressibility, ~ 0.005 $\mathrm{m\,mN^{-1}}$, of a pure DPPC monolayer [153, 108].

It is recalled that, during compression to very low surface tension (even less than 1 - 2 $\mathrm{mN\,m^{-1}}$ [67]), the surface monolayer is believed to become enriched in DPPC [33, 185, 56, 154, 140, 134, 149]. This belief is further supported by measurements of the surface compressibility of clinical pulmonary surfactants at physiologically relevant surface pressures, found to be very close to the compressibility of pure DPPC monolayers [195, 154, 140, 108].

However, a comparison between data and model predictions of compressibility should be viewed with some caution, as the intrinsic compressibility, α, is a property of the molecule, whereas the measured parameter is actually the inverse of the apparent elasticity, $d\sigma/d\ln A$ [195], and therefore its value depends on the characteristics of the $\sigma - A$ curve. Thus, predictions of elasticity are worth considering in more detail, in particular in comparison with relevant data.

Finally, a note about the values of minimum surface tension, σ_{min}, appearing in Table 5.1, which were selected based on the appearance of the data. They are all in the range $\sigma_{\mathrm{min}} \leq 5$ $\mathrm{mN\,m^{-1}}$ as expected, with the exception of the dense BLES solution at 100% RH. The value used in the latter case results in better agreement with the data at the low-left corner of the dynamic cycle, and it was considered fair to go by it. Given that the BLES mixtures at high humidity are deemed by the authors of the experimental paper as less stable than those at dry conditions, it is thought that a degraded performance, with film collapsing at higher surface tension than normally expected, is possible.

5.5.2 Sensitivity of model parameters

The sensitivity of the model to the key parameters, σ_{eq}, α, k_{ads} and k_{r} is quantified by the uncertainty intervals in Table 5.1. The effect of these parameters is also demonstrated graphically, by re-plotting the $\sigma - A$ curves with the best-fit values modified consecutively by ±10%. The outcome of this exercise for the representative cases of Fig. 5.3a (wet air) and Fig. 5.3b (dry air) is shown in Fig. 5.6.

In the case of wet air (Figs 5.6a,5.6c,5.6e), it is observed that the equilibrium surface tension has a very strong effect on the fit to the data. In particular, an increase in σ_{eq} moves the entire loop up, while it also widens it. The intrinsic compressibility has also a strong effect, which however is mainly restricted to the compression leg of the loop. Thus, a decrease in ϵ moves the leg to the right (widens the loop) and increases its slope, i.e. the elasticity of compression. Finally, the kinetic constant, $k_{\mathrm{ads}}C_{10}$, has a weaker effect. Its increase widens the loop by moving the expansion and compression legs in opposite directions, but it affects more the expansion leg. As the extent of collapse is insignificant,

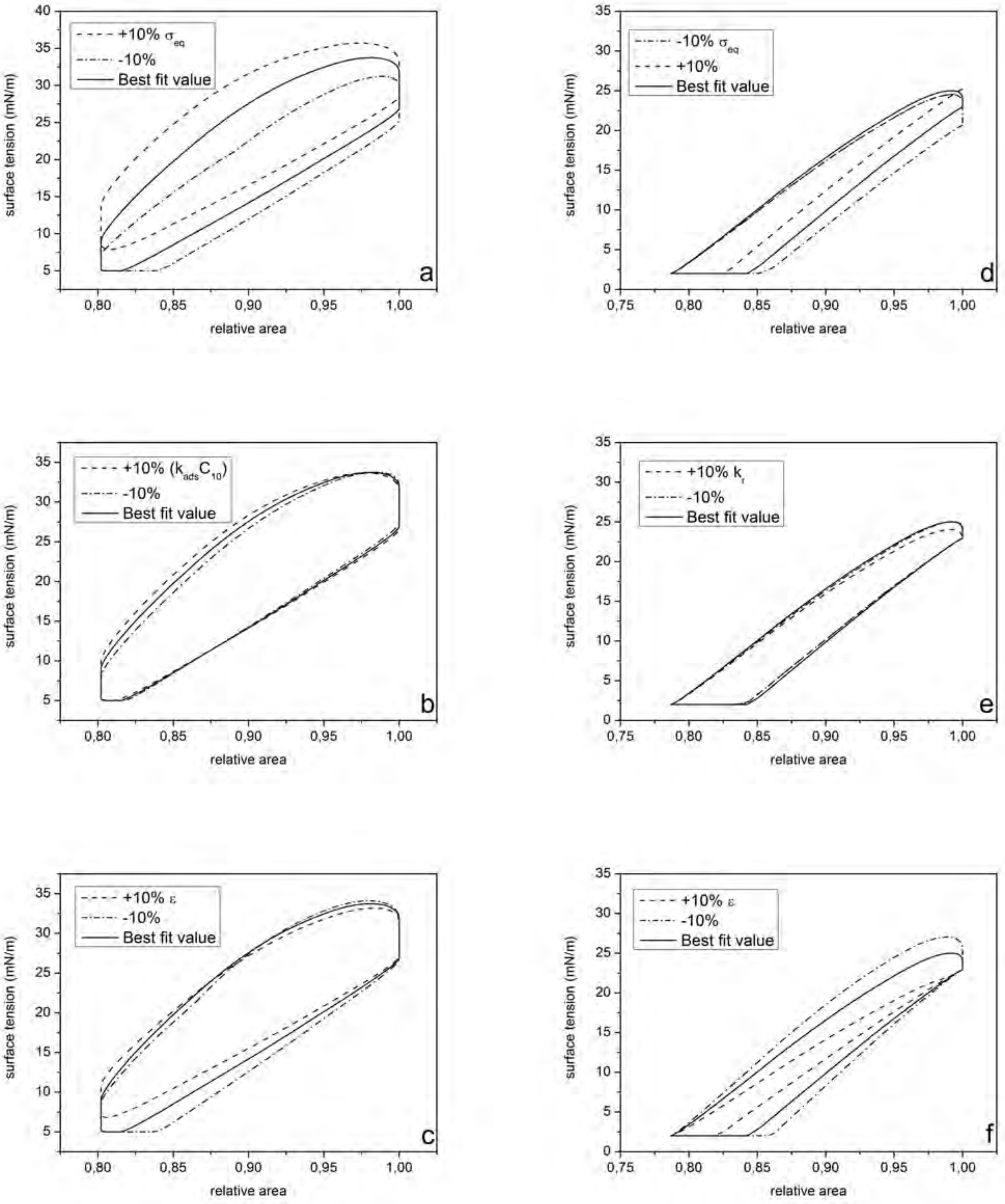

Figure 5.6: The effect of ±10% variation in the best fit values of the model parameters on the predicted surface tension versus relative area loops. Left Column: $C = 0.5$ mg ml^{-1} and wet air. Right Column: $C = 0.5$ mg ml^{-1} and dry air. (a,b): variation of $\sigma_{\rm eq}$, (c): variation of $k_{\rm ads}C_{10}$, (d): variation of $k_{\rm r}$, (e,f) variation of ϵ.

variation of the k_r value has no visible effect on the results and is not depicted in Fig. 5.6.

In the case of dry air (Figs 5.6b,5.6d,5.6f), the strong effect of equilibrium surface tension is confirmed again. The intrinsic compressibility is also very important, as it changes drastically the slopes of both the compression and the expansion legs of the loop. The kinetic constant, k_r, which describes the re-insertion of surfactant from the reservoir to the adsorbed monolayer, has a much weaker effect, and serves to fine-tune the expansion part of the $\sigma - A$ loop.

5.5.3 The Frumkin interaction parameter

Generally, the dimensionless Frumkin parameter is commonly positive, implying the dominance of surface adsorption over desorption as θ increases and can also be negative [129]. Numerically, it lies in the range $O(10^{-1})$. However, as the authors state in the review of Peng et al [129], this parameter corresponds more to a matching parameter rather than to one with physical importance. For this reason, we decided to exclude it from our analysis by considering it always zero. As it is seen in Fig. 5.7, where we plot the $\sigma - A$ curve of the parameter set of the 1st row of Table 5.1 for various values of a, it seems to slightly rotate the curve without altering its qualitative behavior. As its absolute value increases, the curve shrinks or expands during the deflation ($dA/dt > 0$) and compression ($dA/dt < 0$), respectively. Its typical values are $0.1-0.5$. What we observe then is that including a non-zero Frumkin parameter only provides a better fitting of the curve in contrast with other parameters presented in the section 5.5.2, being in agreement with the thesis of Kovalchuk et al in [129]. For this reason and in order to keep the model we develop minimum, we considered $a = 0$.

5.5.4 Dilatational Elasticity

Surface rheology is an important component in the characterization of pulmonary surfactants. The rheological behavior of a monolayer is generally described by two dilatational parameters, surface elasticity and surface viscosity, as seen in a previous Chapter. The former expresses the variation of surface tension in-phase with the deformation and the latter the variation in- phase with the rate of deformation. However, pulmonary surfactant monolayers subjected to deformation in the usual range of breathing frequencies, have been shown to exhibit a purely elastic behavior, with negligibly low surface viscosity values [185, 184]. Hence, only elasticity is discussed next.

Though dilatational elasticity may be considered a corollary of the general

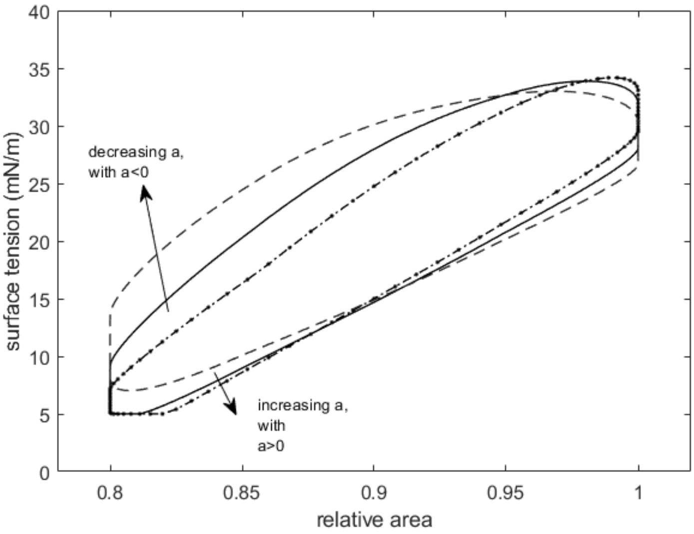

Figure 5.7: The effect of a on the data set corresponding to the C =0.5 mg ml^{-1} (humid air) case.

$\sigma - A$ variation, its representative values serve to characterize the overall behavior of the monolayer film. For example, measurements of elasticity have provided indirect evidence for the pulmonary film stability and for the role of surfactant proteins [183, 187, 186, 184, 185]. Higher elasticity is considered beneficial, as it is related to more drastic changes in surface tension [1]. It has even been argued that elasticity is actually more important than ultra-low surface tension for normal lung function [110]. Though there are many works measuring film elasticity under a variety of temperatures and deformation rates (e.g. [183, 187, 186, 184, 24, 23, 25]), we focus mainly on measurements taken with dynamic cycling at physiological conditions and for the same surfactant [1, 149, 150].

At first, it is necessary to differentiate between the well-known Gibbs elasticity, E_{G}, and the apparent dilatational elasticity, E_{A}, which relates changes in surface tension directly to changes in surface area. The former, was briefly previously mentioned as Marangoni or limiting elasticity, eq.(3.61) expresses the film elasticity due to the activity of the surfactant. In the above model, Gibbs elasticity may be directly derived from the equation of state, and is given by the following expression

$$\frac{1}{E_{\mathrm{G}}} = \left(-\frac{d\sigma}{d\ln\Gamma}\right)^{-1} = \frac{\Omega_{\mathrm{o}}}{\mathcal{R}T}\frac{(1-\alpha\Pi)}{\left(\frac{\theta}{1-\theta} - 2a\theta^2\right)} + \frac{\alpha}{1-\alpha\Pi} \tag{5.15}$$

The latter, the dilatational part, is simply $d\sigma/d\ln A$ and has widely been used in order to study monolayers of pulmonary surfactants. The reader is referred to the works mentioned in the previous paragraph. E_{G} and E_{A} coincide

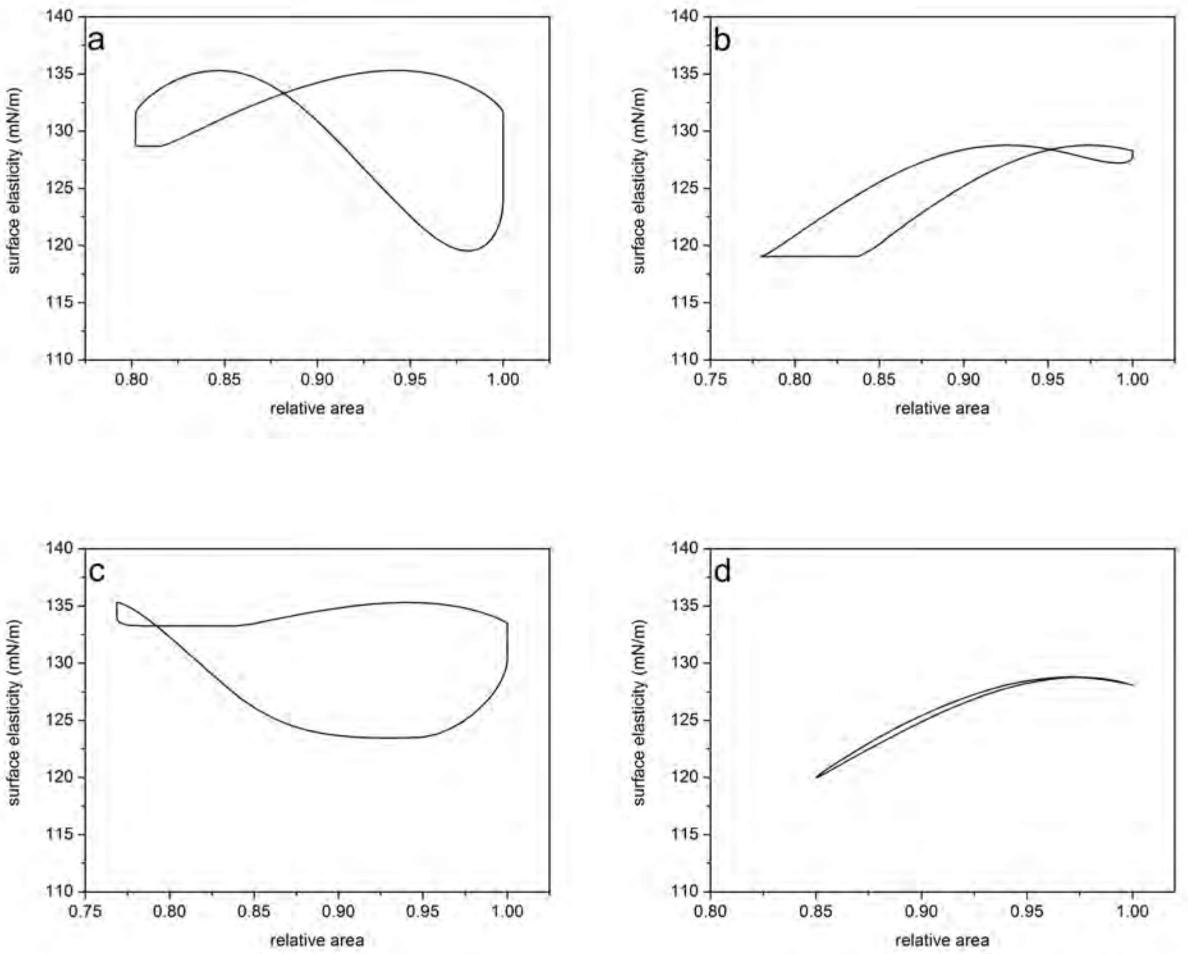

Figure 5.8: Variation of Gibbs elasticity with relative area during the compression/expansion cycles of Fig. 5.3. a) C =0.5 $\mathrm{mg\,ml^{-1}}$ (humid air), b) C =0.5 $\mathrm{mg\,ml^{-1}}$ (dry air), c) C =2 $\mathrm{mg\,ml^{-1}}$ (humid air), d) C =2 $\mathrm{mg\,ml^{-1}}$ (dry air).

only if the monolayer is insoluble, which is the case for pulmonary surfactant. Nevertheless, in the present model, the monolayer is not strictly insoluble in the sense that the collapse mechanism enables exchange of material with the sublayer. Insolubility holds only in the absence of collapse.

The above allow one to relate the two elasticities as [111]

$$E_A = A\frac{d\sigma}{dA} = -E_G\frac{d\ln\Gamma}{d\ln A} = E_G\left(-\frac{A}{\Gamma}\frac{d\Gamma}{dA}\right) \tag{5.16}$$

Notice that if $E_\mathrm{G} = E_\mathrm{A}$ then eq.(5.16) is re-arranged as $d(\Gamma A) = 0$, implying insolubility. According to eq.(5.15), Gibbs elasticity is the combination of a compositional and an intrinsic contribution. For convenience, recalling that $\Pi = \sigma_\mathrm{o} - \sigma$, we can write eq.(5.15) below in terms of surface tension for $a = 0$

$$\frac{1}{E_{\mathrm{G}}}=\frac{\Omega_{\mathrm{o}}}{\mathcal{R}T}\frac{(1-\alpha\sigma_0+\alpha\sigma)(1-\theta)}{\theta}+\frac{1}{1/\alpha-\sigma_{\mathrm{o}}+\sigma} \tag{5.17}$$

E_{G} is high when both terms on the rhs (I:compositional and II:intrinsic) are small and declines when either one grows. Term (I) increases with surface tension, but is insignificant at high compressions, where the covered fraction, θ, is practically equal to one. On the contrary, term (II) decreases with surface tension.

The variation of Gibbs elasticity during the compression-expansion cycles of Fig. 5.3 is shown in Fig. 5.8. The vertical segments, prominent in Figs. 5.8a and 5.8c, are the result of relaxation under constant surface area (see $A(t)$ in Fig. 5.2) while the horizontal segment in Fig. 5.8b corresponds to collapse of the monolayer. The non-monotonic change of E_{G} during each of the half-cycles (with the ensuing crossing of the two curves) may be physically understood by considering the variations in surface tension as a result of the relaxation processes during the idle periods between compressions and expansions.

Taking Fig. 5.8a as an example, we follow E_{G} that grows during the idle period and the onset of expansion, reaches a maximum and then declines strongly during the late stages of expansion. The initial growth is due to the decrease in term (II), caused by the desorption of surfactant and the ensuing increase in surface tension. The subsequent strong decline is due to the increase of term (I), as surface tension grows further while θ becomes smaller than one. During the second idle period and the onset of compression, E_{G} grows strongly, reaches a maximum and then declines again down to collapse at the late stages of compression. The initial growth is caused by the drastic decrease of term (I), as surfactant is adsorbed and surface tension drops. The subsequent decline of E_{G} is caused by the increase of term (II) when surface tension becomes small enough.

According to Fig. 5.8, maximum Gibbs elasticities are in the range $E_{\mathrm{G}} = 128 - 135\ \mathrm{mN\,m^{-1}}$. This narrow range, which is roughly independent of concentration and humidity, does not always compare favorably with the best-fit elasticities of expansion and compression given by Saad et al [149] and reproduced in Table 5.2. The discrepancy points to the necessity to consider in detail the apparent dilatational elasticity, E_{A}.

While E_{G} and E_{A} coincide for insoluble films that do not collapse, the experimentally determined dilatational elasticity is expected to depend on solubility and on the extent of collapse. An estimate for its value is offered by the model, because the variation of Γ with A in eq. (5.16) may be calculated from eqs (5.7a),(5.8),(5.9). Precisely, the total rate of change of interfacial concentration due to area variations, $d\Gamma/dA$ can be calculated by re-writing eq.(3.37) as

$$\frac{d\Gamma}{dA} = \left(\frac{\partial\Gamma}{\partial t}\right)_{\mathrm{A}} \frac{dt}{dA} + \left(\frac{\partial\Gamma}{\partial A}\right)_{t} \tag{5.18}$$

It was explained in the previous chapter that $(\partial\Gamma/\partial t)_A$ expresses the variation of surfactant at the surface due to kinetic exchange only. The current model incorporates the exchange of surfactant material with the reservoir as well, so $(\partial\Gamma/\partial t)_A = j_{\mathrm{ads}} - j_{\mathrm{des}} + j_{\mathrm{ex}}$. Besides, $(\partial\Gamma/\partial A)_t$ is simply $-\Gamma/A$ [159]. The end result, using also eq. (5.1) to eliminate the equilibrium constant, K, in favor of equilibrium coverage, θ_{eq}, is

$$E_A = E_G\left[1 + \frac{k_{ads}C_{10}}{d(\ln A)/dt}\left(\frac{1-\theta_{eq}}{\theta_{eq}} - \frac{1-\theta}{\theta}\right) - \frac{k_r}{d(\ln A)/dt}\left(\frac{1-\theta}{\theta}\right)\right] \tag{5.19}$$

Note that the last term in eq. (5.19) is included only during relaxation after film collapse, and only for as long as the reservoir content, B, is nonzero.

According to eq.(5.19), for soluble surfactants the two elasticities coincide at equilibrium conditions, whereas $E_{\mathrm{A}} < E_{\mathrm{G}}$ for small deviations from equilibrium in both directions, i.e. $\Pi > \Pi_{\mathrm{eq}}$ (small compression, $dA/dt < 0$) and $\Pi < \Pi_{\mathrm{eq}}$ (small expansion, $dA/dt > 0$). However, during the full dynamic cycle, large changes in both Γ and Π occur, and as a result E_{A} exhibits strong and non-monotonic temporal variation.

One example that parallels the wet-air data of [149], is a soluble surfactant which is compressed without (or with negligible) collapse. The second term inside the brackets in eq. (5.19) is negative during compression below the equilibrium surface pressure, but becomes positive with the onset of re-expansion. As a result, elasticity of expansion is predicted higher than elasticity of compression. The values of E_{A} derived from the model at the onset of the compression and the expansion ramps are quoted in Table 5.2. Compared to the best-fit data of Saad et al [149], our predictions are in quantitative agreement for the low surfactant concentration but only in qualitative agreement for the high surfactant concentration. However, for the latter case, it appears that the values

Table 5.2: Compression/expansion elasticity values in $\mathrm{mN\,m^{-1}}$ compared with data from [149].

Concentration ($\mathrm{mg\,ml^{-1}}$)	compression/expansion [149]	Present Model
0.5 (humid)	125.1/157.8	122/152
0.5 (dry)	112.7/120	128/113
2.0 (humid)	126.3/136	104/122
2.0 (dry)	123.1/129.9	129/123

reported by Saad et al [149] are higher than what would be expected based on the shape of their $\sigma - \mathrm{A}$ curve.

Moving next to the dry-air cases, where the monolayer is modeled as insoluble, it is concluded that the only significant term in eq. (5.19) is the last one in the brackets. If film collapse is negligible, elasticities of expansion and contraction are the same as Gibbs elasticity. If however there is significant compression beyond collapse, then the elasticity of expansion is predicted to be somewhat lower than that of compression, because in the former stage the last term is positive whereas in the latter it is zero. The values predicted by the model at the onset of the compression and expansion ramps are included in Table 5.2. Compared to the best-fit data of Saad et al [149], the predictions are for both cases in the same range as the data, but they differ in trend (i.e. elasticity of expansion predicted lower than that of compression).

Next, we provide a note on the validity of our model by examining the behavior of the inverse of Gibbs elasticity close to the value of $\sigma_{\min}$. The limit $\lim_{\theta \to 1}(E_G^{-1})$ from eq.(5.15) for $a = 0$ corresponds to maximum compression, from which we obtain

$$\lim_{\theta \to 1} \left(\frac{\Omega_{\mathrm{o}}}{\mathcal{R}T} \frac{(1-\theta)(1-\alpha\Pi)}{\theta} + \frac{\alpha}{1-\alpha\Pi} \right) = \frac{\alpha}{1-\alpha\Pi_{\max}} \tag{5.20}$$

The above analytical formula is also exactly the dilatational elasticity at maximum compression, where a PS film is expected to attain a constant value. Applying eq.(5.20) for the 2 insoluble cases presented above (Table 5.1) we obtain 0.008 $\mathrm{m\,mN^{-1}}$ for compressibility at maximum compression. Under maximum compression and area reduction not exceeding 20-30 %, Zuo et al 2008 [199] state that $dlnA/d\sigma$ should not exceed 0.01 $\mathrm{m\,mN^{-1}}$ for film stability to be ensured. Our model predictions provide a reasonable margin. For the soluble cases, we can use the formula provided for the apparent elasticity, E_A. Of course, as is the case with all analytical models, there is an important limitation to our model as far as dilatational elasticity is concerned. E_A is inversely proportional to the surface strain rate in eq.(5.19), $d\ln A/dt = \dot{A}/A$. The compression trend imposed on the surface, either trapezoidal or sinusoidal, has time intervals where $dA/dt = 0$ which implies that eq.(5.19) is invalid at specific time instants and gives unphysically high elasticity values as $\dot{A}$ approaches zero. As a consequence, this formula should be used only at stages away from maximum compression.

A final prediction based on eq.(5.19) concerns the role of the rate of change of surface area. For constant compression ratio, this parameter is inversely proportional to the cycling period (or, equivalently, it is proportional to the compression ratio for constant cycling period as stated before). By increasing the period, the rate of surface area change decreases, and - as a result of the second term in the brackets of eq. (5.19) - the difference between expansion and compression elasticity increases. This is precisely the behavior demonstrated by the data of Zuo et al [1] in their figures 6a and 6b, which are taken with wet air, and thus the aforementioned term is relevant. When the film behaves as insoluble, only the last term in brackets survives, and this has a very small effect because the ratio $(1-\theta)/\theta$ is very small. Thus, the elasticities of expansion and compression are predicted to vary only slightly, again in agreement with figure 6c in the data of Zuo et al [1].

5.6 Concluding Remarks

A simple mathematical model of the interfacial dynamics of a pulmonary surfactant preparation under cyclic compression and expansion is formulated and tested. Thermodynamic equilibrium is described by a Langmuir isotherm and by an equation of state derived by Gibbs theory. A key ingredient of the model is the inclusion of the intrinsic compressibility, α, of the densely packed monolayer, a parameter that expresses the linear decrease in the molar area of adsorbed surfactant with surface pressure. As has been shown in the literature by rigorous thermodynamic analysis [46, 97, 98] the isotherm remains intact and the equation of state is appropriately modified.

When equilibrium is disturbed, the surfactant monolayer is assumed to exchange molecules with the bulk by kinetically-limited adsorption or desorption, a process quantified by the adsorption rate constant, k_{ads}. Film collapse is taken to occur at a given surface pressure, $\Pi_{\max}$, leading to the formation of a sublayer reservoir of surfactant molecules. The reservoir serves to replenish the film during re-expansion, at a rate described by the constant k_r.

The model is validated by reproducing the experimental data of Saad et al. [149] and Xu et al. [189], using as adjustable parameters the variables $\sigma_{\mathrm{eq}}, k_{\mathrm{ads}}, \alpha$ and k_{r}. It is encouraging that the best-fit values are all physically meaningful. In particular, the equilibrium surface tension is in the range $22-25$ $\mathrm{mN\,m^{-1}}$, as found by numerous measurements in the literature. The intrinsic compressibility is around $0.005-0.0055\ \mathrm{m\,mN^{-1}}$, which corresponds very closely to the behavior of a film enriched in DPPC.

The values of the adsorption rate constant that fit the data are found to increase with the bulk concentration of the preparation. Considering that the surfactant resides in the bulk almost exclusively in the form of aggregates, this outcome appears to confirm that solubility effects in the dynamics of the compression/expansion cycle are governed by the direct interaction between monolayer and aggregates.

Finally, the monolayer elasticity, as given by Gibbs expression for an insoluble, non-collapsing film and by the apparent dilatational elasticity when solubility effects are significant, is investigated. It is noteworthy that in the present approach, elasticity is a direct outcome of the model, unlike the approach of Saad et al. [149] where the elasticities of compression and expansion are best-fit parameters. According to the model predictions, solubility effects at high surface coverages render the apparent elasticity of expansion higher than the apparent elasticity of compression. For an insoluble monolayer that is compressed beyond collapse, the opposite effect is predicted, i.e. an apparent elasticity of expansion slightly lower than that of compression.

Chapter 6

Hydrodynamics of the alveolar fluid - Linear and weakly nonlinear approximation

6.1 Introduction

Lung alveoli are lined with a thin liquid layer, estimated as $0.1 - 1$ μm thick, depending on lung inflation and health condition [11, 179]. The interface of this layer, which is always in contact with the alveolar gas, is coated by a monolayer of special surface-active agents that constitute the pulmonary surfactant. The pulmonary surfactant is a combination of lipids and proteins, which—apart from populating the adsorbed monolayer—are also suspended in the liquid in the form of aggregates [199]. The surfactant acts to reduce drastically surface tension, making the alveoli more compliant and minimizing the metabolic work of breathing [193, 146, 195]. In particular, the adsorbed surfactant monolayer is able to sustain large compressions during contraction, resulting in extremely low values of surface tension, This behavior is accompanied by a rapid replenishment of the monolayer content during expansion, which restricts the increase of surface tension at the inhalation stage of the breathing cycle [183, 128].

The hydrodynamics of the thin liquid layer lining the alveoli has been repeatedly the topic of investigation during the last decades [137, 139, 45, 63, 178, 179, 65, 89]. The reason for this interest is that slow convective motions, which may develop triggered by the radial oscillation of the alveolar wall, are potentially of importance for lung homeostasis. In particular, it has been proposed that flow in the liquid lining may help cleanse the alveolus from deposited particles, and it may provide a potential route for cell-cell signaling. Such convective motions are also important when it is desired to transport macromolecules towards the alveoli, as for example in the clinical practices of surfactant replacement therapy and partial liquid ventilation.

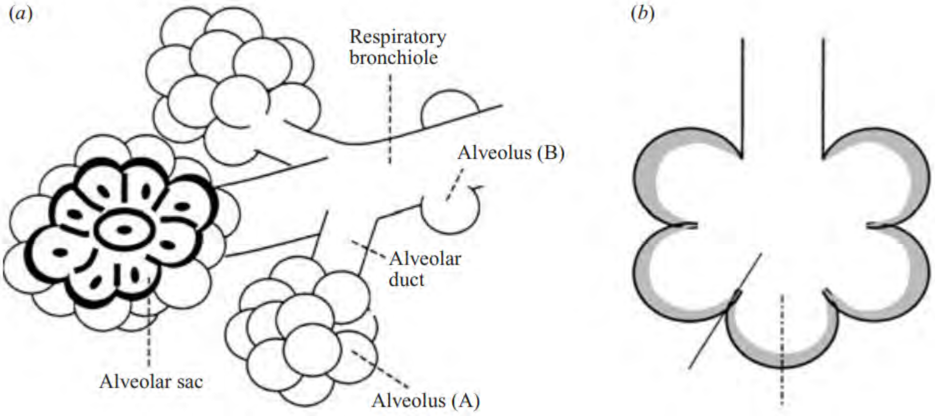

Figure 6.1: a) Schematic arrangement of alveoli in the respiratory region. Insolated alveoli, type B, are adjacent to conducting airways while type A are met in the terminal parts of the respiratory system. b) Cluster of alveoli. Notice the continuity of the alveolar fluid (grey color) between alveoli, a central notion in this Chapter. The schematic is adapted from [178].

From a different perspective, the interfacial motion of the liquid layer sets the true boundary condition for the airflow that enters and leaves the alveolus during breathing. In this respect, it is recalled that studies neglecting the liquid layer showed that chaotic mixing may occur inside the first alveolar generations, leading to enhanced particle transport and deposition [170, 169, 172, 167, 31]. It is of evident interest to consider how is the prediction of the airflow field modified by the inclusion of the liquid flow.

Analysis of the dynamics of an oscillating alveolus necessitates also consideration of its neighborhood. It is recalled that, in generic lung models, alveoli start to appear beyond the 15th airway generation (respiratory bronchioles). They are scattered at first on the bronchiolar epithelium and gradually increase in density, until—beyond the 17th generation—airway ducts are fully covered by alveoli in close contact with each other [181, 169]. The scattered alveoli are termed ”type B” and the densely packed ”type A”. A schematic representation of the aforementioned types of alveoli is depicted in Fig.6.1. It has been argued in the literature [178, 179] that different boundary conditions should apply for alveoli of type A and type B. For example, [137] model type B alveoli and pose constant values of film thickness and surfactant concentration at the rim. In order to model a type A alveolus, [178] also fix the film thickness at the rim but set the local flux equal to zero. [179] focus on the strong surface tension limit, as in an alveolus with severe surfactant deficiency. They assume a film that is thick in the interior (flooded alveolus) but diminishes in thickness at the rim.

In all cases considered, the liquid layer lining the alveolus is modeled by quasi-steady Stokes flow, an approach which is justified by the very small velocities involved and the relatively slow timescale of breathing [179, 89]. Two key mechanisms that may create shearing motion, i.e. velocities parallel to the alveolar epithelium, are Marangoni (elastic) stresses that result from spatial variation of surface tension and capillary stresses that result from spatial variation of interfacial curvature. Although surface tension is drastically lowered during a large part of the breathing cycle, the relative significance of Marangoni and capillary stresses is subject to discussion [178, 179, 89].

Studies in the literature that aim at estimating the pattern and magnitude of shearing flow may be broadly classified in two categories, in relation to the posited deformation of the alveolar wall. In the first category, the epithelium is taken for simplicity as flat, with one end pinned and the other experiencing periodic motion in the tangential direction [137, 45, 178]. Thus, the wall is subjected to non-uniform stretching, which—by the no-slip boundary condition—introduces directly a varying tangential velocity along the liquid layer.

In the second category, the alveolus is modeled as a spherical cap subjected to radial oscillation. In this case, the wall deformation is uniform and thus imparts no tangential motion to the liquid. The only way to break the radial symmetry is through appropriate boundary conditions. Thus, the boundary conditions at the rim emerge as a delicate component of the overall alveolar modeling. Positing constant film thickness or/and surfactant concentration at the rim (as in some previous works), forces the development of gradients with the inner interface, because the variation of the wall area during cap oscillation leads to inverse variation of film thickness and surfactant concentration inside the alveolus. However, the physical relevance of such boundary conditions is not always clear.

In the present Chapter[1], the problem is studied in the spherical geometry and solved in the Stokes limit, using a lubrication approximation and extending the approach of [89]. A new boundary condition is formulated for the alveolar rim, by matching the "large-scale" dynamics of the alveolus to "small-scale" equilibrium over the finite thickness of the mid-alveolar wall. The complex dynamics of the pulmonary surfactant is described by a recently developed model [20], which was found to predict with quantitative accuracy the surface tension-surface area hysteresis loops measured independently for various lung surfactant preparations [149, 189].

Small-amplitude oscillations around the equilibrium conditions of the alveolus are considered. The simplification permits expansion of the equations and boundary conditions in the oscillation amplitude a, and also allows a somewhat simpler treatment of the complex dynamics of the pulmonary surfactant. The

---

[1] This chapter is a published work in [21]

resulting systems for the linear and the weakly nonlinear problem are solved by a standard Galerkin finite-element method and provide estimates of the pattern and size of shearing motions and of the modes of interaction between the rim and the interior of the alveolus. In particular, the significance of non-zero film thickness at the rim is demonstrated and the role of Marangoni and capillary stresses in determining the flow field is interrogated. The role of surfactant solubility is also investigated.

6.2 Development of governing equations and boundary conditions

6.2.1 The flow problem

The alveolus is modeled as a spherical cap of periodically varying radius $R(t)$ with an opening of angle $2\theta_0$, as shown in Fig. 6.2. The truncated sphere is the most common model geometry, not only in the older but also in the recent literature [96]. In particular, it has been argued [68], based on SEM images, that the apparent polygonal shape of alveoli is associated with non-uniform thickness of the wall septa, so that the actual airspace is closer to spherical. Also, there is evidence that the precise shape of the alveolus does not affect greatly the resulting flow and transport [71].

The liquid layer is considered Newtonian [57], with constant density ρ and viscosity μ. Its flow field is assumed to be symmetric in the circumferential direction and is analysed in a spherical coordinate system (r, θ, ϕ) located at the center of the cap. Thus, the velocity in the liquid film is described as $\boldsymbol{u}(\boldsymbol{x}, t) = (u_r(r, \theta, t), u_\theta(r, \theta, t), 0)$ and the air-liquid interface is located at $r = r_s = R(t) - h(\theta, t)$, where $h(\theta, t)$ is the liquid film thickness and subscript 's' indicates value at the interface.

Following standard practice in the literature [62, 178, 179, 63, 89], the flow is posited to obey the continuity and the quasi-steady Stokes equation

$$\boldsymbol{\nabla} \cdot \boldsymbol{u} = 0 \tag{6.1}$$

$$\mu \nabla^2 \boldsymbol{u} = \boldsymbol{\nabla} p \tag{6.2}$$

where p is the pressure field and gravitational and inertial effects are ruled out from the onset. During breathing, the alveolus is taken to deform in a self-similar fashion, and thus the opening angle θ_0 remains constant. Following this assumption, [62] and [179] described the motion of the wall as

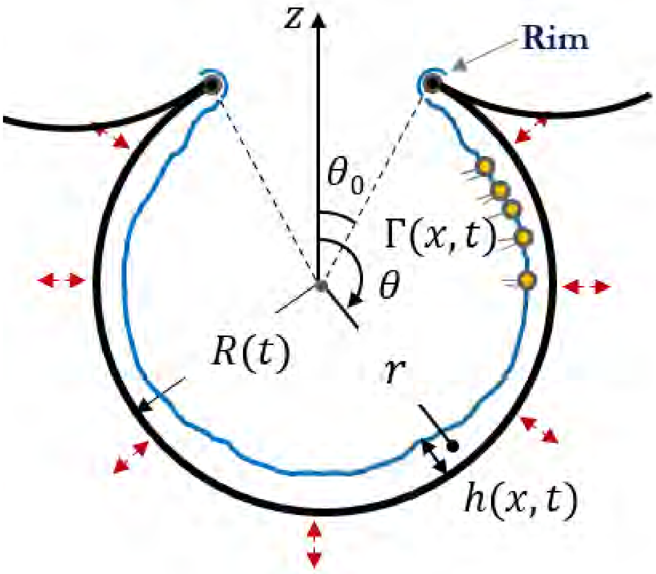

Figure 6.2: A simple yet accurate schematic of the model alveolus internally lined with a thin liquid film (blue sketchy line; here shown relatively thicker than in reality for clarity) which is laden with PS (yellow double-tailed molecules; double tails underline the phospholipid content of PS). Film thickness and interfacial concentration are h and Γ, respectively. The rim is just the opening of the alveolus, the point where the exchange of liquid/surfactant or even deposited particles with neighboring alveoli or alveolar ducts takes place.

$$\boldsymbol{u}_w = \dot{R}((1+\cos\theta\cos\theta_0)\,\boldsymbol{i}_r - \sin\theta\cos\theta_0\,\boldsymbol{i}_\theta) = \dot{R}\,\boldsymbol{i}_r + \dot{R}\cos\theta_0\,\boldsymbol{i}_z = \boldsymbol{u}_{w,sym} + \boldsymbol{u}_{w,sb} \tag{6.3}$$

where $\boldsymbol{u}_{w,sym}$ represents a spherically symmetric oscillation and $\boldsymbol{u}_{w,sb}$ a time-dependent solid-body motion along the symmetry axis of the opening. It is presently desirable to describe the flow in a moving reference frame attached to the center of the spherical cap. Such a reference frame is noninertial, as $\boldsymbol{u}_{w,sb}$ varies with time, and would in general necessitate the introduction of a fictitious acceleration term, $d\boldsymbol{u}_{w,sb}/dt$, in the Navier-Stokes equation. However, in the quasi-steady Stokes limit this term is negligible and may be omitted. Therefore, from now on the wall motion is described only by the symmetric term $\boldsymbol{u}_{w,sym} = \dot{R}\,\boldsymbol{i}_r$.

Equations (6.1) and (6.2) above are supplemented by the kinematic and the dynamic boundary conditions at the air/liquid interface, and by the no-slip condition on the alveolar wall. Liquid particles at the interface satisfy $S(r,\theta,t) = r - R(t) + h(\theta,t) = 0$ and the kinematic condition, $DS/Dt = 0$, becomes

$$\frac{\partial h}{\partial t} = \dot{R}(t) - u_r - \frac{u_\theta}{r}\frac{\partial h}{\partial \theta} \tag{6.4}$$

The dynamic condition expresses the balance of forces at the interface and is given by

$$\boldsymbol{n}\cdot\boldsymbol{\tau} = -p_{air}\boldsymbol{n} + \sigma(\boldsymbol{\nabla}_s\cdot\boldsymbol{n})\,\boldsymbol{n} - \boldsymbol{\nabla}_s\sigma \tag{6.5}$$

where σ is the local value of surface tension, $\boldsymbol{n}$ is the unit normal pointing towards the liquid, $\boldsymbol{\tau} = -p\boldsymbol{I} + \mu(\boldsymbol{\nabla u} + \boldsymbol{\nabla u}^{\mathrm{T}})$ is the stress tensor and $\boldsymbol{\nabla}_s = (\boldsymbol{I} - \boldsymbol{nn})\cdot\boldsymbol{\nabla}$ is the gradient operator along the interface. It is noted that eq.(6.5) does not include rheological stresses, following experimental evidence [185] that, for timescales relevant to breathing, phenomena can be characterized by only the elasticity modulus (i.e. the effect of surface viscosity is negligible). Finally, on the alveolar wall, $r = R(t)$, we have

$$u_\theta = 0\ , \quad u_r = \dot{R}(t) \tag{6.6}$$

and symmetry at $\theta = \pi$

$$\left.\frac{\partial h}{\partial \theta}\right|_{\theta=\pi} = 0 \tag{6.7}$$

6.2.2 Surfactant dynamics

Pulmonary surfactant is a mixture of lipids and proteins, which are practically insoluble in water. This mixture is presently modeled by a single generic surfactant, which mimics the dynamic behavior of the actual preparation [185]. A monolayer forms at the interface, with the excess amount residing in the bulk in the form of aggregates [199, 25]. The surface concentration of surfactant is described by the function $\Gamma(\theta, t)$, whose spatial variation along the interface couples the flow and mass transfer problems through the dynamic boundary condition, eq.(6.5). Thus,

$$\boldsymbol{\nabla}_s\sigma = \frac{d\sigma}{d\Gamma}\boldsymbol{\nabla}_s\Gamma \tag{6.8}$$

where surface tension is related to the local surface concentration, $\sigma = \sigma(\Gamma)$, through the surfactant EOS, to be developed shortly. The sensitivity of σ to Γ is expressed by the Gibbs elasticity, E, where

$$E = -\frac{d\sigma}{d\ln\Gamma} = -\Gamma\frac{d\sigma}{d\Gamma} \tag{6.9}$$

Mass conservation is imposed by the following equation [164, 130]:

$$\frac{\partial\Gamma}{\partial t} + \boldsymbol{u}\cdot\boldsymbol{\nabla}_s\Gamma + \Gamma(\boldsymbol{\nabla}_s\cdot\boldsymbol{u}) = \mathcal{D}_s\nabla_s^2\Gamma + j_b \tag{6.10}$$

Equation (6.10) takes into account convection and diffusion along the interface, and mass exchange, j_b, between the interface and the bulk. The latter is assumed to be governed by a kinetic resistance at the interface (rather than by diffusion) an assumption which is strongly supported by the literature [80, 149]. As the typical surfactant loading is many orders of magnitude higher than the critical micelle concentration of the monomer, and the effect of bulk diffusion is taken negligible, there is no need for a mass balance in the bulk. Boundary conditions for Γ are applied at $\theta = \pi$ and $\theta = \theta_0$. The former is determined by symmetry,

$$\left.\frac{\partial \Gamma}{\partial \theta}\right|_{\theta=\pi} = 0 \tag{6.11}$$

but discussion and justification of the latter is discussed later on.

Surfactant equilibrium is taken to obey the Langmuir isotherm utilized in the problem investigated in the previous chapter

$$KC_{10} = \frac{\Gamma_{\mathrm{eq}}}{\Gamma_{\infty,\mathrm{eq}} - \Gamma_{\mathrm{eq}}} \tag{6.12}$$

where again, Γ_{eq} is the equilibrium surfactant concentration, $\Gamma_{\infty,\mathrm{eq}}$ saturation at equilibrium. In a similar fashion, mass exchange with the bulk is:

$$j_b = k_{\mathrm{ads}} C_{10} \left[(\Gamma_\infty - \Gamma) - \frac{\Gamma}{K\,C_{10}} \right] \tag{6.13}$$

Nonetheless, a major difference with the model presented in the previous chapter is to be noted; in this study the alveolus pulsates harmonically in the limit of small compression ratios and the entire configuration departs only slightly from its equilibrium configuration. In this case, exchange of subsurface material, i.e., surfactant material ejected from the interface due to collapse of the monolayer, does not take place since the monolayer surface tension attains values closely around σ_{eq}. An equation, henceforth, for B need not be accounted for. By equilibrium we denote, as it will thoroughly be discussed later, the motionless layer along with the static cap where every spatial gradient which may generate shearing motion is zero.

Surfactant kinetics is supplemented by eq.(5.4),(5.5) and eq.(5.15) where the Frumkin interaction parameter, a, is set to zero.

6.2.3 Lubrication Theory

The equations and boundary conditions of the problem are simplified by invoking a lubrication approximation [103]. The mathematical procedure for the spherical geometry was outlined long ago by [139] and was more recently exposed in detail by [89]. Thus, we present a brief outline and emphasize only the key points and the final results.

Integrating the equation of continuity in the $r-$direction, and combining with the kinematic boundary condition and the wall velocity in the $r-$direction, the following evolution equation is derived:

$$(R-h)^2\frac{\partial h}{\partial t}+(2Rh-h^2)\dot{R}+\frac{1}{\sin\theta}\frac{\partial}{\partial\theta}\int_{R-h}^{R} r u_\theta \sin\theta\, dr=0 \tag{6.14}$$

The lubrication form of the Navier-Stokes equations in spherical coordinates is

$$\frac{\partial p}{\partial r}=0 \tag{6.15}$$

$$\mu\frac{\partial}{\partial r}\left(r^2\frac{\partial u_\theta}{\partial r}\right)=r\frac{\partial p}{\partial\theta} \tag{6.16}$$

where gravitational effects are neglected [45]. Combining eq.(6.15) with the normal force boundary condition at the interface, and taking into account that viscous stresses are negligible in the lubrication approximation [179, 89], pressure across the film is derived as

$$p(\theta,t)=p_{air}-\sigma\boldsymbol{\nabla}_s\cdot\boldsymbol{n}=p_{air}-\sigma\left[\frac{2}{R}+\frac{2\,h}{R^2}+\frac{1}{R^2\sin\theta}\frac{\partial}{\partial\theta}\left(\sin\theta\frac{\partial h}{\partial\theta}\right)\right] \tag{6.17}$$

Thus, eq.(6.16) is readily integrated in the $r-$direction and gives

$$u_\theta=\frac{r}{2\mu}\frac{\partial p}{\partial\theta}-\frac{C_1}{r}+C_2 \tag{6.18}$$

Integration constants C_1, C_2 are determined by the tangential no-slip condition on the wall and the tangential force balance on the interface, the latter expressed in the lubrication approximation as

$$\mu\, r\frac{\partial}{\partial r}\left(\frac{u_\theta}{r}\right)=-\frac{1}{r}\frac{\partial\sigma}{\partial\theta}\quad \text{at}\quad r=R(t)-h(\theta,t) \tag{6.19}$$

Thus, again in the lubrication limit,

$$C_1=-\frac{1}{2\mu}\frac{\partial p}{\partial\theta}R^2\left(1-\frac{2h}{R}\right)-\frac{1}{\mu}\frac{\partial\sigma}{\partial\theta}R\left(1-\frac{2h}{R}\right) \tag{6.20}$$

$$C_2=-\frac{1}{\mu}\frac{\partial p}{\partial\theta}R\left(1-\frac{h}{R}\right)-\frac{1}{\mu}\frac{\partial\sigma}{\partial\theta}\left(1-\frac{2h}{R}\right) \tag{6.21}$$

Substituting the above results for u_θ in eq.(6.14), performing the integration and taking the lubrication limit, results in the following evolution equation for the liquid film thickness, which is identical with the one derived by Kang et al [89]:

$$\frac{\partial h}{\partial t}+\frac{2h\dot{R}}{R}-\frac{1}{R^2\sin\theta}\frac{\partial}{\partial\theta}\left(\frac{h^3\sin\theta}{3\mu}\frac{\partial p}{\partial\theta}-\frac{h^2\sin\theta}{2\mu}\frac{\partial\sigma}{\partial\theta}\right)= \\ \frac{\partial h}{\partial t}+\frac{2h\dot{R}}{R}+\frac{1}{R^2\sin\theta}\frac{\partial}{\partial\theta}\left(\frac{Q}{2\pi}\right)=0 \quad (6.22)$$

where $Q(\theta,t)$ is in the lubrication limit the volumetric flow rate along the entire $\phi-$circumference at an elevation $z=R\cos\theta$, evaluated in the lubrication limit.

$$Q(\theta,t)=2\pi R\,\sin\theta\int_{R-h}^{R}u_\theta\,dr\,, \quad (6.23)$$

A similar evolution equation is derived for the surface concentration, Γ, of the surfactant by simplifying eq.(6.10) according to the lubrication approximation. The respective result is

$$\frac{\partial\Gamma}{\partial t}+\frac{2\Gamma\dot{R}}{R}-\frac{1}{R^2\sin\theta}\frac{\partial}{\partial\theta}\left(\frac{\Gamma h^2\sin\theta}{2\mu}\frac{\partial p}{\partial\theta}-\frac{\Gamma h\sin\theta}{\mu}\frac{\partial\sigma}{\partial\theta}\right)-\frac{\mathcal{D}_s}{R^2\sin\theta}\frac{\partial}{\partial\theta}\left(\sin\theta\frac{\partial\Gamma}{\partial\theta}\right)= \\ \frac{\partial\Gamma}{\partial t}+\frac{2\Gamma\dot{R}}{R}+\frac{1}{R^2\sin\theta}\frac{\partial}{\partial\theta}\left(\frac{Q_\Gamma}{2\pi}\right)=j_b \quad (6.24)$$

where $Q_\Gamma(\theta,t)$ is the interfacial flow rate of surfactant along the entire $\phi-$circumference at an elevation $z=R\cos\theta$, evaluated in the lubrication limit.

$$Q_\Gamma(\theta,t)=2\pi R\,\sin\theta\left(u_s\Gamma-\frac{\mathcal{D}_s}{R}\frac{\partial\Gamma}{\partial\theta}\right) \quad (6.25)$$

and u_s is the interfacial water velocity,

$$u_s=-\frac{1}{2\mu}\frac{\partial p}{\partial\theta}\frac{h^2}{R}+\frac{1}{\mu}\frac{\partial\sigma}{\partial\theta}\frac{h}{R} \quad (6.26)$$

Equations (6.22) and (6.24) come to their final form by substitution of pressure from eq.(6.17). This will be undertaken in the following section, after performing a change of independent variable. However, there is a subtle point related to this substitution, which was noted by [90] and is worth mentioning. When taking the derivative of eq.(6.17) with respect to θ, additional terms containing $\partial\sigma/\partial\theta$ seem to come into play. However, these terms are of higher order in the ratio (h/R) than the original $\partial\sigma/\partial\theta$ term in eqs.(6.22) and (6.24), and are thus negligible in the lubrication approximation. A more detailed reasoning is presented in Appendix B.

6.2.4 Deriving novel boundary conditions at the rim

It has already been argued that the boundary conditions imposed at the rim of the spherical cap have a strong influence on the resulting dynamics. However, it appears that their physical origin is to some extent uncertain. For example, Gradon and Podgorski in [137] set constant values of h and Γ, in their pioneering work modeling type B alveoli. They justify their choice by arguing that bronchioles are less extensible than alveoli, because—as they claim—the former change their surface area in proportion to their diameter and the latter in proportion to its square. However, it is presently accepted that bronchioles are equally extensible, because they expand/contract roughly isotropically, i.e. they also change in length [40, 30]. In later work, [139] neglect capillary forces and leave only the Marangoni term in their evolution equation for h. Thus, they apply a condition at the rim only for Γ, one based on a kind of "sketchy" mass balance. Capillary forces are neglected also by [45], who set the flux of surfactant at the rim equal to zero.

Wei et al 2003 [178] consider the effect of both Marangoni and capillary forces in their modeling of a type A alveolus. The conditions they impose are constant film thickness and zero liquid flux at the rim. Consequently, they employ a matching solution close to the rim, as the lubrication approximation locally breaks down because of the simultaneous existence of finite film thickness and zero flow rate. Wei et al 2005 [179] focus on the strong surface tension limit, as in an alveolus with severe surfactant deficiency, and thus take the interface to be spherical. They further assume a film that is thick in the interior (flooded alveolus) and diminishes in thickness at the rim. They admit however that at the rim the film is actually "finite but thin". In our understanding, the condition of constant film thickness at the rim appears physically questionable, given that the liquid thickness inside the alveolus changes continuously with time.

Before developing the presently proposed condition, two other interesting approaches are mentioned. Zelig and Haber [63] circumvent the direct definition of a boundary condition for h. Instead, they use information about the average amount of surfactant expectorated and assume that the resulting mean per alveolus dictates the flow rate exiting at the alveolar rim. The more recent study of [89] includes, in the mass balance, source terms for surfactant production and degradation, however considers a complete sphere without an opening and a rim.

The present approach treats the rim of the alveolus as a region where liquid and surfactant may accumulate. Thus, the rate of inflow to (or outflow

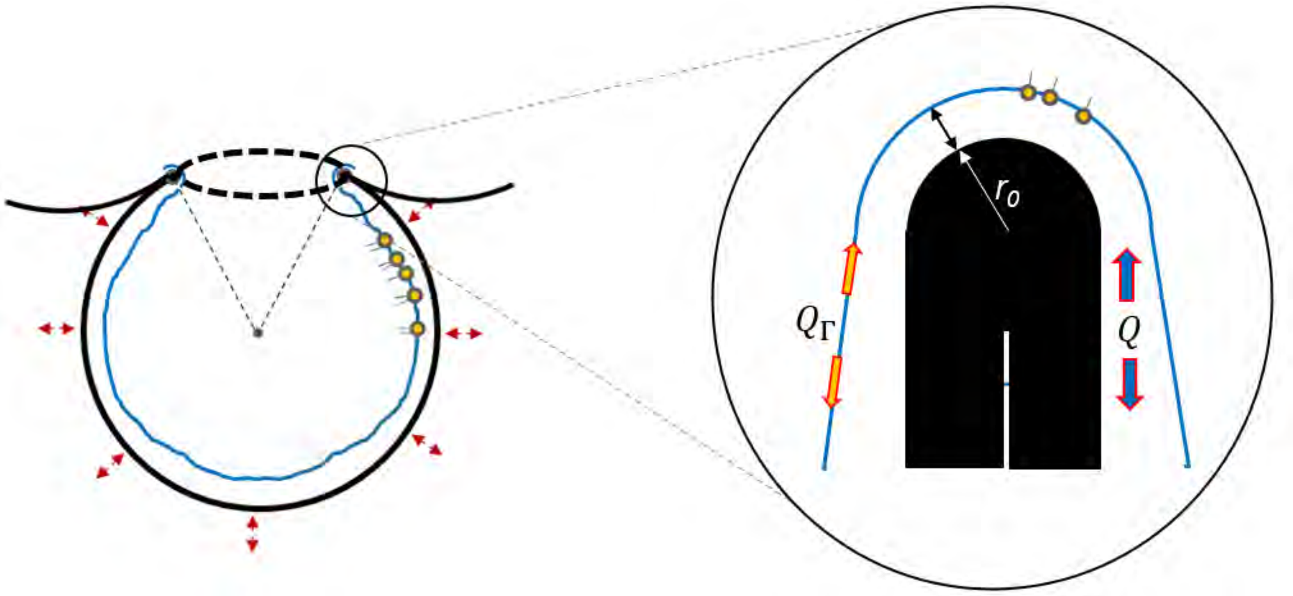

Figure 6.3: Left: The already shown schematic of the model alveolus, containing the alveolar fluid with a blowup of the alveolar tip, marked by a thin solid circle. Right: A magnified view of the rim. Notice that the watery film is uniform across the rim and, by hypothesis, the rim may exchange both liquid and surfactant from both sides of the tip on the understanding that terminal alveoli communicate with adjacent ”neighbours” via various transport phenomena.

from) the alveolus is set equal to the accumulation rate over the rim. This approach is supported by two sets of microscopic observations. Characterizing microscopic sections by stereology, [174] confirmed that the alveolar entrance rings are formed by strong fiber tracts in the free edges of the alveolar septa, resulting in rim thickness of a few micrometers.

Second, using low-temperature microscopy of anesthetized rats, with their lungs inflated at 80% of total lung capacity, [11] observed that the liquid lining of the alveolar epithelium is continuous over faces, ridges and protrusions. In particular, its area-weighted average thickness is around 0.2 µm, and its thickness over protrusions and mid-alveolar walls is about half of that (0.09 µm). Based on the above characteristics, the alveolar rim (assumed symmetric in the $\phi-$direction) is taken to have a semi-circular cross-section of radius r_0, and to be covered by a liquid layer of finite and spatially uniform thickness, $h_0(t)$, which varies with time (Fig. 6.3b). Similarly, the rim is also characterized by a spatially uniform but time-varying surfactant concentration, $\Gamma_0(t)$. As $r_0 \ll R$, the rim shrinks to a line when viewed in the ”large-scale” frame of the entire alveolus. Thus, $h_0(t)$ and $\Gamma_0(t)$ provide the boundary values for the system of evolution equations (6.22) and (6.24), i.e. $h_0(t) \equiv h(\theta_0, t)$ and $\Gamma_0 \equiv \Gamma(\theta_0, t)$.

The final assumption, which permits closure of the problem, is that the dynamics of the layer covering the rim is entirely enslaved to the dynamics of the alveolar cap. Thus, only mass balances need to be satisfied, and the temporal variation of h_0 and Γ_0 is dictated by the respective fluxes from/to the alveolus. The key assumptions in the above approach, i.e. the magnitude of the equilibrium film thickness at the rim, the spatial uniformity of film thickness and surfactant concentration over the rim, and the enslaved dynamics, will be further discussed and justified in the Concluding Remarks.

The mass balance of water at the rim is formulated taking into account the symmetry in the $\phi-$direction and states that the volumetric flow rate towards the rim from adjacent alveoli equals the time change of water volume over the rim. Thus,

$$\begin{aligned} -2\,Q(\theta_0,t) &= \frac{d}{dt}\left[2\pi R\sin\theta_0\left(\pi\frac{(r_0+h_0)^2}{2}-\pi\frac{r_0^2}{2}\right)\right] \Rightarrow \\ -2\int_{R-h}^{R} u_\theta\,dr\bigg|_{\theta_0} &= \pi(r_0+h_0)\frac{dh_0}{dt}+\pi h_0\left(r_0+\frac{h_0}{2}\right)\frac{\dot{R}}{R} \end{aligned} \tag{6.27}$$

where subscript 0 signifies value at the rim, $x=x_0$. A similar mass balance for the surfactant, taking into account convection and diffusion along the interface and exchange by adsorption or desorption with the bulk, leads to the following expression:

$$\begin{aligned} -2\,Q_\Gamma(\theta_0,t)+2\pi R\sin\theta_0\pi(r_0+h_0)j_b|_{\theta_0} &= \frac{d}{dt}\left[2\pi R\sin\theta_0\pi(r_0+h_0)\Gamma_0\right] \Rightarrow \\ -2\left(u_s\Gamma-\frac{\mathcal{D}_s}{R}\frac{\partial\Gamma}{\partial\theta}\right)\bigg|_{\theta_0}+\pi(r_0+h_0)j_b|_{\theta_0} &= \pi(r_0+h_0)\frac{d\Gamma_0}{dt}+\pi\Gamma_0\frac{dh_0}{dt}+\pi\Gamma_0(r_0+h_0)\frac{\dot{R}}{R} \end{aligned} \tag{6.28}$$

The multiplier two in eqs. (6.27) and (6.28) accounts for alveoli of type A, i.e. flux coming to the rim from both sides of the mid-alveolar wall. Alveoli of type B are not presently considered, though it may be argued that a similar approach is applicable. The minus sign indicates flow in the negative $\theta-$direction, i.e. towards the rim.

It is noted that loss terms could readily be incorporated in the boundary conditions, eqs. (6.27) and (6.28), in order to account for the possibility of water and surfactant entrainment from the rims by the airflow along the duct. Such a tentative entrainment mechanism resembles the suggestion of [63], and is in accord with recent findings that identify surfactant from the deep lung in the exhaled breath of human subjects [124]. However, unlike the approach of [63], with the above boundary conditions the flow of water and surfactant at the alveolar rim is not restricted by the entrainment rate.

6.3 Scaling, expansion around equilibrium and numerical solution

6.3.1 The reduced system and its equilibrium solution

The problem is now described by eqs.(6.17), (6.22) and (6.24), subject to the aforementioned boundary conditions. However, following [89, 90], it is more convenient to reformulate the system in terms of the new independent variable $x = -\cos\theta$.

Thus, the pressure field depends on the azimuthial - now the x direction - direction only, simply expressed as

$$p(x,t) = p_{air} - \frac{2\sigma}{R} - \frac{\sigma}{R^2}\left[2h + \frac{\partial}{\partial x}\left((1-x^2)\frac{\partial h}{\partial x}\right)\right] \tag{6.29}$$

Transforming eqs.(6.22) and (6.24) in terms of x, and substituting pressure from eq.(6.29), the following final form of the evolution equations is obtained:

$$\begin{aligned} \frac{\partial h}{\partial t} + \frac{2h\dot{R}}{R} + \frac{1}{3\mu R^4}\frac{\partial}{\partial x}\left(\sigma h^3(1-x^2)\frac{\partial}{\partial x}(2h+g)\right) + \\ \frac{1}{2\mu R^2}\frac{\partial}{\partial x}\left(h^2(1-x^2)\frac{d\sigma}{d\Gamma}\frac{\partial\Gamma}{\partial x}\right) = 0 \end{aligned} \tag{6.30}$$

and

$$\begin{aligned} \frac{\partial\Gamma}{\partial t} + \frac{2\Gamma\dot{R}}{R} + \frac{1}{2\mu R^4}\frac{\partial}{\partial x}\left(\Gamma h^2(1-x^2)\,\sigma\frac{\partial}{\partial x}(2h+g)\right) + \\ \frac{1}{\mu R^2}\frac{\partial}{\partial x}\left(\Gamma h(1-x^2)\frac{d\sigma}{d\Gamma}\frac{\partial\Gamma}{\partial x}\right) = \frac{\mathcal{D}_s}{R^2}\frac{\partial}{\partial x}\left((1-x^2)\frac{\partial\Gamma}{\partial x}\right) + j_b \end{aligned} \tag{6.31}$$

where D_s and μ are assumed constant, and we have defined

$$g(x,t) = \frac{\partial}{\partial x}\left((1-x^2)\frac{\partial h}{\partial x}\right) \tag{6.32}$$

The use of function g is not only intended to make the equations more compact but is also necessary for the finite-element solution of the problem, as the definition of the new function $g(x,t)$ eliminates the higher than second-order derivatives in h. The set of eqs.(6.30,6.31) constitute a system of nonlinear evolution equations needed to describe the spatiotemporal evolution of the alveolar lining, similar to that presented in [126, 38, 41].

A reference frame for the present problem is the equilibrium film thickness, $H(x)$, in a non-oscillating spherical cap of constant radius $\bar{R}$. Equilibrium requires that $\partial\sigma/\partial x = \partial p/\partial x = 0$, i.e. the surfactant is equi-distributed and the interface is a perfect spherical cap, say of radius R_s. If the uniform capillary pressure is termed $\bar{p}$, eq.(6.29) gives

$$2H + \frac{\partial}{\partial x}\left((1-x^2)\frac{\partial H}{\partial x}\right) = \frac{p_{air}-\bar{p}}{\sigma}\bar{R}^2 - 2\bar{R} = 2\bar{R}\left(\frac{\bar{R}}{R_s}-1\right) = 2K \tag{6.33}$$

Equation (6.33) has the trivial linear solution, $H(x) = \kappa x + \lambda$, with $\kappa = (H_0 - K)/x_0$ and $\lambda = K$ in terms of the constant $2K$ and the film thickness $H_0 = H(x_0)$ at the rim of the cap ($x_0 = -\cos\theta_0$). Term H_0 is a key parameter for the problem, and its magnitude will be estimated from direct experimental evidence [11, 189]. Parameter K is determined from the total volume of liquid in the cap, which in the lubrication limit is

$$V_{water} = 2\pi\int_{\theta_0}^{\pi}\int_{R-h}^{R} r^2\sin\theta\,drd\theta \approx 2\pi R^2\int_{\theta_0}^{\pi} h(\theta)\sin\theta d\theta = 2\pi R^2\int_{x_0}^{1} h(x)dx \tag{6.34}$$

Equivalently, a convenient input is the mean liquid film thickness, $\bar{H}$, which is related to the liquid volume by the expression

$$V_{water} = 2\pi R^2\,(1-x_0)\,\bar{H} \tag{6.35}$$

For given total volume of water, a simple mass balance shows that the equilibrium film thickness, $H(x)$, varies inversely with the square of the cap radius. Thus, it is verified by inspection that the function

$$h(x,t) = H(x)\,\frac{\bar{R}^2}{R^2(t)} \tag{6.36}$$

together with a spatially uniform surface concentration of surfactant, satisfies eq.(6.30) for arbitrary oscillation pattern, $R(t)$. When $j_b \equiv 0$, surface concentration has a similar form, $\Gamma(x,t) = \bar{\Gamma}[\bar{R}/R(t)]^2$, but when $j_b \neq 0$ it is a more complicated function of time [111]. The above solution corresponds to a purely axial motion, i.e. with no gradients in the $\theta-$direction. However the boundary conditions (6.27)-(6.28) are not satisfied, except for the special case $h(x_0,t) = 0$. This behavior is a first indication of the significance of the finite liquid film thickness at the rim in triggering tangential motion.

6.3.2 Scaling and dimensionless numbers

The characteristic scales used to non-dimensionalise the problem variables are mainly taken from the equilibrium conditions. Thus, we consider a motionless alveolar cap of radius $\bar{R}$, coated by a liquid film whose mean thickness is $\bar{H}$. With these choices, the lubrication parameter is formally defined as

$$\epsilon = \frac{\bar{H}}{\bar{R}} \tag{6.37}$$

The liquid is loaded by surfactant aggregates and equilibrates with an adsorbed monolayer of surface concentration Γ_{eq}, which results in surface tension σ_{eq} and surface elasticity $E_{\text{eq}} = -\left.(d\sigma/d\ln\Gamma)\right|_{\Gamma=\Gamma_{\text{eq}}}$. Finally, the characteristic time is the breathing period, T.

With the above scales, the following dimensionless variables are defined: $h^* = h/\bar{H}$, $H^* = H/\bar{H}$, $R^* = R/\bar{R}$, $t^* = t/\mathrm{T}$, $\Gamma^* = \Gamma/\Gamma_{\text{eq}}$, $\sigma^* = \sigma/\sigma_{\text{eq}}$, $E^* = E/E_{\text{eq}}$, $p^* = p\,\bar{R}^2/(\sigma_{\text{eq}}\bar{H})$, $j_b^* = j_b\mathrm{T}/\Gamma_{\text{eq}}$ and $g^* = g/\bar{H}$. Substituting the dimensionless variables, and also taking into account the definition of surface elasticity, eq.(6.9), the system (6.30)-(6.31) is transformed as follows:

$$\frac{\partial h^*}{\partial t^*} + \frac{2h^*\dot{R}^*}{R^*} + \frac{1}{R^*}\frac{\partial F_h}{\partial x} = 0 \tag{6.38}$$

and

$$\frac{\partial \Gamma^*}{\partial t^*} + \frac{2\Gamma^*\dot{R}^*}{R^*} + \frac{1}{R^*}\frac{\partial F_\Gamma}{\partial x} - j_b^* = 0 \tag{6.39}$$

where

$$F_h = \frac{Q^*}{R^*} = \epsilon^3\frac{Ca^{-1}}{3R^{*3}}\sigma^* h^{*3}(1-x^2)\frac{\partial}{\partial x}(2h^*+g^*) - \epsilon\frac{Ma}{2R^*}h^{*2}(1-x^2)\frac{E^*}{\Gamma^*}\frac{\partial\Gamma^*}{\partial x} \tag{6.40}$$

$$\begin{aligned} F_\Gamma = \frac{Q_\Gamma^*}{R^*} = \epsilon^3\frac{Ca^{-1}}{2R^{*3}}\Gamma^*\sigma^* h^{*2}(1-x^2)\frac{\partial}{\partial x}(2h^*+g^*) - \\ \epsilon\frac{Ma}{R^*}\Gamma^* h^*(1-x^2)\frac{E^*}{\Gamma^*}\frac{\partial\Gamma^*}{\partial x} - \frac{Pe_s^{-1}}{R^*}(1-x^2)\frac{\partial\Gamma^*}{\partial x} \end{aligned} \tag{6.41}$$

and

$$j_b^* = St\left[(\Gamma_\infty^* - \Gamma^*) - \frac{\Gamma^*}{KC_{10}}\right] \tag{6.42}$$

Terms Q^*, Q_Γ^* are respectively the dimensionless volumetric water and interfacial surfactant flow rates, scaled by $\bar{Q} = 2\pi\bar{R}^2\bar{H}/\mathrm{T}$ and $\bar{Q}_\Gamma = 2\pi\bar{R}^2\Gamma_{\text{eq}}/\mathrm{T}$. The dimensionless numbers that appear in the above equations are

$$Ca^{-1} = \frac{\sigma_{eq}}{\mu(\bar{R}/\mathrm{T})}\,, \quad Ma = \frac{E_{eq}}{\mu(\bar{R}/\mathrm{T})}\,, \quad Pe_s^{-1} = \frac{\mathcal{D}_s\mathrm{T}}{\bar{R}^2}\,, \quad St = \frac{\mathrm{T}}{1/(k_{\text{ads}}C_{10})} \tag{6.43}$$

which are the inverse capillary number, Ca^{-1}, that compares capillary to viscous stresses, the Marangoni number, Ma, that compares elastic to viscous stresses, the inverse Peclet number, Pe_s^{-1} that compares surface diffusion to surface convection, and a Stanton number, St, that compares characteristic times of breathing and surfactant adsorption [111]. The ratio of alveolar radius to breathing period that appears in these dimensionless numbers defines the characteristic velocity scale $\bar{U} = \bar{R}/\mathrm{T}$.

With the above scaling and function definitions, the boundary conditions at the rim, eqs. (6.27) and (6.28), take the following dimensionless form

$$-2F_h|_{x_0} = \sqrt{1 - x_0^2}\,\pi \left[(r_0^* + \epsilon h_0^*) \frac{dh_0^*}{dt^*} + h_0^* \left(r_0^* + \epsilon \frac{h_0^*}{2} \right) \frac{\dot{R}^*}{R^*} \right] \tag{6.44}$$

$$-2F_\Gamma|_{x_0} = \sqrt{1 - x_0^2}\,\pi \left[(r_0^* + \epsilon h_0^*) \left(\frac{d\Gamma_0^*}{dt^*} - j_{b0}^* \right) + \epsilon \Gamma_0^* \frac{dh_0^*}{dt^*} + \Gamma_0^* (r_0^* + \epsilon h_0^*) \frac{\dot{R}^*}{R^*} \right] \tag{6.45}$$

where subscript 0 signifies value at the rim, $x = x_0$, and $r_0^* = r_0/\bar{R}$ is the dimensionless radius of curvature of the rim. It is also noted that the symmetry boundary conditions at $\theta = \pi$ are trivially satisfied in the present frame, provided the derivatives $\partial h/\partial x$ and $\partial \Gamma/\partial x$ are finite at $x = 1$. Thus, eqs.(6.38) and (6.39), together with the above boundary conditions, eqs.(6.44), (6.45) and the model of surfactant dynamics provide the full description of the problem.

6.3.3 Expansion around equilibrium

Thus far, we have derived the final form of the governing equations along with novel boundary conditions and rendered the problem dimensionless, without assuming any specific form for the alveolus oscillation, via $R(t)$. We assume that the alveolus is perturbed from its equilibrium configuration subjected to small amplitude oscillations - small compression ratios. Besides, for the sake of notational convenience, the dimensionless variables are henceforth represented without the asterisk superscript. Thus we write

$$R(t) = 1 + a\,\mathfrak{Re}[e^{i\,2\pi t}] \tag{6.46}$$

with $a \ll 1$. The dimensionless film thickness, h, its function g and the surface concentration of surfactant, Γ, are expanded as follows, to capture linear and weakly nonlinear effects

$$\begin{aligned} h(x,t) &= H(x) + a\,\mathfrak{Re}[h_1(x)\,e^{i\,2\pi t}] + a^2 \left(\mathfrak{Re}[h_2(x)\,e^{i\,4\pi t}] + h_S(x) \right) \\ g(x,t) &= G(x) + a\,\mathfrak{Re}[g_1(x)\,e^{i\,2\pi t}] + a^2 \left(\mathfrak{Re}[g_2(x)\,e^{i\,4\pi t}] + g_S(x) \right) \\ \Gamma(x,t) &= 1 + a\,\mathfrak{Re}[\Gamma_1(x)\,e^{i\,2\pi t}] + a^2 \left(\mathfrak{Re}[\Gamma_2(x)\,e^{i\,4\pi t}] + \Gamma_S(x) \right), \end{aligned} \tag{6.47}$$

with the above expressions calculated as $Re[ze^{i\,\phi}] = \frac{1}{2}\left(ze^{i\,\phi} + \bar{z}e^{-i\,\phi}\right)$. By indices 1, 2, S is denoted the amplitude of each parameter in the respective order of approximation. Steady terms are included at second order in order to balance the "steady streaming" resulting from products of first-order contributions. As a generic example, given two complex functions $z_1(x)$, $w_1(x)$

$$\mathfrak{Re}[z_1 e^{i\,2\pi t}] \cdot \mathfrak{Re}[w_1 e^{i\,2\pi t}] = \frac{1}{2}\mathfrak{Re}[z_1 w_1 e^{i\,4\pi t}] + \frac{1}{2}\mathfrak{Re}[z_1 \bar{w}_1] \tag{6.48}$$

Term G, the equilibrium value of function $g(x,t)$, is eliminated by application of the equilibrium balance, eq.(6.33), and the dimensionless fluxes, F_h, F_Γ, are expanded as

$$F_h = a\,\mathfrak{Re}[F_{h1} e^{i\,2\pi t}] + a^2\left(\mathfrak{Re}[F_{h2} e^{i\,2\pi t}] + F_{hS}\right) \tag{6.49}$$

$$F_\Gamma = a\,\mathfrak{Re}[F_{\Gamma 1} e^{i\,2\pi t}] + a^2\left(\mathfrak{Re}[F_{\Gamma 2} e^{i\,2\pi t}] + F_{\Gamma S}\right), \tag{6.50}$$

where F_{hi}, $F_{\Gamma i}$, $i = 1, 2, S$, are functions of x, given in terms of h_i, g_i, Γ_i in the appendix. The dimensionless mass exchange with the bulk, j_b, is also expanded as follows

$$\begin{aligned} j_b = St_1 \left(a\,\mathfrak{Re}[\Gamma_1\, e^{i\,2\pi t}] + a^2 \mathfrak{Re}[\Gamma_2\, e^{i\,4\pi t}] + a^2 \Gamma_S\right) + \\ a^2\,\frac{1}{4} St\,\Gamma_{\infty,\Gamma\Gamma}\left(\mathfrak{Re}[\Gamma_1^2\, e^{i\,4\pi t}] + \Gamma_1 \bar{\Gamma}_1\right) \end{aligned} \tag{6.51}$$

where St_1 is

$$St_1 = St\left(\Gamma_{\infty,\Gamma} - 1 - \frac{1}{KC_{10}}\right) \tag{6.52}$$

with

$$\Gamma_{\infty,\Gamma} = \left.\frac{d\Gamma_\infty}{d\Gamma}\right|_{\text{eq}}, \quad \Gamma_{\infty,\Gamma\Gamma} = \left.\frac{d^2\Gamma_\infty}{d\Gamma^2}\right|_{\text{eq}} \tag{6.53}$$

It is noted that the surface concentration at close packing is not constant but is a function of surface pressure, hence the derivatives in eqs.(6.51) and(6.52).

The following orders of the evolution equations result by straightforward substitution of the above into eqs.(6.38) and (6.39) and neglect of higher than second-order terms. Primes denote derivatives with respect to x and, as shown below, terms F'_{h1}, $F'_{\Gamma 1}$ that appear in the second-order and steady equations are replaced by the respective first-order result.

$$2\pi i h_1 + F'_{h1} + 4\pi i H = 0 \tag{6.54}$$

$$2\pi i \Gamma_1 + F'_{\Gamma 1} - St_1 \Gamma_1 + 4\pi i = 0 \tag{6.55}$$

$$\begin{aligned} 4\pi i h_2 + 2\pi i h_1 - 2\pi i H + F'_{h2} - \frac{1}{2}F'_{h1} = 0 \Rightarrow \\ 4\pi i h_2 + 3\pi i h_1 + F'_{h2} = 0 \end{aligned} \tag{6.56}$$

$$\begin{gathered}4\pi i\Gamma_2 + 2\pi i\Gamma_1 - 2\pi i + F'_{\Gamma 2} - \frac{1}{2}F'_{\Gamma 1} - St_1\Gamma_2 - \frac{St}{4}\Gamma_{\infty,\Gamma\Gamma}\Gamma_1^2 = 0 \Rightarrow \\ 4\pi i\Gamma_2 + 3\pi i\Gamma_1 + F'_{\Gamma 2} - St_1\left(\Gamma_2 + \frac{1}{2}\Gamma_1\right) - \frac{St}{4}\Gamma_{\infty,\Gamma\Gamma}\Gamma_1^2 = 0\end{gathered} \tag{6.57}$$

$$\mathfrak{Re}\left[2\pi i\bar{h}_1\right] + F'_{h0} - \frac{1}{2}\mathfrak{Re}\left[F'_{h1}\right] = 0 \Rightarrow F'_{hS} + \pi\,\mathfrak{Im}\left[h_1\right] = 0 \tag{6.58}$$

$$\begin{gathered}\mathfrak{Re}\left[2\pi i\bar{\Gamma}_1\right] + F'_{\Gamma S} - \frac{1}{2}\mathfrak{Re}\left[F'_{\Gamma 1}\right] - St_1\Gamma_S - \frac{St}{4}\Gamma_{\infty,\Gamma\Gamma}\mathfrak{Re}\left[\Gamma_1\bar{\Gamma}_1\right] = 0 \Rightarrow \\ F'_{\Gamma S} + \pi\,\mathfrak{Im}\left[\Gamma_1\right] - St_1\left(\Gamma_S + \frac{1}{2}\mathfrak{Re}\left[\Gamma_1\right]\right) - \frac{St}{4}\Gamma_{\infty,\Gamma\Gamma}\left(\Gamma_1\bar{\Gamma}_1\right) = 0\end{gathered} \tag{6.59}$$

The system is completed by the expansions of g

$$\left((1-x^2)h'_i\right)' - g_i = 0 \quad i = 1, 2, S \tag{6.60}$$

and by the boundary conditions at $x = x_0$. The latter are evaluated by expanding the rhs of eqs. (6.44), (6.45), and the respective coefficients $F_{hi}|_{x_0}$, $F_{\Gamma i}|_{x_0}$, $i = 1, 2, S$ are given in the appendix at the end of the dissertation.

6.3.4 Steady streaming

The weakly nonlinear problem was formulated taking into consideration the possibility of steady streaming, with the inclusion of time-independent terms identified throughout the text by the subscript "S". It will now be shown that steady streaming of water is always identically zero, as is also the steady streaming of insoluble surfactant. The exceptional (and important) case of a soluble surfactant is singled out, and will be considered further in the later part of this dissertation, along with other parameters concerning the surfactant and the alveolar geometry.

First, the dimensionless volumetric flow rate of water, $Q = RF_h$, is calculated as follows:

$$Q = a\,\mathfrak{Re}[F_{h1}\,e^{i\,2\pi t}] + a^2\mathfrak{Re}\left[\left(F_{h2} + \frac{1}{2}F_{h1}\right)\,e^{i\,4\pi t}\right] + a^2\left(F_{hS} + \frac{1}{2}\mathfrak{Re}[F_{h1}]\right) \tag{6.61}$$

Straightforward combination of eqs.(6.54),(6.58) shows that $\left(F'_{hS} + \frac{1}{2}\mathfrak{Re}[F'_{h1}]\right) = 0$. Also, the boundary conditions, eqs. (A.7), (A.9), indicate that $\left(F_{hS} + \frac{1}{2}\mathfrak{Re}[F_{h1}]\right)|_{x_0} = 0$. Thus, the steady flow of water is identically zero, i.e.

$$Q_S = F_{hS} + \frac{1}{2}\mathfrak{Re}[F_{h1}] = 0 \tag{6.62}$$

An expansion for the flow rate of surfactant, $Q_\Gamma = RF_\Gamma$, leads to the similar result

$$Q_\Gamma = a\,\mathfrak{Re}[F_{\Gamma 1}\,e^{i\,2\pi t}] + a^2\mathfrak{Re}\left[\left(F_{\Gamma 2} + \frac{1}{2}F_{\Gamma 1}\right)\,e^{i\,4\pi t}\right] + a^2\left(F_{\Gamma S} + \frac{1}{2}\mathfrak{Re}[F_{\Gamma 1}]\right) \tag{6.63}$$

and combination of eqs. (6.55), (6.59) gives

$$Q'_{\Gamma S} = F'_{\Gamma S} + \frac{1}{2}\mathfrak{Re}[F'_{\Gamma 1}] = St_1\,(\Gamma_S + \mathfrak{Re}[\Gamma_1]) + \frac{1}{4}St\,\Gamma_{\infty,\Gamma\Gamma}(\Gamma_1\bar{\Gamma}_1) \tag{6.64}$$

Also, the boundary conditions, eqs.(A.10), (A.12) lead to the result

$$\left.\left(F_{\Gamma S} + \frac{1}{2}\mathfrak{Re}[F_{\Gamma 1}]\right)\right|_{x_0} = \sqrt{1-x_0^2}\,\pi\left[\frac{1}{2}(r_0 + \epsilon H_0)\left\{St_1\left(\Gamma_S + \frac{1}{2}\mathfrak{Re}[\Gamma_1]\right) + \frac{1}{4}St\,\Gamma_{\infty,\Gamma\Gamma}(\Gamma_1\bar{\Gamma}_1)\right\} + \frac{1}{4}\epsilon\,St_1\,\mathfrak{Re}[\Gamma_1\bar{h}_1]\right] \tag{6.65}$$

Thus, it is evident that, for an insoluble surfactant ($St = St_1 = 0$), steady streaming along the interface is also identically zero. This, however, is not necessarily the case with a soluble surfactant, and the calculation of $Q_{\Gamma S}$ for a representative value of $k_{ads} \neq 0$ will be undertaken later on.

6.4 Numerical procedure

The linear and weakly nonlinear periodic problems, consisting of eqs. (6.54)-(6.57), and subject to the boundary conditions eqs. (6.44)-(6.45), are discretized and solved by a standard Galerkin finite-element method, where the unknowns h_i, Γ_i and g_i are approximated by Lagrangian basis functions $\phi_k(x)$. Applying integration by parts, the following weak forms of the governing equations are derived, where primes denote derivatives of functions of x:

$$2\pi i\int_{x_0}^{1} h_1\phi_k dx + [F_{h1}\,\phi_k]_{x_0}^1 - \int_{x_0}^{1} F_{h1}\,\phi'_k dx + 4\pi i\int_{x_0}^{1} H\phi_k dx = 0 \tag{6.66}$$

$$2\pi i\int_{x_0}^{1}\Gamma_1\phi_k dx + [F_{\Gamma 1}\,\phi_k]_{x_0}^1 - \int_{x_0}^{1} F_{\Gamma 1}\,\phi'_k dx - St_1\int_{x_0}^{1}\Gamma_1\phi_k dx + 4\pi i\int_{x_0}^{1}\phi_k dx = 0 \tag{6.67}$$

$$\int_{x_0}^{1}(1-x^2)h'_1\phi'_k dx + \int_{x_0}^{1} g_1\phi_k dx - \left[(1-x^2)h'_1\phi_k\right]_{x_0}^1 = 0 \tag{6.68}$$

$$4\pi i\int_{x_0}^{1} h_2\phi_k dx + \left[F_{h2}\,\phi_k\right]_{x_0}^{1} - \int_{x_0}^{1} F_{h2}\,\phi_k' dx + 3\pi i\int_{x_0}^{1} h_1\phi_k dx = 0 \tag{6.69}$$

$$\begin{gathered}4\pi i\int_{x_0}^{1}\Gamma_2\phi_k dx + \left[F_{\Gamma 2}\,\phi_k\right]_{x_0}^{1} - \int_{x_0}^{1} F_{\Gamma 2}\,\phi_k' dx + 3\pi i\int_{x_0}^{1}\Gamma_1\phi_k dx \\ -St_1\int_{x_0}^{1}\Gamma_2\phi_k dx - \frac{1}{2}St_1\int_{x_0}^{1}\Gamma_1\phi_k dx - \frac{1}{4}St\Gamma_{\infty,\Gamma\Gamma}\int_{x_0}^{1}\Gamma_1^2\phi_k dx = 0\end{gathered} \tag{6.70}$$

$$\int_{x_0}^{1}(1-x^2)h_2'\phi_k' dx + \int_{x_0}^{1} g_2\phi_k dx - \left[(1-x^2)h_2'\phi_k\right]_{x_0}^{1} = 0 \tag{6.71}$$

The integrated terms in eqs. (6.66)-(6.71) are equal to zero at $x = 1$ and are evaluated from the (natural) boundary conditions at $x = x_0$. The computational domain is discretized with 160 elements in all the computations presented in this study. Numerical accuracy was checked by doubling and halving the number of elements, and also by clustering nodes close to x_0, where the solution changes faster.

According to the findings of §6.3.4, in the case of an insoluble surfactant the above equations contain all the dynamics of the flow (while the steady terms, h_S, Γ_S, only provide order $O(a^2)$ corrections to the mean film thickness and surfactant concentration). However, in the case of a soluble surfactant, we need Γ_S in order to calculate the interfacial flow rate of surfactant, $Q_{\Gamma S}$. To this end, the following weak form of eq.(6.59) is employed:

$$\begin{gathered}\left[F_{\Gamma S}\,\phi_k\right]_{x_0}^{1} - \int_{x_0}^{1} F_{\Gamma S}\phi_k' dx - St_1\int_{x_0}^{1}\Gamma_S\phi_k dx + \pi\int_{x_0}^{1}\mathfrak{Im}[\bar{\Gamma}_1]\phi_k dx - \\ \frac{1}{2}St_1\int_{x_0}^{1}\mathfrak{Re}[\Gamma_1]\phi_k dx - \frac{1}{4}St\Gamma_{\infty,\Gamma\Gamma}\int_{x_0}^{1}\left(\Gamma_1\bar{\Gamma}_1\right)\phi_k dx = 0\end{gathered} \tag{6.72}$$

Also, instead of combining it with eq.(6.58) or its weak form, we invoke eq.(6.62), which, when substituted in eq.(6.72), renders the latter a function of only Γ_S and the—already known—amplitudes of the first and second-order harmonics.

6.5 Results and discussion

6.5.1 Parameter values and dimensionless estimates

The equilibrium alveolar radius is taken as $\bar{R}$ =100 μm, following recent morphometric studies [123, 174], which indicate that the size of a single human alveolus varies little around this mean, and it is mainly the number of alveoli that accounts for different lung volumes. The above studies also confirm that the free edges of the alveolar septa that form the entrance rings are thicker than the rest of the alveolar walls, as they are reinforced by strong fiber tracts (in fully alveolated airways, these structures essentially define the airway duct). Thus, the radius of curvature of the alveolar rim is taken as $r_0 = 2\,\mu\text{m}$, in accordance with [70]. Also, all the results to be presented next, are for breathing period $\mathrm{T} = 3\,\text{s}$.

The liquid layer has the properties of pure water at the physiological temperature, $T = 37\,°\text{C}$, i.e. density $\rho = 993\,\text{kg}\,\text{m}^{-3}$ and dynamic viscosity $\mu = 0.000\,69\,\text{Pa}\,\text{s}$. Also, the surface tension of pure water, which is required in the definition of surface pressure Π, is $\sigma_\text{o} = 70\,\text{mN}\,\text{m}^{-1}$. According to the literature [185, 128], the pulmonary surfactant has an equilibrium surface tension in the range $22 - 24\,\text{mN}\,\text{m}^{-1}$, which is roughly constant irrespective of bulk loading and air humidity. Thus, we presently set $\sigma_\text{eq} = 23\,\text{mN}\,\text{m}^{-1}$. Also, the surface coverage at zero surface pressure is taken as $\Omega_\text{o} = 3.0 \times 10^5\,\text{m}^2\,\text{mol}^{-1}$, according to [20] who extrapolated the data of [198], and the surface diffusivity is taken as $\mathcal{D}_s = 10^{-9}\,\text{m}^2\,\text{s}^{-1}$ [178, 179]. The equilibrium elasticity, E_eq, may be predicted by the above data using eq.(6.9). Both this prediction and experimental data [1, 149, 150] give values in the range $100 \lesssim E < 200\,\text{mN}\,\text{m}^{-1}$.

Estimates for the parameters of surfactant kinetics are provided by [20], who fit their model to the dynamic data of [149]. Representative values for bovine lipid extract surfactant (BLES) at bulk concentration $C = 0.5$ mg/ml are $KC_{10} = 120$, $\alpha = 5.2\,\text{m}\,\text{N}^{-1}$ and $k_\text{ads}C_{10} = 13\,\text{s}^{-1}$ in contact with humid air ($RH = 100\%$) and $k_\text{ads}C_{10} = 0\,\text{s}^{-1}$ in contact with dry air($RH < 20\%$). Indeed, it has been shown in the literature that air humidity affects adsorption kinetics, though not equilibrium surface tension [197]. The BLES preparation in contact with dry air, which behaves as essentially insoluble, provides a simpler basis for understanding the flow dynamics. Thus, the results to be presented from this point on refer to it, i.e. are for $k_\text{ads}C_{10} = 0\,\text{s}^{-1}$. Surfactant solubility introduces hysteresis effects and is considered in a separate section (§6.5.4) at the end of the thesis using the aforementioned value $k_\text{ads}C_{10} = 13\,\text{s}^{-1}$ which corresponds to humid air and bulk concentration $C = 0.5$ mg/ml.

Given the above parameter estimates, it is pertinent to consider the time scales of the problem. The main dimensionless numbers, Ca^{-1}, Ma, Pe_s^{-1} and St, as they explicitly appear in the formulation, may be perceived as the following ratios of characteristic times

$$Ca^{-1} = \frac{\mathrm{T}}{t_{cap}}\,, \quad Ma = \frac{\mathrm{T}}{t_{elast}}\,, \quad Pe_s^{-1} = \frac{\mathrm{T}}{t_{diff}}\,, \quad St = \frac{\mathrm{T}}{t_{ads}} \tag{6.73}$$

Terms $t_{cap} = \mu\bar{R}/\sigma_\text{eq} \approx 3 \times 10^{-6}\,\text{s}$ and $t_{elast} = \mu\bar{R}/E_\text{eq} \approx 5 \times 10^{-7}\,\text{s}$ are respectively the characteristic times for establishment of flow due to capillary and Marangoni (elastic) forcing [111]. Terms $t_{diff} = \bar{R}^2/\mathcal{D}_s \approx 10\,\text{s}$ and

$t_{ads} = 1/(k_{\text{ads}} C_{10}) \approx 8 \times 10^{-2}\,\text{s}$ are respectively the times for diffusion and adsorption effects to become significant.

It is observed that the capillary and elastic timescales are many orders of magnitude shorter than the characteristic oscillation time, T, thus the assumption of quasi-steady Stokes flow, eq.(6.2), is fully justified. Also, $St \approx 40$ and thus kinetic effects cannot be ruled out. On the contrary, surface diffusion is very slow, and is expected to be negligible in comparison to surface convection.

6.5.2 Equilibrium film thickness at the rim and the onset of shearing flow

A key input to the problem is the equilibrium liquid film thickness, $H(x)$, for a non-oscillating cap. This was shown above to be a linear function of variable x, and is presently determined by two equilibrium parameters, the mean film thickness, $\bar{H}$, and the film thickness, H_0, at the rim of the cap. Reliable estimates of these parameters are provided by the experimental study of [11]. These authors used low-temperature microscopy to freeze the watery layer inside and around the alveoli of anesthetized rats and measured an area-weighted average thickness of ≈ 0.2 μm and a thickness over protrusions and mid-alveolar walls of ≈ 0.09 μm. Taking into account that the rat lungs were inflated to around 80% of their total lung capacity (TLC), and assuming that the alveolar radius scales with the cubic root of the inhaled volume and the film thickness is inversely proportional to the square of the radius, we derive the estimates $\bar{H} \approx 0.3$ μm and $H_0 \approx 0.14$ μm for a lung at equilibrium. Apart from the parametric investigation of the effect of varying H_0, to be undertaken next, the values $\bar{H} = 0.3$ μm and $H_0 = 0.14$ μm are kept constant for the rest of the study. The validity of the selected value of H_0 is further supported in the Concluding Remarks, by discussing and interpreting additional experimental evidence [189].

It is recalled first that, if H_0 is set equal to zero, the problem has the trivial solution given by eq.(6.36), which corresponds to pure axial flow with uniform surfactant distribution. Expanding to second-order in the oscillation amplitude, this trivial solution results in the film thickness distribution

$$h(x,t) = H(x)\left(1 - 2a\,\mathfrak{Re}[e^{i2\pi t}] + \frac{3}{2}a^2\,\mathfrak{Re}[e^{i4\pi t}] + \frac{3}{2}a^2\right), \tag{6.74}$$

with the first-order perturbation 180^o out-of-phase with the wall oscillation and the second-order perturbation in-phase with the wall oscillation. More generally, in the frame of harmonic analysis, the spatial and temporal variation of all the variables of the problem may be described by the respective magnitudes and

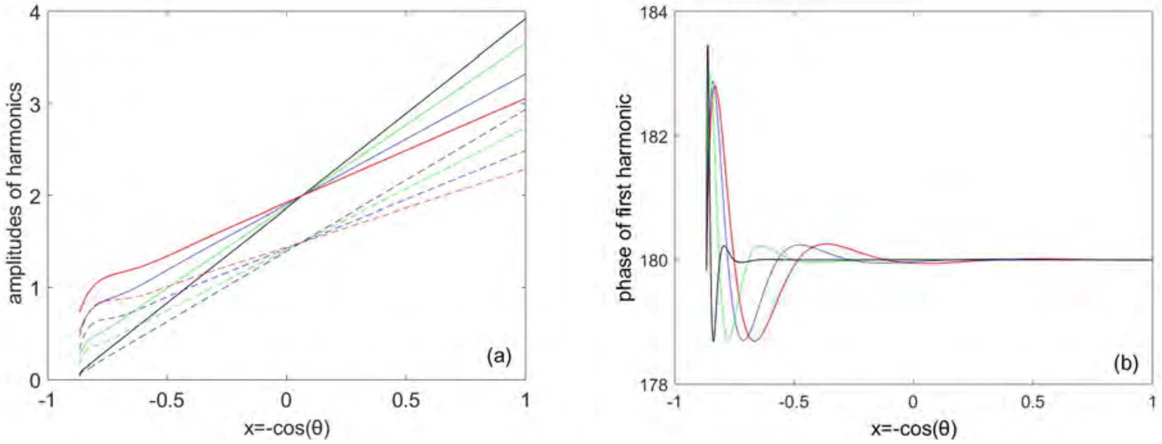

Figure 6.4: (a) The magnitude of the first and second harmonic of the film thickness perturbation (continuous and dashed lines respectively). (b) The phase of the first harmonic. Results are given for four different values of equilibrium film thickness at the rim, H_0 =0.01 µm(black), 0.05 µm(green), 0.1 µm(blue) and 0.14 µm(red).

phases of their perturbation amplitudes. Taking the liquid film thickness as an example, we define the magnitudes, $|h_i(x)|$, and phases, $\omega_i(x)$, of the thickness perturbation as follows

$$\begin{aligned} h &= H + a\,\mathfrak{Re}[h_1 e^{i2\pi t}] + a^2\,\mathfrak{Re}[h_2 e^{i4\pi t}] + a^2\,h_S \\ &= H + a|h_1(x)|\cos(2\pi t + \omega_1(x)) + a^2|h_2(x)|\cos(4\pi t + \omega_2(x)) + a^2\,h_S \end{aligned} \tag{6.75}$$

where

$$|h_i| = \sqrt{[\mathfrak{Re}(h_i)]^2 + [\mathfrak{Im}(h_i)]^2}; \qquad \tan\omega_i = \frac{\mathfrak{Im}(h_i)}{\mathfrak{Re}(h_i)} \tag{6.76}$$

Because liquid film thickness and surfactant surface concentration are to leading order 180^o out of phase with the wall oscillation, the branch-cut in the definition of $\omega_i(x)$ is taken at 270^o, i.e. $\omega_i(x) \in [-90^o, 270^o)$.

In order to compare the numerical analysis with the asymptotic behavior for $H_0 = 0$, a liquid film of mean thickness $\bar{H} = 3$ µm lined with insoluble surfactant is considered, and the problem is solved for the cases $H_0 = 0.01, 0.05, 0.10$ and 0.14 µm. The results of the computation are depicted in Fig. 6.4. Figure 6.4 a) shows the amplitudes of the two harmonics and indicates that, when $H_0 \to 0$, the solution approaches the aforementioned axial flow. More specifically, $|h_i|$ become linear functions of x, with $|h_i(x_0)| \to 0$, $|h_1(1)| \to 4$ and $|h_2(1)| \to 3$. Noting that when $H_0 = 0$, $H(1) = 2$, it becomes evident that the magnitudes of the two harmonics approach the limits $|h_1(x)| \to 2H(x)$ and $|h_2(x)| \to (3/2)H(x)$ respectively, in agreement with eq.(6.74).

As shown in Fig. 6.4a, an overshoot in the perturbation amplitude of the film is observed in the neighborhood of the rim when H_0 is non-zero. This overshoot gradually extends toward the interior with increasing H_0, and appears to affect a significant part of the cap at the physiologically relevant film thickness H_0 =0.14 µm. Figure 6.4b shows that the perturbation film thickness is roughly 180^o out-of-phase with the wall oscillation (note that the y-axis ranges from 178^o to 184^o). However, significant variation in phase is observed close to the rim. The main characteristic of this variation is that its amplitude remains roughly constant with decreasing H_0, but its length scales with H_0 and thus shrinks as $H_0 \rightarrow 0$.

The characteristics of shearing motion are investigated next. The film thickness at the rim is taken as H_0 =0.14 µm, and this will be the standard value for the rest of the study. In order to obtain a first feeling for the flow, we focus at the rim ($x = x_0$) and compare in Fig. 6.5 the temporal variation of the local perturbations in film thickness, surfactant concentration, surface velocity and volumetric flow rate to the temporal variation of the alveolar radius. Figure 6.5a shows the linear prediction, i.e. the first term in the expansions normalized by the amplitude a. It is noted that liquid film thickness and surface concentration of surfactant are 180^o out-of-phase with the wall oscillation, whereas interfacial velocity and volumetric flow rate are further 90^o out-of-phase. Thus, shearing motion at the rim attains maximum values when Γ varies the fastest and becomes zero when Γ is stationary (at the crest and the trough). Figure 6.5b demonstrates the weakly nonlinear effects by including both order a and a^2 terms. The second-order terms are evaluated with an exaggerated value $a = 0.2$ in order to make visible the differences with the linear prediction. It is noted that the oscillations of film thickness and surfactant concentration at the rim remain anti-symmetric with respect to $R(t)$, but exhibit steeper crests and flatter troughs. The surface velocity and the volumetric flow increase slightly in amplitude and steepen in time, i.e. the minimum moves forward in phase and the maximum backwards. The above behavior argues in favor of a flow mechanism that is triggered by gradients of surface concentration of surfactant between the interior and the rim. However, the amplitude of $\Gamma(x_0)$ in Fig. 6.5a —which is equal to 2 in the linear limit—implies an inverse proportionality to R^2 and thus to the interfacial area (see eq.6.36). Consequently, gradients of Γ are expected to be very small, given that the inverse dependence on surface area points to a spatially uniform concentration.

This expectation is confirmed by Fig. 6.6, which depicts the spatial variation of the harmonics of $[\Gamma(x,t) - \Gamma(1,t)]$ at four time instants during one half of a cycle. This term has been chosen so that all curves collapse at $x = 1$ (which corresponds to the apex of the spherical cap), and thus variations along x become visible. Figure 6.6 a) shows the linear prediction and fig. 6.6 b) the periodic second-order contribution. Indeed, maximum deviation amplitudes

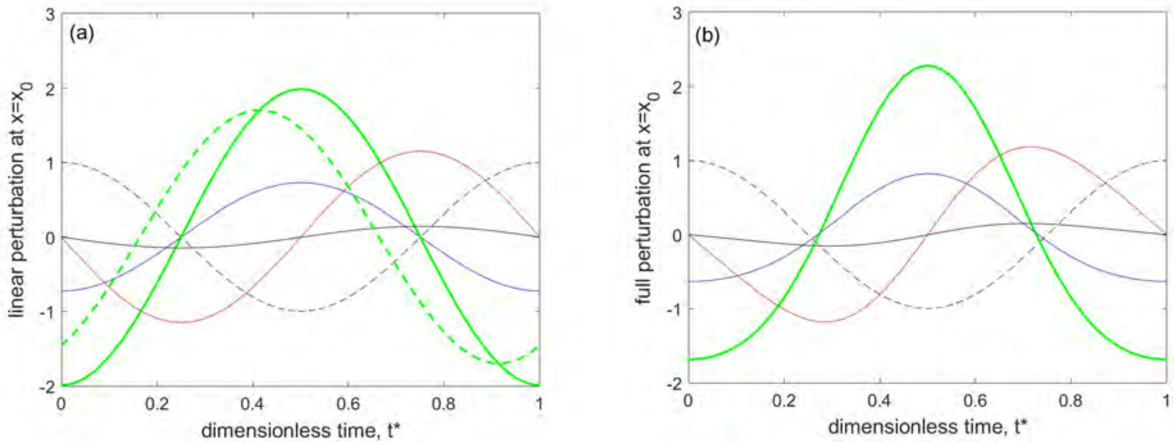

Figure 6.5: The temporal variation of the cap radius (black dashed line), compared to the temporal variation at the rim ($x = x_0$) of the perturbations in film thickness (blue), surfactant concentration (bold green), (5x)surface velocity (red) and (5x)volumetric flow rate (black). (a) The linear prediction normalized by the oscillation amplitude a. (b) Inclusion of second-order effects with $a = 0.2$. The dashed, bold, green line in figure (a) shows the temporal variation of surfactant concentration for a soluble surfactant ($k_{\text{ads}}C_{10} = 13\,\text{s}^{-1}$), to be discussed in §6.5.4.

are in the order of 10^{-5}. The spatial gradients at $x = x_0$ indicate the driving force for Marangoni flow (and exchange of surfactant) between the rim and the interior. However, the modulations of Γ observed deeper inside the cap—which lead to an oscillatory spatial gradient both at first and second-order—are puzzling, and their explanation is deferred until the next section. It is pertinent at this point to raise an argument of criticism for boundary conditions at the rim of the form Γ = constant. The present approach, which invokes a mass balance as boundary condition, indicates that Marangoni flows occur by very small gradients of Γ. In retrospect, this appears reasonable, given that Marangoni number is very large, and thus the product $Ma(\partial\Gamma/\partial x)$ generates an order-one effect. On the contrary, setting Γ = constant at the rim would create an order-one gradient $(\partial\Gamma/\partial x)$ and thus a large transfer rate of surfactant. In other words, the edge should act as a very large source of surfactant during half of the cycle and as an equally large sink during the other half. In this respect and to the best of our knowledge, a boundary condition of the form Γ = constant appears as physically questionable.

6.5.3 The velocity field and the role of capillary pressure

A closer investigation of the flow field is undertaken next. Starting with the surface velocity, the following expansion is derived. The amplitudes u_{s1}, u_{s2} and u_{sS} are given in the Appendix.

$$u_s(x,t) = a\,\mathfrak{Re}[u_{s1}e^{i2\pi t}] + a^2\left(\mathfrak{Re}[u_{s2}e^{i4\pi t}] + u_{sS}\right) \tag{6.77}$$

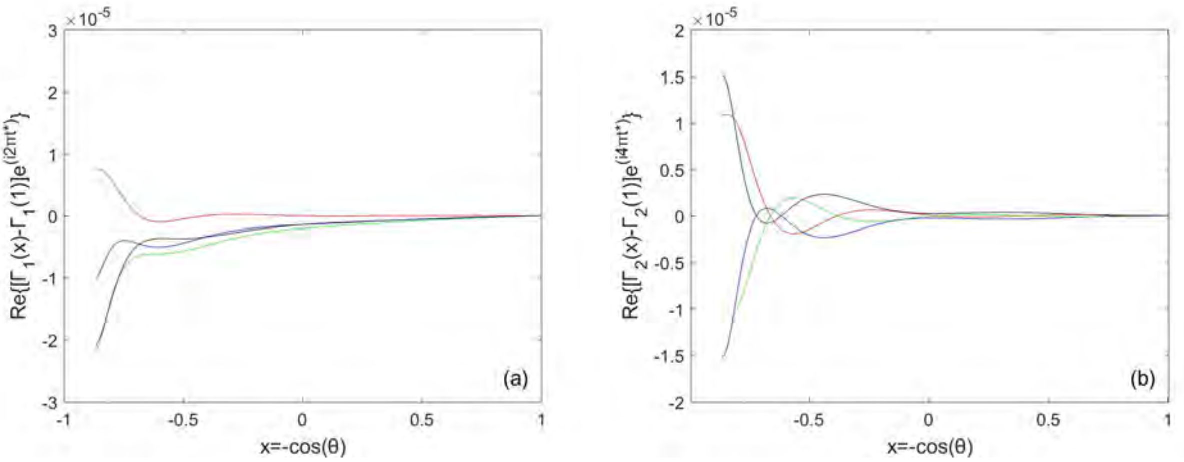

Figure 6.6: The spatial variation of the two harmonics of $[\Gamma^*(x,t^*)-\Gamma^*(1,t^*)]$ for dimensionless times t^* =0(red), 0.125(blue), 0.25(green) and 0.375(black).(a) The first-order and (b) the second-order contribution.

Figure 6.7a depicts the amplitudes u_{s1} (red), u_{s2} (blue) and u_{sS} (black line) at each location along the interface. First, it is observed that the steady term is everywhere practically zero (actually, it is of the order $O(10^{-4})$. This result is set in perspective with the findings of §6.3.4, where it was proven that the steady term of the volumetric flow rate is identically zero. However, in the case of surface velocity, the result is only approximate. It is further noted from Fig. 6.7a that the first and second-order amplitudes are highest at the rim and decrease smoothly towards the interior. However, they still remain significant for a major part of the alveolar interface. The above indicate that the interfacial velocity is roughly an order of magnitude slower than the axial velocity of the wall ($u_w = dR/dt \sim \pi$).

Setting Fig. 6.7 a) and Fig. 6.6 in perspective, it is noted that the smooth decrease of surface velocity with x is not in accord with the oscillatory spatial gradient of the surfactant concentration observed in Fig. 6.6. In order to explain this discrepancy, the capillary and the Marangoni contribution to the surface velocity (the two terms of the expression for u_{s1} in the appendix) are considered separately, and their magnitude is depicted in Fig. 6.7 b) for two time instants. It is observed that the capillary contribution induces significant tangential velocities, but these are roughly canceled by equal and opposite Marangoni contributions. Thus, a kind of inverse Marangoni flow is instantaneously established [111], which results in the smooth variation of surface velocity observed in Fig. 6.7.

The above information supports the following overall mechanism: The surface concentration of surfactant in the interior of the cap varies inversely with the periodic wall inflation and deflation, creating gradients with the concentra-

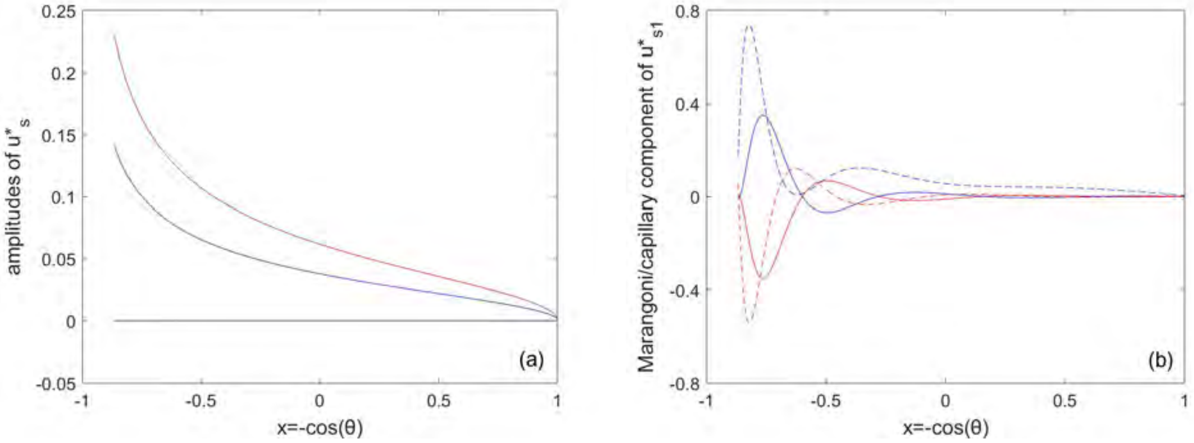

Figure 6.7: (a) The first-order (red) and second-order (blue) amplitude of u_s^* along the interface, and the steady, second-order term (black). (b) The spatial variation of the Marangoni (blue) and the capillary (red) components of $\mathfrak{Re}[u_{s1}e^{i2\pi t}]$ at dimensionless times $t^* = 0$ (continuous lines) and 0.75 (dashed lines).

tion at the rim. These gradients give rise to Marangoni flows, which lead in turn to changes in film thickness that result in variations of curvature along the film. The ensuing gradients in capillary pressure tend to drive additional flow. However, and this is the key point, $t_{elast} \ll t_{cap}$, i.e. the timescale for establishment of Marangoni flows is an order of magnitude shorter than that for the establishment of capillary flows. As a result, fine-tuning of surfactant concentration at the interface instantly cancels capillary flow on the surface. This fine-tuning of Γ manifests in the modulations observed in Fig. 6.6. Incidentally, this behavior also explains the near-zero magnitude of the steady, second-order term of the surface velocity, u_{sS}, which results from the elimination on the surface of any capillary contribution. Indeed, decreasing drastically the elasticity, leads to a non-zero distribution of steady surface velocity.

However, Marangoni (elastic) forces affect rapidly only the interface. Deeper inside the liquid layer, velocity variations are transported by the action of viscosity, and thus it is plausible that both Marangoni and capillary driving forces have an effect. A first step to interrogate this possibility is by examination of the dimensionless volumetric flow rate, Q. The amplitudes of the first and second-order contribution to Q are depicted in Fig. 6.8 as red ($|Q_1|$) and blue line ($|Q_2|$) respectively. Strong spatial oscillations in the flow rate are evident, which point to a significant contribution of capillary forces. The role of surface tension is confirmed by repeating the calculation for $\sigma = 0$ (black dashed lines), and observing that the oscillations disappear at both orders.

The distinct effect of capillary pressure on the overall flow, depicted in Fig. 6.8, is contrasted with the behavior of the surface velocity. Indeed, the

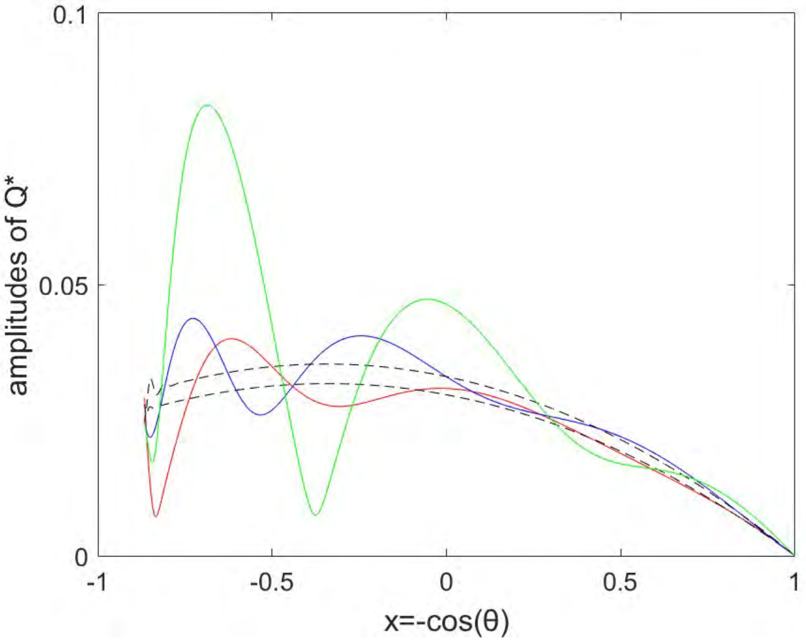

Figure 6.8: The first-order (red) and second-order (blue) amplitude of Q as function of position x. Black dashed lines show the same amplitudes for $\sigma = 0\ N/m$. The green line shows the second-order amplitude for a soluble surfactant ($k_{ads}C_{10} = 13\ \mathrm{s}^{-1}$), to be discussed in §6.5.4.

data in Fig. 6.7 remain unaffected when the standard value σ =0.023 N/m is substituted by σ =0 N/m.

The above interpretation of the interplay between elastic and capillary forces is further strengthened by quantifying the spatial lengthscale of the capillarity-induced modulations. To this end, the first-order amplitude of the volumetric flow rate, $|Q_1(x)|$, is plotted in Fig. 6.9 a) for the following values of surface tension: $\sigma = 10^{-1}$, 0.023, 10^{-2}, 10^{-3} and 10^{-4}N/m. For each curve, the $x-$values at the crest and the trough of the spatial modulation are noted, and the dimensionless capillary length, L^*, is defined as the respective arclength, $L = \bar{R}(\theta_{tr} - \theta_{cr})$, divided by the mean cap radius, $\bar{R}$, i.e. $L^* = L/\bar{R} = cos^{-1}(-x_{tr}) - cos^{-1}(-x_{cr})$. The values of L^* are plotted versus σ as circles in Fig. 6.9 b), and it is evident that the length shrinks with the decrease in surface tension. The dependence of L^* on σ may be predicted by considering the balance between capillary and viscous forces in the $\theta-$component of the Navier-Stokes equation (6.16), which leads to the following scaling [85, 86, 16]:

$$\mu\frac{\partial}{\partial r}\left(r^2\frac{\partial u_\theta}{\partial r}\right) = r\frac{\partial p}{\partial \theta} \Rightarrow \mu\frac{\bar{U}}{\bar{H}^2} \sim \sigma\frac{\bar{H}}{L^3} \Rightarrow \frac{L}{\bar{H}} \sim Ca^{-1/3} \sim \sigma^{1/3} \tag{6.78}$$

The line in Fig. 6.9b has slope 1/3, and confirms the agreement between the observed and the predicted dependence.

The aforementioned, oscillatory in x, variation of the volumetric flow rate,

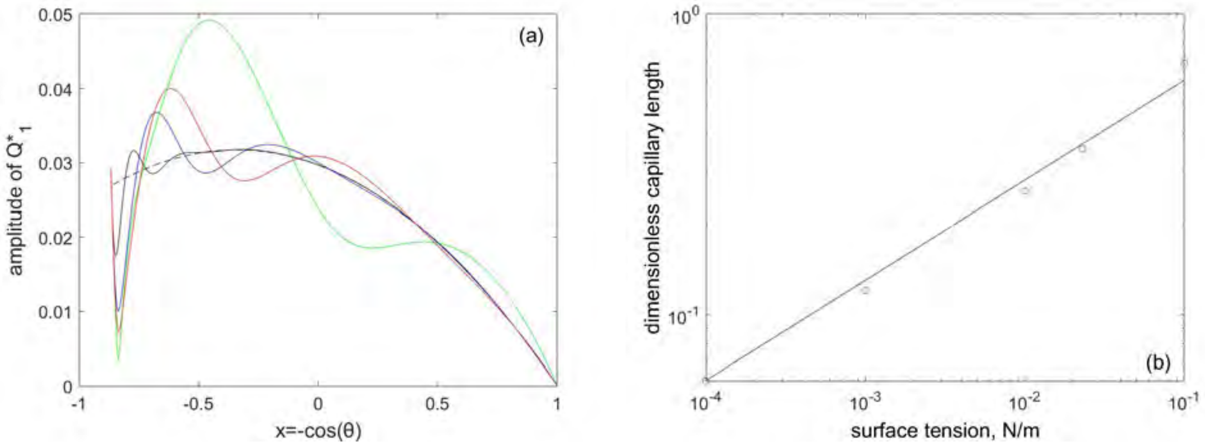

Figure 6.9: (a) The variation of $|Q_1|$ with x for surface tension $\sigma = 10^{-1}$(green), 0.023(red), 10^{-2}(blue), 10^{-3}(black) and 10^{-4}N/m (dashed black). (b) The dependence of the capillary length, L^*, on surface tension (circles) and a line of slope (1/3).

Q, indicates that velocity profiles may not be monotonic and that the shear stress on the wall and along the interface may change sign along x. In order to consider the flow field in more detail, the instantaneous tangential velocity, $u_\theta(r, x, t)$, is calculated from eq.(6.18), using the values of constants C_1 and C_2 from eqs. (6.20) and (6.21). The result in the lubrication approximation is as follows:

$$u_\theta(r, x, t) = \frac{1}{2\mu}\frac{\partial p}{\partial \theta}\frac{(R-r)^2}{R} - \frac{1}{\mu}\frac{\partial p}{\partial \theta}\frac{h}{R}(R-r) + \frac{1}{\mu}\frac{\partial \sigma}{\partial \theta}\frac{(R-r)}{R} \tag{6.79}$$

Taking the linear limit, the following expression is derived for the amplitude of velocity perturbation at first-order in terms of $\delta = (1-r)/\epsilon$, where $\delta \in [0, H]$

$$u_{\theta 1}(r, x) = \sqrt{1-x^2}\left[\frac{\epsilon^3 Ca^{-1}}{2}\delta(2H-\delta)(2h_1' + g_1') - \epsilon Ma\,\delta\,\Gamma_1'\right] \tag{6.80}$$

The shear stress at the wall is calculated in the lubrication approximation as

$$\tau_w = \mu\left[r\frac{\partial}{\partial r}\left(\frac{u_\theta}{r}\right) + \frac{1}{r}\frac{\partial u_r}{\partial \theta}\right]_{r=R} = \mu\left.\frac{\partial u_\theta}{\partial r}\right|_{r=R} = \frac{h}{R}\frac{\partial p}{\partial \theta} - \frac{1}{R}\frac{\partial \sigma}{\partial \theta} \tag{6.81}$$

and is expressed in non-dimensional form as follows,

$$\tau_w^* = \frac{\tau_w}{(\mu\bar{U}/\bar{R})} = a\,\mathfrak{Re}[\tau_{w1}\,e^{i\,2\pi t}] + a^2\,\mathfrak{Re}[\tau_{w2}\,e^{i\,4\pi t}] + \tau_{wS} \tag{6.82}$$

with the amplitudes given in the appendix.

Computations using the above expressions, offer additional information on the characteristics of the flow. The velocity distribution is considered first, which can be better visualized by a contour map. Thus, Figs. 6.10a-e on the left show iso-contours of the tangential velocity $\mathfrak{Re}[u_{\theta 1}(\delta/H, x, t)\, e^{i\,2\pi t}]$ during half of the oscillation cycle ($t = 0 - 0.5$). The $x-$axis is $x \in [x_0, 1]$ and the $y-$axis is $\delta/H = (R - r)/H \in [0, 1]$. The figures on the right are magnifications close to the rim. It is noted that the second half of the oscillation cycle is anti-symmetric with respect to the first, i.e. velocities have the same distribution but with opposite sign. Figures 6.10 a)-e), and in particular the magnifications, demonstrate that the velocity profile close to the alveolar opening involves fluid motion towards the rim at the top layer of the film and away from the rim at the bottom layer.

Next, the wall shear stress is considered, and the amplitudes are plotted in Fig. 6.11 a). It is observed that the first harmonic (red line) and the second harmonic (blue line) peak at roughly the same location, $x \approx -0.8$. It is also notable that a steady stress distribution develops at second order, which is independent of surfactant solubility, and whose magnitude is shown in Fig. 6.11a by a dashed black line. It is further observed that the total steady force by the flow on the epithelium (the integral under the dashed black line) is not zero. This should come as no surprise. What should be—and is indeed—identically zero is the total steady force on the mass of water, i.e. the sum of the force by the epithelium and the force due to Marangoni stresses along the interface.

In order to appreciate the temporal variation of the wall shear stress Fig. 6.11 b) shows the spatial distribution of order $O(a)$, $\mathfrak{Re}[\tau_{w1}\, e^{i\,2\pi t}]$, at five time instants in the first half of the oscillation cycle, $t \in [0, 0.5]$. It is observed from Fig. 6.11 b) that the wall shear stress changes direction at a point moving in time back and forth in the region $x \in [-0.8, -0.6]$. Taking into account that positive stress signifies force pointing towards the rim and negative stress force pointing away from the rim, and recalling that the first half of the cycle corresponds to exhalation, it is concluded that fluid motion close to the wall is towards this stagnation region during exhalation and away from it during inhalation.

6.5.4 The role of surfactant solubility

Results presented up to this point refer to an insoluble surfactant ($k_{\text{ads}} C_{10} = 0\,\text{s}^{-1}$). The effect of solubility will now be given some preliminary consideration by repeating the calculations for the value $k_{\text{ads}} C_{10} = 13\,\text{s}^{-1}$, which corresponds to BLES surfactant at bulk concentration $C = 0.5$ mg/ml, in contact with humid air ($RH = 100\%$) if we recall the analysis presented in the previous Chapter.

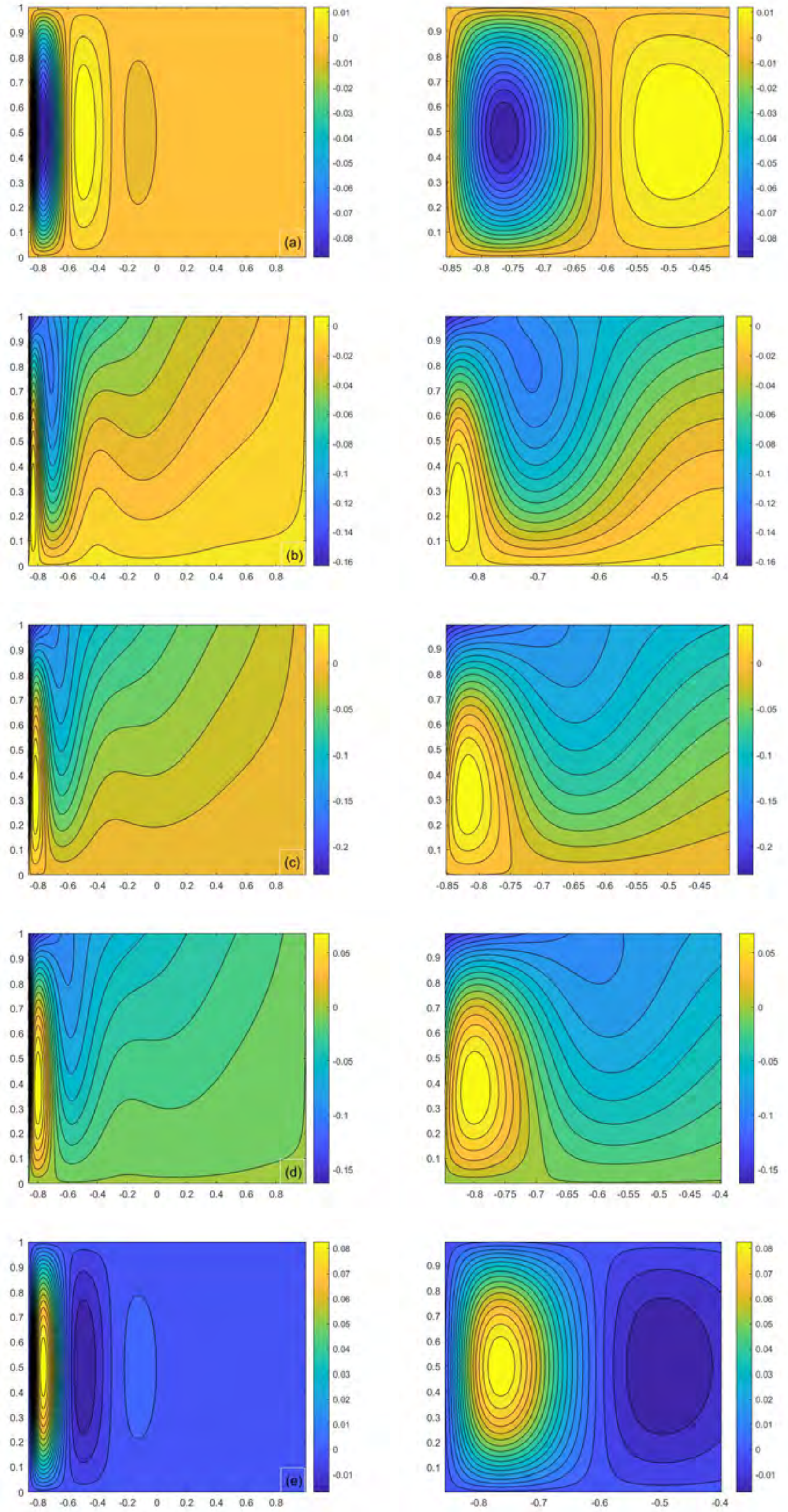

Figure 6.10: Iso-contours of tangential velocity, $\mathfrak{Re}[u_{\theta 1}(\delta/H, x, t)\, e^{i2\pi t}]$, for $t = 0$ (a), $t = 0.125$ (b), $t = 0.25$ (c), $t = 0.3755$ (d) and $t = 0.5$ (e). The $x-$axis is $x = -cos(\theta)$ and the $y-$axis δ/H. Figures on the right are magnifications of those on the left close to the rim.

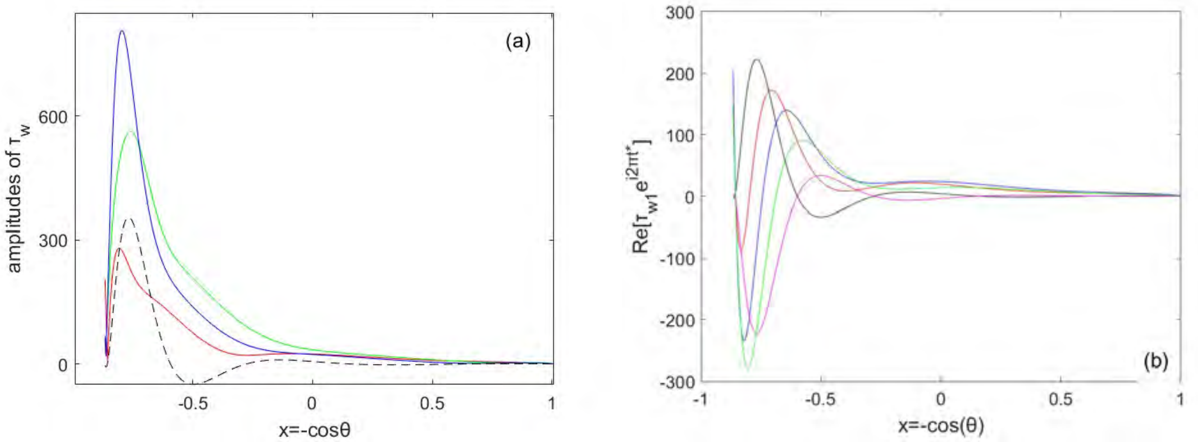

Figure 6.11: (a) The first-order (red), second-order (blue) and steady (dashed black) amplitude of the dimensionless wall shear stress. The green line shows the second-order amplitude for a soluble surfactant ($k_{\text{ads}}C_{10} = 13\,\text{s}^{-1}$), to be discussed in §6.5.4. (b) The spatial distribution of wall shear stress at first order, $\mathfrak{Re}[\tau_{w1}\, e^{i2\pi t}]$, for time t =0(black), 0.125(red), 0.25(blue), 0.375(green) and 0.5(magenta).

An important first outcome is that all variables remain unaffected *at leading order*, with the exception of $\Gamma(x,t)$. The first-order temporal variation of surfactant concentration at the rim ($\mathfrak{Re}[\Gamma_1 e^{i2\pi t}]$) is shown in Fig. 6.5 by a green dashed line, and is observed to decrease in amplitude and move forward in phase (maxima and minima occur earlier). This trend (which is representative of the behavior of surfactant concentration everywhere inside the spherical cap, given that the phase and magnitude of Γ are practically uniform in x) may be understood as follows: During alveolar contraction the surface concentration increases beyond equilibrium and surfactant is desorbed at an increasing rate. Thus, the maximum is reduced compared to the insoluble case, and it appears earlier. The opposite phenomenon occurs during alveolar expansion, when the concentration decreases below equilibrium and surfactant is increasingly adsorbed, leading again to the earlier appearance of a weaker minimum.

The first-order shift of surfactant concentration with solubility interacts with the first-order perturbation in film thickness, and changes appear in all variables at second order. In particular the second-order contribution to the volumetric flow rate increases significantly, as shown by the green line in Fig. 6.8. Also, the second-order contribution to the wall shear stress, shown by the green line in Fig. 6.11a, exhibits a decrease in magnitude and deeper penetration inside the alveolus. On the contrary, the second-order variation of the interfacial velocity is very small, and would not be visible in Fig. 6.7. Thus, it is confirmed once again that Marangoni stresses dominate the interfacial dynamics, but cannot eliminate the effect of the other forces in the interior flow.

However, the most important second-order effect of surfactant solubility is that it sets a constant drift of surfactant molecules towards the rim, because the term $Q_{\Gamma S}$ is now nonzero and negative. More specifically, it has the form $Q_{\Gamma S}(x) = Q_{\Gamma S0}(1-x)/(1-x_0)$ where $Q_{\Gamma S0} < 0$ is the flow rate of surfactant leaving the alveolus. In particular, for $k_{\mathrm{ads}}C_{10} = 13\ \mathrm{s}^{-1}$, $Q_{\Gamma S0} = -0.051$. This result stems from the addition of surfactant flux along the entire circumference, starting from zero at the apex and gradually increasing towards the rim. The linear form is a result of the surface concentration being spatially uniform (according to Fig. 6.6, gradients are of the order 10^{-5}), rendering gradual contributions proportional to the local alveolus surface area.

It is stressed that the interfacial flux of surfactant is not a result of mean surface flow (the steady component, $a^2 u_{sS}(x)$, of u is always identically zero). It is rather an effect of the shift in phase of the temporal variation of Γ, which results in a nonzero mean of the product $u\Gamma$. This may become evident by a closer look at Fig. 6.5, which indicates that the above product is identically zero for the insoluble surfactant (continuous green and red lines) and negative for the soluble surfactant (dashed green and continuous red line).

6.5.5 Physiological implications

Having acquired a satisfactory understanding of the flow field inside the liquid layer lining the alveolus, we speculate on the potential role of this flow field in various physiological processes. The possibility of modification of the airflow pattern inside the alveolus is considered first. Computations neglecting the liquid layer (i.e. setting zero air velocity on the wall) have predicted the occurrence of chaotic mixing, as a result of the coupling of axial flow due to expansion/contraction with recirculation due to shear imposed by the airflow in the alveolar duct [170, 169, 71]. Strong recirculation is essential to this mechanism, and as a result chaotic mixing is predicted to occur in the proximal alveolated generations.

It is recalled from Fig. 6.7 that the interfacial velocity of the liquid layer is symmetric around the axis of the alveolus and is directed towards the interior during inhalation and towards the alveolar opening during exhalation. Its dimensional amplitude, as estimated by linear theory, is $u_s \approx 0.25a(\bar{R}/\mathrm{T})$. Thus it is 25 times slower than the radial velocity of the wall, which has amplitude $2\pi a(\bar{R}/\mathrm{T})$ and is characteristic of the airflow entering the alveolus during inhalation. As demonstrated by the original simulations [170], the air enters from the distal end of the alveolar opening and drives the recirculation eddy that is displaced towards the proximal end of the opening.

Thus, during inhalation, the direction of air recirculation close to the rim, predicted with the neglect of the liquid film, is opposite to the local direction of interfacial flow of the liquid layer, predicted with the neglect of air flow. The two views may be reconciled by considering that the viscosity of air is much lower than that of the liquid. As a result, (i) shear by the airflow will change very little the presently predicted flow field in the liquid, and (ii) the true interfacial velocity of air will be roughly equal to the liquid velocity presently computed neglecting airflow. It is concluded from the above that the liquid layer may modify significantly the pattern of air flow, and the air/liquid interaction deserves further consideration.

A second issue involves the deposition of particles inside the alveolus and in particular the potential role of the liquid layer dynamics on their spatial distribution. As it has been repeatedly observed and predicted [194, 100, 61, 171], particles deposit preferentially close to the alveolar entrance rings. It is accepted that the airflow determines the initial deposition trend, because the particle-laden air stream passes first very close to the proximal tip of the alveolar opening, before entering the alveolus from the distal end of the opening [71]. However, the fate of particles that touch the liquid layer will also be influenced by liquid flow dynamics. In particular, the presently predicted formation of a stagnation region at $x \in (-0.8, -0.6)$ i.e. at $10^o - 20^o$ radial distance from the opening, where the wall shear changes direction, may have a contribution in the accumulation of deposited particles close to the opening.

More generally, hydrophobic nanoparticles will be affected mostly by the surface velocity, and thus will be sucked towards the interior during alveolar inflation (see Fig. 6.7). On the other hand, hydrophilic nanoparticles will enter more easily the liquid layer, and will experience the entire flow field. Macromolecules secreted from the epithelium and cell-cell signaling molecules with be predominantly influenced by the wall shear stress. Larger particles, with aerodynamic diameter of a few μm, will be only partly immersed in the liquid layer, but their dissolution rate (a critical parameter for pharmaceutical applications) will be affected by the liquid flow field.

Another consideration concerns the predicted magnitude of shear stress imposed on the alveolar wall by the liquid flow. According to physiology findings [144, 158, 53], long-term exposure of alveolar epithelial cells to excessive shear stress can cause damage by deforming the cytoskeleton (the network of protein filaments and microtubules that maintains cell shape and intracellular organization) and also by triggering the production of inflammatory mediators. An indicative threshold for the onset of shear stress-inflicted damage is $\tau_{w,max} = 1.5\,\mathrm{Pa}$ (Chen et al. 2015 [29]). In order to obtain order-of-magnitude estimates from the present study, the value of the linearization parameter is set equal to $a = 0.1$. Then, maximum shear stress is predicted as $\tau_w \approx 300a(\mu/\mathrm{T}) \approx 0.007\,\mathrm{Pa}$, a value two orders of magnitude lower than the threshold for damage, which is a reasonable safety margin for a healthy lung.

A rough estimate for conditions in a diseased lung (due for example to bronchitis, bronchial asthma or cystic fibrosis) may be provided by taking the viscosity of the liquid layer as two orders of magnitude higher than normal [29]. Maximum shear stress computed under these conditions is $\tau_w \approx 200a(\mu/\mathrm{T}) \approx 0.45\,\mathrm{Pa}$. This value, which is of the same order as the threshold limit, is applied repeatedly during each breathing cycle. Thus, the possibility of damage by a cumulative effect seems plausible. It is also notable that the predicted location of damage, i.e. close to the alveolar inlet, is consistent with pulmonary emphysema, a condition characterized by abnormal, permanent enlargement of air spaces distal to the terminal bronchioles, resulting from the gradual destruction of intra-alveolar walls [95].

Last but not least, the predicted constant drift of surfactant from the alveolus is of particular interest, in relation to recent techniques for probing exhaled air for micro-droplets originating from distal lung areas [157]. It has been hypothesized that these droplets form during reopening of the small airways, after their closure at exhalation down to residual volume [5, 57]. Airway lining fluid is known to contain surfactant molecules, whose analysis indicates that they most probably originate from the alveoli, where they are actually produced [13]. Thus, the presently predicted drift provides a new mechanism for transport of surfactant from the alveoli to the airways.

6.6 Concluding Remarks

An oscillating spherical cap, lined internally with a surfactant-laden liquid film, is considered as a model of the dynamics of a single alveolus. The flow in the liquid film is analyzed in the quasi-steady Stokes limit by a lubrication approximation, and the free-surface boundary conditions are imposed on the interface. The problem is studied by weakly nonlinear analysis around the equilibrium conditions in a non-oscillating cap. In the case of soluble surfactant, the adsorption to the liquid-air interface is assumed to be kinetically limited, and is described according to Langmuir kinetics, modified by the inclusion of the intrinsic compressibility of the adsorbed monolayer. This modification is significant for dense monolayers and was shown to model successfully the behavior of actual lung surfactants [20].

It is argued that the boundary conditions imposed at the rim of the spherical cap are critical for correct modeling, as the flow and transport phenomena are actually driven by gradients between the rim and the interior of the alveolus. A novel boundary condition is presently applied, which enforces mass conservation of water and surfactant over the alveolar rim. The validity of this condition rests on the assumptions that (i) the liquid film is continuous over the rim and has a finite equilibrium thickness, (ii) the film thickness and surfactant concentration over the rim are spatially uniform and vary only in time and (iii) the dynamics of the rim is enslaved to that of the alveolus. These assumptions are presently reconsidered in the light of the findings of the study and are further supported by recent experimental findings and scaling arguments.

The existence of a continuous liquid layer over the sharp rim with a rather high equilibrium thickness, $H_0 = 0.14\ \mu m$, is supported by the data of [11], but merits further discussion, given that a stagnant film is expected to drain away from a sharp rim due to capillarity. Therefore the continuity of the liquid layer may only be understood as the result of the action of repulsive disjoining pressure. Though disjoining pressure probably determines H_0, its role in the dynamics may be safely neglected, because its characteristic timescale is very small, even compared to the breathing frequency [126, 63].

Equilibrium films resulting from the action of repulsive disjoining pressure are typically thinner, i.e. in the order of nanometers or few tens of nanometers. However, things may be different for the pulmonary surfactant because of the existence of aggregates dispersed in the interior of the film. It is recalled that, as the pulmonary surfactant is practically insoluble, its excess resides in the bulk in the form of vesicles-aggregates [199, 25]. Thus, the electrostatic and/or steric interactions that create the repulsive forces are not only between the substrate and the surface layer but also between these two surfaces and the vesicles trapped in-between.

The above view is supported by the recent experiment of Xu et al [189], who investigated by atomic-force microscopy (AFM) in situ Langmuir-Blodgett films of pulmonary surfactant preparations, i.e. structures trapped on a mica substrate moved from the interior of the liquid towards the interface. Though intended for a different purpose, this experiment mimics the creation of an equilibrium film because it forces a substrate against the adsorbed layer. The AFM images showed protrusions of height $100 - 120$ nm, which were attributed to trapped aggregates. When the sub-surface aggregates were removed (by repeated replacement-washing of the sub-surface liquid volume), the protrusions were in the range $20 - 30\,$nm, attributed to the adsorbed layer. These data support an equilibrium film thickness in the range $100 - 150$ nm, in striking agreement with the estimate extracted from the measurements of [11].

The second assumption in the derivation of the boundary conditions at the alveolar opening is that the film thickness and surfactant concentration are spatially uniform over the rim and only vary in time. This is justified by considering that the fluxes leaving the alveolus and entering the rim are matched, and therefore the gradients $(\partial h/\partial x)_{rim}$, $(\partial h/\partial x)_{alv}$ and $(\partial \Gamma/\partial x)_{rim}$, $(\partial \Gamma/\partial x)_{alv}$ are of the same order. However, $(\partial/\partial x)_{rim} \sim \Delta_{rim}/r_0$ and $(\partial/\partial x)_{alv} \sim \Delta_{alv}/R$. Thus the variation of film thickness and surface concentration over the rim scales as r_0/R with the variation in the alveolus, and may be neglected in the limit $r_0 \ll R$.

The last—and probably most critical—assumption in the derivation of the boundary conditions is that the dynamics of the rim is enslaved to that of the alveolus. To confirm this assumption, it is necessary to estimate the characteristic time of reaction of the film covering the rim, when disturbed from equilibrium, and to compare this to the timescale of the fastest process driving the flow. Our investigation demonstrated that the periodic wall oscillation leads to an inverse variation of surfactant concentration inside the alveolus, and thus creates gradients with the concentration at the rim. These gradients give rise to Marangoni stresses that drive the flows. The characteristic time for establishment of flow due to Marangoni forcing was previously estimated in eq.(6.43) as $t_{elast} = \mu \bar{R}/E_{\mathrm{eq}} \approx 5 \times 10^{-7}\,\mathrm{s}$.

The characteristic response time to disturbances of the liquid film over the rim may be estimated by adopting an expression for the disjoining pressure. Using $\Phi(h_0) = A/(6\pi h_0^3)$ [126], and taking advantage of the equilibrium condition with the capillary pressure, $A/(6\pi H_0^3) = \sigma/(r_0 + H_0)$, leads to the estimate

$$t_{drain} = \frac{\mu \pi^2 (r_0 + H_0)}{8\sigma} \left(\frac{r_0}{H_0}\right)^2 \approx 5 \times 10^{-4}\,\mathrm{s} \tag{6.83}$$

It is concluded that Marangoni forcing is three orders of magnitude faster that capillary drainage, rendering the latter insignificant and enslaving the dynamics of the rim to the dynamics of the alveolar oscillation.

Continuing with the results of the study, it is recalled that a key finding is the relation between the intensity of shearing motion in the liquid layer and the thickness H_0 of the film over the rim of the alveolar opening. In particular, the amplitude of the interfacial velocity decreases monotonically from a maximum at the rim to zero at the symmetry axis, and, for the physiologically relevant value $H_0 \approx 0.14\,\mu\mathrm{m}$, is roughly an order-of-magnitude lower than the amplitude of the wall motion in the radial direction.

A complex interplay between Marangoni and capillary stresses is revealed. The former dominate the interfacial dynamics, but the latter may not be neglected, because they affect significantly the interior flow field. As a result of capillary stresses, spatial modulations appear in the surface concentration of surfactant, the volumetric flow rate of the film and the wall shear stress. The lengthscale of these modulations varies with $Ca^{-1/3}$, and is predicted by a balance of capillary and viscous forces. Adsorption kinetic effects of soluble surfactants are shown to modify the amplitude and phase of surface concentration Γ at first order, and to affect the other variables at second order. Most important, a constant drift of surfactant towards the rim is predicted at second-order.

It is speculated that the above behavior of flow variables is potentially of significance to physiological processes. In particular, the interfacial liquid velocity may modify the air recirculation inside the alveolus, and the spatially non-uniform flow field inside the liquid layer may affect the preferential deposition of inhaled particles. Also, the maximum values of wall shear stress predicted for a healthy and a diseased lung appear reasonable when compared to the experimentally determined stress levels that inflict damage to epithelial cells. Finally, the predicted drift of surfactant towards the rim provides a mechanism for the observed appearance of alveolar surfactant along the small airways.

The preliminary results for nonzero adsorption kinetics highlight the importance of nonlinear coupling between flow dynamics and surfactant solubility. In this respect, it is interesting to recall from the literature [107, 99, 152, 104] that, at large compressions—representative of physiological conditions during deep exhalation—the surfactant monolayer collapses forming protrusions that extend in various directions, while surface tension remains constant at a minimum value $\sigma \approx 0.002 - 0.010\,\mathrm{N/m}$. These protrusions are continuous with the interfacial layer and act as reservoirs for rapid replenishment of the monolayer during re-expansion. The behavior of an alveolus under such conditions is evidently beyond the power of the present, weakly nonlinear approach, and calls for a numerical solution of the fully nonlinear problem.

Chapter 7

Parametric analysis and physiological/pathophysiological implications

The last chapter of this dissertation is concerned with deriving possible physiological and pathophysiological implications based on the linear and weakly-nonlinear analysis presented in Chapter 6. Before moving on with the analysis, it is important to support the physiological validity of the expansion utilized in Chapter 6. As already stated, the analysis preceding this Chapter assumes small variations of the alveolar radius $R(t)$ around the equilibrium configuration where $\bar{R} = 100\,\mu\text{m}$, a typical value for an alveolus deep in the lungs [166].

According to [166], in the acinar region where alveoli are located, the conducting airways are mainly static for conditions of quiet breathing and the physiological linear wall strains in the acinus lie between $\epsilon_l = 4 - 10\%$, or equivalently, the lung volumes expands 15-20%. At the same time, it is generally accepted that self-similarity dictates the motion of lungs [169, 166], the volume of which scales as $\mathcal{V} \sim l^3$ where l is an arbitrary characteristic length scale of the lung; it can even denote an alveolar dimension [166]. Thus we set $l = \bar{R}$ and $\bar{R}$ is the alveolar radius of the undisturbed shell or the equilibrium configuration.

The linear wall strain for an alveolus is simply defined as [145]

$$\epsilon_l = (l_f - l_o)/l_o \tag{7.1}$$

where ϵ_l is used to denote the strain. The latter is commonly symbolized as ϵ is Solid Mechanics, so we will henceforth denote it with the subscript l to avoid any confusion with the Lubrication parameter used in Chapter 6. l_o and l_f represent the initial and final length scales mentioned in [166], thus they represent initial and final alveolar radii. According to eq.(6.46), the maximum stretching rate is

$$\epsilon_l = \left(\bar{R}(1 + a\,\mathfrak{Re}[e^{i\,2\pi t}]_{max}) - \bar{R}\right)/\bar{R} = a \tag{7.2}$$

Assuming conditions of tidal breathing[1], the maximum expansion of lung reveals that any acinar length scale is maximally expanded by 5.3 % over one inspiration phase, corresponding to 16.7 % expansion of the lung volume [165]. Taking as $\epsilon_l \sim a$, it may be safely assumed that the weakly nonlinear analysis will provide qualitatively valid predictions up to $a \sim 0.1$, i.e. for quiet and intermediate breathing. However, during increased physical activity or specific diseased conditions under which lung compliance is significantly decreased [166], $\epsilon_l \sim 15 - 20$ % and fully nonlinear analysis may be necessary.

7.1 Geometrical parameters

We first investigate the effect of the geometrical parameters of the model alveolus, in particular the opening angle θ_0, the alveolar radius at equilibrium, $\bar{R}$ and the radius of curvature of the rim. r_0. Accordingly, we assume the properties of the surfactant to be unchanged and we alter only these geometrical parameters. Thus we utilize $\sigma_{\mathrm{eq}} = 23\ \mathrm{mN\,m^{-1}}$, $\alpha = 0.0052\ \mathrm{m\,mN^{-1}}$, unless otherwise stated.

Larger opening angles, θ_0, represent a seriously deceased condition, called emphysema. In emphysema, the alveolar septum is progressively lost and, as a result, a collection of small and highly compliant volumes representing a group of alveoli is gradually replaced by a larger and bulkier cavity with reduced alveolar-capillary exchange area [117]. The first-order effect of the opening angle predicted by our model is indicated in Fig. 7.1. A strong increase in the amplitude of the dimensionless wall shear stress is noted, which is three times the normal value when the alveolus becomes really shallow ($\theta_o = 120^o$). This prediction indicates that the destruction of the alveolar septum may be a self-accelerated process, i.e. affected alveoli experience higher wall shear stress values that increase the rate of destruction of the epithelial wall.

Another result that points in the same direction is depicted in Fig.7.2, which shows the variation in the amplitude of wall shear stress with increasing thickness of the alveolar rim. Note that the figure is an amplification close to the inlet, and indicates that, for thick rims, a steep maximum occurs right at the inlet. The thickness of the rim may increase as a result of local injury of the alveolar opening that leads to substitution of epithelial septum by fibrus flesh. Thus, an intensification of the wall shear stress at the opening is predicted to

---

[1] A typical lung volume at FRC is $V_{\mathrm{FRC}} = 3000$ mL and the volume intake during tidal breathing is $V_T = 500$ mL

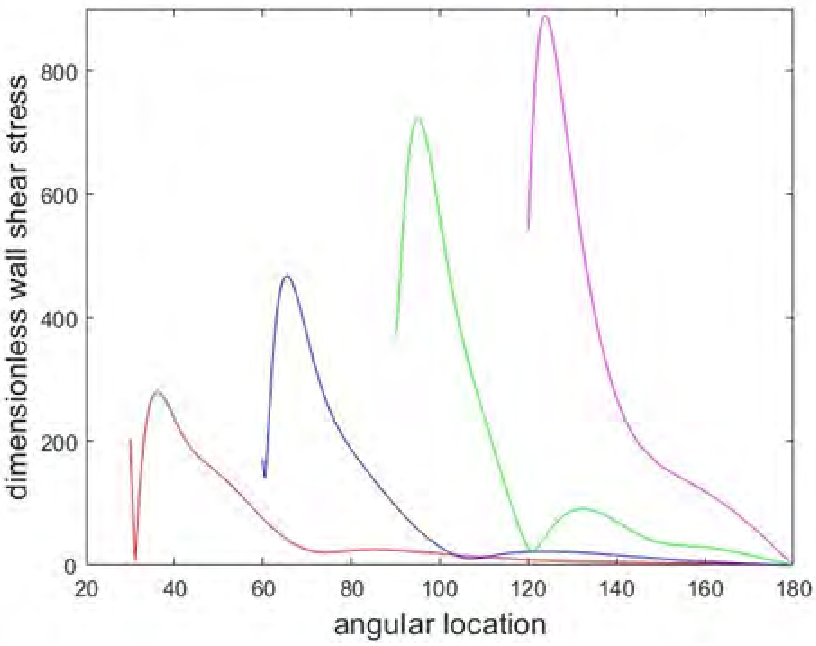

Figure 7.1: The dimensionless wall shear stress for alveolar opening angle $\theta_0 = 30^o$ (red), $\theta_0 = 60^o$ (blue), $\theta_0 = 90^o$ (green) and $\theta_0 = 120^o$ (purple).

occur during the onset of emphysematic degradation, exactly at the location where the degradation occurs.

The above predictions may be questioned when considering the developing lung of a newborn infant. Premature alveoli are smaller and with thinner septa, but are also very shallow and grow in size and depth during development [75, 74]. Thus, the above result for shallow alveoli could potentially indicate an increased wall shear stress, something that evidently does not occur as it would be detrimental for the delicate infant epithelium.

In order to test correctly the predictions of the model for an infant lung, we consider the effect of alveolar radius, $\bar{R}$, by keeping constant the ratio $r_0/\bar{R}$, thus modeling the gradual increase of alveolar size and septal thickness. The result is shown in Fig. 7.3 for two opening angles $\theta_0 = 30^o$ (continuous lines) and 90^o (dashed lines). Note that the result for $\bar{R} = 100$ μm and $\theta_0 = 90^o$, which is not depicted as it is contained in Fig. 7.1, indicates the drastic increase of wall shear stress previously discussed. However, the new –and very interesting– result is that, for smaller alveoli with thinner septa, $\bar{R} = 12.5$ and 25 μm, there is no significant increase in wall shear stress. Thus, the model correctly predicts that the premature alveoli are not subject to excessive wall shear stress.

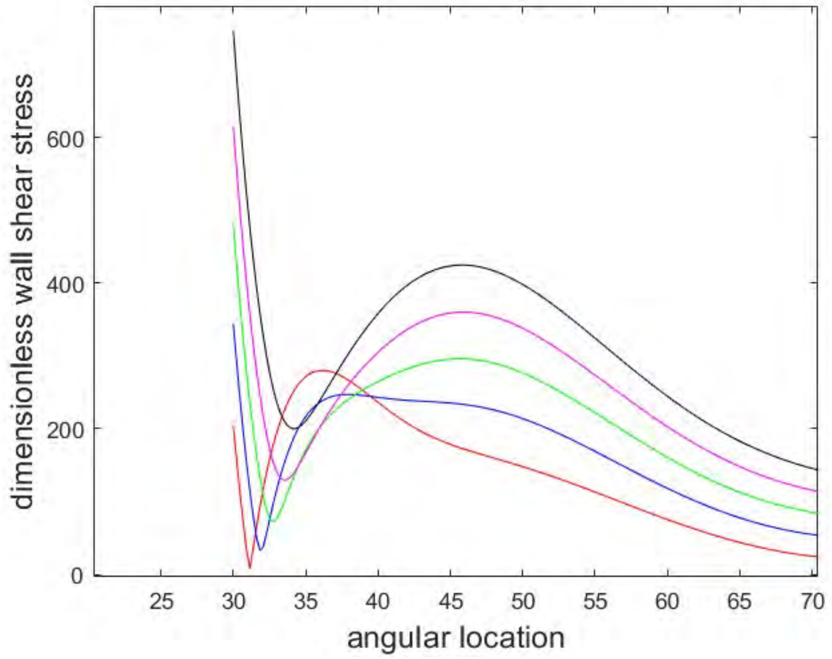

Figure 7.2: The dimensionless wall shear stress for alveolar opening angle $\theta_0 = 30^o$ and increasing thickness of the alveolar rim r_0 =2 (red), 4 (blue), 6 (green), 8 (purple) and 10 µm (black).

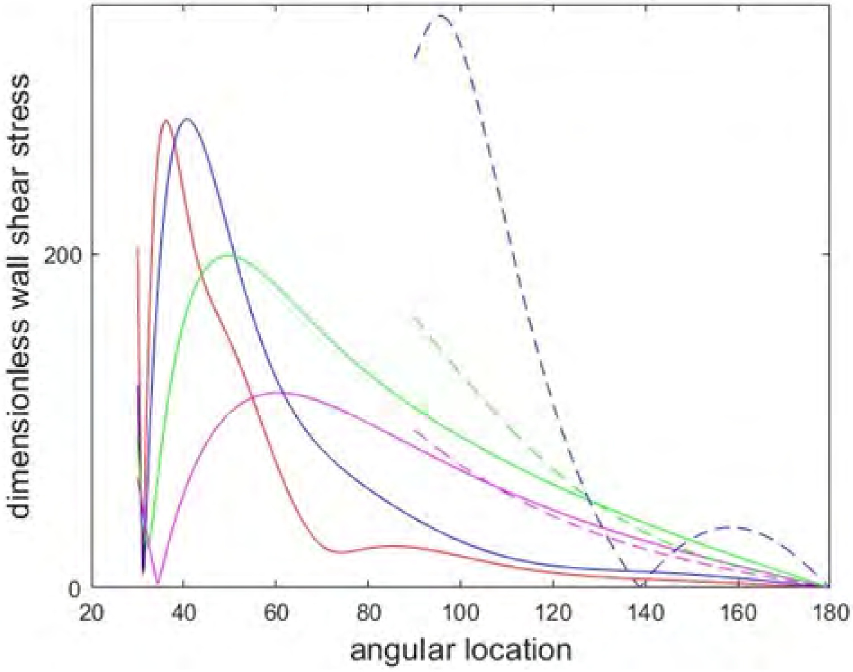

Figure 7.3: The dimensionless wall shear stress for constant ratio $r_0/\bar{R}$ and $\bar{R}$ = 100, 50, 25 and 12.5 µm. Continuous lines represent $\theta_0 = 30^o$ and dashed for $\theta_0 = 90^o$, respectively.

7.2 Effect of surfactant properties

The effect of the surface diffusion coefficient is addressed by plotting the magnitude of the volumetric flow rate at 1st and 2nd order along the periphery. Typical values of $\mathcal{D}_s$ are in the range $10^{-10} - 10^{-9}\mathrm{m}^2\,\mathrm{s}^{-1}$ [114] thus we choose the broader range of $10^{-11} - 10^{-8}\mathrm{m}^2\,\mathrm{s}^{-1}$. Fig.7.4 reveals a zero effect of $\mathcal{D}_s$ on Q as all curves collapse into a single curve, illustrated by black color. The outcome should not be considered a surprise since the corresponding Pe_s is $0.33 - 333$ implying the dominance of surface convective over diffusive transport. Since the flow rate depends on the flowfield of the subphase, no effect on the velocity field of the inner layer is anticipated.

Besides, we choose the exaggerated value of 10^{-3} as a reference case with the corresponding results depicted by orange color. Only in the reference case, an important change in Q at every order is observed where $Pe_s = O(10^{-6})$, however, its value is unphysically high. Nonetheless, the maximum flowrate addressed at 1st order is ≈ 0.04 for $10^{-11} - 10^{-8}$ $\mathrm{m}^2\,\mathrm{s}^{-1}$. Increasing $\mathcal{D}_s$ by five orders of magnitude shows a maximum flowrate of ≈ 0.07 thus the order of magnitude pertaining to $|Q_1|$ is the same. The correction at second order (dashed lines) conserves this trend where the maximum of $|Q_2|$ is almost twice the value 10^{-8} $\mathrm{m}^2\,\mathrm{s}^{-1}$. Thus, no effect of varying $\mathcal{D}_s$ in the physiological range of PS is anticipated.

Continuing with surfactant properties, the distinct effect of solubility on the volumetric flowrate, Q and the rate of surfactant flow, Q_Γ, is set into perspective. We examine a set of $k_{\mathrm{ads}}C_{10}$ values corresponding to increasing bulk concentrations, C, mainly adapted from the fitting procedure in Chapter 5 and the parameter set in Table 5.1. Though the values of $k_{\mathrm{ads}}C_{10}$ in Table 5.1 concern different values of the 2D surface compressibility, α, the latter was found to be ~ 0.005 $\mathrm{m\,mN}^{-1}$, thus due to small differences we keep $\alpha = 5.2$ $\mathrm{m\,N}^{-1}$ (0.0052 $\mathrm{m\,mN}^{-1}$) as utilized in Chapter 6. The resultant effect is depicted in Fig.7.5 where the temporal variation of the volumetric flowrate at the edge of the alveolus at 1st (solid lines) and 2nd (dashed lines) order is plotted against time. The insoluble case, $k_{\mathrm{ads}}C_{10} = 0$, is depicted as well (red color) for comparison. As shown by the analysis in the previous Chapter, increasing $k_{\mathrm{ads}}C_{10}$ does not affect the flow rate and $Q_1(x_0, t)$ is the same for every value of the adsorption rate, depicted by black solid curves. At 2nd order, little difference is observed in amplitude between $k_{\mathrm{ads}}C_{10} = 13$ s^{-1} and the insoluble case (red dashed). As we further increase the bulk concentration by setting $k_{\mathrm{ads}}C_{10} = 22$ and 35 s^{-1} an increase in the oscillation amplitude is evident. This observation points toward an increased liquid flow rate at the rim. Also, in order to obtain a

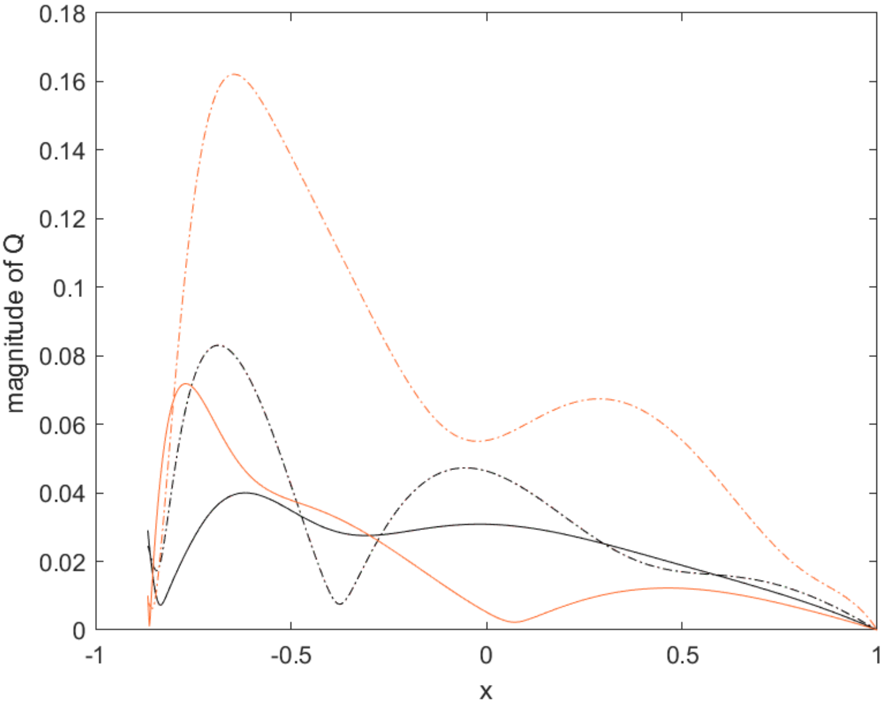

Figure 7.4: Magnitude of Q at 1st (continuous lines) and 2nd (dashed-dotted lines) order. The range of $10^{-11} - 10^{-8}$ $\mathrm{m^2\,s^{-1}}$ is represented by the black curves only. Orange colours represents the $\mathcal{D}_s = 10^{-3}$ $\mathrm{m^2\,s^{-1}}$ case.

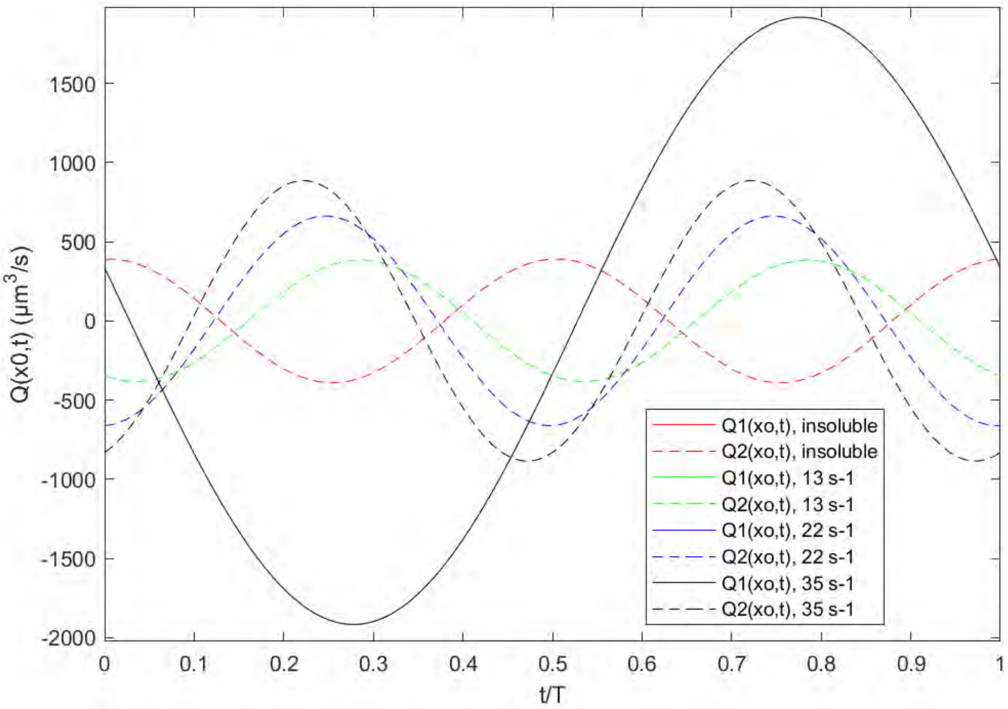

Figure 7.5: Effect of the adsorption rate, $k_{ads}C_{10}$, on the flowrate exactly at the rim, $Q(x_0, t)$. Negative values correspond to outflow.

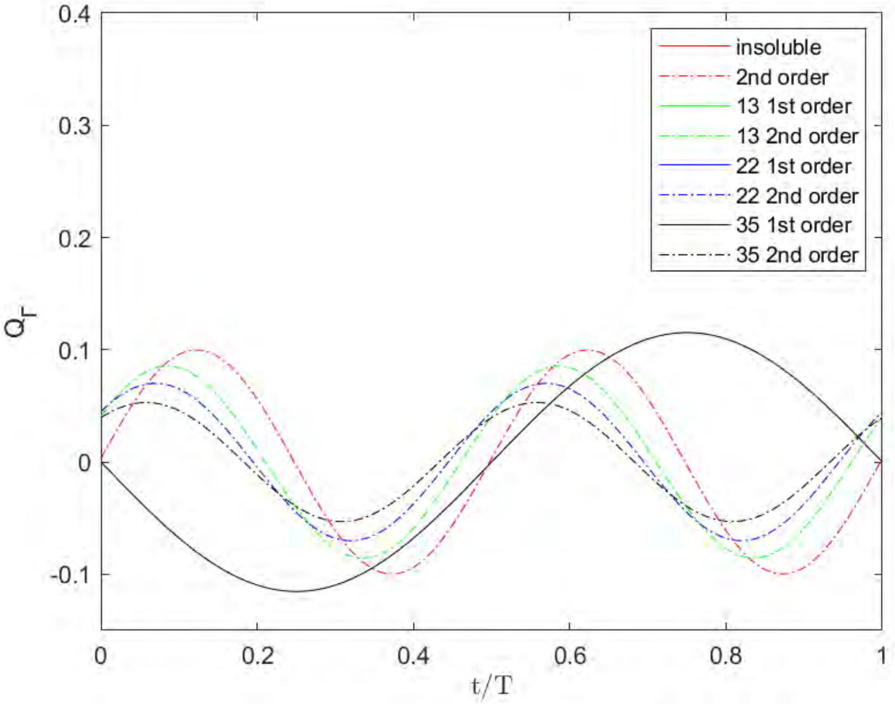

Figure 7.6: Effect of the adsorption rate, $k_{\mathrm{ads}}C_{10}$, on the surfactant flowrate exactly at the rim, $Q_\Gamma(x_0,t)$. Negative values correspond to surfactant drift away from the alveolus.

quantitative insight into the flow rate at x_0, the latter is plotted in dimensional form by multiplying it with $\bar{R}^3/\mathrm{T}$. The characteristic values at 1st order are $\sim 10^3$ $\mu\mathrm{m}^3\,\mathrm{s}^{-1}$ and choosing $a = 0.1$ for the expansion parameter we obtain $aQ_1(x_0,t) \sim 100$ $\mu\mathrm{m}^3\,\mathrm{s}^{-1}$. For comparison, we address the work of Gradon and Podgorski in [139]. These authors examined the flowrate at the alveolus edge, predicting an oscillatory flowrate with a maximum lying between $10^3 - 2.10^3$ $\mu\mathrm{m}^3\,\mathrm{s}^{-1}$ and thus our model provides a reasonable estimation of the net flow of liquid at the rim.

In conjunction with the liquid flow rate, the surfactant flow rate at $x = x_0$ is plotted against time in Fig. (7.6). It is observed that at 2nd order the amplitude of the surfactant mass rate gradually decreases with $k_{\mathrm{ads}}C_{10}$. The effect of solubility on steady streaming is set into perspective next by plotting $Q_{\Gamma S}$ against x, as seen in Fig. 7.7. The weakly nonlinear analysis in Chapter 6 showed that steady streaming induces a constant drift of surfactant away from the alveolus in the soluble case. Increasing $k_{\mathrm{ads}}C_{10}$ reveals a maximum $Q_{\Gamma S}(x_0)$ is obtained for $k_{\mathrm{ads}}C_{10} = 22$ s^{-1} corresponding to bulk concentration of $C = 1$ $\mathrm{mg\,ml}^{-1}$ of BLES surfactant. Further increase of $k_{\mathrm{ads}}C_{10}$ reduces $Q_{\Gamma S}(x_0)$ and the latter may become lower (in absolute value) than the initially examined case of $k_{\mathrm{ads}}C_{10} = 13$ s^{-1}.

In the acinar region, alveoli are organized in a densely packed fashion, as

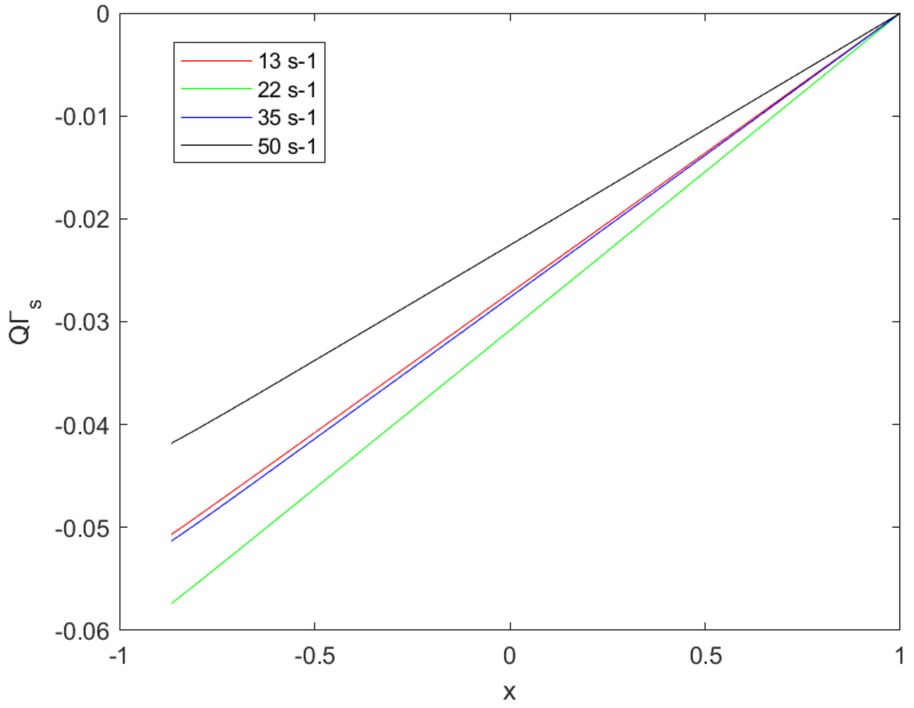

Figure 7.7: Surfactant flowrate owing to steady streaming, $Q_{\Gamma S}(x)$ vs x for different values of the adsorption rate, $k_{ads}C_{10}$.

can be seen by recalling Fig.2.2. Thus, a single alveolus communicates with adjacent alveoli via transfer of liquid and surfactant across the rim. The results above may provide indications about enhanced pulmonary drug delivery in the form of surfactants and optimal delivery in the terminal part of the acinar region by identifying mechanisms that contribute to increased Q, Q_Γ at the rim.

7.3 Effect of viscosity

As stated, in the case of a diseased lung, the pulmonary fluid tends to become more viscous. An example is Cystic Fibrosis, an obstructive lung disease, in which airway mucus becomes dehydrated and viscous and, as a result, cannot be cleared effectively paving the way for bacterial infection [162]. In such cases, the dynamic viscosity, μ, of the liquid layer can be two orders of magnitude higher than normal [29]. Motivated by this fact, we plot the volumetric flowrate along the periphery of the alveolus starting from the standard value of 0.00069 $\mathrm{kg\,m^{-1}\,s^{-1}}$ and increasing by a factor of 100. The results, shown in Fig.7.8, clearly depict a strong decrease of Q at every order. Specifically, focusing on the 1st order approximation, reveals a maximum Q_1 which is roughly 0.02; increasing μ up to 69 cP decreases the maximum slightly below 0.005 which is an order of magnitude decrease. From the physiological point of view, this

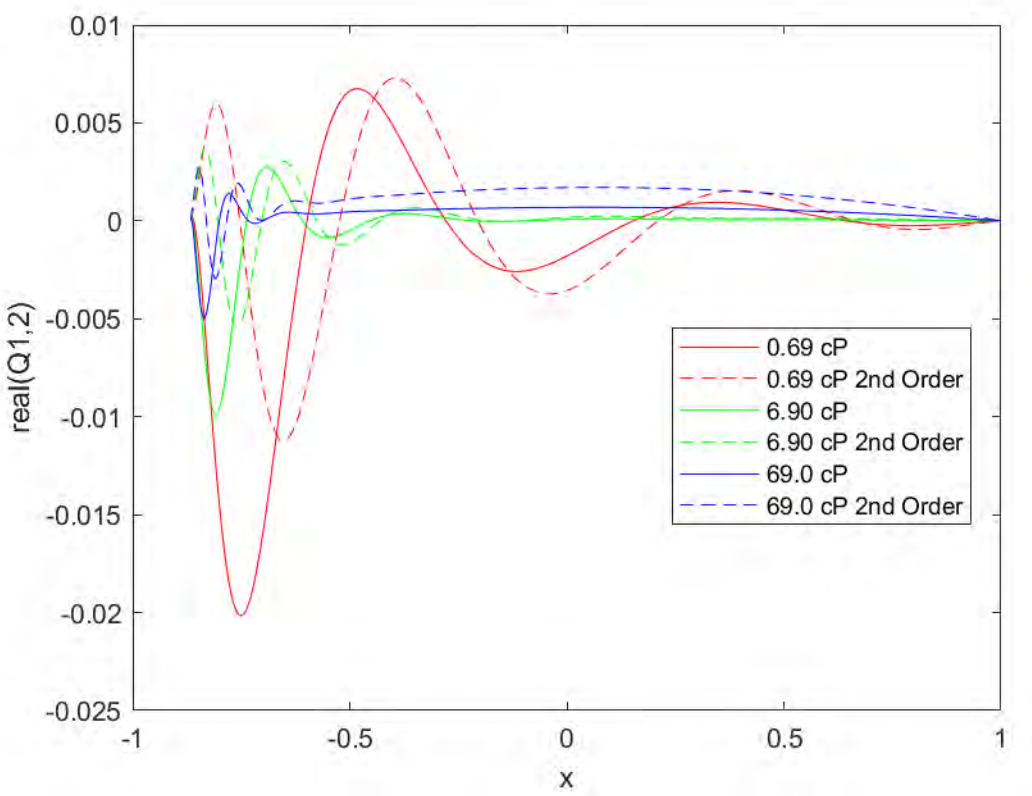

Figure 7.8: Effect of dynamic viscosity, μ, on $\mathfrak{Re}[Q_1]$ (solid lines) and $\mathfrak{Re}[Q_2]$ (dashed lines). Surfactant solubility was set to zero, $k_{ads}C_{10} = 0$.

decrease restricts the alveolus from pumping liquid and possibly surfactant and other materials to adjacent alveoli, contributing to the accumulation of noxious material and pathogens in the site of gas exchange. At the same time, the region of capillary influence is expressed by the range of x where spatial modulations are observed; for the healthy case of $\mu = 0.69$ cP, these modulations extend from the rim x_0 up to positive values of x (red lines) whereas for the case of disease (blue lines) this range seems to be restricted in the neighborhood of the rim and for values $x < -0.5$.

Chapter 8

Conclusions and future prospects

The research presented in this dissertation is an attempt to further elucidate the dynamics of pulmonary surfactant under physiological conditions, and the flow and transport phenomena on the liquid layer lining the alveolar epithelium. In particular, the current investigation is comprised of two main computational studies.

The first study concerns the development of a novel analytical model of lung surfactant dynamics based on fundamental thermodynamics and on kinetically controlled adsorption. The surfactant interfacial concentration varies with time due to adsorption/desorption kinetics and expansion/contraction of the interfacial area. Adsorption is assumed to be spatially uniform, neglecting flow in the bulk of the subphase owing to gravity, viscosity or pressure. Marangoni flows are disregarded as well. Surfactant sorption kinetics accounts for pulmonary surfactant monolayer collapse, accounting for the exchange of surfactant material between the interface and the sublayer reservoir. Mathematically, it is expressed by a Langmuir-like kinetic expression for monolayer replenishment during re-expansion. The novelty of the model advocated is the inclusion of an intrinsic two-dimensional compressibility of the adsorbed monolayer. Mathematically, the mean molar area at saturation, which is the inverse of the saturation concentration, $\Omega = 1/\Gamma_\infty$, was assumed to vary linearly with surface pressure utilizing the model presented in [46]. The proposed model is found to be in good agreement with independent experimental data concerning BLES surfactant preparations at physiologically relevant compression ratios, concentrations, and temperature, by best-fit of a small number of parameters. Results pertaining to the surface elasticity values were acceptable according to literature.

The second study presented in this dissertation is an attempt to study the hydrodynamics of the pulmonary surfactant in alveoli by considering a model of a single human alveolus. The latter is modeled as an oscillating spherical cap, lined internally with a surfactant-laden liquid film. The dynamics of the layer is modeled employing the quasi-steady Stokes equation along with the surfactant mass transport equation. Surfactant behavior is modeled using the analytical model presented in the first part of the dissertation. The thickness of the layer, being orders of magnitude lower than the alveolar radius, allows utilizing the lubrication theory in order to combine momentum and mass transfer along with dynamic and kinematic boundary conditions at the surface of the layer into a set of coupled nonlinear evolution equations with the interfacial surfactant concentration and the film thickness being the unknowns of the problem. A novel boundary condition is applied at the alveolar opening, which enforces mass conservation of water and surfactant over the rim. The model is studied by weakly nonlinear analysis around the equilibrium conditions, hence departure from equilibrium was assumed small and reservoir content B was assumed zero.

The main findings pertaining to our models can be summarised as follows

- The best-fit values of the proposed analytical model about surface tension - area loops regarding BLES preparations reveal a 2-D intrinsic surface compressibility of $\sim 0.005\ \mathrm{m\,mN^{-1}}$. This value is very close to the surface compressibility $(d\sigma/d\ln A)^{-1}$ of pulmonary surfactant monolayers at maximum compression.

- Best fit values equilibrium surface tension, σ_{eq}, lies in the narrow range of $22-25\ \mathrm{mN\,m^{-1}}$ independent of the humidity content as has been shown in the literature; air humidity has been shown to affect adsorption kinetics but not σ_{eq}, which is commonly examined for the characterization of PS preparations.

- The finite film thickness at the alveolus rim marks the onset of shearing motion within the alveolar liquid lining. By setting a zero film thickness at the entrance the results correspond to purely radial motion.

- Marangoni stresses dominate the interfacial dynamics owing to the very short characteristic time scale, t_M compared to that corresponding to capillary phenomena. Nonetheless, capillary stresses affect the interior flow, in balance with viscous stresses. In particular, we found spatial modulations in the distribution of the volumetric flow rate along the alveolar periphery whose characteristic length scales as $Ca^{-1/3}$.

- The inclusion of the possibility of steady streaming surfactant solubility imposes a steady drift of surfactant at the entrance of the alveolus. As the bulk concentration increases by increasing $k_{\mathrm{ads}}C_{10}$ in the range $O(10)$

s^{-1}, the surfactant mass rate, $Q_{\Gamma S}(x_0)$ reaches a maximum value around $k_{\text{ads}}C_{10} \sim 22$ s^{-1}. Further increase in $k_{\text{ads}}C_{10}$ gradually reduces $Q_{\Gamma S}(x_0)$. Based on the fitting procedure conducted in the 1st problem for BLES preparations, this corresponds to bulk concentration ~ 1 mg ml^{-1}, the same order of magnitude as concentrations used in SRT. This observation may provide implications for optimal pulmonary drug delivery via Marangoni transport, since, in reality, when surfactant needs to be delivered to the distal parts of the respiratory system, its path includes transport between neighboring alveoli.

- Increasing the opening angle of the alveolar cap reveals an increased wall shear, which is maximized in the neighborhood of the rim. This observation may provide physiological and clinical implications for emphysema.

- Hydrodynamic model predictions concerning the shear stress exerted on the alveolar wall/epithelium reveal a time-independent shear at 2nd order which is continuously applied on the epithelium during breathing. Order-of-magnitude estimates about healthy and diseased lungs are compared with an experimental threshold from independent literature [29], beyond which cell damage may be inflicted, with the corresponding results being reasonable. Besides, the damage location, near the alveolar inlet is in accordance with emphysema.

8.1 Directions for future work

Several research concepts may be proposed for future work. First and foremost, it would be particularly interesting to solve the coupled set of equations of the problem in Chapter 6 in their initial nonlinear form for large compression ratios in the range 10 - 30%. Accordingly, simulations could provide the possibility to investigate the interplay of capillary and Marangoni phenomena in the limit of large alveolar deformations. To the best of the author's knowledge, the effect of the intrinsic surface compressibility on the alveolar hydrodynamics in the nonlinear limit can be investigated for the first time. Specifically, surfactant kinetics could first be modeled without accounting for the exchange of material between the surface and the surfactant reservoir, thus modeling j_b using Langmuir kinetics, only incorporating the intrinsic surface compressibility. Such modeling would first provide the possibility to study the effect of α during end exhalation on the layer dynamics and the surfactant and liquid mass rate at the alveolus entrance as well. Further, modeling surfactant kinetics as such could allow investigation of the effect of the intrinsic surface compressibility on the adsorption rate of pulmonary surfactant molecules and compare the results with the $\alpha = 0$ case as assumed by prior literature. Besides, it would be interesting to address its effect on mechanical entities such as wall shear and Marangoni stresses.

Later, the hydrodynamic model could be extended by including a third transport equation accounting for the collapsed surfactant material, B. This equation would essentially be the generalization of the model in Chapter 5. Initial tests of the proposed model could utilize the values of Table 5.1 pertaining to k_r about soluble and insoluble cases.

An alternative proposal is the modification of the boundary conditions. As per the authors in [179] the film is locally thin but finite, therefore it would be interesting to incorporate the effect of disjoining pressure terms at the rim and investigate its effect on the flow rates of liquid and surfactant. Lastly, a worth investigating aspect of the hydrodynamic problem is the possibility of slip between the liquid layer and the alveolar epithelium, that is $r = R(t)$. Matar et al. 2003 [115] developed a set of coupled nonlinear evolution equations similar to our hydrodynamic model describing the spatiotemporal response of a thin surfactant-laden film overlying a flat hydrophobic substrate as a model of surfactant-induced flow within the lung, used in SRT, in order to examine the effect of slip on film rupture. Contrary to intuition, that the alveolar epithelium is hydrophilic, they assumed the substrate as hydrophobic motivated by an extensive body of research indicating that a hydrophilic liquid layer flowing over a hydrophobic surface can exhibit slip and that epithelial surfaces in the body can be hydrophobic. Mathematically, slip flow at the substrate was modeled by incorporating the Navier slip boundary condition instead of the classic no-slip boundary condition. The model also accounted for van der Waals forces in the form of disjoining pressure. Hence, based on the above our hydrodynamic model can be modified accordingly. First, the constants C_1, C_2 in velocity profile, u_θ in eq.(6.18) will be determined by the stress balance at $r = R - h$ and the Navier slip condition at $r = R$ instead of $u_\theta(x, r = R, t) = 0$. Following Karapetsas and Mitsoulis [92], we write

$$(\boldsymbol{u} - \boldsymbol{u}_{wall}) \cdot \boldsymbol{t} = \frac{l_s}{\mu} \boldsymbol{t}\boldsymbol{n} : \boldsymbol{\tau} \tag{8.1}$$

where $(\boldsymbol{u} - \boldsymbol{u}_{wall}) \cdot \boldsymbol{t}$ is the velocity difference between the fluid and the solid boundary along the tangential direction, $\boldsymbol{t}$ the tangential unit vector and $\boldsymbol{\tau}$ is the viscous stress tensor of the fluid calculated exactly at the boundary, which is $r = R(t)$ in this case. Most importantly, however, the significance of the relation above lies in the slip length, l_s. The alveolus oscillates along the radial direction, so $\boldsymbol{u}_{wall} \cdot \boldsymbol{t} = 0$ yielding

$$u_\theta(x, r = R, t) = -\frac{l_s}{\mu}\tau_{r\theta} = -\, l_s r \frac{\partial}{\partial r}\left(\frac{u_\theta}{r}\right)\Bigg|_{r=R} \tag{8.2}$$

Following the procedure presented in Chapter 6, the new velocity profile will be used to derive a new set of coupled nonlinear evolution equations with unknowns h and Γ. At the same time, the inclusion of a van der Waals disjoining pressure term can account for possible hydrophobicity of the epithelium via augmenting eq.(6.29). The resultant system of equations can first be investigated by linear and weakly non-linear analysis in order to examine how the slip length modifies the results presented in this dissertation. Depending on the preliminary results, the full nonlinear problem can be solved next accounting for large compression ratios.

Appendix A

Linear and weakly nonlinear amplitudes

In this appendix are summarised the expressions for the main variables of interest presented in Chapter 6. These terms are the primary unknowns h_i, g_i, Γ_i, $i = 1, 2$, as derived by expanding up to second-order in the oscillation amplitude a. In particular, the dimensionless fluxes F_h, F_Γ are expanded in eq. (6.50) in terms of the following components:

$$F_{h1} = \frac{\epsilon^3 Ca^{-1}}{3} H^3 (1-x^2)(2h_1' + g_1') - \frac{\epsilon Ma}{2} H^2 (1-x^2) \Gamma_1' \tag{A.1}$$

$$\begin{aligned} F_{h2} = \frac{\epsilon^3 Ca^{-1}}{3} H^3 (1-x^2)(2h_2' + g_2') - \frac{\epsilon Ma}{2} H^2 (1-x^2) \Gamma_2' + \\ \frac{\epsilon^3 Ca^{-1}}{6} (1-x^2) \left(3H^2 h_1 + H^3 \sigma_\Gamma \Gamma_1 - 3H^3\right)(2h_1' + g_1') - \\ \frac{\epsilon Ma}{4} (1-x^2) \left(-H^2 \Gamma_1 + H^2 E_\Gamma \Gamma_1 + 2H h_1 - H^2\right) \Gamma_1' \end{aligned} \tag{A.2}$$

$$\begin{aligned} F_{hS} = \frac{\epsilon^3 Ca^{-1}}{3} H^3 (1-x^2)(2h_S' + g_S') - \frac{\epsilon Ma}{2} H^2 (1-x^2) \Gamma_S' + \\ \frac{\epsilon^3 Ca^{-1}}{6} (1-x^2) \mathfrak{Re} \left[\left(3H^2 \bar{h}_1 + H^3 \sigma_\Gamma \bar{\Gamma}_1 - 3H^3\right)(2h_1' + g_1')\right] - \\ \frac{\epsilon Ma}{4} (1-x^2) \mathfrak{Re} \left[\left(-H^2 \bar{\Gamma}_1 + H^2 E_\Gamma \bar{\Gamma}_1 + 2H \bar{h}_1 - H^2\right) \Gamma_1'\right] \end{aligned} \tag{A.3}$$

$$F_{\Gamma 1} = \frac{\epsilon^3 Ca^{-1}}{2} H^2 (1-x^2)(2h_1' + g_1') - \epsilon Ma H (1-x^2) \Gamma_1' - Pe_s^{-1} (1-x^2) \Gamma_1' \tag{A.4}$$

$$
\begin{aligned}
F_{\Gamma 2} = {} & \frac{\epsilon^3 Ca^{-1}}{2} H^2 (1-x^2)(2h_2' + g_2') - \epsilon Ma H (1-x^2)\Gamma_2' - Pe_s^{-1}(1-x^2)\Gamma_2' + \\
& \frac{\epsilon^3 Ca^{-1}}{4}(1-x^2)\left(2Hh_1 + H^2 \sigma_\Gamma \Gamma_1 + H^2 \Gamma_1 - 3H^2\right)(2h_1' + g_1') \\
& - \frac{\epsilon Ma}{2}(1-x^2)\left(HE_\Gamma \Gamma_1 + h_1 - H\right)\Gamma_1' + \frac{1}{2} Pe_s^{-1}(1-x^2)\Gamma_1'
\end{aligned}
\tag{A.5}
$$

$$
\begin{aligned}
F_{\Gamma S} = {} & \frac{\epsilon^3 Ca^{-1}}{2} H^2 (1-x^2)(2h_S' + g_S') - \epsilon Ma H (1-x^2)\Gamma_S' - Pe_s^{-1}(1-x^2)\Gamma_S' + \\
& \frac{\epsilon^3 Ca^{-1}}{4}(1-x^2)\mathfrak{Re}\left[\left(2H\bar{h}_1 + H^2 \sigma_\Gamma \bar{\Gamma}_1 + H^2 \bar{\Gamma}_1 - 3H^2\right)(2h_1' + g_1')\right] \\
& - \frac{\epsilon Ma}{2}(1-x^2)\mathfrak{Re}\left[\left(HE_\Gamma \bar{\Gamma}_1 + \bar{h}_1 - H\right)\Gamma_1'\right] + \frac{1}{2} Pe_s^{-1}(1-x^2)\mathfrak{Re}(\Gamma_1')
\end{aligned}
\tag{A.6}
$$

Expansion of the boundary conditions results in the following first and second-order expressions, where symbols like h_{i0} signify amplitude i evaluated at $x = x_0$:

$$
-F_{h1}|_{x_0} = \sqrt{1-x_0^2}\,(i\pi^2)\left[(r_0 + \epsilon H_0)\,h_{10} + H_0\left(r_0 + \epsilon\frac{H_0}{2}\right)\right]
\tag{A.7}
$$

$$
\begin{aligned}
-F_{h2}|_{x_0} = \sqrt{1-x_0^2}\,(i\pi^2)\Bigg[& (r_0 + \epsilon H_0)\,2h_{20} + \frac{1}{2}\epsilon h_{10}^2 + \frac{1}{2}(r_0 + \epsilon H_0)\,h_{10} - \\
& \frac{1}{2}H_0\left(r_0 + \epsilon\frac{H_0}{2}\right)\Bigg]
\end{aligned}
\tag{A.8}
$$

$$
-F_{hS}|_{x_0} = \sqrt{1-x_0^2}\left(\frac{\pi^2}{2}\right)(r_0 + \epsilon H_0)\,\mathfrak{Re}\left[i\,\bar{h}_1\right]
\tag{A.9}
$$

$$
-F_{\Gamma 1}|_{x_0} = \sqrt{1-x_0^2}\,\pi\left[(r_0 + \epsilon H_0)\left(i\pi - \frac{St_1}{2}\right)\Gamma_{10} + i\pi\epsilon h_{10} + i\pi(r_0 + \epsilon H_0)\right]
\tag{A.10}
$$

$$
\begin{aligned}
-F_{\Gamma 2}|_{x_0} = \sqrt{1-x_0^2}\,\pi\Bigg[& (r_0 + \epsilon H_0)\left(2i\pi - \frac{St_1}{2}\right)\Gamma_{20} - \frac{St}{8}(r_0 + \epsilon H_0)\,\Gamma_{\infty,\Gamma\Gamma}\Gamma_{10}^2 + \\
& \left(i\pi - \frac{St_1}{4}\right)\epsilon h_{10}\Gamma_{10} + i\pi\epsilon\left(2h_{20} + \frac{h_{10}}{2}\right) - \frac{1}{2}i\pi(r_0 + \epsilon H_0)(1 - \Gamma_{10})\Bigg]
\end{aligned}
\tag{A.11}
$$

$$
\begin{aligned}
-F_{\Gamma S}|_{x_0}= \sqrt{1-x_0^2}\,\pi \left[-\frac{1}{2}(r_0+\epsilon H_0)\left(St_1\Gamma_S+\frac{1}{4}St\,\Gamma_{\infty,\Gamma\Gamma}\left(\Gamma_1\bar{\Gamma}_1\right)+\pi\mathfrak{Re}[i\Gamma_1]\right)-\right. \\
\left.\frac{1}{4}\epsilon St_1\mathfrak{Re}[\Gamma_1\bar{h}_1]+\frac{1}{2}\pi\epsilon\mathfrak{Re}[i\bar{h}_1]\right]
\end{aligned}
\tag{A.12}
$$

The surface velocity and the volumetric flow rate of the liquid film are expanded in terms of the following amplitudes, with the steady term at second order being identically zero for both of them:

$$
u_{s1}=\sqrt{1-x^2}\left[\frac{\epsilon^3Ca^{-1}}{2}H^2(2h_1'+g_1')-\epsilon MaH\Gamma_1'\right]
\tag{A.13}
$$

$$
\begin{aligned}
u_{s2}=\sqrt{1-x^2}\left[\frac{\epsilon^3Ca^{-1}}{2}\left(H^2(2h_2'+g_2')+\right.\right. \\
\left.\frac{1}{2}\left(-3H^2+2Hh_1+H^2\Gamma_1\,\sigma_\Gamma\right)(2h_1'+g_1')\right) \\
\left.-\epsilon Ma\left(H\Gamma_2'+\frac{1}{2}(-H+h_1-H\Gamma_1+H\Gamma_1\,E_\Gamma)\,\Gamma_1'\right)\right]
\end{aligned}
\tag{A.14}
$$

$$
\begin{aligned}
u_{sS}=\sqrt{1-x^2}\left\{\frac{\epsilon^3Ca^{-1}}{2}\left(H^2(2h_S'+g_S')+\right.\right. \\
\left.\frac{1}{2}\mathfrak{Re}[\left(-3H^2+2H\bar{h}_1+H^2\bar{\Gamma}_1\,\sigma_\Gamma\right)(2h_1'+g_1')]\right) \\
\left.-\epsilon Ma\left(H\Gamma_S'+\frac{1}{2}\mathfrak{Re}[\left(-H+\bar{h}_1-H\bar{\Gamma}_1+H\bar{\Gamma}_1\,E_\Gamma\right)\Gamma_1']\right)\right\}
\end{aligned}
\tag{A.15}
$$

$$
Q_1=(1-x^2)\left[\frac{\epsilon^3Ca^{-1}}{3}H^3(2h_1'+g_1')-\frac{\epsilon Ma}{2}H^2\Gamma_1'\right]
\tag{A.16}
$$

$$
\begin{aligned}
Q_2=(1-x^2)\left[\frac{\epsilon^3Ca^{-1}}{3}\left(H^3(2h_2'+g_2')+\right.\right. \\
\left.\frac{1}{2}\left(3H^2h_1+H^3\Gamma_1\,\sigma_\Gamma-2H^3\right)(2h_1'+g_1')\right)- \\
\left.\frac{\epsilon Ma}{2}\left(H^2\Gamma_2'+\frac{1}{2}\left(2Hh_1-H^2\Gamma_1+H^2\Gamma_1\,E_\Gamma\right)\Gamma_1'\right)\right]
\end{aligned}
\tag{A.17}
$$

The wall shear stress is expanded in terms of the following amplitudes:

$$
\tau_{w1}=\sqrt{1-x^2}\left[-\epsilon^2Ca^{-1}H(2h_1'+g_1')+Ma\Gamma_1'\right]
\tag{A.18}
$$

$$\tau_{w2} = \sqrt{1-x^2}\Big[-\epsilon^2 Ca^{-1}\Big(H(2h_2'+g_2') + \frac{1}{2}\left(h_1 + H\Gamma_1\,\sigma_\Gamma - 3H\right)(2h_1'+g_1')\Big) \\ +Ma\Big(\Gamma_2' + \frac{1}{2}\left(-\Gamma_1+\Gamma_1\,E_\Gamma - 1\right)\Gamma_1'\Big)\Big] \tag{A.19}$$

$$\tau_{wS} = \sqrt{1-x^2}\Big[-\epsilon^2 Ca^{-1}\Big(H(2h_S'+g_S') + \frac{1}{2}\mathfrak{Re}\Big[\left(\bar{h}_1 + H\bar{\Gamma}_1\,\sigma_\Gamma - 3H\right)(2h_1'+g_1')\Big]\Big) \\ +Ma\Big(\Gamma_S' + \frac{1}{2}\mathfrak{Re}\Big[\left(-\bar{\Gamma}_1+\bar{\Gamma}_1\,E_\Gamma - 1\right)\Gamma_1'\Big]\Big)\Big] \tag{A.20}$$

Finally, the terms σ_Γ, E_Γ, $\Gamma_{\infty,\Gamma}$ and $\Gamma_{\infty,\Gamma\Gamma}$ that appear in the above equations and represent derivatives evaluated at Γ_{eq}, are calculated from the following expressions:

$$\sigma_\Gamma = \left.\frac{d\sigma}{d\Gamma}\right|_{\text{eq}} = -\frac{E_{\text{eq}}}{\sigma_{\text{eq}}} \tag{A.21}$$

$$E_\Gamma = \left.\frac{dE}{d\Gamma}\right|_{\text{eq}} = \frac{E_{\text{eq}}}{\mathcal{R}T\Gamma_{\text{eq}}} - \frac{\alpha\Omega_{\text{o}}}{\mathcal{R}T}E_{\text{eq}}^2 - \left(\frac{\alpha E_{\text{eq}}}{1-\alpha\Pi_{\text{eq}}}\right)^2 \tag{A.22}$$

$$\Gamma_{\infty,\Gamma} = \left.\frac{d\Gamma_\infty}{d\Gamma}\right|_{\text{eq}} = \frac{\alpha}{(1-\alpha\Pi_{\text{eq}})^2}\frac{E_{\text{eq}}}{\Omega_{\text{o}}\Gamma_{\text{eq}}} \tag{A.23}$$

$$\Gamma_{\infty,\Gamma\Gamma} = \left.\frac{d^2\Gamma_\infty}{d\Gamma^2}\right|_{\text{eq}} = \alpha E_{\text{eq}}\Gamma_{\infty,\text{eq}}\left[2\Gamma_{\infty,\Gamma} + \frac{\Gamma_{\infty,\text{eq}}}{\Gamma_{\text{eq}}}\left(E_\Gamma - 1\right)\right] \tag{A.24}$$

The tangential component of the dynamic boundary condition, eq.(6.5), is

$$\boldsymbol{n}\cdot\boldsymbol{\tau}\cdot\boldsymbol{t} = \boldsymbol{t}\cdot\boldsymbol{\nabla}_s\sigma \tag{A.25}$$

where $\boldsymbol{t}$ is the unit tangent to the interface $r = R - h$ and due to Lubrication approximation we can writte $\boldsymbol{t} \approx \boldsymbol{e}_\theta, \boldsymbol{n} \approx -\boldsymbol{e}_r$. Now it is evident that Marangoni stresses scale as viscous surface tractions and we can non-dimensionalize the former with $\mu U/R$. The Marangoni stress is

$$\tau_M = \left(\frac{1}{r}\frac{\partial\sigma}{\partial\theta}\right)_{r=R-h} \approx \frac{1}{R}\frac{\partial\sigma}{\partial\theta} \tag{A.26}$$

In dimensionless form

$$\frac{\mu U}{R}\tau_M^* = \left(\frac{1}{r}\frac{\partial\sigma}{\partial\theta}\right)_{r=R-h} \approx \frac{\sigma_{\text{eq}}}{R^*R}\frac{\partial\sigma^*}{\partial\theta} \tag{A.27}$$

dropping asterisks for the shake of convenience and accounting for eq.(6.8), we have

$$\tau_M = -Ca^{-1}\frac{\sqrt{1-x^2}}{R}\sigma_\Gamma\frac{\partial\Gamma}{\partial x} \tag{A.28}$$

where $\sigma_\Gamma = (d\sigma/d\Gamma|_{\mathrm{eq}})$ since deviations from equilibrium are small [44]. Expanding τ_M as

$$\tau_M = a\,\mathfrak{Re}[\tau_{M1}(x)\,e^{i\,2\pi t}] + a^2\left(\mathfrak{Re}[\tau_{M2}(x)\,e^{i\,4\pi t}] + \tau_{MS}(x)\right) \tag{A.29}$$

leads to

$$\tau_{M1} = -Ca^{-1}\sqrt{1-x^2}\sigma_\Gamma\Gamma_1' \tag{A.30}$$

$$\tau_{M2} = -Ca^{-1}\sqrt{1-x^2}\sigma_\Gamma(\Gamma_2' - \frac{1}{2}\Gamma_1') \tag{A.31}$$

$$\tau_{MS} = -Ca^{-1}\sqrt{1-x^2}\sigma_\Gamma[\Gamma_S' - \frac{1}{2}\mathfrak{Re}(\Gamma_1')] \tag{A.32}$$

Appendix B

Scaling Marangoni phenomena with capillarity

Here we will directly show that the surface tension gradient appearing in $\partial p/\partial x$ in Chapter 6 can be omitted allowing, eventually, a simplified set of 2 evolution equations. The arguments on which the derivation is based are similar to those presented in Kang et al [90] concerning thermocapillary Marangoni phenomena on a thin film covering a spherical surface, a geometry very close to the problem investigated in this dissertation. To prove this statement, we demand both gradients appearing in eq.(6.22) to be important

$$\frac{h^3}{\mu R^2}\frac{\partial p}{\partial x} \sim \frac{h^2}{\mu R^2}\frac{\partial \sigma}{\partial x} \tag{B.1}$$

The pressure gradient, $\partial p/\partial x$ is derived by differentiation of eq.(6.29)

$$\frac{\partial p}{\partial x} = \frac{\partial}{\partial x}\left[\frac{\sigma}{R^2}\left(2h + 2R + \frac{\partial}{\partial x}\left((1-x^2)\frac{\partial h}{\partial x}\right)\right)\right] = \frac{1}{R^2}\frac{\partial(\sigma\mathcal{C})}{\partial x} = \frac{1}{R^2}\left(\sigma\frac{\partial \mathcal{C}}{\partial x} + \mathcal{C}\frac{\partial \sigma}{\partial x}\right) \tag{B.2}$$

where $\mathcal{C}$ denotes the curvature of the surface, $\boldsymbol{\nabla}_s \cdot \boldsymbol{n}$. Rendering the above equation dimensionless using the equilibrium parameters, see again 6.3.2, leads to (now we use the $*$ superscript to denote dimensionless arguments and avoid any confusion)

$$\frac{\partial p^*}{\partial x} = \frac{1}{R^{*2}}\left(\sigma^*\frac{\partial \mathcal{C}^*}{\partial x} + \mathcal{C}^*\frac{\partial \sigma^*}{\partial x}\right) \tag{B.3}$$

From eq.(B.2), however, we have demanded that

$$\epsilon^2 h^*\frac{\partial p^*}{\partial x} = \frac{\partial \sigma^*}{\partial x} \tag{B.4}$$

Thus it emanates from eq.(B.4) that the surface tension gradient in eq.(B.3) is $O(\epsilon^2)$ and, eventually, can be omitted

$$\frac{\partial p^*}{\partial x} = \frac{\sigma^*}{R^{*2}}\frac{\partial \mathcal{C}^*}{\partial x} = \frac{\sigma^*}{R^{*2}}\frac{\partial}{\partial x}\left(2h^* + 2R^* + \frac{\partial}{\partial x}\left((1-x^2)\frac{\partial h^*}{\partial x}\right)\right) \tag{B.5}$$

Note that the last result was extracted without making any specific assumption about the form of the state equation $\sigma = \sigma(\Gamma)$, therefore eq.(B.5) is generally valid regardless of the state equation and the boundary conditions; it is a direct consequence of the lubrication theory and the assumption that both capillary and Marangoni effects drive the liquid flow in the subphase and on the interface.

Bibliography

[1] E.J. Acosta, R. Gitiafroz, Y.Y. Zuo, Z. Policova, P.N. Cox, M.L. Hair, and A.W. Neumann. Effect of humidity on lung surfactant films subjected to dynamic compression/expansion cycles. Respiratory Physiology & Neurobiology, 155:255–267, 2007.

[2] A. Adamson and A. Gast. Physical Chemistry of Surfaces. Wiley, 1997.

[3] A. B. Afsar-Siddiqui, P. F. Luckham, and O. Matar. The spreading of surfactant solutions on thin liquid films. Advances in Colloid and Interface Science, 106:183–236, 2003.

[4] V. S. Ajaev. Interfacial Fluid Mechanics: A Mathematical Modeling Approach. Springer, 2012.

[5] A.-C. Almstrand, B. Bake, E. Ljungström, P. Larsson, A. Bredberg, E. Mirgorodskaya, and A.-C. Olin. Effect of airway opening on production of exhaled particles. J. Appl. Physiol., 108:584—-588, 2010.

[6] C. Alonso, T. Alig, J. Yoon, F. Bringezu, H. Warriner, and J.A. Zasadzinski. More than a monolayer: Relating lung surfactant structure and mechanics to composition. Biophysical Journal, 87(6):4188–4202, 2004.

[7] S. Baoukina, L. Monticelli, H.J. Risselada, S.J. Marrink, and D.P. Tieleman. The molecular mechanism of lipid monolayer collapse. PNAS, 105(31):10803–10808, 2008.

[8] S. Baoukina and D.P. Tieleman. Lung surfactant protein SP-B promotes formation of bilayer reservoirs from monolayer and lipid transfer between the interface and subphase. Biophys. J., 100:1678–1687, 2011.

[9] S. Baoukina and D.P. Tieleman. Computer simulations of lung surfactant. Biochimica et Biophysica Acta, 1858:2431–2440, 2016.

[10] S. Barman, M. L. Davidson, L. M. Walker, S. L. Anna, and J. A. Zasadzinski. Inflammation product effects on dilatational mechanics can

trigger the laplace instability and acute respiratory distress syndrome. Soft Matter, 16:6890, 2020.

[11] J. Bastacky, C. Y. Lee, J. Goerke, H. Koushafar, D. Yager, L. Kenaga, T. P. Speed, Y. Chen, and J. A. Clements. Alveolar lining layer is thin and continuous: low-temperature scanning electron microscopy of rat lung. J. Appl. Physiol., 79:1615–1628, 1995.

[12] John C. Berg. An introduction to Interfaces & Colloids: The Bridge to Nanoscience. World Scientific, 2010.

[13] W. Bernhard, H.P. Haagsman, T. Tschernig, C.F. Poets, A.D. Postle, M.E. van Eijk, and H. von der Hardt. Conductive airway surfactant: Surface-tension function, biochemical composition, and possible alveolar origin. Am. J. Respir. Cell Mol. Biol., 17:41–50, 1997.

[14] M. G. Blyth and C. Pozrikidis. Effect of surfactant on the stability of film flow down an inclined plane. Journal of Fluid Mechanics, 521:241–250, 2004.

[15] V. Bontozoglou. The effect of adsorption modeling on the stability of surfactant-laden liquid film flow. Acta Mech, 229:535–547, 2018.

[16] V. Bontozoglou and K. Serifi. Steady free-surface thin film flow over two-dimensional topography. Intl. J. Multiphase Flow, 34:734—-747, 2008.

[17] R. P. Borwankar and D. T. Wasan. The kinetics of adsorption of surface active agents at gas-liquid surfaces. Chemical Engineering Science, 38:1637–1649, 1983.

[18] R. P. Borwankar and D.T. Wasan. Equilibrium and dynamics of adsorption of surfactants at fluid-fluid interfaces. Chemical Engineering Science, 43:1323–1337, 1988.

[19] R.P. Borwankar and D.T. Wasan. The kinetics of adsorption of ionic surfactants at gas liquid surfaces. Chemical Engineering Science, 41:199–201, 1986.

[20] K. Bouchoris and V. Bontozoglou. A model of lung surfactant dynamics based on intrinsic interfacial compressibility. Colloids and Surfaces A: Physicochemical and Engineering Aspects, 624:126839, 2021.

[21] K. Bouchoris and V. Bontozoglou. Surfactant-laden film lining an oscillating cap: problem formulation and weakly nonlinear analysis. Journal of Fluid Mechanics, 944:A50, 2022.

[22] Hans-Jurgen Butt, K. Graf, and M. Kappl. Physics and Chemistry of Surfaces. Wiley, 2003.

[23] A.G. Bykov, G. Loglio, R. Miller, O.Y. Milyaeva, A.V. Michailov, and B.A. Noskov. Dynamic properties and relaxation processes in surface layer of pulmonary surfactant solutions. Colloids and Surfaces A: Physicochemical and Engineering Aspects, 573:14–21, 2019.

[24] A.G. Bykov, G. Loglio, F. Ravera, L. Liggieri, R. Miller, and B.A. Noskov. Dilational surface elasticity of spread monolayers of pulmonary lipids in a broad range of surface pressure. Colloids and Surfaces A: Physicochemical and Engineering Aspects, 541:137–144, 2018.

[25] A.G. Bykov, O.Y. Milyaeva, N.A. Isakov, A.V. Michailov, G. Loglio, R. Miller, and B.A. Noskov. Dynamic properties of adsorption layers of pulmonary surfactants. Influence of matter exchange with bulk phase. Colloids and Surfaces A: Physicochemical and Engineering Aspects, 611:125851, 2021.

[26] C.-H. Chang and E. I. Franses. Modified langmuir-hinshelwood kinetics for dynamic adsorption of surfactants at the air/water interface. Colloids and Surfaces, 69:189–201, 1992.

[27] C.-H. Chang and E.I. Franses. Dynamic tension behavior of aqueous octanol solutions under constant-area and pulsating-area conditions. Chemical Engineering Science, 49:313–325, 1994.

[28] Chien-Hsiang Chang and E.I. Franses. Adsorption dynamics of surfactants at the air/water interface: a critical review of mathematical models, data, and mechanisms. Colloids and Surfaces A: Physicochemical and Engineering Aspects, 100:1–45, 1995.

[29] Z. Chen, Y. Song, Z. Hu, S. Zhang, and Y. Chen. An estimation of mechanical stress on alveolar walls during repetitive alveolar reopening and closure. J. Appl. Physiol., 119:190–201, 2015.

[30] J.-I. Choi and S. C. Kim. Mathematical analysis of particle deposition in human lungs: An improved single path transport model. Inhal. Toxicol., 19:925—-939, 2007.

[31] D. Ciloglu. A numerical study of the aerosol behavior in intra-acinar region of a human lung. Phys. Fluids, 32:103305, 2020.

[32] Clara O. Ciutara, Sourav Barman, Steven Iasella, Boxun Huang, and Joseph A. Zasadzinski. Dilatational and shear rheology of soluble and insoluble monolayers with a langmuir trough. Journal of Colloid and Interface Science, 629:125–135, 2023.

[33] J.A. Clements. Functions of the alveolar lining. Am. Rev. of Respir. Dis., 115:67–71, 1977.

[34] J.A. Clements and M. E. Avery. Lung surfactant and neonatal respiratory distress syndrome. Am J Respir Crit Care Med, 157:S59–S66, 1998.

[35] G. Colacicco, M.K. Basu, and E.M. Scarpelli. pH, temperature, humidity and the dynamic force-area curve of dipalmitoyl lecithin. Respir. Physiol., 27:169–186, 1976.

[36] C.R. Constante-Amores, A. Batchvarov, L. Kahouadji, S. Shin, J. Chergui, D. Juric, and O.K. Matar. Role of surfactant-induced marangoni stresses in drop-interface coalescence. Journal of Fluid Mechanics, 925:A15, 2021.

[37] J.M. Crane, G. Putz, and S.B. Hall. Persistence of phase coexistence in disaturated phosphatidylcholine monolayers at high surface pressures. Biophys. J., 77:3134–3143, 1999.

[38] R.V. Craster and O.K. Matar. Dynamics and stability of thin liquid films. Reviews of Modern Physics, 81:1131–1198, 2009.

[39] S.J.D. D'Alessio and J.P. Pascal. Long-wave instability in thin heated films doped with soluble surfactants. Intl. J. Non-Linear Mech., 136:103784, 2021.

[40] C. Darquenne and M. Paiva. One-dimensional simulation of aerosol transport and deposition in the human lung. J. Appl. Physiol., 77:2889—-2898, 1994.

[41] A. De Witt, D. Gallez, and C.I. Cristov. Nonlinear evolution equations for thin liquid films with insoluble surfactants. Physics of Fluids, 6:3256, 1994.

[42] J. Deng, M. Molaei, G. C. Chisholm, T. Yao, A. Read, and K. J. Stebe. Active colloids on fluid interfaces. Current Opinion in Colloid & Interface Science, 61:101629, 2022.

[43] J. Eastoe and J.S. Dalton. Dynamic surface tension and adsorption mechanisms of surfactants at the air-water interface. Advances in Colloid and Interface Science, 85:103–144, 2000.

[44] D. A. Edwards, H. Brenner, and D. T. Wasan. Interfacial Transport Processes and Rheology. Butterworth-Heinemann, 1991.

[45] F. F. Espinosa and R.D. Kamm. Thin layer flows due to surface tension gradients over a membrane undergoing nonuniform periodic strain. Ann. Biomed. Eng., 25:913–925, 1997.

[46] V.B. Fainerman, R. Miller, and V.I. Kovalchuk. Influence of the compressibility of adsorbed layers on the surface dilational elasticity. Langmuir, 18:7748–7752, 2002.

[47] V.B Fainerman, R. Miller, and V.I. Kovalchuk. Influence of the two-dimensional compressibility on the surface pressure isotherm and dilational elasticity of dodecyldimethylphosphine oxide. Journal of Physical Chemistry B, 107:6119–6121, 2003.

[48] J.G. Fernsler and J.A. Zasadzinski. Competitive adsorption: A physical model for lung surfactant inactivation. Langmuir, 25(14):8131–8143, 2009.

[49] M. Filoche, C.-F. Tai, and J.B. Grotberg. Three-dimensional model of surfactant replacement therapy. Proc. Natl. Acad. Sci. USA, 112:9287–9292, 2015.

[50] A. L. Frenkel and D. Halpern. Stokes-flow instability due to interfacial surfactant. Physics of Fluids, 14:L45–L48, 2002.

[51] C. Garcia-Mouton, A. Hidalgo, A. Cruz, and J. Perez-Gil. The lord of the lungs: The essential role of pulmonary surfactant upon inhalation of nanoparticles. European Journal of Pharmaceutics and Biopharmaceutics, 144:230–243, 2019.

[52] D. P. Gaver and J. B. Grotberg. The dynamics of a localized surfactant on a thin film. Journal of Fluid Mechanics, 213:127–148, 1990.

[53] D.P. Gaver and S.N. Ghadiali. Biomechanics of liquid-epithelium interactions in pulmonary airways. Respiratory Physiology & Neurobiology, 163:232–243, 2008.

[54] S.N. Ghadiali and D.P. Gaver. An investigation of pulmonary surfactant physicochemical behavior under airway reopening conditions. Journal of Applied Physiology, 88(5):493–506, 2000.

[55] A. Gopal and K.Y.C. Lee. Headgroup percolation and collapse of condensed langmuir monolayers. J. Phys. Chem. B, 110(44):22079–22087, 2006.

[56] D.O. Grigoriev, J. Kragel, A.V. Akentiev, B.A. Noskov, R. Miller, and U. Pison. Relation between rheological properties and structural changes in monolayers of model lung surfactant under compression. Biophysical Chemistry, 104:633–642, 2003.

[57] J. B. Grotberg. Respiratory fluid mechanics. Physics of Fluids, 23:021301, 2011.

[58] James B. Grotberg. Biofluid Mechanics. Cambridge Texts in Biomedical Engineering. Cambridge University Press, 2021.

[59] J.B. Grotberg. Pulmonary flow and transport phenomena. Annual Reviews in Fluid Mechanics, 26:529–571, 1994.

[60] E. Guzman, L. Liggieri, E. Santini, M. Ferrari, and F. Ravera. Mixed dppc–cholesterol langmuir monolayers in presence of hydrophilic silica nanoparticles. Colloids and Surfaces B: Biointerfaces, 105:284–293, 2013.

[61] S. Haber, J. P. Butler, Brenner H., I. Emmanuel, and A. Tsuda. Shear flow over a self-similar expanding pulmonary alveolus during rhythmical breathing. Journal of Fluid Mechanics, 405:243–268, 2000.

[62] S. Haber, A. Tsuda, J.P. Butler, I. Emanuel, and H. Brenner. Shear flow over a self-similar expanding pulmonary alveolus during rhythmical breathing. Journal of Fluid Mechanics, 405:243–268, 2000.

[63] S. Haber and D. et al Zelig. Hydrodynamic cleansing of pulmonary alveolus. SIAM J. Appl. Math., 63:195–221, 2000.

[64] T. Haller, P. Dietl, H. Stockner, M. Frick, N. Mair, I. Tinhofer, A. Ritsch, G. Enhorning, and G. Putz. Tracing surfactant transformation from cellular release to insertion into an air–liquid interface. Am. J. Physiol. Lung Cell. Mol. Physiol., 286:L1009–L1015, 2004.

[65] D. Halpern, H. Fujioka, S. Takayama, and J.B. Grotberg. Liquid and surfactant delivery in the pulmonary airways. Respiratory Physiology and Neurobiology, 163:222–231, 2008.

[66] D. Halpern, O. E. Jensen, and Grotberg J. B. A theoretical study of surfactant and liquid delivery into the lung. J. Appl. Physiol., 85:333—-352, 1998.

[67] S. Han and R.K. Mallampalli. The role of surfactant in lung disease and host defense against pulmonary infections. Ann. Am. Thorac. Soc., 12:765–774, 2015.

[68] E. M. Harding and R. J. Robinson. Flow in a terminal alveolar sac model with expanding walls using computational fluid dynamics. Inhal. Toxicol., 22:669—-678, 2010.

[69] Y. He, P. Yazhgur, A. Salonen, and D. Langevin. Adsorption–desorption kinetics of surfactants at liquid surfaces. Advances in Colloid and Interface Science, 222:377–384, 2015.

[70] F. S. Henry, J. P. Butler, and A. Tsuda. Kinematically irreversible acinar flow: a departure from classical dispersive aerosol transport theories. J Appl Physiol, 92:835–845, 2002.

[71] S. Henry and A. F. Tsuda. Flow and particle tracks in model acini. ASME J. Biomech. Eng., 132:101001, 2010.

[72] E. Hermans, M. Bhamla, P. Kao, G.G. Fuller, and J. Vermant. Lung surfactants and different contributions to thin film stability. SoftMatter, 11:8048, 2015.

[73] E. Hermans, M.S. Bhamla, P. Kao, G.G. Fuller, and J. Vermant. Lung surfactants and different contributions to thin film stability. Soft Matter, 11(41):8048—8057, 2015.

[74] M. J. Herring, L. F. Putney, G. Wyatt, W. E. Finkbeiner, and D. M. Hyde. Growth of alveoli during postnatal development in humans based on stereological estimation. Am. J. Physiol. Lung Cell Mol. Physiol., 307:L338–L344, 2014.

[75] A. A. Hislop, J. S. Wigglesworth, and R. Resai. Alveolar development in the human fetus and infant. Early Human Development, 13:1–11, 1986.

[76] W. Hofman. Modeling inhaled particle deposition in the lung: A review. Journal of Aerosol Science, 72:693–724, 2013.

[77] L. W. Horn and S. H. Davis. Apparent surface tension hysteresis of a dynamical system. Journal of Colloid and Interface Science, 51:459–476, 1975.

[78] K. Horsefield and G. Cummings. Morphology of the bronchial tree in man. Journal of Applied Physiology, 24:373–383, 1968.

[79] T. Hu, Q. Fu, and L. Yang. Falling film with insoluble surfactants: Effects of surface elasticity and surface viscosities. Journal of Fluid Mechanics, 873:18–48, 2020.

[80] E.P. Ingenito, L. Mark, J. Morris, F.F. Espinosa, R.D. Kamm, and M. Johnson. Biophysical characterization and modeling of lung surfactant components. J. Appl. Physiol., 86(5):1702–1714, 1999.

[81] J. Craig Jackson. Chapter 46 - respiratory distress in the preterm infant. In Christine A. Gleason and Sherin U. Devaskar, editors, Avery's Diseases of the Newborn (Ninth Edition), pages 633–646. W.B. Saunders, Philadelpia, ninth edition edition, 2012.

[82] O. E. Jensen and J. B. Grotberg. Insoluble surfactant spreading on a thin viscous film: shock evolution and film rupture. Journal of Fluid Mechanics, 259-288:58, 1992.

[83] O. E. Jensen and J. B. Grotberg. The spreading of heat or soluble surfactant along a thin liquid film. Physics of Fluids A: Fluid Dynamics, 5:58, 1993.

[84] D.O. Johnson and K.J. Stebe. Oscillating bubble tensiometry: A method for measuring the surfactant adsorptive-desorptive kinetics and the surface dilatational elasticity. Journal of Colloid and Interface Science, 168:21–31, 1994.

[85] S. Kalliadasis, C. Bielarz, and G. M. Homsy. Steady free-surface thin film flow over two-dimensional topography. Physics of Fluids, 12:1889—-1898, 2000.

[86] S. Kalliadasis and G. M. Homsy. Stability of free-surface thin-film flows over topography. Journal of Fluid Mechanics, 448:387–410, 2001.

[87] A. Kalogirou. Nonlinear dynamics of surfactant–laden multilayer shear flows and related systems. PhD thesis, Imperial College London, Department of Mathematics, 2014.

[88] A. Kalogirou and D.T. Papageorgiou. Nonlinear dynamics of surfactant-laden two-fluid couette flows in the presence of inertia. Journal of Fluid Mechanics, 802:5–36, 2015.

[89] D. Kang, M. Chugunova, A. Nadim, A.J. Waring, and F.J. Walther. Modeling coating flow and surfactant dynamics inside the alveolar compartment. J. Eng. Math., 113:23–43, 2018.

[90] D. Kang, A. Nadim, and M. Chugunova. Marangoni effects on a thin liquid film coating a sphere with axial or radial thermal gradients. Physics of Fluids, 29(7):072106, 2017.

[91] G. Karapetsas and V. Bontozoglou. The role of surfactants on the mechanism of the long-wave instability in liquid film flows. Journal of Fluid Mechanics, 741:139–155, 2014.

[92] G. Karapetsas and E. Mitsoulis. Some experiences with the slip boundary condition in viscous and viscoelastic flows. Journal of Non-Newtonian Fluid Mechanics, 198:96–108, 2013.

[93] A. Katsiavria and V. Bontozoglou. Stability of liquid film flow laden with the soluble surfactant sodium dodecyl sulphate: predictions versus experimental data. Journal of Fluid Mechanics, 894:A18, 2020.

[94] K. Kim, S. Q. Choi, J. A. Zasadzinski, and T. M. Squires. Interfacial microrheology of dppc monolayers at the air–water interface. Soft Matter, 7:7782–7789, 2011.

[95] M. Kohlhäufl, P. Brand, C. Rock, T. Radons, G. Scheuch, T. Meyer, H. Schulz, J. Pfeifer, K. Häussinger, and J. Heyder. Noninvasive diagnosis of emphysema: Aerosol morphometry and aerosol bolus dispersion in comparison to hrct. Am. J. Respir. Crit. Care Med., 160:913–918, 1999.

[96] A. V. Kolanjiyil and C. Kleinstreuer. Modeling airflow and particle deposition in a human acinar region. Comp. Math. Methods Medicine, 2019:5952941, 2019.

[97] V.I. Kovalchuk, G. Loglio, V.B. Fainerman, and R. Miller. Interpretation of surface dilational elasticity data based on an intrinsic two-dimensional interfacial compressibility model. Journal of Colloid and Interface Science, 270:475–482, 2004.

[98] V.I. Kovalchuk, R. Miller, V.B. Fainerman, and G. Loglio. Dilational rheology of adsorbed surfactant layers - role of the intrinsic two-dimensional compressibility. Advances in Colloid and Interface Science, 114-115:303–312, 2005.

[99] M.A. Krueger and D.P. Gaver III. A theoretical model of pulmonary surfactant multilayer collapse under oscillating area conditions. Journal of Colloid and Interface Science, 229:353–364, 2000.

[100] H. Kumar, M. H. Tawhai, E. A. Hoffman, and C. L. Lin. The effects of geometry on airflow in the acinar region of the human lung. J. Biomech., 42:1635–1642, 2009.

[101] D. Langevin, Y. He, P. Yazhgur, and A. Salonen. Adsorption-desorption kinetics of surfactants at liquid surfaces. Advances in Colloid and Interface Science, 222:377–384, 2015.

[102] D. Langevin and F. Monroy. Adsorption dynamics of surfactants at the air/water interface: a critical review of mathematical models, data, and mechanisms. Advances in Colloid and Interface Science, 206:141–149, 2014.

[103] L. Gary Leal. Advanced Transport Phenomena: Fluid Mechanics and Convective Transport Processes. Cambridge University Press, 2007.

[104] K.Y.C. Lee. Collapse mechanisms of langmuir monolayers. Annu. Rev. Phys. Chem., 59:771–791, 2008.

[105] F. Lhert, W. Yan, S.C. Biswas, and S.B. Hall. Effects of hydrophobic surfactant proteins on collapse of pulmonary surfactant monolayers. Biophys. J., 93(12):4237–4243, 2007.

[106] S. Lin, K. McKeigue, and C. Maldarelli. Effect of cohesive energies between adsorbed molecules on surfactant exchange processes: Shifting from diffusion control for adsorption to kinetic-diffusive control for reequilibration. Langmuir, 10(10):3442–3448, 1994.

[107] M.M. Lipp, K.Y.C. Lee, D.Y. Takamoto, J.A. Zasadzinski, and A.J. Waring. Coexistence of buckled and flat monolayers. Phys. Rev. Lett., 81(8):1650–1653, 1998.

[108] J.Y. Lu, J. Distefano, K. Philips, P. Chen, and A.W. Neumann. Effect of the compression ratio on properties of lung surfactant (bovine lipid extract surfactant) films. Respiration Physiology, 115:55–71, 1999.

[109] E.H. Lucassen-Reynders, A. Cagna, and J. Lucassen. Gibbs elasticity, surface dilational modulus and diffusional relaxation in nonionic surfactant monolayers. Colloids and Surfaces A: Physicochemical and Engineering Aspects, 186:63–72, 2001.

[110] K. Lunkenheimer, K. Winsel, H. Fruhner, J. Fang, K.-D. Wantke, and K. Siegler. Dynamic surface tension and surface area elasticity of adsorbed

pulmonary surfactant layers. Colloids and Surfaces A: Physicochemical and Engineering Aspects, 114:199–210, 1996.

[111] H. Manikantan and T.M. Squires. Surfactant dynamics: hidden variables controlling fluid flows. Journal of Fluid Mechanics, 892:P1 1–115, 2020.

[112] C. Marquez-Beltran, I. Martinez-Balbuena, A. Arteaga-Jimenez, and E. Hernandez-Zapata. Applicability of the gibbs adsorption isotherm to the analysis of experimental surface-tension data for ionic and nonionic surfactants. Advances in Colloid and Interface Science, 247:178–184, 2017.

[113] D. Marsh and M.D. King. Prediction of the critical micelle concentrations of mono- and di-acyl phospholipids. Chem. Phys. Lipids, 42:271–277, 1986.

[114] A. Martinez-Calvo and A. Sevilla. Temporal stability of free liquid threads with surface viscoelasticity. Journal of Fluid Mechanics, 846:877–901, 2018.

[115] O. Matar, Y.L. Zhang, and R.V. Craster. Surfactant driven flows overlying a hydrophobic epithelium: film rupture in the presence of slip. Journal of Colloid and Interface Science, 264:160–175, 2003.

[116] R. Miller, P. Joos, and V.B. Fainerman. Dynamic surface and interfacial tensions of surfactant and polymer solutions. Advances in Colloid and Interface Science, 49:249–302, 1994.

[117] D. G. Moris and D. Sheppard. Pulmonary emphysema: When more is less. Physiology, 21:396–403, 2006.

[118] J. Morris, E.P. Ingenito, L. Mark, R.D. Kamm, and M. Johnson. Dynamic behavior of lung surfactant. ASME J. Biomech. Eng., 123:106–113, 2001.

[119] M. Muradoglu, F. Romanò, H. Fujioka, and J.B. Grotberg. Effects of surfactant on propagation and rupture of a liquid plug in a tube. Journal of Fluid Mechanics, 872:407–437, 2019.

[120] D. Myers. Surfaces, Interfaces and Colloids. Wiley, 1999.

[121] R. H. Notter. Lung Surfactant: Basic Science and Clinical Applications. CRC Press, 2000.

[122] R.H. Notter, P.R. Chess, and Z. Wang. Surfactant — overview. In Geoffrey J. Laurent and Steven D. Shapiro, editors, Encyclopedia of Respiratory Medicine, pages 135 – 143. Academic Press, Oxford, 2006.

[123] M. Ochs, J.R. Nyengaard, A. Jung, L. Knudsen, M. Voigt, T. Wahlers, J. Richter, and H.J.G. Gundersen. The number of alveoli in the human lung. Am. J. Respir. Crit. Care Med., 169:120–124, 2004.

[124] M. J. Oldham and O. R. Moss. Pores of kohn: forgotten alveolar structures and potential source of aerosols in exhaled breath. J. Breath Res., 13:021003, 2019.

[125] U. Olgac and Muradoglu. Computational modeling of unsteady surfactant-laden liquid plug propagation in neonatal airways. Physics of Fluids, 25:071901, 2013.

[126] A. Oron, S. H. Davis, and G. S. Bankoff. Long-scale evolution of thin liquid films. Reviews of Modern Physics, 69:931–980, 1997.

[127] D.R. Otis, E.P. Ingenito, R.D. Kamm, and M. Johnson. Dynamic surface tension of surfactant TA: experiments and theory. J. Appl. Physiol., 77(6):2681–2688, 1994.

[128] E. Parra and J. Perez-Gil. Composition, structure and mechanical properties define performance of pulmonary surfactant membranes and films. Chemistry and Physics of Lipids, 185:153–175, 2015.

[129] M. Peng, A. V. Nguyen, J. Wang, and R. Miller. A critical review of the model fitting quality and parameter stability of equilibrium adsorption models. Advances in Colloid and Interface Science, 262:50–68, 2018.

[130] A. Pereira and S. Kalliadasis. On the transport equation for an interfacial quantity. Eur. Phys. J. Appl. Phys., 44:211–214, 2008.

[131] A. Pereira, P. M. J. Trevelyan, U. Thiele, and S. Kalliadasis. Dynamics of a horizontal thin liquid film in the presence of reactive surfactants. Physics of Fluids, 19:112102, 2007.

[132] J. Perez-Gil. Structures of pulmonary surfactant membranes and films: The role of proteins and lipid-proteins interactions. Biochimica et Biophysica Acta, 1778:1676–1695, 2008.

[133] J. Perez-Gil. A recipe for a good clinical pulmonary surfactant. Biomedical Journal, 45:615–628, 2022.

[134] J. Perez-Gil and T.E. Weaver. Pulmonary surfactant pathophysiology: Current models and open questions. Physiology, 25:132–141, 2010.

[135] M.D. Phan, J. Lee, and K. Shin. Collapsed states of langmuir monolayers. Journal of Oleo Science, 65:385–397, 2016.

[136] U. Pison, R. Herold, and S. Schürch. The pulmonary surfactant system: biological functions, components, physicochemical properties and alterations during lung disease. Colloids and Surfaces A: Physicochemical and Engineering Aspects, 114:165–184, 1996.

[137] A. Podgorski and L. Gradon. Hydrodynamic model of pulmonary clearance. Chemical Engineering Science, 44:741–749, 1989.

[138] A. Podgorski and L. Gradon. Dynamics of pulmonary surfactant system and its role in alveolar cleansing. Ann. Occup. Hyg, 34:137–147, 1990.

[139] A. Podgorski and L. Gradon. An improved mathematical model of hydrodynamical self-cleansing of pulmonary alveoli. Ann. Occup. Hyg., 37:347—-365, 1993.

[140] F. Possmayer, K. Nag, K. Rodriguez, R. Qanbar, and S. Schürch. Surface activity in vitro: role of surfactant proteins. Comparative Biochemistry and Physiology Part A, 129:209–220, 2001.

[141] Ronald F. Probstein. Physicochemical Hydrodynamics. John Wiley and Sons, Ltd, 1994.

[142] A.J. Prosser and E.I. Franses. Adsorption and surface tension of ionic surfactants at the air-water interface: review and evaluation of equilibrium models. Colloids and Surfaces A: Physicochemical and Engineering Aspects, 178:1–40, 2001.

[143] F. Ravera, M. Ferrari, E. Santini, and L. Liggieri. Influence of surface processes on the dilational visco-elasticity of surfactant solutions. Advances in Colloid and Interface Science, 117:75–100, 2005.

[144] K. M. Ridge, L. Linz, F. W. Flitney, E. R. Kuczmarski, Y. H. Chou, M. B. Omary, J. I. Sznajder, and R. D. Goldman. Keratin 8 phosphorylation by protein kinase c δ regulates shear stress-mediated disassembly of keratin intermediate filaments in alveolar epithelial cells. J. Biol. Chem., 280:30400–30405, 2005.

[145] E. Roan and C. M. Waters. What do we know about mechanical strain in lung alveoli? Am J Physiol Lung Cell Mol Physiol, 301:L625–L635, 2011.

[146] S. Rugonyi, S.C. Biswas, and S.B. Hall. The biophysical function of pulmonary surfactant. Respir. Physiol. Neurobiol., 163:244–255, 2008.

[147] S. M. I. Saad. Axisymmetric drop shape analysis (ADSA) and lung surfactant. PhD thesis, University of Toronto, 2011.

[148] S.M. Saad, Z. Policova, E.J. Acosta, M.L. Hair, and A.W. Neumann. Mixed DPPC/DPPG monolayers at very high film compression. Langmuir, 25:10907–10912, 2009.

[149] S.M.I. Saad, A.W. Neumann, and E.J. Acosta. A dynamic compression-relaxation model for lung surfactants. Colloids and Surfaces A: Physicochemical and Engineering Aspects, 354:34–44, 2010.

[150] S.S.I. Saad, Z. Policova, E.J. Acosta, and A.W. Neumann. Effect of surfactant concentration, compression ratio and compression rate on the surface activity and dynamic properties of a lung surfactant. Biochimica et Biophysica Acta, 1818:103–116, 2012.

[151] A. Samanta. Effect of surfactant on the linear stability of a shear-imposed fluid flowing down a compliant substrate. Journal of Fluid Mechanics, 920:A23, 2021.

[152] W.R. Schief, M. Antia, B.M. Discher, S.B. Hall, and V. Vogel. Liquid-crystalline collapse of pulmonary surfactant monolayers. Biophys. J., 84(6):3792–3806, 2003.

[153] A. Schürch, F.H.Y. Green, and H. Bachofen. Formation and structure of surface films: captive bubble surfactometry. Biochim. Biophys. Acta, 1408:180–202, 1998.

[154] A. Schürch, D. Schürch, T. Curstedt, and B. Robertson. Surface activity of lipid extract surfactant in relation to film area compression and collapse. J. Appl. Physiol., 77(2):974–986, 1994.

[155] S. Schürch, R. Qanbar, H. Bachofen, and F. Possmayer. The surface-associated surfactant reservoir in the alveolar lining. Biol Neonate, 67(suppl 1):61–76, 1995.

[156] L.E. Scriven. Equation of motion for newtonian surface fluids. Chemical Engineering Science, 12:98–108, 1960.

[157] A. Shmyrov, A. Mizev, I. Mizeva, and A. Shmyrova. Electrostatic precipitation of exhaled particles for tensiometric examination of pulmonary surfactant. J. Aerosol Sci., 151:105622, 2021.

[158] S. Sivaramakrishnan, J. V. DeGiulio, L. Lorand, R. D. Goldman, and K. M. Ridge. Micromechanical properties of keratin intermediate filament networks. Proc. Natl. Acad. Sci. USA, 105:889–894, 2008.

[159] R.D. Smith and J.D. Berg. The collapse of surfactant monolayers at the air-water interface. Journal of Colloid and Interface Science, 74:273–286, 1980.

[160] V. Starov and I. Ivanov. FLUID MECHANICS OF SURFACTANT AND POLYMER SOLUTIONS. Springer-Verlag Wien GmbH, 2004.

[161] V.M. Starov and M.G. Velarde. Surface forces and wetting phenomena. J. Phys. : Condens. Matter, 21:464121, 2009.

[162] A. Stetten, S.V. Iasella, T.E. Corcoran, S. Garoff, T.M. Przybycien, and R.D. Tilton. Surfactant-induced marangoni transport of lipids and theurapetics within the lung. Current Opinion in Colloid & Interface Science, 36:58–69, 2018.

[163] P. Stevenson, X. Li, R. Shaw, and G.M. Evans. A simple numerical solution to the ward–tordai equation for the adsorption of non-ionic surfactants. Computers & Chemical Engineering, 34:146–153, 2010.

[164] H.A. Stone. A simple derivation of the time-dependent convective-diffusion equation for surfactant transport along a deforming interface. Physics of Fluids A: Fluid Dynamics, 2:111–112, 1990.

[165] J. Sznitman. Respiratory microflows in the pulmonary acinus. Journal of Biomechanics, 46:284–298, 2013.

[166] J. Sznitman. Revisiting airflow and aerosol transport phenomena in the deep lungs with microfluidics. Chemical Reviews, 122:7182–7204, 2022.

[167] J. Sznitman, T. Heimsch, J. H. Wildhaber, A. Tsuda, and T. Rosgen. Respiratory flow phenomena and gravitational deposition in a three-dimensional space-filling model of the pulmonary acinar tree. J. Biomech. Eng., 131:031010, 2009.

[168] R. Todorov, D. Exerowa, D. Platikanov, F. Bianco, and R. Razzetti. Evaluation of therapeutic pulmonary surfactants by thin liquid film methods. Advances in Colloid and Interface Science, 222:709–715, 2015.

[169] A. Tsuda, F.S. Henry, and J.B. Butler. Gas and aerosol mixing in the acinus. Respiratory Physiology & Neurobiology, 163:139–149, 2008.

[170] A. F. Tsuda, S. Henry, and J. P. Butler. Chaotic mixing of alveolated duct flow in rhythmically expanding pulmonary acinus. J. Appl. Physiol., 79:1055–1063, 1995.

[171] A. F. Tsuda, S. Henry, and J. P. Butler. Particle transport and deposition: basic physics of particle kinetics. Compr. Physiol., 3:1437—-1471, 2013.

[172] A. F. Tsuda, E. Laine-Pearson, and P. E. Hydon. Why chaotic mixing of particles is inevitable in the deep lung. J. Theor. Biol., 286:57–66, 2011.

[173] M. van den Tempel, J. Lucassen, and E.H. Lucassen-Reynders. Application of surface thermodynamics to gibbs elasticity. Journal of Physical Chemistry, 69(6):1798–1804, 1965.

[174] D. M. Vasilescu, Z. Gao, P. K. Saha, L. Yin, G. Wang, B. Haefeli-Bleuer, M. Ochs, E. R. Weibel, and E. A. Hoffman. Assessment of morphometry of pulmonary acini in mouse lungs by nondestructive imaging using multiscale microcomputed tomography. Proc. Natl. Acad. Sci. USA, 109:17105—-17110, 2012.

[175] R.W. Walters, R.R. Jenq, and S.B. Hall. Distinct steps in the adsorption of pulmonary surfactant to an air–liquid interface. Biophys. J., 78:257–266, 2000.

[176] F. Wang, J. Liu, and H. Zeng. Interactions of particulate matter and pulmonary surfactant: Implications for human health. Advances in Colloid and Interface Science, 284:102244, 2020.

[177] P. Warszynski, K-D. Wantke, and H. Fruhner. Surface elasticity of oscillating spherical interfaces. Colloids and Surfaces A: Physicochemical and Engineering Aspects, 139:137–153, 1998.

[178] H.-H. Wei, S. W. Benintendi, D. Halpern, and J. B. Grotberg. Cycle-induced flow and transport in a model of alveolar liquid lining. Journal of Fluid Mechanics, 483:1–36, 2003.

[179] H.-H. Wei, H. Fujioka, R. B. Hirschl, and J. B. Grotberg. A model of flow and surfactant transport in an oscillatory alveolus partially filled with liquid. Phys. Fluids, 17:031510, 2005.

[180] E. R. Weibel. The Morphometry of the Human Lung. Academic Press: New York, 1963.

[181] E.R. Weibel. The Pathway for Oxygen. Harvard University Press, Cambridge Mass, 1984.

[182] F. Wildeboer-Venema. The influences of temperature and humidity upon the isolated surfactant film of the dog. Respir. Physiol., 39:63–71, 1980.

[183] N. Wüstneck, R. Wüstneck, V.B. Fainerman, R. Miller, and U. Pison. Interfacial behaviour and mechanical properties of spread lung surfactant protein/lipid layers. Colloids and Surfaces B: Biointerfaces, 21:191–205, 2001.

[184] N. Wüstneck, R. Wüstneck, and U. Pison. Surface dilatational behavior of pulmonary surfactant components spread on the surface of a captive bubble. 3. dipalmitoyl phosphatidylcholine, surfactant protein c, and surfactant protein b. Langmuir, 19:7521–7527, 2003.

[185] R. Wüstneck, J. Perez-Gil, N. Wüstneck, A. Cruz, V.B. Fainerman, and U. Pison. Interfacial properties of pulmonary surfactant layers. Adv. Colloid Interface Sci., 117:33–58, 2005.

[186] R. Wüstneck, N. Wüstneck, B. Moser, B. Karageorgieva, and U. Pison. Surface dilatational behavior of pulmonary surfactant components spread on the surface of a pendant drop. 1. dipalmitoyl phosphatidylcholine and surfactant protein c. Langmuir, 18:1119–1124, 2002.

[187] R. Wüstneck, N. Wüstneck, B. Moser, and U. Pison. Surface dilatational behavior of pulmonary surfactant components spread on the surface of a pendant drop. 2. dipalmitoyl phosphatidylcholine and surfactant protein b. Langmuir, 18:1125–1130, 2002.

[188] G. Xu, C. Hao, L. Zhang, and R. Sun. Investigation of surface behavior of DPPC and curcumin in langmuir monolayers at the air-water interface. Scanning, 2017:1–12, 2017.

[189] L. Xu, Y. Yang, and Y.Y. Zuo. Atomic force microscopy imaging of adsorbed pulmonary surfactant films. Biophys. J., 119:756–766, 2020.

[190] W. Yan, B. Piknova, and S.B. Hall. The collapse of monolayers containing pulmonary surfactant phospholipids is kinetically determined. Biophysical Journal, 89:306–314, 2005.

[191] W.F. Yan and S.B. Hall. The melting behaviors of supercompressed metastable pulmonary surfactant film. Biophys. J., 88:531a, 2005.

[192] S.-H. Yu, F.X. McCormack, D.R. Voelker, and F. Possmayer. Interactions of pulmonary surfactant protein SP-A with monolayers of dipalmi-

toylphosphatidylcholine and cholesterol. roles of SP-A domains. J. Lipid Res., 40:920–929, 1999.

[193] J.A. Zasadzinski, J. Ding, H.E. Warriner, F. Bringezu, and Alan J. Waring. The physics and physiology of lung surfactants. Current Opinion in Colloid & Interface Science, 6:506–513, 2001.

[194] T. B. Zeltner, T. D. Sweeney, W. A. Skornik, H. A. Feldman, and J. D. Brain. Retention and clearance of 0.9-micron particles inhaled by hamsters during rest or exercise. J. Appl. Physiol., 70:1137—-1145, 1991.

[195] H. Zhang, Y.E. Wang, Q. Fan, and Y.Y. Zuo. On the low surface tension of lung surfactant. Langmuir, 27:8351–8358, 2011.

[196] Y. Zheng, H. Fujioka, and J. B. Grotberg. Effects of gravity, inertia, and surfactant on steady plug propagation in a two-dimensional channel. Physics of Fluids, 19:082107, 2007.

[197] Y.Y. Zuo, R. Gitiafroz, E. Acosta, Z. Policova, P.N. Cox, M.L. Hair, and A.W. Neumann. Effect of humidity on the adsorption kinetics of lung surfactant at air-water interfaces. Langmuir, 21(23):10593–10601, 2005.

[198] Y.Y. Zuo, C. Rimei, W. Xianju, Y. Jinlong, Z. Policova, and A.W. Neumann. Phase transitions in dipalmitoylphosphatidylcholine monolayers. Langmuir, 32(33):8501–8506, 2016.

[199] Y.Y. Zuo, R. Veldhuizen, A.W. Neumann, N. O. Petersen, and F. Possmayer. Current perspectives in pulmonary surfactant—inhibition, enhancement and evaluation. Biochimica et Biophysica Acta, 1778:1947–1977, 2008.